EXPLORING APPLICATIONS OF GRAPHENE ELECTRICAL PROPERTIES

MARCOS FERNANDO PEREZ-PUCHETA

Exploring Applications of Graphene Electrical Properties

A thesis submitted for the partial fulfilment of the requirement for the degree of

Doctor of Philosophy

In the faculty of Science of Durham University

Marcos Fernando Pérez-Pucheta

Department of Chemistry

Durham University

September 2023

Abstract

Graphene has attracted the attention of the scientific community over the last decade due to its outstanding properties, such as high thermal and high electrical conductivity and remarkable mechanical properties. Intensive research has focussed on developing applications to harness these properties. The broad range of applications includes developing long-lasting batteries, flexible and transparent screens, super tough polymer composite materials, and highly selective sensors for early disease detection.

Since graphene was discovered, its high conductivity inspired the development of conductive polymers and composites. Graphene platelets and their derivatives can be readily used in various polymer-based applications since they are commercially available and readily prepared in wet conditions starting from graphite. However, it has been found that uniform graphene dispersion in polymer matrices is extremely difficult. Here, we describe a novel way in which graphene can be preferentially located at the interface of immiscible polymer blends during extrusion so the polymer microstructure can be used as a scaffold for graphene to form a conductive network. Furthermore, this approach can be used to make two immiscible polymers more compatible and improve the rheological properties of the blend.

In addition to platelets, graphene films synthesized by chemical vapour deposition (CVD) can be used in applications such as developing graphene-based sensors that can detect picomolar concentrations of analytes. Graphene growth on copper by CVD is the accepted method for high-quality monolayer graphene synthesis. This makes graphene transfer between surfaces an unavoidable step for any application. Although several protocols have been proposed to transfer graphene, they are difficult to reproduce, particularly over large areas. By applying a conformability concept, here we describe a protocol for a successful transfer of graphene on substrates with different roughness using Si/SiO_2 as a typical rigid and flat widely used in electronic applications and the skin as an example of a highly rough and soft substrate.

Declaration

The work presented was undertaken within the Department of Chemistry of the University of Durham.

Graphene synthesized by chemical vapour deposition mentioned in Chapter 6 was kindly provided by Selene Muñoz-Vargas.

XPS data collection was performed at the EPSRC National Facility for XPS ('Harwell XPS'), operated by Cardiff University and UCL, under contract No. PR16195. XPS fitting and analysis was done by Dr David Morgan.

"Look at the sky. Ask yourselves: Has the sheep eaten the flower, yes or no? And you will see how everything changes."

Antoine de Saint-Exupéry

The Little Prince

Acknowledgements

First, Thanks to my supervisors, Professors Karl Coleman and Robert Pal. Thank you, Professor Karl, for letting me work in your group and for your advice and support at any moment. Thanks for letting me explore ideas from a curious, adventurous, and critical perspective. Also, thanks to Robert Pal for his support during the last stage of the PhD, which was crucial for me to finish this journey. Thanks for always cheering me up to finish and helping me see far beyond what I thought was possible.

Thank you, Selene! For being my partner, counsellor, lab buddy, engineer, pastry cook, nurse, etc. Thank you for being by my side in good and bad times and every adventure. You have been the best person I could ever imagine, and I learned a lot from you, not only chemistry-related stuff. Thank you for letting me be part of your life.

Also, my deepest gratitude to Stephen Boothroyd. There is so much I learned from you, and above all, thank you for being so patient and generous during the first year. Also, thank you to Dr Richard Thompson for letting me work in his lab.

I want to thank all the staff at Durham University for being so helpful. My deepest gratitude to the fantastic people from the glassblowing workshops (Aaron Brown and Malcolm Richardson), mechanical workshops (Neil Holmes, Paul White and Tony Newman) and electrical workshops (Kelvin Appleby and Bryan Denton). You are absolutely brilliant people! Literally, I could not have done anything without your help and ideas. Also, thanks to the rest of the staff from all departments. Thanks to Helene Rusby, Tony Humphries, Tony Baxter, Annette Passmoor, and Jean Eccleston. I am so grateful to Emily Chester for being so kind and helpful during the last year.

Special thanks to Douglas Carswell for running all those TGA and DSC. Also, thank you to all who contributed and helped me during training or data analysis: Dominikus Heift, Juan Aguilar, Diana Alvarez, Leon Bowen, Gary Oswald, Gary Southern, Clare Mahon and Aileen Congreve.

Last but not least, thanks to my family and friends for their support along this way. *Gracias, mamá y papá por su apoyo y consejos hasta el final. Igualmente, te agradezco Carlos por estar ahí desde que empezó esta aventura. Muchas gracias a todos por confiar en mí.*

Thanks to The National Council of Humanities, Science and Technology of Mexico (Conahcyt) for the scholarship 2018-000009-01EXTF-00294.

Table of contents

Abbreviations

AFM	Atomic Force Microscopy
AgNWs	Silver nanowires
CRGO	Chemically Reduced Graphene Oxide
CVD	Chemical Vapor Deposition
DMF	Dimethylformamide
DTG	First Derivative of The Weight Loss With Respect to Temperature
ECG	Electrocardiogram
EVA	Ethyl Vinyl Acetate
FLG	Few-Layer Graphene
GO	Graphene Oxide
GPTMS	3-Glycidyloxypropyl Trimethoxysilane
HOPG	Highly Ordered Pyrolytic Graphite
MWCNTs	Multiwall Carbon Nanotubes
PC	Poly bisphenol A Carbonate
PET	Polyethylene Terephthalate
PLA	Polylactic Acid
PMMA	Polymethyl Methacrylate
PS	Polystyrene
PS-COOH	Carboxyl Terminated Polystyrene
PXRD	Powder X-Ray Diffraction
RGO	Reduced Graphene Oxide
SAED	Selected Area Electron Diffraction
SEM	Scanning Electron Microscopy
TEM	Transmission Electron Microscopy
TGA	Thermogravimetric Analysis
TRGO	Thermally Reduced Graphene Oxide
XPS	X-Ray Photoelectron Spectroscopy

1 Introduction

1.1 Background

The word graphene was first introduced in 1968 by Hans-Peter to describe an allotrope of carbon of a single planar sheet of sp^2-bonded carbon atoms, densely packed in a honeycomb. Back then, the word graphene was used in the context of graphite intercalated compounds (GIC), which today are considered precursors in many chemical processes for graphene production.[1,2] Graphene was first theoretically predicted in 1974 by Phillip Wallace[3] but it was not until 2004 when Andre Geim and Konstantin Novoselov from Manchester University first isolated high-quality monolayer graphene and proved the existence of this 2D material.[4] Nowadays, graphene can be considered as the building block of other carbon structures such as (Figure 1.1):[5,6]

- Graphite: A three-dimensional structure formed by stacks of graphene layers.
- Carbon nanotubes: A one-dimensional structure that emerges when a graphene sheet is rolled.
- Fullerenes: A zero-dimensional structure where pentagonal carbon rings are intercalated with hexagonal ones to form a ball structure.

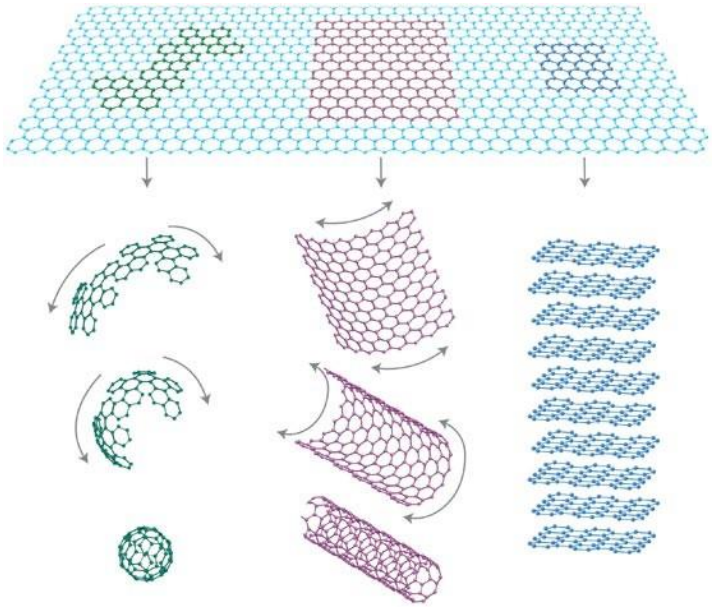

Figure 1.1 Graphene as building block of fullerenes, carbon nanotubes and graphite. Reproduced from reference 5.

The outstanding properties of graphene come from its unique structure. Graphene sheets have σ-bonds and π-bonds. The delocalized π-bonds contribute to electron conduction and provide a weak interaction between graphene layers. On the other hand, the σ-bonds form a rigid backbone of the hexagonal structure.[7] Even when sharing a similar structure, bilayer graphene exhibits significantly different properties when stacked. When two single crystal graphene films, which have a hexagonal periodic pattern, are overlaid with a relative twist angle θ a moiré pattern is formed, where the unit cell is the minimum repetitive unit (Figure 1.2). Therefore, tuning of the electronic structure and energy band make it possible to obtain properties different from the monolayer graphene. For example, when the relative twist angle in a bilayer graphene stack is ~1.1° it can exhibit superconductive and insulating properties depending on the number of charges per moiré unit cell.[8–10]

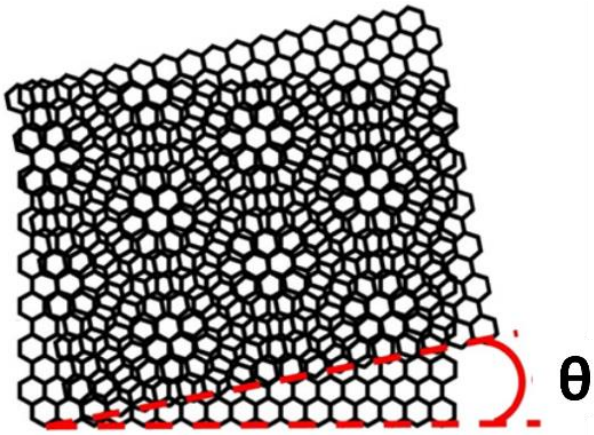

Figure 1.2 Moiré superlattice formed by the twisted graphene layers. Adapted from reference 9.

1.2 Graphene properties

1.2.1 Mechanical and thermal properties

The mechanical properties of monolayer graphene were first measured by nanoindentation using atomic force microscopy (AFM). In this experiment, graphene flakes were deposited on a silicon substrate with circular holes. Then, the tip of the AFM was placed in the centre of the hole to induce the film's breaking. The breaking strength was estimated to be 42 N/m. The Young's modulus was calculated to be around $E = 1 \pm 0.1$ TPa and the intrinsic strength $\sigma = 130$ GPa. These outstanding mechanical properties were attributed to

the strong σ bonds in the sp^2 network and motivated several investigations on graphene composites, that is, the use of graphene to reinforce a matrix, such as polymers, metals and ceramics.[11]

Graphene obtained from mechanical exfoliation of graphite[1] shows a good thermal conductivity of ~5000 W $m^{-1}K^{-1}$ even in ambient conditions,[12] much higher than that for single, ~3000 W $m^{-1}K^{-1}$, and multiwalled carbon nanotubes, ~3500 W $m^{-1}K^{-1}$,[7] However, measurements on graphene grown by chemical vapour deposition (CVD) showed a much lower value of ~ 2500 W $m^{-1}K^{-1}$. It was hypothesized that the number of layers, type of stacking, defects and doping could have an influence.[13] Given its thermal properties graphene has been proposed for applications as heat sinks to improve the performance of electronic devices.[14,15]

1.2.2 Optical and electrical properties

Electrical conductivity and transparency are requirements for thin conductive films. Single-layer graphene can meet these two requirements as it only absorbs 2.3 % of white light. As expected, transmittance decreases with the number of layers. Three and four layers of graphene have a transmittance of 92.9 % and 90.1 %, respectively in the visible region at 550 nm.[16,17]

Also, graphene exhibits a low sheet resistance for the monolayer graphene (275 Ω/sq) which can be decreased to 168 Ω/sq for a trilayer structure.[18] High transparency and low resistivity suggest its potential use to replace indium tin oxide (ITO), which is frequently used in displays, touch panels, light-emitting diodes and solar cells. For graphene to replace ITO, it must have a sheet resistance lower than 100 Ω/sq and have a transmittance higher than 90% in the visible range. However, for novel applications lower resistivity values (<20 Ω/sq) are often desired.

[1] Mechanical exfoliation of graphene is explained and illustrated in section 1.3.1 and Figure 1.4 respectively.

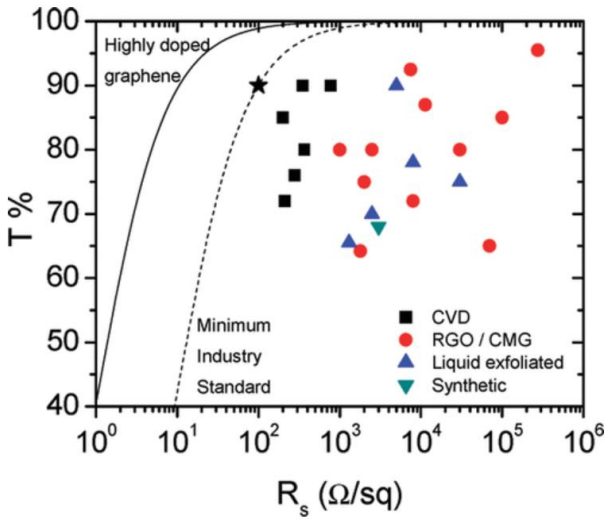

Figure 1.3 Transmittance and sheet resistance of data published in papers (given in the supporting information from reference [19]. The dashed line represents σ_{DC}/σ_{OP} =35 and the star the minimum standard requirements (transmittance:90 % and sheet resistance 100 Ω/sq). The solid line represents σ_{DC}/σ_{OP} =330 for highly doped. RGO and CMG stand for reduced graphene oxide and chemically modified graphene. Reproduced from reference 19.

While the sheet resistance of graphene is controlled by the electrical conductivity (σ_{DC}), the optical transmittance is controlled by the optical conductivity (σ_{OP}).[19] In an early review it was proposed that the σ_{DC}/σ_{OP} ratio can be used as a metric to assess the performance of graphene when compared to ITO. It was estimated that $\frac{\sigma_{DC}}{\sigma_{OP}}$>35 for graphene to compete with ITO, but even graphene-grown CVD did not meet the standard, as the theoretical ratio σ_{DC}/σ_{OP} was estimated to be around 2.6. However, theoretical derivations determined that a practical value of around 330 could be obtained if graphene is doped.[19] Graphene doping can be done by directly replacing carbon atoms in the lattice with others such as nitrogen and boron.[20] It can also be doped by adsorption of electron withdrawing or electron donating molecules. For example, doping graphene films grown by chemical vapour deposition (CVD) with $AuCl_3$ improves the sheet resistance (150 Ω/sq) while keeping the transparency of the films, making them competitive with ITO (5-60 Ω/sq).[20]

Figure 1.3 summarizes typical sheet resistance and transmittance values from the literature and compares them against the minimum standard requirements and the potential value for highly doped graphene. Therefore, it is clear why so many research efforts have been focused on doping graphene to improve its electrical properties.[21–24]

1.3 Production methods

1.3.1 Micromechanical cleavage

Andre Geim and Konstantin Novoselov first employed micromechanical cleavage to isolate graphene in 2004. Because graphene layers are held together by relatively weak van der Waals forces, continuously peeling off graphene layers from highly ordered pyrolytic graphite (HOPG) using scotch tape eventually leads to the isolation of single-layer graphene.[4] Figure 1.4 illustrates the process of isolation and transfer to a substrate. Although this method is not scalable, it has become very popular to create novel 2D heterostructures, resulting in different properties from their bulk structures.[25,26]

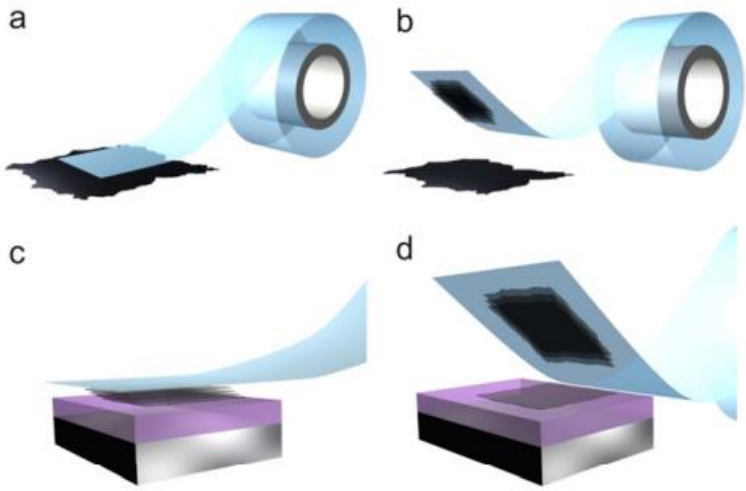

Figure 1.4 Micromechanical cleavage procedure. a, b) adhesive tape is pressed against a 2D crystal and a few crystals remain attached to the tape. This process is repeated several times. c) The tape with crystals is pressed against the substrate used for transfer. d) Upon peeling off, a layer of crystals is transferred. Adapted from reference 25.

1.3.2 Liquid phase exfoliation: Sonication and shear mixing

In principle, any external force that supplies enough energy to overcome weak van der Waals forces in graphite will result in graphene exfoliation. The phenomenon behind the exfoliation through sonication is cavitation. During cavitation, the sound waves create zones of low pressure and high pressure. When the pressure is reduced, part of the liquid vaporizes creating bubbles, which implode during the high-pressure cycle (Figure 1.5a). The collapse of a bubble near the edges of graphite can also induce a wedging effect, inducing exfoliation to some extent. However, one of the shortcomings is that during the cavitation, high

temperature and pressure localized zones can cause defects such as holes (Figure 1.5b) and can introduce functional groups such as -COOH and C-O-C due to the presence of oxygen from air in the solvents, ultimately disrupting the graphitic lattice.[27,28] These defective sites cause scattering of the charge carrier, decreasing the mobility of graphene, which is important for electronic applications.[29]

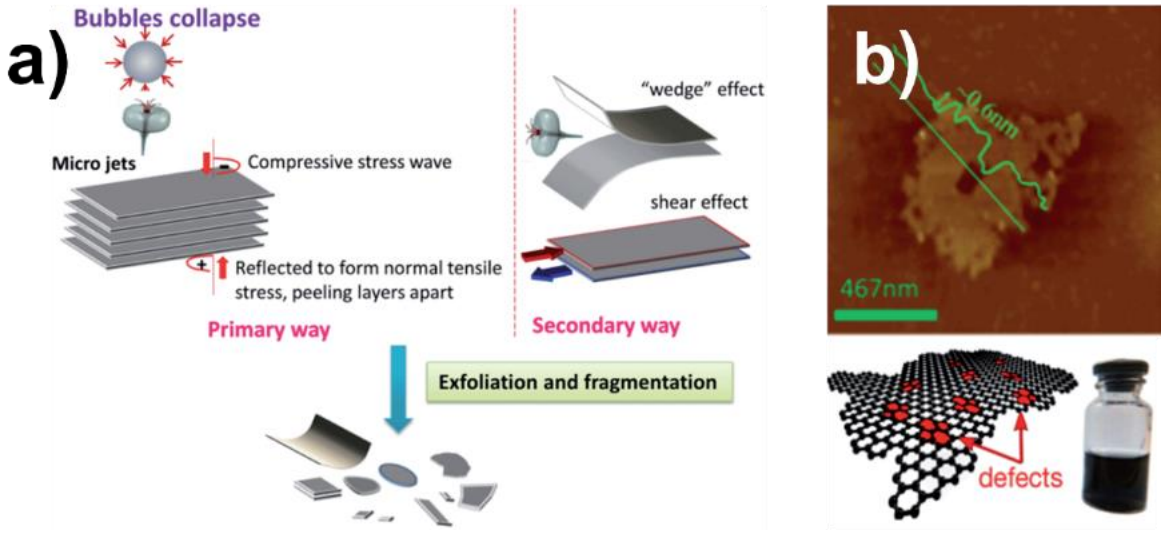

Figure 1.5 a) Two main mechanisms behind exfoliation through sonication: unbalanced compressive forces that create a shear effect and the wedging effect from microjets. b) Exfoliated graphite flake around 0.6 nm thickness obtained through sonication exhibiting a hole in the centre and irregular edges, typical features of defective flakes. Adapted from references 27,30.

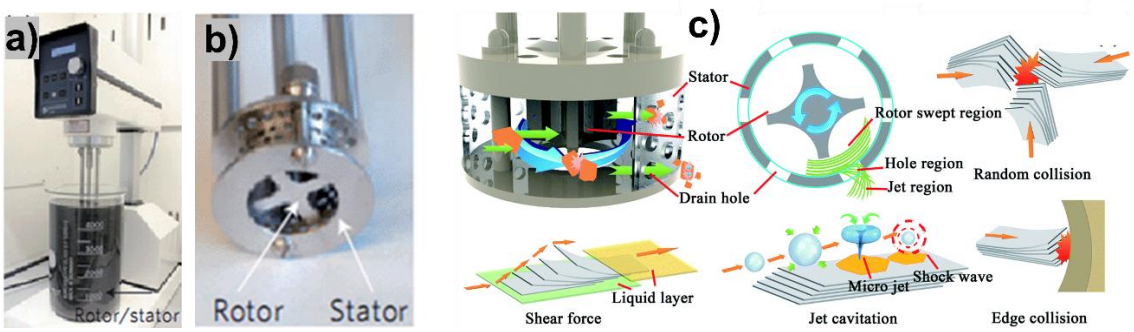

Figure 1.6 a,b) Typical shear mixer consisting of a rotor/stator system. c) Main mechanisms through which exfoliation occurs due to shear forces in the liquid media, collisions among graphite flakes, cavitation, and collisions against the stator. Adapted from references 31,32

Shear mixing is a well-known technology that can be easily scaled to produce graphene dispersions and does not involve any chemical step. Figure 1.6a,b illustrates a typical rotor/stator system and the phenomena behind exfoliation, the dominant one being the shear forces exerted in the small region created by the stator and rotor (Figure 1.6c). Paton *et al.* explored the large-scale production of graphene from the exfoliation of graphite

in sodium cholate using a rotor/stator system like the one shown in Figure 1.6a. They demonstrated it was possible to achieve high rates of graphene production (5.3 g/h) with low defects. The model they developed showed that exfoliation occurs when the local minimum shear rate exceeds 10^4 s^{-1} even if a turbulent flow regime was not reached.[31] Their theory was also tested using a kitchen blender as the source of the shearing force, demonstrating it was possible to obtain graphene flakes in a simple way.[33] This seminal work inspired others to use the laminar flow to exfoliate graphite on large scales and optimize the experimental conditions and also paved the way to exfoliate other 2D materials using this approach, such as MoS_2 and WS_2, which have a non-zero bandgap, making them suitable for electronic applications.[34–37] One of the benefits of this technology is that the amount produced linearly escalates with time.[31] However, cavitation can also happen due to high shear rates around the rotor/stator system. The shear rate can, however, be indirectly controlled by adjusting the speed to the rotor.

In any liquid phase exfoliation process, the solvent plays an important role. From the thermodynamic perspective, exfoliated graphene sheets will remain stable in solution if the energetic cost for the system graphene/solvent is small. The enthalpy of mixing of a solvent and graphite can be determined by calculating the energy required to separate all the components (solvent/graphene sheet) to infinity minus the energy to bring them back together in the form of a solvent/graphene dispersion but with flakes of different thickness.[38] Hernandez *et al.* derived Eq. 1.1 to estimate the enthalpy of mixing per unit volume as function of the surface energy and thickness of graphene and the surface energy of the solvent:[38]

$$\frac{\Delta H_{mix}}{V_{mix}} \sim \frac{2}{t_{flake}} (\delta_G - \delta_{solv})^2 \varphi \qquad \text{Eq. 1.1}$$

Where δ_G and δ_{solv} are the root squares of the surface energy of graphene and the solvent, respectively, t_{flake} is the thickness of the graphene flakes and φ is the graphene volume fraction. Then, the system's energy is minimized when the surface energy of the solvent matches the surface energy of graphene. However, there is some debate on the true value of the surface energy of graphene. Measurements based on the contact angle report values in the range of 57.4-62.2 mJ/m^2 [39] but more sophisticated measurements based on direct measurements of the adhesive force report higher values in the range of 115-119

mJ/m^2.[40] However, experimental work demonstrated that good solvents for graphene have a surface energy in the range of 40-50 mJ/m^2.[41] Some well-known good solvents meet this requirement and have been successfully used for suspensions of carbon nanotubes such as N-methyl 2-pyrrolidone (NMP, 40.8 mJ/m^2), dimethylformamide (DMF, 37.1 mJ/m^2) or γ-butyrolactone (GBL, 46.1 mJ/m^2). However, these solvents have a high boiling point, are toxic and difficult to remove.[38,42,43] This is why solvent exchange or a combination of solvents have been proposed as alternatives to incorporate low boiling point solvents like chloroform, isopropanol or acetone.[44,45]

Usually, the amount of graphene that can be dispersed in solution is low (< 0.1 mg/ml), therefore one alternative is the use of surfactants which allow exfoliation in aqueous solutions, reaching yields in the range of a few mg/ml, an order of magnitude higher than when using only solvents.[46] Typical surfactants used are sodium cholate ($C_{24}H_{41}NaO_6$), sodium dodecylbenzene sulfonate (SDBS), cetyltrimethylammonium (CTAB:$C_{19}H_{42}N_4BrN$) and,7,8,8-tetracyanoquinodimethane (TCNQ: $C_{12}H_4N_4$).[47–49]

1.3.3 Graphene oxide

Currently, graphene oxide is considered one of the most important precursors in graphene-based technology. Graphite oxide was first reported in 1840 by Schafhaeutl and in 1859 by Brodie.[50,51] However, the origins of current methodologies can be traced back to 1958 when Hummers and Offeman proposed a method to produce graphite oxide. In this method, graphite is treated with a mixture of concentrated sulfuric acid, sodium nitrate and potassium permanganate.[52] This procedure allowed the intercalation of sulfuric acid between the layers conforming the graphite and promoting their oxidation at the same time.[53] Here, the term graphite oxide refers to the graphite intercalated compound (GIC). On the other hand, the term graphene oxide is used when the GIC is subject to an exfoliation process to separate the individual graphene flakes. Currently, most methods for graphene oxide production can be considered as modifications of the Hummers method to obtain graphite oxide and an exfoliation step to obtain the graphene oxide (GO).[54–57] One of the main disadvantages of the Hummers' method was the evolution of toxic gases such as NO_2, N_2O_4 and the risk of explosion due to the highly exothermic reaction.[58] A good alternative was developed by Marcano *et al.* that included the use of a combination of phosphoric acid and sulfuric acid[2]. This procedure was less exothermic and was proven to induce less disruption

in the graphitic basal plane when compared to the Hummers' method. Marcano *et al*. argued that the preservation of the basal plane was due to the formation of five-membered cyclic phosphate groups between phosphoric acid and two vicinal diols formed on the basal plane, which prevents overoxidation to the diones.[2] This protective effect of phosphoric acid was also observed during the preparation of graphene nanoribbons by unzipping of carbon nanotubes.[59]

The graphene oxide structure has been proposed as one with non-oxidized regions, where the sp^2 network is preserved, and regions containing oxygen functional groups from the oxidation process.[60] Oxygen groups cause the localization of the π electrons, therefore carrier mobility and concentration are reduced significantly. One of the most accepted structural models was proposed by Lerf and Klinowski based on ^{13}C NMR observations (Figure 1.7). In this model, the plane contains hydroxyl and epoxy functional groups. On the other hand, carboxylic groups are located along the edges.[61,62] Other studies also suggested the presence of esters and tertiary alcohols on the surface and the 5 or 6-membered lactols on the edges as determined from ^{13}C solid state NMR experiments.[63,64]

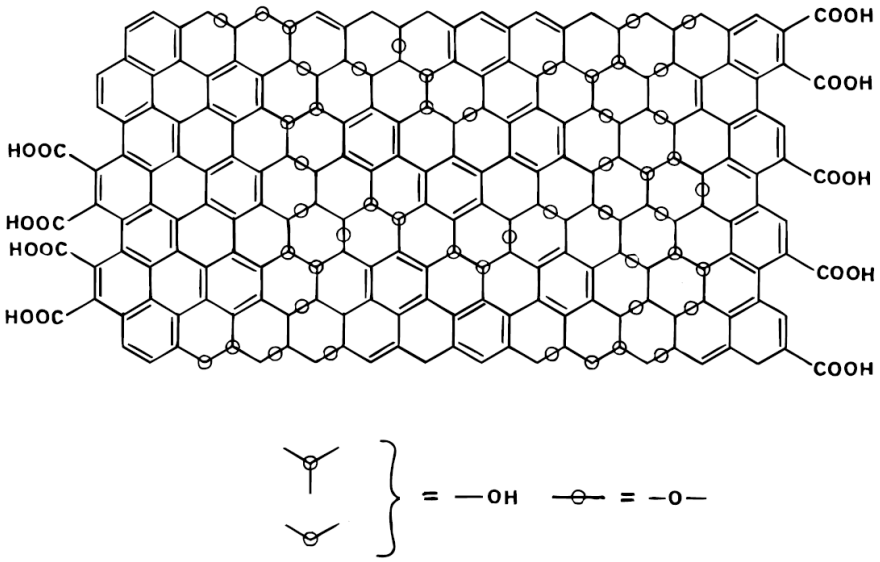

Figure 1.7 Structural model of graphene oxide (GO) proposed by Lerf *et al*. Reproduced from reference 61.

Moreover, the absence of a percolated electrical pathway in sp^2 domains in GO is responsible for a high sheet resistance, typically in the range of 10^{12} Ω/sq.[54,57,65,66] Therefore, many reduction methods have been proposed to recover the graphitic sp^2 network and restore its electrical properties, but they remain limited.[67]As a comparison, from Table 1.1, CVD

monolayer graphene is estimated to have a conductivity of around 3.1×10^6 S cm^{-1}, while graphene oxide reduced by thermal annealing shows conductivities ~ 10^3 S cm^{-1} which is three orders of magnitude lower.[68] Table 1.1 also shows some typical conductivity values using different reducing agents such as hydrazine, ascorbic acid and hydroiodic acid. So, even when the synthesis of graphene oxide is a scalable way to produce graphene, reduction is necessary to partially recover its electrical properties.

Table 1.1 Typical conductivities obtained from different reductions methods reported in the literature and comparison with the conductivity from graphene produced by chemical vapour deposition.

Reduction method	**Conditions**	**Electrical conductivity (S/cm)**	**Reference**
Graphene growth by chemical vapor deposition	-------	3.1×10^6	69
Hydrazine	GO (1 mg/ml)+ hydrazine hydrate (1:1 w/w) and heated at 95 °C for 3 h	5	70
Hydrazine hydrate	GO (0.5 mg/mL in DMF) + 198 µl hydrazine hydrate and autoclaved at 180 °C for 12 h	23.8	71
Hydrazine hydrate+ammonia	7:10 wt ratio of hydrazine to GO + ammonia (and heated at ~ 95 °C for 1 h, pH ~ 10	72	72
Ascorbic acid	50 mg of ascorbic acid in 50 mL GO (0.1 mg/ml)	8	73
Hydroiodic acid followed by thermal reduction	Graphene film on SiO_2 was exposed to HI vapour for 5 minutes followed by annealing at 200 °C for 6 h under vacuum	263	74
Thermal Reduction	3 hours at 1100 °C in ultrahigh vacuum ($<10^{-5}$ Torr)	~10^3	75

1.3.4 Chemical vapour deposition

Graphene was first synthesized on copper using chemical vapour deposition in 2009.[76] Since then, this method has become very popular because it can produce large area, high-uniform and high-quality graphene. Furthermore, this method has proven scalable and controllable, so many research efforts were focused on optimising growth conditions.[76,77] Although the CVD approach is promising, it still has some drawbacks, such as the polycrystalline nature,[78] slow growth rate, high energy consumption[77] and a transfer process that often is complicated and can potentially introduce contamination.[79]

In the CVD process to grow graphene a hydrocarbon source is thermally decomposed on the surface of a catalytic substrate. It involves the following steps: heating, substrate annealing, graphene growth and cooling. Furthermore, the growth step is divided into elemental reactions that occur in the gas phase due to the thermal decomposition of the gas precursor and the presence of a catalytic metal. Even when several studies have shed some light on the graphene growth mechanism, there is no consensus on the true one.[80–83] The inherent complexity of the process allows for a wide range of conditions to be explored. However, previous studies can be used as guidelines for designing customized setups.[84]

The ability of different metal substrates to grow graphene is determined by the number of unoccupied d orbitals, which play a role in bonding with a carbon atom. According to this criterion, catalytic activity is as follows: Ru≈Rh≈Ir > Co≈ Ni > Cu > Au ≈ Ag.[84] From this list, copper is more cost-effective and commercially available than the others. The low reactivity of copper is attributed to the filled 3d shell ($[Ar]3d^{10}4s^{1}$). Therefore, copper can only form weak bonds with carbon through charge transfer from π electrons from the sp^2 carbon graphene network and the empty 4s states of copper.[85] Moreover, carbon has a low solubility on copper at high temperatures (~0.008 wt% at 1084 °C).[86] These two properties have a positive impact on graphene growth as carbon will only be adsorbed by weak forces on the copper surface, preventing it from diffusing through it.[84] Seminal work by Li *et al.* exploited copper properties and showed that it was possible to produce high-quality single-layer graphene and further research validated it.[76,80,87]

Independent of the choice of the metallic substrate, annealing in a reducing environment, such as H_2, at high temperatures is a necessary step. It will eliminate any organic impurities and the native oxide layer, also affecting the grain size and orientation.

Polycrystallinity of the substrate will induce the formation of grain boundaries while graphene domains are merging. It has been observed that graphene can grow with a preferential orientation on the Cu [111] face.[84]

Although the CVD graphene growth mechanism is still debatable, a well-accepted general mechanism is illustrated in Figure 1.8a: 1) Thermal reaction occurs in the gas phase and the carbon active species diffuse towards the substrate through the boundary layer (Figure 1.8b). 2) Adsorption of the species and dehydrogenation of carbon precursors to form active carbon species. 3) Diffusion of the active carbon on the surface. 4) Nucleation of and growing of graphene domains, 5-6) Merging of the graphene domains to form a continuous film and diffusion of reactants from the surface to the bulk phase.[84,88]

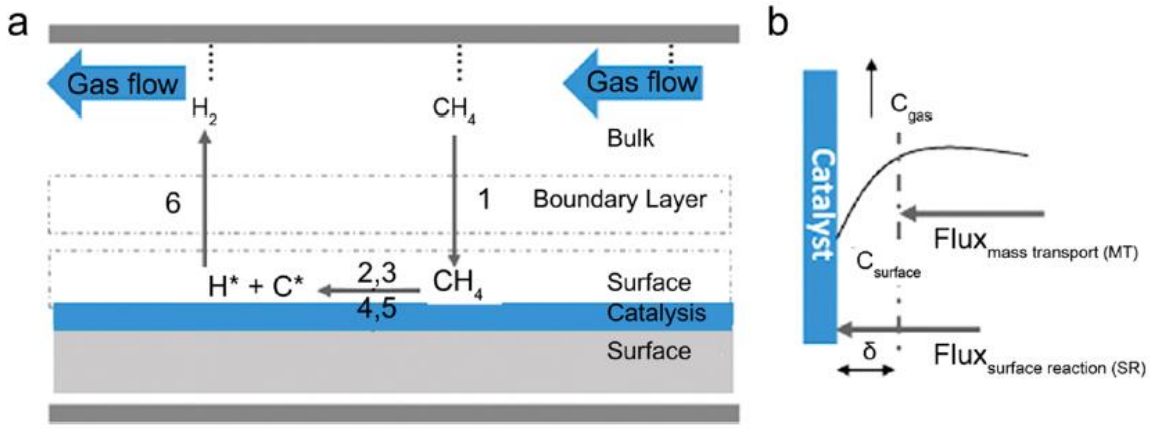

Figure 1.8 a) General mechanism of CVD growth graphene on copper using methane and hydrogen as precursors b) Illustration of the flux of species through the boundary layer. Reproduced from references 82,84.

Although Atmospheric-Pressure CVD (APCVD) eliminates the need for using a vacuum system, it normally deposits few-layer graphene or films with defects.[89] On the other hand, Low-Pressure CVD (LPCVD) has proven to get a more uniform and controllable monolayer graphene. In this work we will refer to Low-Pressures as those less than the atmospheric pressure. This behaviour can be explained by the differences in the boundary layer. Let us consider equations describing the flux transport, that is, the rate of mass transport per unit area, in the boundary layer (Eq. 1.2) and on the substrate surface (Eq. 1.3):[82]

$$F_{\text{mass transport}} = h_g(C_g - C_s) \qquad \text{Eq. 1.2}$$

$$F_{surface} = K_s C_s \qquad \text{Eq. 1.3}$$

where C_g and C_s are the concentration of active species in the bulk gas phase and on the surface and h_g and K_s are the mass transport coefficient and the surface reaction constant (assuming a first-order kinetics). Under the steady state assumption, both fluxes must be equal to the total flux (F_{total}) obtaining Eq. 1.4[2]:[82]

$$F_{total} = \left[\frac{K_s h_g}{(K_s + h_g)}\right] C_g \qquad \text{Eq. 1.4}$$

From Eq. 1.4 three regimes can be established: a surface reaction-controlled regime ($K_s \ll h_g$), a mixed region ($K_s \sim h_g$) or a mass transport limited region ($K_s \gg h_g$). In atmospheric conditions, diffusion through the boundary layer is usually the limiting step. Therefore, geometric factors associated with the gas flow or chamber configurations will have an impact and variations in the thickness of the boundary layer will lead to local variations in the number of active species, resulting in an inhomogeneous growth of graphene. On the other hand, low pressures implicate fewer collisions, thus a higher diffusivity coefficient (D_g). Because $h_g = D_g/\delta$, where δ is the thickness of the boundary layer, lower pressures lead to higher mass transport fluxes, making the process limited by the reaction, which will ultimately depend on the uniformity of the temperature of the substrate.[82]

During the growing stage, hydrogen plays a different role. Once it is adsorbed on the copper substrate, it will dissociate into atomic hydrogen having two effects: 1) it competes against CH_4 for adsorption sites and 2) it creates active sites that lead to the dehydrogenation of carbon species.[90] Higher hydrogen flow has been demonstrated to have an etching effect that controls the size and morphology of the graphene domains.[91] This effect can be more pronounced when oxygen impurities are present in the hydrogen feedstock.[92]

[2] From $F_{mass\ transport} = F_{surface}$ and solving for C_s, we obtain $C_s = \frac{h_g C_g}{(h_g + K_s)}$. Substituting C_s in Eq. 1.3 results in Eq. 1.4.

Lewis *et al*. investigated the influence of the chamber pressure (P_A) and growing temperature for a fixed methane/hydrogen ratio of $R_{C:H} = 0.2$ on the quality of the graphene. They contrasted their results against other studies in the literature under different conditions (Figure 1.9). They concluded that monolayer graphene growth was predominant for $R_{C:H}$ in the range 4×10^{-4} - 0.25. The wide range found could be partly explained because the analysis only considered the growth conditions, ignoring all the effects of the substrate pretreatment and cooling conditions. But, even with such oversimplification, the effect of temperature is evident. Higher temperatures are needed for growing continuous graphene.[93]

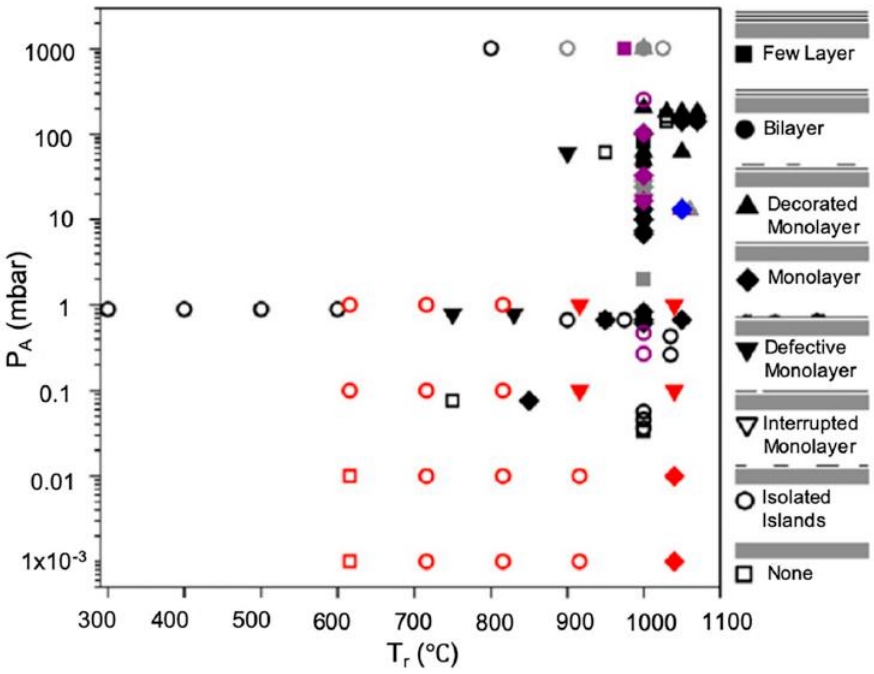

Figure 1.9 Different types of coverage were observed as a function of total pressure in the chamber during the growing step (P_A) and temperature (T_r). Red points represent data from the work by Lewis *et al*. for R_{CH}=0.2. The rest represents data from the literature. Data in black:1> R_{CH}>0.1; data in grey: 1> R_{CH}>0.1; data in purple: 0.01> R_{CH}>0.001; data in blue: 0.001> R_{CH}>0.0001. Reproduced from reference 93.

Temperature effects cannot be ignored as in principle it will increase the rate of the reactions occurring in the gas phase. It can be anticipated that the graphene growth rate could increase but also the rate of etching of hydrogen could increase. Chaitoglu and Bertran tested the effect of temperature in the range of 970 - 1070 °C. Below the lower limit graphene did not grow and the upper limit was very close to the melting point of copper without reaching it (1084 °C).[94] Their results showed that the nucleation sites, which were observed in SEM imaging due to the incomplete growth of the graphene domains, considerably decreased with temperature from 74 to 3.4 nuclei/ 10^4 μm^2 at 970 and 1070 °C, respectively.[95] They also

showed almost ten times higher growth rates were reached at higher temperatures (144 μm^2/20 min at 970 °C and 1369 μm^2/20 min at 1070 °C).[96] A similar effect was found using a cold wall reactor, in which the main difference is that only the substrate is heated and not the whole chamber. It was found that heating at 1000 °C during the growing step created multilayer regions but adlayers were reduced and nucleation density was reduced in half when heating the substrate at 1060 °C.[97] In general, higher temperatures decreased the number of nucleation sites, which increases the size of graphene domains. Ultimately, a single crystal of graphene is desired in sizes comparable to those needed for electronic applications.

1.4 Graphene transfer

Generally, when adopting a CVD approach to produce graphene the metallic substrate is not the desired one. Therefore, a transfer process is unavoidable. Although there is not a specific classification for the transfer processes of 2D materials, most of them include the use of a supporting layer, typically a polymer but also small molecules such as cyclododecane,[98] naphthalene[99] and pentacene[100] and others. The use of small molecules is limited by the mechanical strength of the films since they might break during the transfer limiting it to small areas.[98] However, pentacene has been used to transfer a large area of graphene but this method relies on the thickness control using an organic molecular-beam deposition system, which makes this method less accessible.[100]

One of the most common methods is the transfer using a PMMA supporting layer, as illustrated in Figure 1.10a. Typically, a polymer film such as polymethyl methacrylate (PMMA) is spin-coated on the graphene supported on a metallic substrate. Then the metallic substrate, such as copper is etched. Typical etchants for copper are iron nitrate,[76] ferric chloride,[101] ammonium persulfate and others. Next, the PMMA/graphene film is washed in a deionized water bath and transferred into the target substrate, like Si/SiO_2 or glass, and the polymer film is dissolved in an appropriate solvent, such as acetone. An alternative to avoid the use of etchants is using an electrochemical approach where graphene on copper is the cathode and a potassium persulfate solution is the electrolyte. By applying a potential difference, hydrogen bubbles intercalate between graphene and copper, inducing delamination (Figure 1.10 b).[102] In any case, once the polymer/graphene stack is floating on water it is collected on the desired substrate and the polymer film is dissolved. This method is mainly used to transfer the graphene on rigid substrates such as SiO_2 or quartz. When

flexible substrates are required, polymer films can be laminated at a temperature above its glass transition temperature to improve the conformal contact between the graphene on copper and the supporting polymer. Also, a layer of an adhesive polymer can be added on polyethylene terephthalate (PET) (Figure 1.10c).[103] In any case, the etching step cannot be avoided and, just recently, considerably more attention has been focused on controlling the process for direct peeling of the graphene from the copper. However, resistivities an order of magnitude higher were obtained when compared to using the typical wet transferred method.[104]

The underlying principle behind transferring the graphene onto a substrate relies on the surface energy difference between graphene and the substrates. In general, a lower adhesion energy corresponds to a lower adhesion force, so from the purely physical point of view, using polymers with a lower surface energy will be easier to remove, leaving fewer residues.[105] It must also be true that the surface energy of the substrate must be higher than the polymer to ensure adhesion while keeping the graphene from detaching when dissolving the polymer film.[106] The thermal expansion coefficient is another important factor to be considered. While most polymers have a positive coefficient, graphene has a negative value of -3.75×10^{-6} K^{-1}, which is in the same order of magnitude as the polymers but with a positive value, meaning that any heating step will lead to wrinkles or cracks.[107]

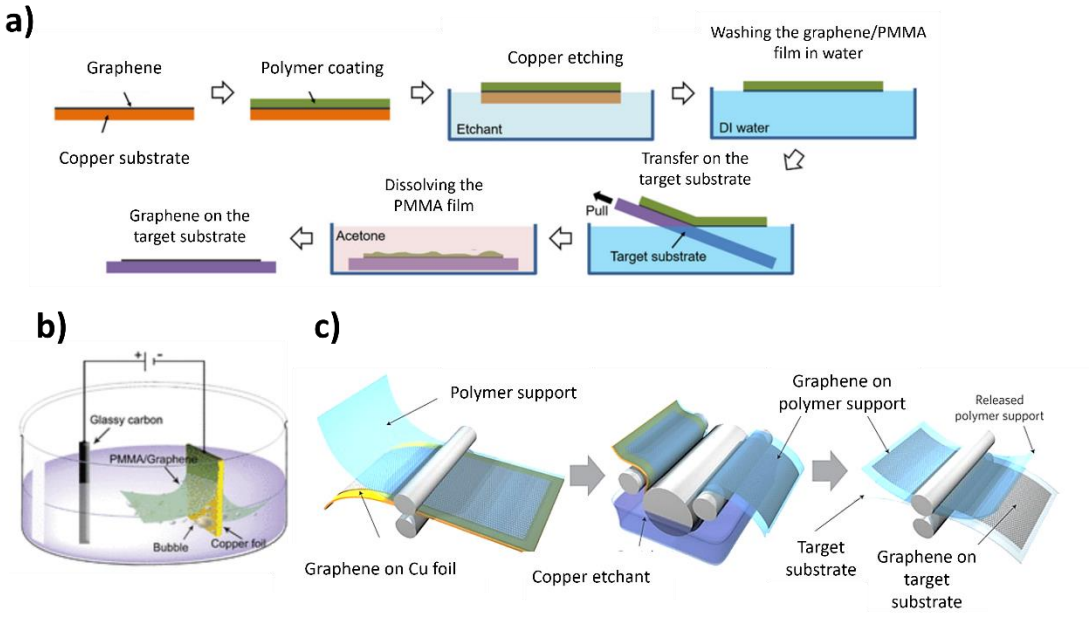

Figure 1.10 a) Typical lab scale transfer process using a spin-coated supporting polymer layer. b) Set up for electrochemical delamination of graphene/PMMA stack in an electrolyte solution. c) Roll to roll for large area graphene transfer (~30 in) using PET as substrate and thermal release tape as supporting layer. Adapted from references 17,102,108.

Polymethyl methacrylate (PMMA) was the first polymer used to transfer mechanically exfoliated graphene flakes.[109,110] After all, PMMA is flexible and has a high mechanical strength, preventing graphene from fragmentation due to the force exerted by the surface tension of the etching solution and water. Also, it is chemically resistant to common etchants, insoluble in water but removable in common organic solvents such as acetone. This method became even more popular in 2008 when Li *et al*. used it to transfer CVD graphene to SiO_2. This method was flexible enough to adapt it to different target substrates.[111,112] However, residual PMMA is difficult to remove, leaving a thin layer estimated to be ~1-2 nm, which will affect graphene electronic properties and, therefore its performance in electronic applications.[98,113] In principle, annealing the samples will induce the thermal decomposition of PMMA chains; however, it was shown that this procedure had limited success even when using temperatures as high as 700 °C.[114,115] Despite much effort devoted to improving this transfer process using a wide range of approaches such as annealing,[114] laser treatment,[116] and electrolytic cleaning,[98] current processes cannot eliminate PMMA residues without introducing defects in the graphene film.

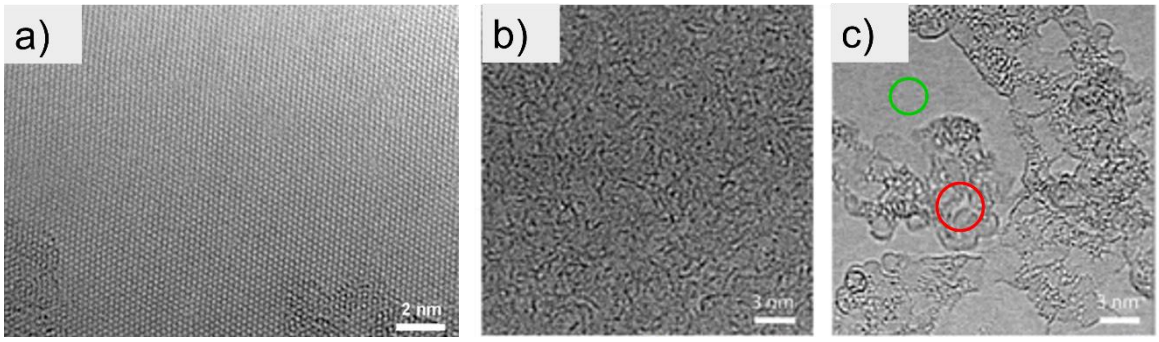

Figure 1.11 a) Graphene transferred using polycarbonate as a supporting layer. b) Graphene transferred using PMMA followed by annealing at 250 °C in H_2 atmosphere. c) High magnification image from b) where green and red circles represent a PMMA free region and residual PMMA respectively. Adapted from reference 113.

In 2011 Lin *et al.* proposed polycarbonate (PC) as a cleaner alternative to PMMA for transferring graphene (Figure 1.11a).[113] Using transmission electron microscopy (TEM) they showed that it was cleaner at the atomic scale while PMMA left a thin layer of residue (Figure 1.11b and c), but the area transferred was relatively small (~ 4 mm^2).[113] Later in 2015, Wood *et al*. also demonstrated that using a PC supporting film provided a cleaner transfer without annealing compared to other polymers such as PLA, PMMA, and PPA (poly phthalaldehyde).[115] Also, polycarbonate has become popular as a method for small-scale transferring 2D materials other than graphene,[117,118] such as MoS_2,[119] WSe_2[120] and WS_2.[117] It was also demonstrated to be helpful in creating clean graphene heterostructures since polycarbonate was easy to wash away with chloroform.[117,118] However, the areas transferred were a few hundred microns large.

1.5 Immiscible polymer blends

Compatibilization in polymer blends is important from an industrial point of view.[121,122] However, the high interfacial tension between polymers makes dispersion difficult. Therefore, poor interfacial adhesion and mechanical properties are expected. The miscibility of components in a blend is described through the Gibbs free energy, ΔG_m (Eq. 1.5). This equation considers contributions from the enthalpy of mixing (ΔH_m), the entropy of mixing (ΔS_m) and temperature (T). For high molecular weight materials such as polymers, $T\Delta S_m$ is negligible, and other factors influence the miscibility, which leads to decreasing the miscibility (phase separation) as the temperature increases.[123]

$$\Delta G_m = \Delta H_m - T\Delta S_m \qquad \text{Eq. 1.5}$$

Traditional methods to compatibilize blends include the use of copolymers, that is a polymer made up of two or more monomeric species. However, fillers with at least one nanometric dimension, such as carbon nanotubes and graphene, can also be located at the interface between polymer blends whenever the interfacial tension is such that its localization minimizes the free energy of the whole system.

1.5.1 Location of filler in an immiscible polymer blend

For simplicity, let us assume a single spherical particle p of radius R at its equilibrium position trapped at the interface between phases A and B, where θ is the contact angle. Let $\gamma_{i\text{-}j}$ be the interfacial tension of the i-j interface form by polymer-polymer or polymer-particle interactions (Figure 1.12). Then, the interfacial energy change caused by the location of this sphere is given by:

$$\Delta G_{interfacial} = 2\gamma_{p-A}(1-\cos\theta)\pi r^2 + 2\gamma_{p-B}(1+\cos\theta)\pi r^2 - \gamma_{AB}(\sin^2\theta)\pi r^2 \qquad \text{Eq. 1.6}$$

where the terms $A_{p\text{-}A} = (1 - \cos\theta)\pi r^2$ and $A_{p\text{-}B} = (1 + \cos\theta)\pi r^2$ are the surface areas where phases A and B are in contact with the particle and $A_{A\text{-}B} = (\sin^2\theta)\pi r^2$ is the area replaced from the interface. From the thermodynamic perspective, the system will minimize the interfacial free energy by optimizing the position of the particles, that is $dG/d\theta = 0$.[124,125] This will give rise to the equation defining the wetting coefficient:

$$\omega = \frac{\gamma_{p-B} - \gamma_{p-A}}{\gamma_{A-B}} \qquad \text{Eq. 1.7}$$

From Eq. 1.7, three cases are possible: If $\omega > 1$ then the particle will be located within the A phase. If $-1 < \omega < 1$ it will distribute at the interface, and if $\omega < -1$ then the particle will distribute within phase B.

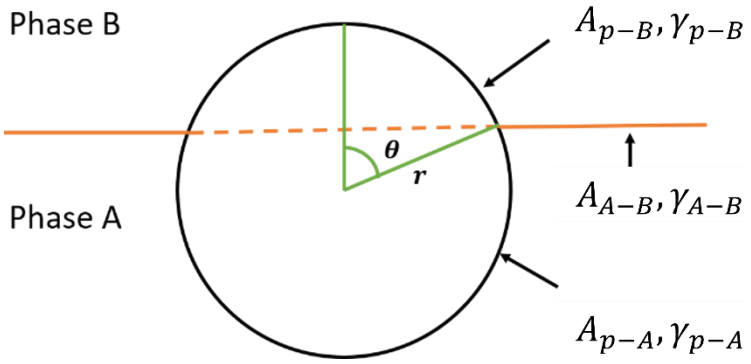

Figure 1.12 Schematic representation of a spherical particle at the interface.

Estimation of the interfacial tensions γ_{i-j} from Eq. 1.7 can be done through contact angle measurements using Young's equation (Eq. 1.8), which makes use of the surface energies from solid (γ_S), liquid (γ_L) and the contact angle θ between the solid and the measuring liquid.[126]

$$\gamma_S = \gamma_{SL} + \gamma_L \cos\theta \qquad \text{Eq. 1.8}$$

The interaction between a solid surface and a liquid is ultimately the result of molecular interaction. Therefore, γ_{SL} can be expressed as the contribution from the dispersion (γ_i^d), polar (γ_i^p), hydrogen bonding (γ_i^h), and other interactions.[127,128] In general, for simplicity, it is accepted the components of interfacial energies are composed of dispersion (non-polar) and polar components (Eq. 1.9), and γ_{i-j} can be calculated using equation 1.10:[129]

$$\gamma_i = \gamma_i^d + \gamma_i^p \qquad \text{Eq. 1.9}$$

$$\gamma_{i-j} = \gamma_i + \gamma_j - 2\sqrt{\gamma_i^d \gamma_j^d} - 2\sqrt{\gamma_i^p \gamma_j^p} \qquad \text{Eq. 1.10}$$

Another relationship proposed by Wu, *et al*. can predict the interfacial tension between polymers or between a polymer and an ordinary liquid is given by:[130]

$$\gamma_{i-j} = \gamma_i + \gamma_j - \frac{4\gamma_i^d\gamma_j^d}{\gamma_i^d + \gamma_j^d} - \frac{4\gamma_i^p\gamma_j^p}{\gamma_i^p + \gamma_j^p} \qquad \text{Eq. 1.11}$$

1.5.2 Effects associated with constituents

In the previous section, it has been highlighted the importance of the wetting parameter on the migration from one phase to the other. However, it is based on a thermodynamical analysis, but in real situations, transport can be considered as a two-step process involving 1) Transport from the bulk phase to the interface and 2) penetration of the particle into the interface. Considering Eq. 1.6 the change in the interfacial energy can be derived when a particle with radius r is transported from phase B to the AB interface[3]:

$$\Delta G_{interfacial} = 4\pi r^2\gamma_{p-B} - \pi r^2\gamma_{AB}(1 - \cos\theta)^2 \qquad \text{Eq. 1.12}$$

The second term from Eq. 1.12 is the energy required to remove the particle from the AB interface. For a micrometric particle, the energy for removing a particle from the interface will be greater than the thermal energy k_BT, where k_B is the Boltzmann constant. It suggests that once a particle has been located at the interface, it is irreversibly adsorbed without any other external forces.[131–133]

1.5.3 Influence of particle size and shape

Expressions in Section 1.5.1 were derived for a spherical particle. However, nanoparticles like carbon nanotubes and graphene sheets have high aspect ratios. Krasovitski and Marmur modelled the penetration of the interface by high aspect-ratio ($b \gg a$) particle from a fluid F into a droplet L (Figure 1.13). They found that the energy of the system was minimized when the contact angles were smaller than 90° and would not migrate for contact angles greater than 90°.[134]

[3] Eq. 1.12 was derived by substituting the Young's equation: $\gamma_{p-A} = \gamma_{AB}\cos\theta + \gamma_{p-B}$ into Eq. 1.6. to obtain $\Delta G_{interfacial} = \pi r^2\left[2\gamma_{AB}\cos\theta - 2\gamma_{AB}\cos^2\theta + 2\gamma_{p-B} - 2\gamma_{p-B}\cos\theta + 2\gamma_{p-B} + 2\gamma_{p-B}\cos\theta - \gamma_{AB}(\sin^2\theta)\right]$, then simplifying to obtain Eq. 1.12.

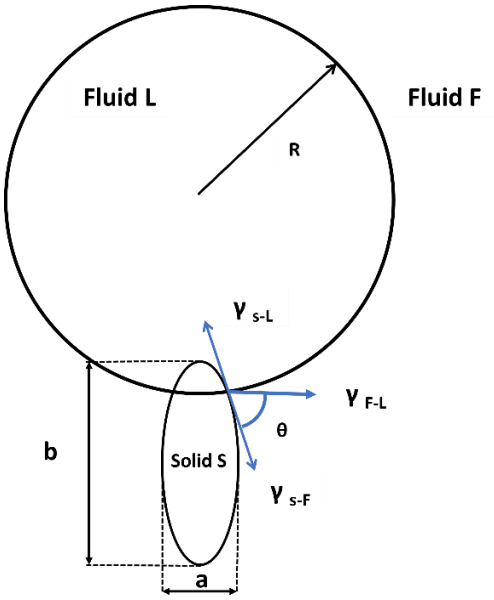

Figure 1.13 Model proposed by Krasovitski and Marmur where a solid particle S transfers from fluid F to a droplet of fluid L and the triple contact angle θ is formed by the different surface tension forces acting on the surface S. Adapted from 134.

Based on this model, Göldel *et al*. proposed a qualitative slim-fast mechanism (SFM).[135] It explained that the migration process started when the particle was in the less thermodynamically favourable phase. Then, the mixing process transfers the particle to the interface. Furthermore, they suggested that once a particle was close to the interface, the instability of the curvature was the driving force for migration, involving faster transfer rates for higher aspect ratios and smaller particles. The relative transfer rates are summarized in Table 1.2.

Table 1.2 Classification of the transfer speed and interfacial stability of small particles in polymer blends during blend mixing. The terms in the table refer to carbon nanotubes (CNT), carbon black (CB), montmorillonite (MMT), carbon nanofibers (CNF). Reproduced from reference 135.

The Slim Fast Mechanism (SFM)						
Group I: Low aspect ratio objects – slow transfer – high interfacial stability						
Class	**CNT**	**CNT**	**CB**	**CB**	**CB**	**MMT/ Clay/ Graphite**
Scale	Macro- micro	Micro	Meso-micro	Micro-nano	Nano	Micro
Description	Primary agglomerate	Coiled CNT	Agglomerate	Aggregate	Nano-Aggregate	Stack
Scheme						
Intermediate transfer speeds/interfacial stabilities		**Group II: High aspect ratio nano objects – fast transfer-low interfacial stability**				
Class	**MMT/Graphene/ Silica**	**CNT**	**CNF**	**Halloysite**	**Other Nanotubes and -fibers**	
Scale	Nano in 1 dimension	Nano in 2 dimensions	Nano in 2 dimensions	Nano in 2 dimensions	Nano in 2 dimensions	
Description	Exfoliated or single sheet	Separated, linear CNT	Separated, linear CNF	Separated, linear tube	Separated, linear tube	
Scheme						

1.5.4 Influence of viscosity

It was experimentally demonstrated that a particle premixed in the less thermodynamically preferred (phase A) will move slower when the viscosity of A increases.[136,137] To provide a better explanation of the role of viscosity in the localization of fillers in non-miscible blends, Plattier *et al*. conducted a set of experiments using the polycaprolactone (PCL) and polypropylene (PP) system.[138] The viscosity ratio $K = \eta_{PCL}/\eta_{PP}$ was varied from 0.06 to 14.7. Results showed that for $K \approx 1$ the carbon particles were localized at the interface, while for $K \gg 1$ or $K \ll 1$ they were extracted from the interface towards the more viscous phase. Results suggested that drag forces acting on the surface of the carbon particles were responsible for the transport. The model proposed considered (Figure 1.14):[138]

1. Interfacial forces are much smaller than hydrodynamic forces produced during mixing, so they are neglected. Furthermore, it does not explain how the particle penetrates the interface.
2. Once at the interface, the drag force acting on the particle by each polymer face is given by the product of the surface S area and the shear stress tensor $\vec{\tau}$. However, it is not possible to know the shear stress distribution given by the

tensor $\vec{\tau}$ and normal stress contribution is neglected. Then, if only the drag forces balance is considered, the following relationship applies:

$$\frac{F_d}{F_m} \approx \frac{1+\cos\theta}{1-\cos\theta}\frac{\eta_d}{\eta_m} \qquad \text{Eq. 1.13}$$

From the last equation, they inferred that for $K \approx 1$ when the particle reaches the interface, it is not extracted from it since the two applied forces almost cancel each other and the localization only depends on the contact angle, which was experimentally estimated to be in the range of $60° < \theta < 120°$.

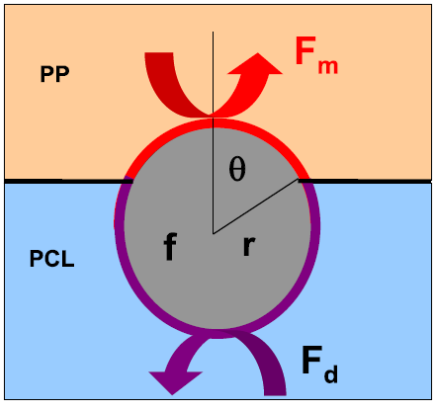

Figure 1.14 Representation of a particle at the interface of a PP/PCL system experiencing dragging forces F_m and F_d due to different viscosities. Reproduced from 138.

1.5.5 Effect of time and shear rate

Ultimately, the compounding time to process a composite is one of the variables that can be controlled accurately. Experimental evidence showed that the transfer of carbon nanotubes from styrene-acrylonitrile (SAN) to polycarbonate (PC) ranges from 90 seconds up to 5 minutes depending on the extrusion method, being faster when using a twin extruder.[139] Such a difference was attributed to the increased number of collisions between the matrix and the droplets of the dispersed phase.[140] This same hypothesis was tested in a system where polycaprolactone (PCL) was premixed with multiwall carbon nanotubes (MWCNTs) and then melt compounded with thermoplastic starch (TPS) in a twin extruder or an internal mixer while keeping all other conditions the same. The twin extruder was more effective for transferring MWCNTs, and authors attributed it to higher shear rates reached.[141]

In another experiment, it took 30 minutes to complete the transfer of MWCNTs from polystyrene (PS) to polyvinylidene fluoride (PVDF) but in this case, it was hypothesized to be due to the large viscosity difference.[142]

Particle localization is a pretty complex problem, and the factors discussed so far seem to have a synergistic effect and cannot be considered alone. In a recent article, Jaensson *et al*. investigated the migration process of a spherical particle near the interface from a viscoelastic liquid to a Newtonian liquid.[143] For a Newtonian fluid, the shear stress (τ) increases proportionally to the shear rate (γ), where the proportionality constant is the viscosity (η). Any fluid whose behaviour deviates from this description are considered viscoelastic fluids. Jaensson *et al*. considered the Giesekus model for a viscoelastic liquid, which captured many features of polymers, including the normal stress produced during a shear flow.[143] The analysis was interpreted based on two non-dimensional numbers: the Weissenberg (W) and the capillary number (Ca). The first one is interpreted as the ratio of elastic forces caused by normal stresses and viscous forces, while the capillary number represents the ratio of viscous forces to surface tension forces. As expected, a higher W number will push the particle to move to the other phase because of normal stresses. However, if interfacial tension is high enough (lower Ca), the particle will remain trapped at the interface. On the other hand, for higher W and lower interfacial tensions (higher Ca) drag forces will transport the particle to the other phase. The model also predicts regimes where migration is halted and the particle steps back instead.[144]

1.5.6 Localizing graphene-based materials in immiscible blends

Graphene oxide (GO) has an amphiphilic character, making it a more accessible material to disperse in a polymer matrix. Aromatic regions can interact with electronegative atoms or through π - π interactions with other moieties from polymers. Also, GO is rich in oxygen functional groups -OH and -COOH, making the interaction through hydrogen bonding with more polar polymers possible.[145,146] This theory was tested using the PMMA/PS system. The ester moiety from PMAA (-O-C=O) can interact through hydrogen bonding with GO and PS through π - π interactions. It was proven through neutron reflectivity that the thickness of the interface was increased, confirming that the interface between deuterated PMMA and PS broadens by 2.2 times in the presence of GO.[147]

The interface of immiscible polymer blends can be used as a scaffold for electrically conductive particles to form a network. The percolation threshold is defined as the minimum amount of these electrically conductive nanoparticles, above which they are connected and form a network. Hence, the importance in modifying the surface chemistry of GO to induce a preferential location at the interface of immiscible polymer blends. For example, by functionalizing GO with a copolymer poly (styrene-co-methyl methacrylate) the percolation threshold was reduced from 0.35 vol% to 0.02 vol%.[148] Although lower percolations can be achieved with surface modification, increasing the amount of modified GO can create a third phase at high loadings, and instead of reinforcing the interface, it can have the opposite effect, showing poor mechanical properties.[149]

Electrical conductivity is one of the properties that polymer can benefit from, and few-layer graphene (FLG) is one of the best options as they are commercially available. However, the high surface energy of graphene and few functional groups on its surface make its dispersion in a polymer matrix difficult but even mild oxidation of FLG can improve the dispersion in polymer systems with polar moieties reducing the electrical percolation threshold several orders of magnitude. Thus, making it clear the importance of the surface chemistry to tailor the interaction with polymers.[150]

Aggregation is another major problem. It was why using few-layer graphene in a thermoplastic polyurethane (TPU) /polypropylene (PP) blend in concentrations over 0.5 wt% yielded a low tensile strength.[151] Also, it is frequently found that high loadings are needed, even close to 10 wt%, to affect the conductivity significantly.[152] Therefore, surface chemistry and high aspect ratios must be considered to reduce the percolation and facilitate the transfer between polymer phases.[153]

In a recent study, Bai *et al*.[154] studied the effect of reduced graphene oxide (RGO) sheets on the electrical conductivity of co-continuous PLA/PS blends. It was found that when RGO was premixed with PLA conductivity, morphological stability and modulus of the blend increased because of the RGO localization at the interface. However, they argue that the time must be carefully controlled to trap the graphene flakes at the interface. An attractive way to compatibilize a blend is using reactive nanoparticles. Zhao *et al.* further explored this idea and synthesized carbon nanotubes containing epoxy groups and PMMA chains. It was hypothesized that when extruding a PLLA/PVDF blend, the epoxy groups react with carboxylic groups from PLLA (Figure 1.15a). Moreover, because PMMA is miscible in

PDVF both effects combined will lead to the preferential location of MWCNTS at the interface as confirmed in TEM observations (Figure 1.15b). Furthermore, they proved the reinforcing effect at low loadings (1 wt%), demonstrating that reactive MWCNTs were even capable of stopping the interfaces at higher loadings (5 wt%). This same approach was previously studied using silica nanoparticles[155], showing it was a robust methodology that could be adapted to graphene-based nanoparticles.

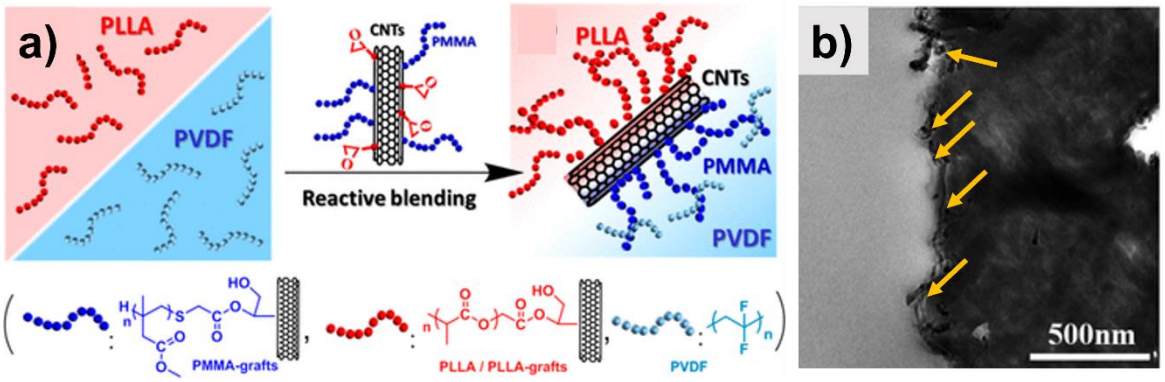

Figure 1.15 a) Reactive blending approach to compatibilize immiscible PLLA/PVDF blend using MWCNTs with epoxy groups and PMMA chains. b) TEM image of reactive MWCNTs localized at the interface of the blend. Adapted from reference 156.

2 Aims and Objectives

One of the most characteristic features of graphene is electrical conductivity, which has inspired and directed its wide range of applications. As already discussed, there are two main precursors of graphene: graphene oxide and graphene grown by chemical vapour deposition (CVD). Although graphene oxide can be produced on a gram scale, CVD graphene grows on a catalytic substrate layer by layer.

These two methods face challenges in exploiting graphene's electrical properties. As highlighted already, graphene tends to form agglomerates in polymer blends, leading to the use of high amounts of graphene. Here, we aim to use the immiscible polylactic acid (PLA) /polystyrene (PS) blend as a scaffold where we can selectively localise graphene on the interface of the two polymers. As the first step, graphene oxide must be synthesised where the thickness and average lateral size are known. Previous research suggested that high aspect ratios increase the transfer rate to the interface. Subsequently these will be incorporated into the applied polymer blend using a mini extruder, and the morphology will be characterised using SEM and rheological measurements to assess their stability. TEM imaging from ultramicrotomed samples will also be collected and analysed to directly observe the reactive graphene platelets localisation.

To harness the electrical properties of CVD graphene, first, it must be transferred from the catalytic substrate. Using a supporting polymer layer to transfer the graphene is quite common and well demonstrated as it makes handling easier. During our investigations two problems are addressed: first, how to transfer graphene onto flat rigid substrates; second, how to transfer it onto a rough and compliant substrate such as skin. Although these two problems seem different, we can state them as an energy balance between the elastic energy stored by the polymer membrane, the elastic energy stored by the substrates, and the energy of adhesion. The goal of this project is to provide guidelines for transferring graphene onto Si/SiO_2 substrates and develop electrodes for on-skin applications.

3 Experimental techniques

3.1 Scanning Electron Microscopy (SEM)

Scanning Electron Microscopy (SEM) is a valuable tool for the characterization of nanomaterials by providing information about the surface and composition at the submicron scale. One of the advantages of SEM is the relatively large depth of field, which makes it possible to obtain 3D-like images.[157]

The major components of the microscope are the electron column, the specimen chamber, and the electronic controls. Figure 3.1a illustrates a typical scanning electron microscope. In brief, the electron column generates an electron beam, which is thermionically generated. Typically, a tungsten filament is used due to its high melting point (3422 ℃). Then, electromagnetic lenses focus the beam, whose diameter will limit the maximum resolution attainable. The scan coils raster the probe over the surface of the sample. Exposure of the sample to the beam will generate various signals from the first few microns of the surface. The most important signals to be collected in the detectors are the secondary and backscattered electrons, which are then processed to obtain the image.[158]

Once the electron beam interacts with the sample, the electrons experience elastic and inelastic interactions. If electrons are deflected by the nucleus without losing kinetic energy, it is said they are elastically scattered. However, electrons inelastically scattered can lose and transfer kinetic energy when interacting with the nuclei or electrons from the specimen. Electrons from elastic collisions are responsible for the backscattered electrons, while electrons from inelastic collisions produced the secondary electrons. So, once the beam hits the surface, electrons will be scattered within the sample, creating an interaction volume as illustrated in Figure 2.1b. Elastic scattering in atoms with high atomic numbers will be more intense, deflecting the electrons through large angles (>90°), and reducing the distance travelled into the sample. This phenomenon is known as backscattering and is responsible for the atomic number contrast.[158]

When inelastic interactions occur, electrons in the beam have enough energy to knock out electrons in the outer shells of atoms. These electrons that initially belonged to the sample are known as secondary electrons and are responsible for the topographic contrast.

Secondary electrons and backscattered electrons are only differentiated based on their energy. Typically, electrons with less than 50 eV are classified as secondary electrons.[158]

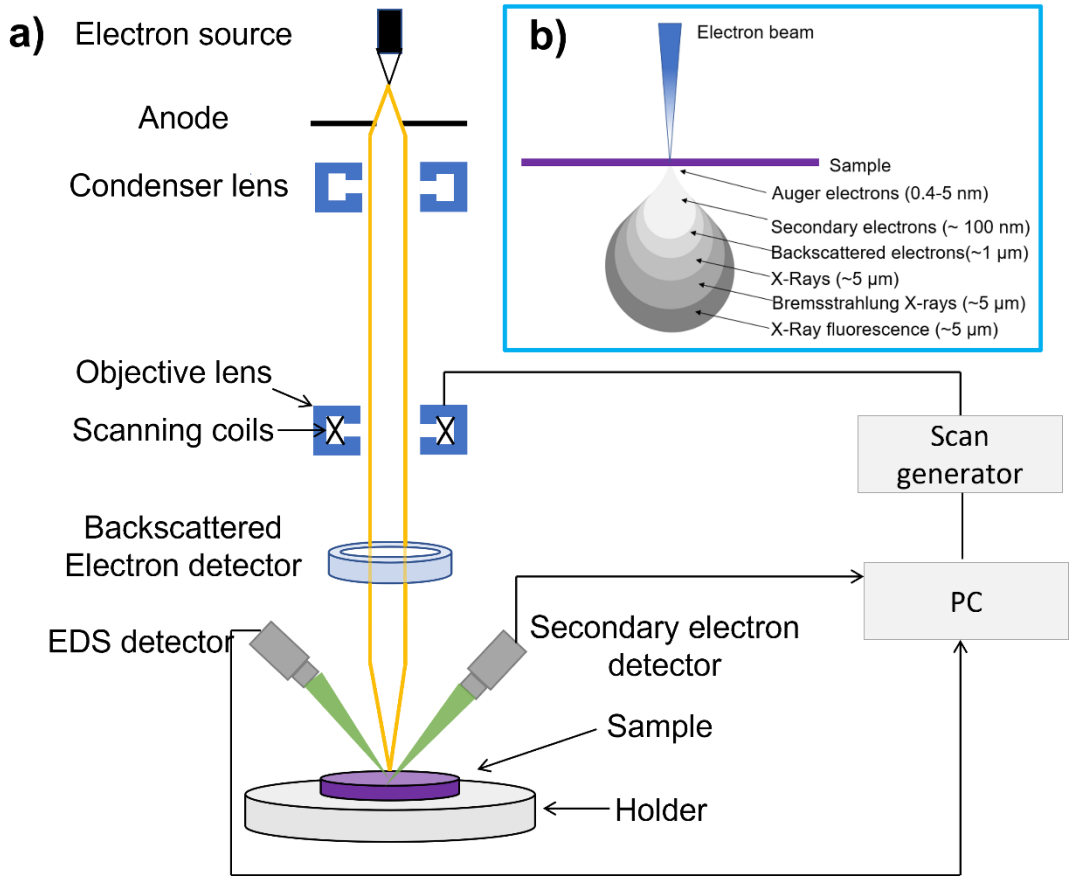

Figure 3.1 a) Main component in a Scanning Electron Microscope. b) Interaction volume and typical depths from where different signals are collected using a 20 keV acceleration voltage and a small probe diameter. Adapted from reference 157.

Undoubtedly, carbon-based nanomaterials such as fullerenes, carbon nanotubes and graphene have benefitted from SEM imaging. It is a non-destructive tool for imaging graphene-based materials as low voltages are enough to get high-contrast images. Such induced contrast is enough to distinguish voids, ruptures, folds and stacking of graphene layers. The choice of the detector also influences such contrast. The In-lens detector collects mainly low-energy secondary electrons very efficiently and has proven to provide much better contrast than the most common Everhart-Thornely detector.[159] The contrast arises from the graphene's attenuation of secondary electrons from the underlying substrate, characterized by the inelastic free mean path.[160] Figure 3.2a, b shows images obtained from graphene oxide (GO) and CVD graphene on Si/SiO_2 from this work. As discussed before, measuring the lateral size from big GO sheets is possible, which could be difficult with AFM due to the limited scanning area. SEM can easily reveal morphological features such as folds,

wrinkles, voids, and stacking. As for CVD-grown graphene, identifying adlayer regions, wrinkles and residues from the transfer process and grain size is possible. Sample preparation details for imaging flakes are given in Section 8.3.

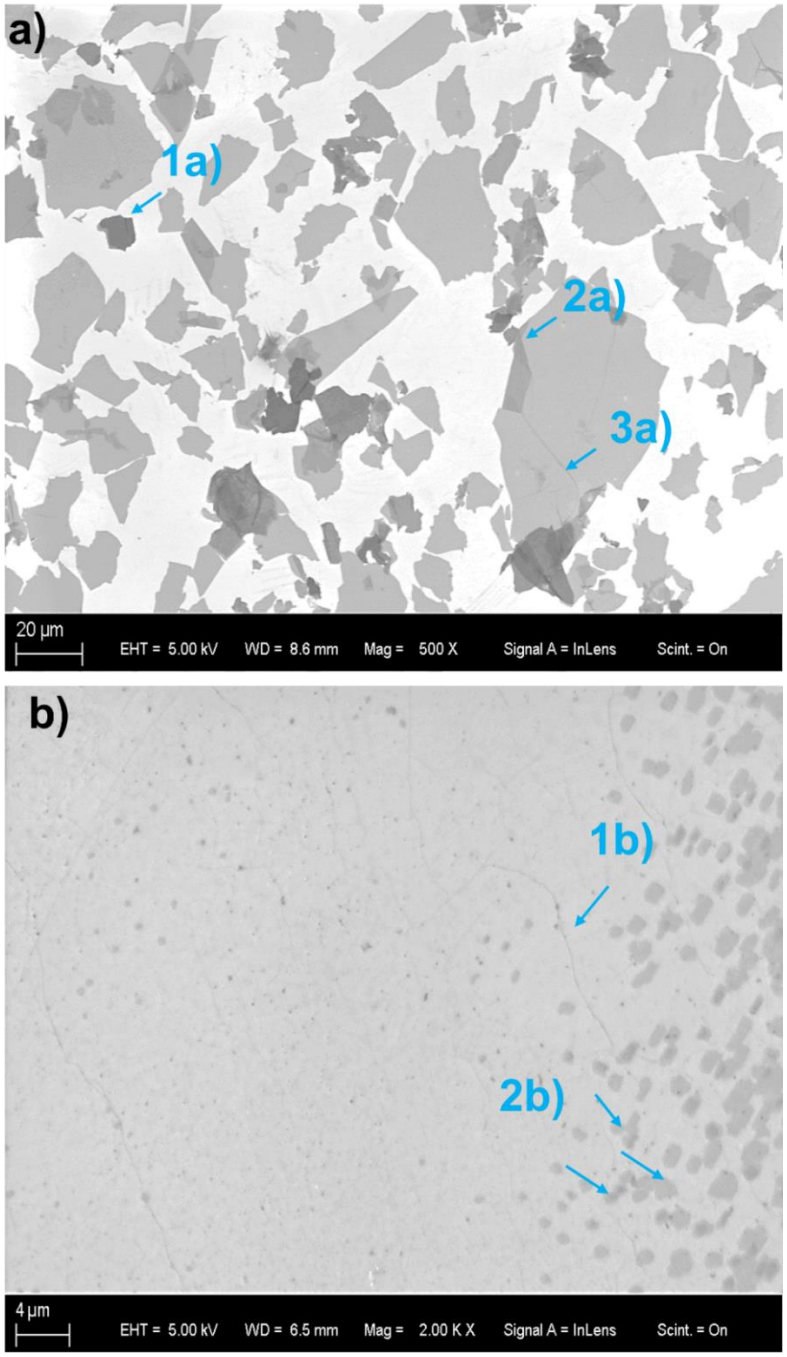

Figure 3.2 a) Graphene oxide sheets from samples from this work using an in-lens detector and 5 kV acceleration voltage. Arrows point out stacks of non-exfoliated graphite oxide (1a), a fold (2a) and a wrinkle (3a) in a graphene oxide sheet. b) CVD-grown graphene on Si/SiO_2 substrate image using in-lens detector showing wrinkles (1b) and adlayer domains (2b).

3.2 Transmission Electron Microscopy (TEM)

TEM is a powerful tool to study the microstructure of samples. It can be considered a complementary tool to SEM imaging as only very small areas can be analysed in the range of a few microns. However, the resolution achievable in TEM is in the subnanometer range, as electrons have short wavelengths, i.e., 0.0123 nm at 10 kV, and can be focused through electromagnetic lenses to produce high-resolution images.[161]

The working principle of TEM shares some similarities with light microscopy, and the main difference is that TEM uses electromagnetic lenses instead of optical lenses to focus the source of electromagnetic radiation. Figure 3.3 shows the main parts of a typical microscope. The image generation is as follows: First, an electron beam is generated and focused in electromagnetic lenses in the condenser before striking the sample. Upon reaching the sample, different signals are formed, like transmitted electrons, elastically scattered and inelastically scattered electrons. Although some other signals are formed, the above signals provide information from electron diffraction and produce contrast when imaging. Electrons transmitted pass through the objective and projector lenses, whose function is to increase the magnification and resolution of the image. Finally, the image formed is projected onto a fluorescent screen or captured with a charge-coupled device (CCD) camera.

TEM has been widely used to investigate graphene structure at the atomic level. Understanding the structure of graphene is not a trivial matter, as defects affect the electronic, chemical, magnetic and mechanical properties of the material.[162] The superior resolving power of modern aberration-corrected TEM has made possible the direct observation of point defects as atomic vacancies[163–165] and Stone-Wales rotations, that occurs when the connectivity of two-bonded carbon atoms changes, causing them to rotate by 90° relative to the midpoint of their bond.[166] Also, grain boundaries[167] and edges[168,169] have been directly observed.

It is of particular interest to know the number of layers to assess the exfoliation process and TEM imaging also provides a simple way to count the number of layers of graphene, even without using high-resolution. The most intuitive way of counting the number of layers is by counting the number of fringes that form at the part of a fold that forms parallel to the beam, as illustrated in Figure 3.4.[170]

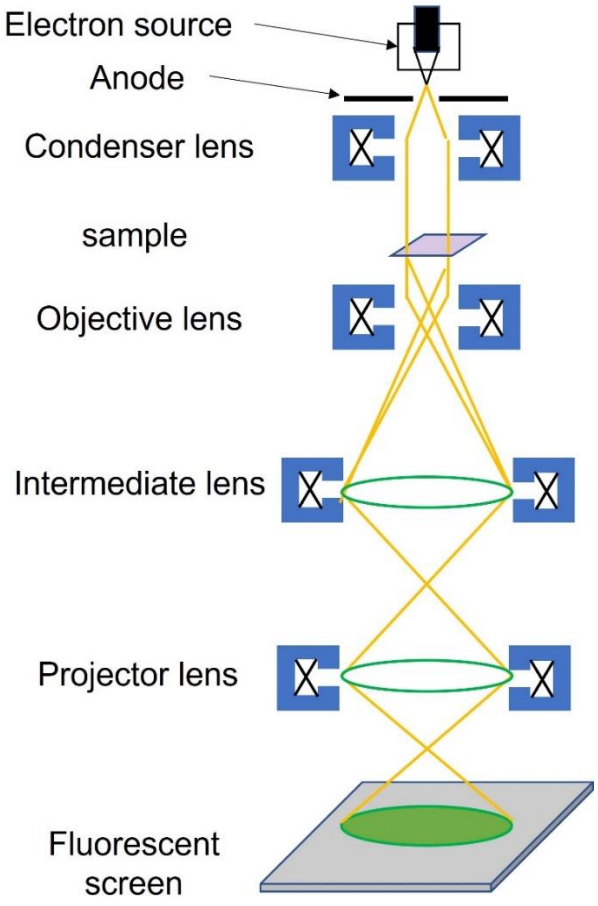

Figure 3.3 Typical components of a Transmission Electron Microscope (TEM). Adapted from reference 157.

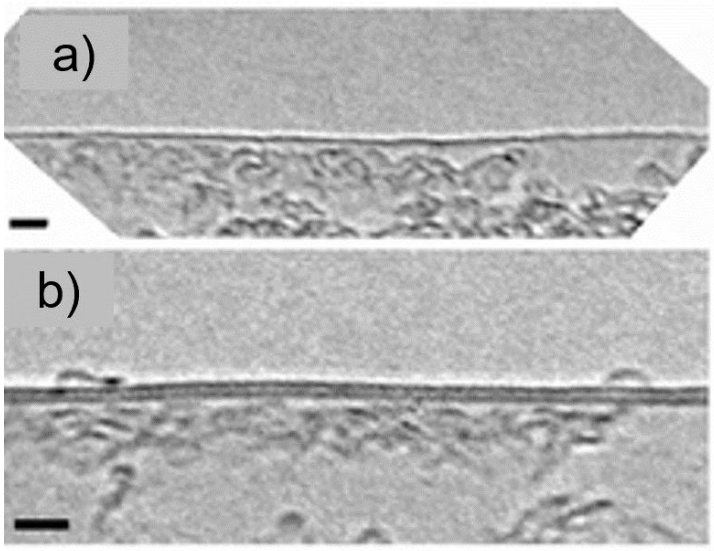

Figure 3.4 a) Folded edge of a single-layer graphene. b) Folded edge of a bilayer graphene. Reproduced from 171.

3.2.1 Selected Area Electron Diffraction (SAED)

Since the wavelength of the electrons is very short, diffraction is expected to happen once the beam interacts with the sample. Such phenomenon can provide information about the structure, symmetry, and lattice parameters. Because a small area is selected for diffraction, getting the SAED pattern of even a single crystal is possible. The same fundamentals apply as in traditional X-ray diffraction (see Section 3.5). However, in the SAED pattern, every plane from the real lattice, becomes a point in the reciprocal lattice. Thus, the whole reciprocal space can be probed by tilting the sample.[161]

The SAED pattern can provide a way to distinguish between monolayer and multiple-layer graphene. Using Miller-Bravais indices (*hkil*) for graphite, it is shown that the innermost hexagon and the outermost one correspond to (0-110) (2.13 Å spacing) and (1-210) (1.23 Å spacing) planes.[172] The key for identifying monolayer graphene is that its reciprocal space has only the zero-order Laue zone, which is the middle part of the diffraction pattern that contains the origin. Therefore, almost no dimming of the diffraction peaks should occur at any angle. Considering that for a single graphene crystal, the reciprocal space is a set of rods and that the intensity profile along any of the rods is given by only the product of the atomic form and effective Debye-Waller factor, there will only be a weak monotonous intensity variation along the rods. This agrees with experimental evidence where changes in the total intensity are minimal when the tilt angle is changed without going through any

minima (Figure 3.5a).[172] Further experimental evidence showed that for bilayer graphene, variation of a few degrees in the tilt angle will lead to substantial variation in the diffraction intensities for all multilayer samples independent of the stacking order, as shown in Figure 3.5b. It also implies that single-layer graphene can be identified by the intensity ratios of the diffraction peaks at zero angle tilt (Figure 3.5c).

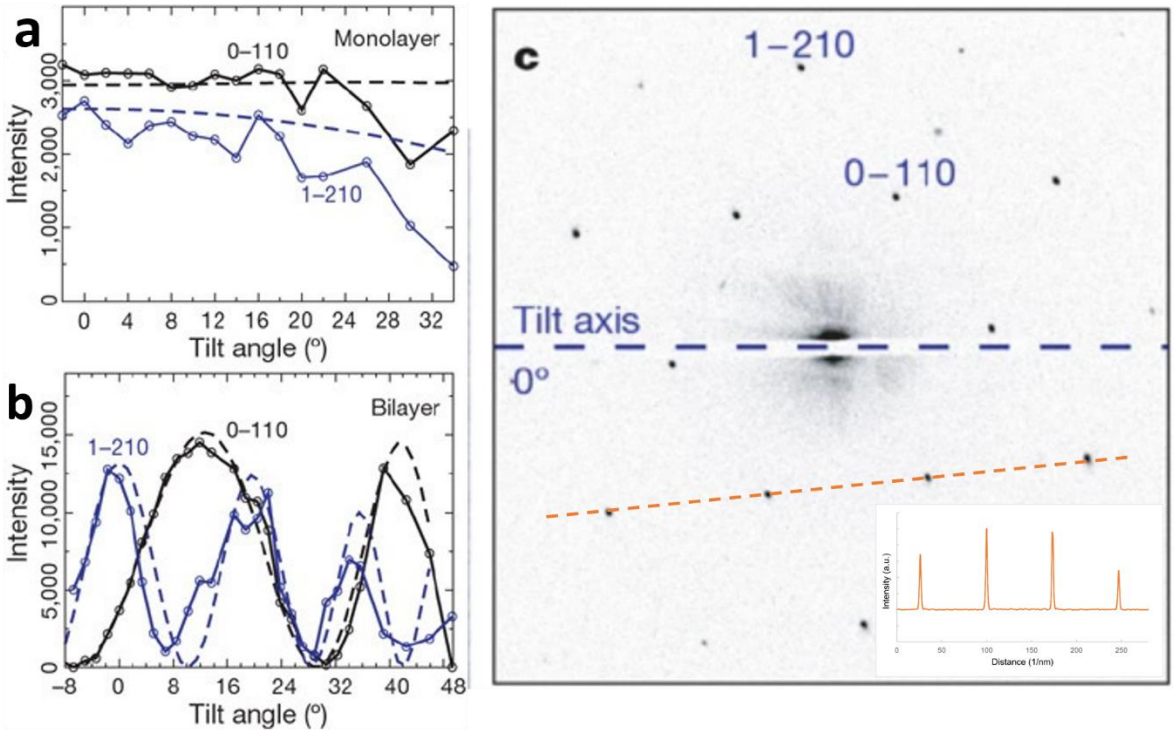

Figure 3.5 a, b) Intensities as a function of the tilt angle for planes 1-210, 0-110 for monolayer and bilayer graphene respectively. c) SAED pattern of monolayer graphene a 0° tilt horizontal tilt axis. The inset shows the variation in intensity typically obtained for monolayer graphene. Adapted from reference 172.

3.3 Atomic Force Microscopy (AFM)

AFM is a high-resolution tool to track the topography of a surface from several microns down to the nanometer scale with a sub-nanometer resolution. The wide range of spring constants of cantilevers (10^{-2} - 10^{2} N/m) results in measurable forces in the range of pico-Newtons to micro-Newtons. Moreover, modern AFMs are provided with highly sensitive photodetectors. These two features enable atomic force microscopes to measure atomic structures.[173]

Traditionally, AFM works in a quasi-static or contact mode, in which a sharp probe is rastered over the sample's surface, so the height is indirectly measured. However, this

mode is more appropriate for rigid samples or nano-patterning, since shear forces might damage delicate samples such as 2D materials, which in principle are one atom thickness. An alternative for such fragile samples is the non-contact AFM, which is discussed next.[173]

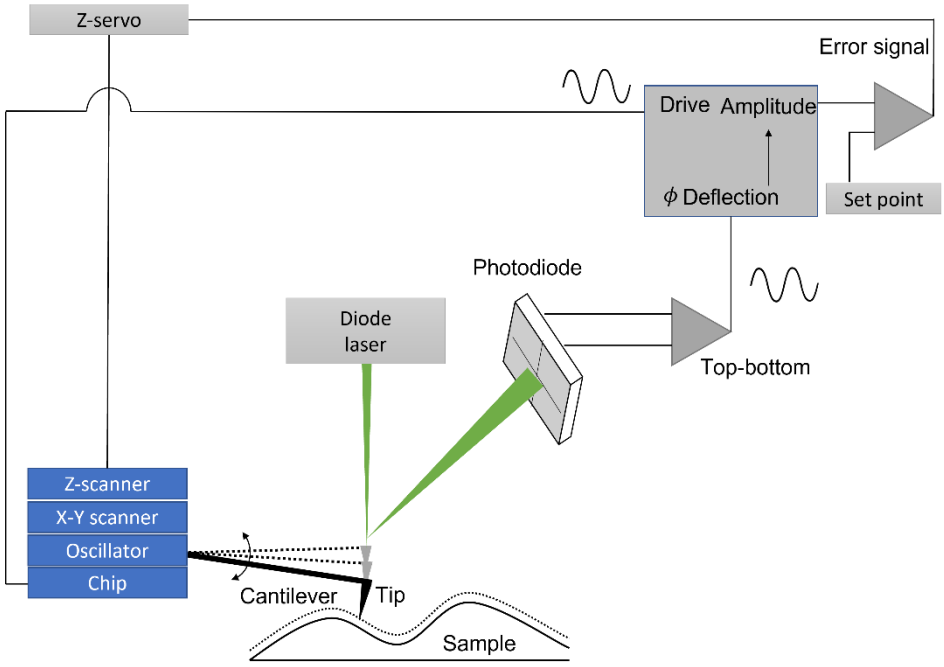

Figure 3.6 Schematic showing typical components involved in a non-contact mode setup. The figure was exaggerated to show that the tip is not in direct contact with the samples but a distance from it. Adapted from reference 173.

3.3.1 Non-contact AFM (NC-AFM)

Non-contact AFM creates a very delicate interaction between the sample and the probe, allowing imaging without any damage such as tearing and puncturing the sample. In this AFM mode, the cantilever vibrates near its resonance frequency tapping the surface many times at the exact pixel location. Thus, a time-averaged interaction results. Because the vertical probe oscillation amplitude is used to track the surface topography, it must be large enough to overcome the adhesion between the tip and the surface.[173]

The core of the working principle is the change in the oscillator net spring constant due to the force gradient (dF/dZ). Once an oscillation has been completed, a net positive or negative shift in the resonance frequency is produced, which will necessarily produce a change in the oscillator amplitude. Thus, a feedback loop is needed to vertically displace the midpoint of the oscillator and keep the amplitude constant to track the surface topography.[173]

Figure 3.6 shows a schematic of the feedback loop control and the hardware when using the non-contact mode. The way the instrument keeps track of the movement of the probe is due to the laser- quad photodiode pair. The photodiode will detect changes in the deflection of the probe and the amplitude of the signal will be compared to the setpoint specified by the user and the z-scanner will shift vertically proportional to the error signal.[173]

AFM is typically used to assess the thickness and roughness of the carbon-based family materials. The NC-AFM mode is typically used to measure the thickness of graphene,[174] but contact mode AFM has also been used.[4,175] Different studies have found that the average step is around 1 nm for monolayer graphene from mechanical exfoliation. Such approximation deviates significantly from the true value close to 0.334 nm. It has been hypothesized that the apparent thickness depends on the force applied from the tip on the surface, such that when increasing the force, it is possible to get more accurate measurements with a 0.1 nm error.[176] The dependence of thickness on the force can be explained by the existence of a buffer layer, formed by adlayers of moisture, which was demonstrated experimentally.[4,177] This is consistent with the measurements done under ultra-high vacuum, measuring a step of 0.4 nm between layers.[178]

Reported values for single-layer graphene oxide (GO) sheets are around 1 nm. In this case, the apparent thickness is strongly influenced by the hydrophilic nature of GO and the structure, which is not atomically flat as in the case of cleaved HOPG.[179,180] In the present work, NC-AFM measurements were done in ambient conditions. Figure 3.7 shows graphene oxide layers deposited on the Si/SiO_2 substrate. Typical heights measured were ~ 1 nm in agreement with previously reported values for monolayer GO.

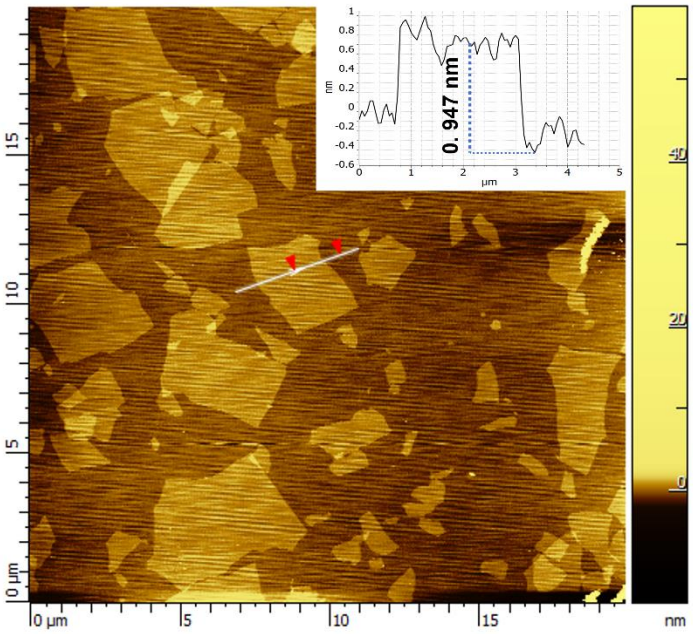

Figure 3.7 AFM image from graphene oxide flakes synthesized in this work using non-contact mode. The inset shows the height profile of an arbitrary flake.

3.4 Raman spectroscopy

Raman spectroscopy has become an important tool for analysing carbon-based materials. Unlike absorption spectroscopy techniques where the energy of the photon must match the energy gap between the ground state and the excited state, scattering will always occur no matter if this condition is met. When scattering occurs, the light is immediately scattered, forming a short-lived complex, often called a virtual state. Although the electronic distribution will be different, it will not represent an equilibrium state. Furthermore, the nuclei will not reach an equilibrium position either. This type of scattering is the most intense one and it is called Rayleigh scattering and is an elastic process.[181]

Raman scattering is a rare process only experienced by one in 10^6 – 10^8 photons. In this mode of scattering, the nuclei and the electrons move at the same time. Since nuclei are much heavier than electrons, it will produce a change in the energy of the molecule as part of the energy from the incident beam is transferred. When the molecule starts from the ground state (m) and goes to a higher vibrational state (n), the scattering is called Stokes-Raman scattering. In this case, the energy difference between the incident photon and the scattered radiation will correspond to the energy vibrations of the molecule. The opposite of

the previous process described is called anti-Stokes scattering and involves the transfer of energy from an excited state n to the scattered photon. However, it is much weaker when compared to stokes scattering, then only stokes scattering is usually recorded. Figure 3.8 illustrates the elastic scattering and Raman scattering that were described. In general, Raman spectroscopy relies on the change in the polarizability of the electron cloud in a molecule, being the symmetric vibrations responsible for the greatest scattering.[181]

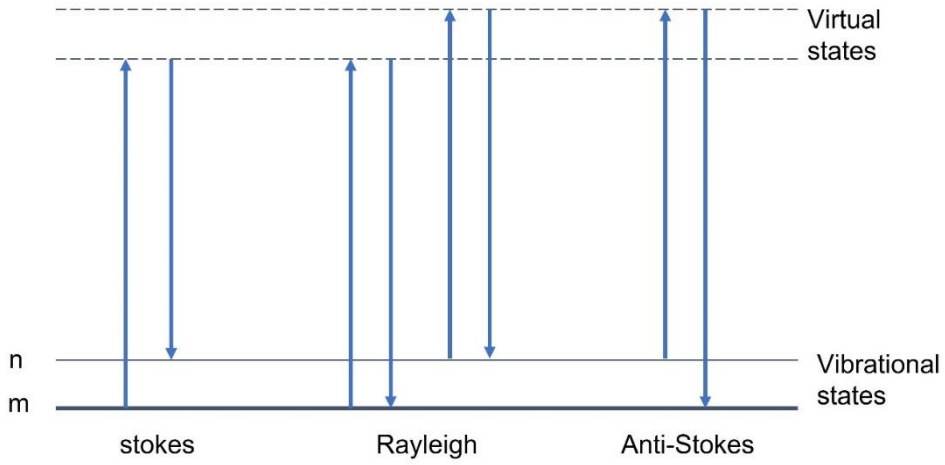

Figure 3.8 schematic of Raman and Rayleigh scattering process. Ground state and excited state are represented by 'm' and 'n' respectively.

Raman spectroscopy is a powerful tool technique to analyse graphene structure. It is fast and non-destructive so it can be potentially used as a quality control tool in large-scale graphene production processes.[182] Furthermore, Raman spectroscopy of graphene has proven to identify structural damage,[183,184] stress,[185] strain,[186,187] doping,[188] chemical functionalization,[189,190] and magnetic fields.[191,192] Since Raman scattering of phonons is essentially due to the interaction and interference of electrons, variations induced by the phenomena listed above will affect the positions, intensities, and width of the peaks. Phonon dispersions of monolayer graphene can be divided into three acoustical (A) and three optical (O) branches. Modes can be out-of-plane (Z), in-plane longitudinal (L) and traverse ones (T). Figure 3.9a and b show the plot of the Brillouin zone of graphene, the first Brillouin zone of the electronic dispersion (Dirac cones). Since graphene has two atoms per unit cell, it has six normal modes. The in-plane optical phonon E_{2g} are Raman active, while B_{2g} out-of-plane is not.[193] Thus, at the centre of the Brillouin zone, the centre of the primate cell in the reciprocal lattice $\Gamma: A_{2u} + B_{2g} + E_{1u} + E_{2g}$. These four modes are illustrated in Figure 3.9c).

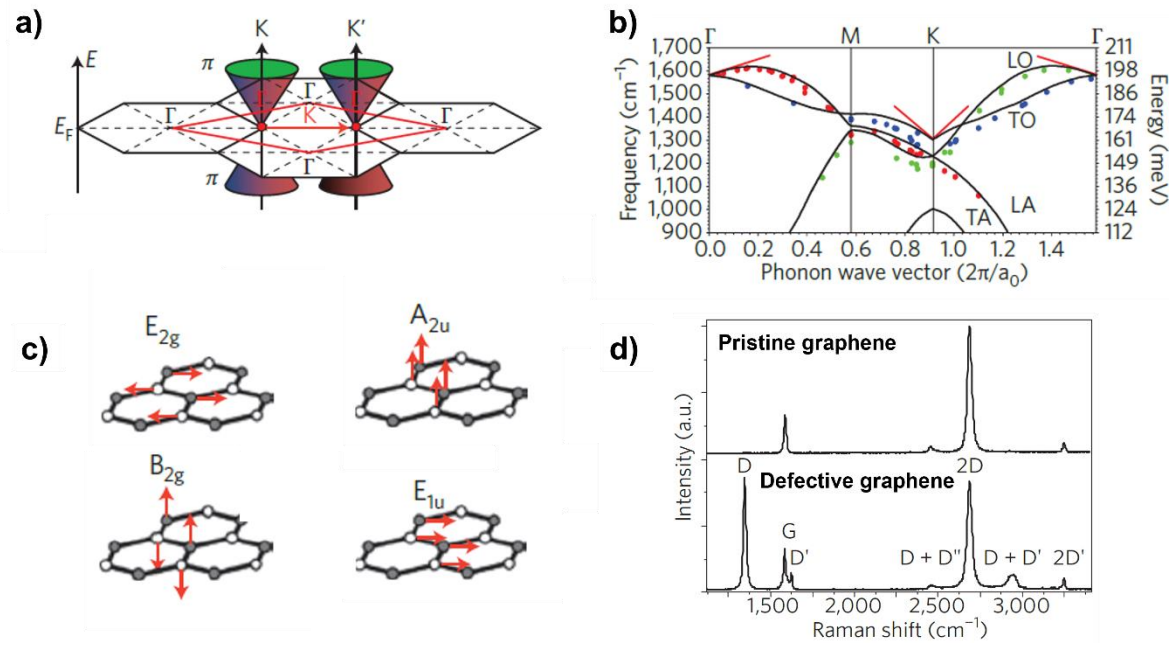

Figure 3.9 a) Electronic Brillouin zones of graphene (black hexagons), First phonon Brillouin zone (red rhombus) and electronic dispersion (Dirac cones). b) The black curves represent the dispersion of in-plane phonon modes in graphene in the energy and frequency range relevant for Raman scattering and points are experimental data from references 194,195. c) Γ-point phonon-displacement pattern for graphene. d) Raman spectra of pristine and defective graphene using a 514 nm laser excitation wavelength. Adapted from reference 196.

The Raman spectrum of graphene shows a characteristic set of bands. Figure 3.9d shows the optical phonon dispersions of single-layer graphene relevant to the interpretation of Raman spectra. In the following discussion, all peaks mentioned were taken at 514 nm. The G peak at 1580 cm^{-1} corresponds to the high-frequency phonon E_{2g} at the Brillouin zone centre Γ. It involves the in-plane bond-stretching motion of pairs of sp^2 carbon atoms. This mode will occur in every sp^2 carbon and does not require the presence of a six-folded ring.[197]

The D peak at 1350 cm^{-1} is linked to the TO phonons around the Brillouin zone corner **K**. This phonon causes the breathing mode of the six-atoms ring and is activated by defects. In the case of graphite, this mode is forbidden. Defects are those related to bond-angle, bond-length and sp^3 hybridization. It means that the D peak will be sensitive to edges, imperfect stitching at the boundaries of graphene domains and functionalization as it will produce the transition from sp^2 to sp^3 hybridization state of the functionalized carbons.[198,199]

The D' peak at ~1620 cm^{-1} comes from the double resonance connecting two points belonging to the same cone around **K** (or **K'**). The 2D at ~2700 cm^{-1} peak is an overtone of the D, and similarly, 2D' is an overtone of D'. Both are always present since no defects are required for their activation as they originate from an event where momentum is conserved. The D+D''peak at ~2450 cm^{-1} was assigned to a combination of a D phonon and a phonon belonging to the LA branch.[171,196]

Early investigations proved that Raman spectroscopy could capture the unique electronic structure of graphene. Graphene has been proven to have a very different Raman spectrum from bilayer graphene and graphite. Graphene shows a single D peak, while graphite D peak can be deconvoluted in D_1 and D_2 peaks (Figure 3.10d).[200,201] Also, the 2D peak shows a different behaviour when increasing the number of layers. Single-layer graphene shows a single symmetrical peak and bilayer graphene shows a similar single but upshifted broader peak (Figure 3.10 a-c). On the other hand, graphite shows a completely different peak with four overlapping components $2D_{1B}$, $2D_{1A}$, $2D_{2A}$ and $2D_{2B}$, giving an overall asymmetrical appearance in shape. It was observed that for more than 5 layers the 2D peak did not look different from graphite (Figure 3.10 a and b).[171] It is also worth mention that the observation of a single 2D peak on its own cannot be considered as a fingerprint for monolayer graphene as turbostratic graphite also has a single 2D peak; however, its full width at half maximum is almost double that of graphene.[202]

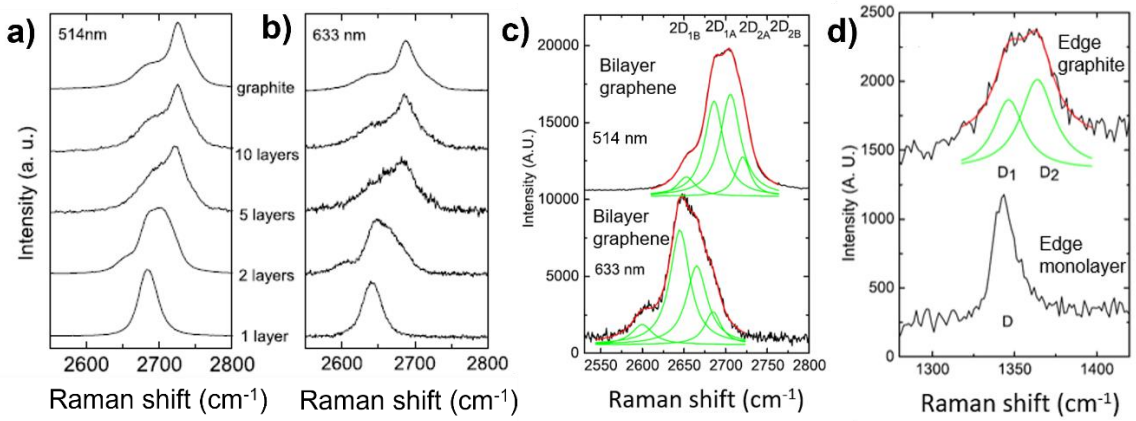

Figure 3.10 a) and b) Evolution of the 2D peak when increasing the number of graphene layers measured at 514 nm and 633 nm respectively. c) Deconvolution of the 2D peak for bilayer graphene at 514 nm. d) Deconvolution of the D peak in the edge of graphite (top) and characteristic single peak in the edge of monolayer graphene (bottom). Adapted from reference 171.

In one of the early works on the Raman spectrum of graphite, it was noted that the I_D/I_G ratio is inversely proportional to the crystal size L_a, so that $I_D/I_G = C(\lambda)/L_a$ where $C(514\ \text{nm}) \sim 4.4\ \text{nm}$.[197] Assuming a sample with an average distance L_D between defects and a laser spot size L_L, it is expected that the average number of defects probed by the laser will be proportional to $(L_D/L_L)^2$, thus $I_D \propto (L_D/L_L)^2$. Also I_G is proportional to the total area probed by the laser, thus $I_G \propto L_L^2$. Then it is inferred that $I_D/I_G = C''(\lambda)/L_D^2$. Lucchese *et al*. subjected a sample of graphene to Ar^+ ion bombardment and quantified the average inter-defect distance L_D using scanning tunnelling microscopy (STM). They found a non-monotonous behaviour, such that for low L_D values I_D/I_G is in good agreement with the relationship $I_D/I_G = 0.0055L_D^2$ proposed by Ferrari *et al*.[198] at 514 nm laser excitation. For higher L_D values it was proposed $I_D/I_G = 102/L_D^2$ at 514 nm laser excitation.[183] In a later study, Cançado *et al*. derived a more general relationship that applies to laser excitations in the visible range in the low-density defect region ($L_D > 10$ nm). They defined the defect density n_D (cm^{-2}) as:[184]

$$n_D(cm^{-2}) = \frac{(1.8 \pm 0.5) \times 10^{22}}{\lambda_L^4}\left(\frac{I_D}{I_G}\right) \qquad \text{Eq. 3.1}$$

The analysis of defects in graphene conducted by Cançado *et al.* was validated in a recent study where defect density and size were systematically varied via ion bombardment,

which induced vacancy defects.[184] The study also reveals that the I_D/I_G ratio can accurately determine the level of disorder in graphene if the average defect size is known according to Eq. 3.2:[203]

$$\left(\frac{I_D}{I_G}\right) = C_A \frac{(r_A^2 - r_S^2)}{(r_A^2 - 2r_S^2)}\left(e^{-\pi r_S^2/L_D^2} - e^{-\pi(r_A^2 - r_S^2)/L_D^2}\right) \qquad \text{Eq. 3.2}$$

where, L_D is the inter-defect distance, r_S is the radius of the vacancy defect, r_A is the distance from the centre of the defect equal to r_S+L_σ, where L_σ is the relaxation length while C_A is approximated as $160E_L^{-4}$. Figure 3.11a shows the agreement of experimental data to Eq. 3.2. Figure 3.11b shows the Raman spectra evolution when decreasing the interdefect distance L_D. Figure 3.11b shows absence of the D peak for defect free single layer graphene, which can be described as stage 1. As defect density increases, so too does the I_D/I_G ratio. Stage 2 is reached when vacancy defects coalesce and the number of six atom rings is reduced. This structural disorder causes broadening of the G and D peaks, reduction on the 2D peak intensity and activation of the D' peak.[203]

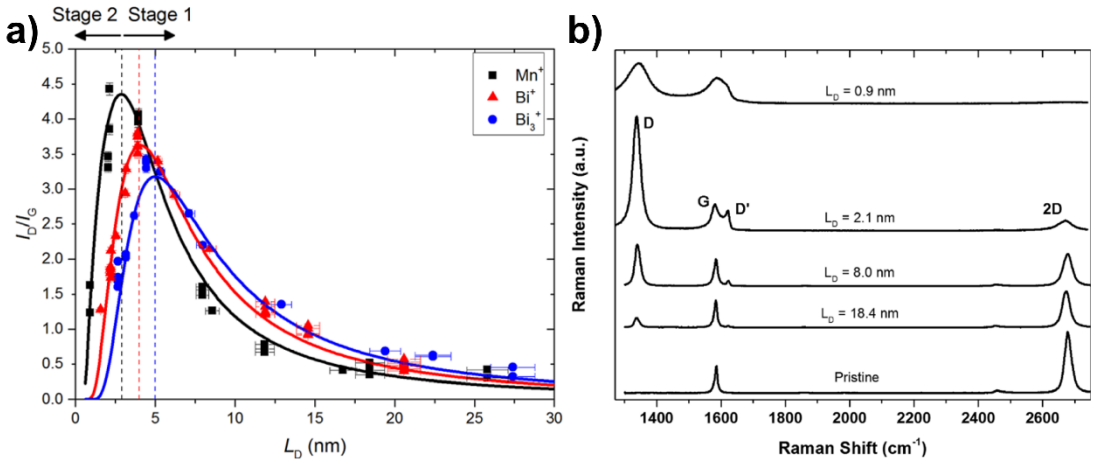

Figure 3.11 a) I_D/I_G ratio versus the inter-defect distance, L_D, for bombardment with Mn^+, Bi^+ and Bi_3^+ at 25 keV. Data were fitted to Eq. 2.2. b) Raman spectra of single layer graphene bombarded with Mn^+ ions at 25 keV obtained using a 532 nm excitation laser. L_D is the average inter-defect distance, which is larger for lower defect density. Reproduced from reference 203.

3.5 Powder X-ray Diffraction (PXRD)

PXRD is a bulk technique that provides information about sample purity, crystallite size and even morphology. As mentioned previously, atoms can elastically scatter X-rays. When scattered waves are coherent, they constructively interact creating a wave with a higher amplitude. Then, the diffraction of these waves will only occur in specific directions, which are governed by Bragg's law:[204]

$$\lambda = 2d \sin \theta \qquad \text{Eq. 3.3}$$

where λ is the wavelength of the source, d is the distance between two parallel planes in the crystal lattice and θ is the angle of diffraction. Figure 3.12 illustrates this concept.

The three main components of an X-ray diffractometer are the X-ray source, the specimen and the X-ray detector. In most diffractometers, the source is Cu Kα radiation, because of its high intensity, with an average wavelength $\lambda = 1.54$ Å. Normally, powders should be less than 50 μm, since small grains (< 1 μm) will produce broadening of the peaks. Thereby, crystalline materials will produce sharp peaks and amorphous materials will produce broader peaks. In general, the diffraction pattern is formed because each plane of the lattice crystal with distance d is diffracted at every θ angle that satisfies Bragg's law. After the beam has been diffracted, the signal is filtered so that background radiation is reduced and only the X-rays coming from the samples are collected.

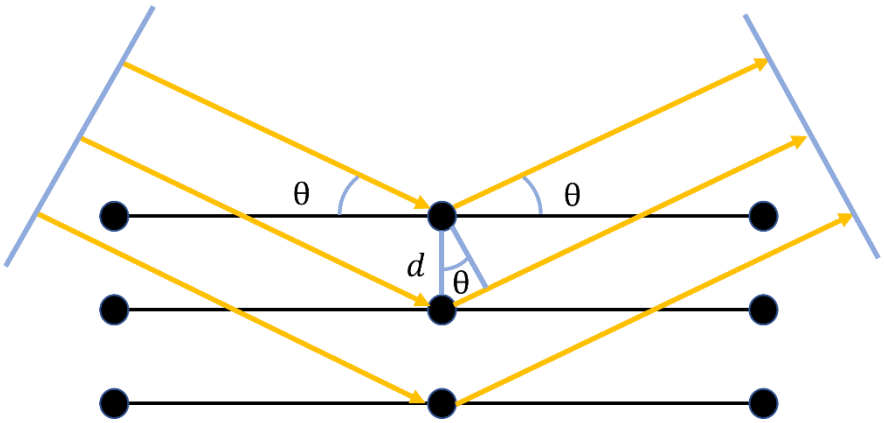

Figure 3.12 Schematic of diffraction of X-rays by a set of parallel planes in a crystal structure.

Graphite intercalated compounds (GICs) are materials formed by the intercalation of ions between the layers of graphite. The stage index, n, is the number of graphene layers between two adjacent intercalant layers. XRD is a useful tool for the assessment of graphite intercalation, being able to distinguish between the different stages.[205,206] Figure 3.13 shows a typical diffraction pattern corresponding to different stages of a GIC before and after exfoliation.

Because graphite has a very strong peak at 26.7° corresponding to the (002) plane, this is commonly also used to estimate the interlayer distance between adjacent graphene layers according to Bragg's equation. In many processes involving graphene production, graphite intercalation is a previous step to obtain graphene. In the case of graphene oxide production, stage 1 GIC is a precursor formed when graphite is mixed with sulfuric acid and strong oxidant $KMnO_4$ after the reaction has been quenched in water, graphene oxide is obtained.[207] In both cases, the diffractogram will show a shift of the [002] peak towards lower angles because of the increase in the interlayer distance.

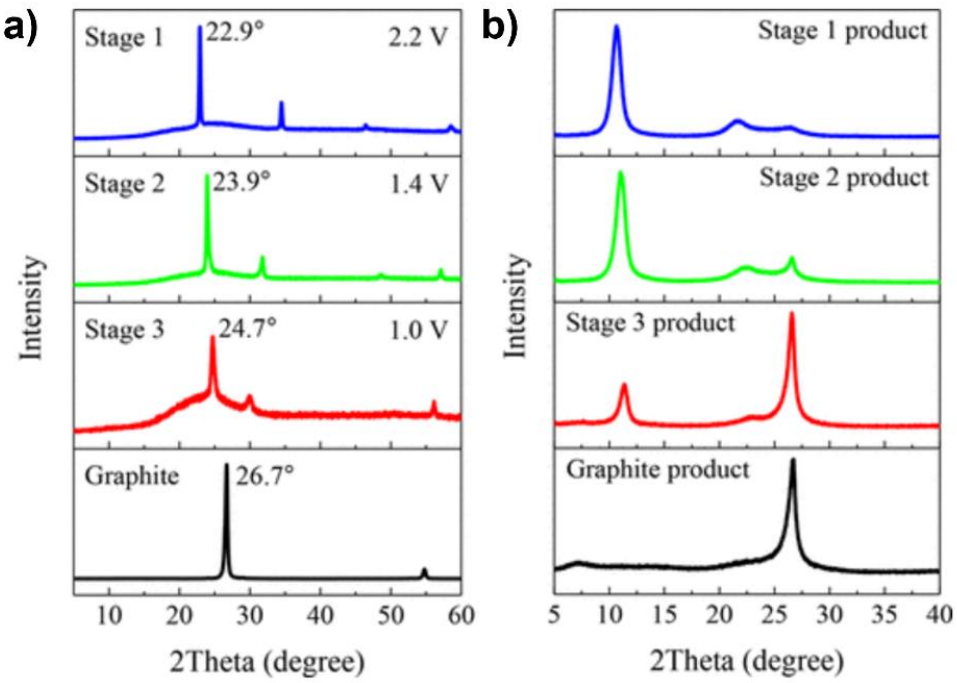

Figure 3.13 a) XRD from GICs at different intercalation voltages in concentrated H_2SO_4. b) XRD after exfoliation of the GICs in $(NH_4)_2SO_4$ 0.1 M at 10 V. Adapted from 206.

3.6 Infrared spectroscopy

Infrared spectroscopy is an easy way to identify chemical bonds within a molecule. When molecules are exposed to infrared radiation, those frequencies that match the natural vibration frequencies of the molecules are absorbed, and the amplitude of those vibrations is amplified. As expected, every bond has a different natural frequency vibration, and the nature of the environment will influence its position in the spectra. Therefore, the spectrum for each molecule can be considered as a fingerprint.[208]

Fundamental vibrations can be classified as stretching and bending. In any group of three or more atoms, where at least two are the same, there are two stretching modes: symmetric and asymmetric. Bending vibration modes are scissoring, rocking, wagging, and twisting. These fundamental vibrations can interact by addition, difference, or overtones of one. Even when only certain combinations are allowed, the resulting spectrum is complicated and judicious analysis must be done and complemented by other techniques. [208]

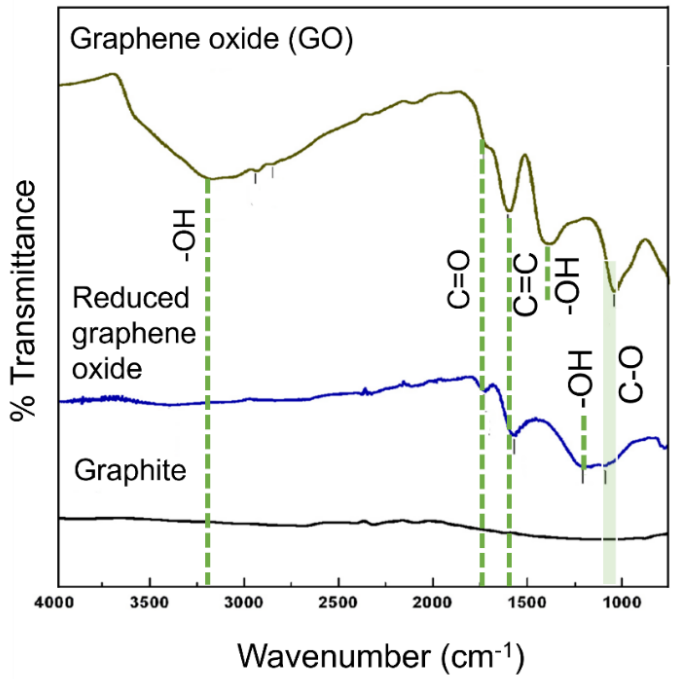

Figure 3.14 Typical infrared spectrum of graphite, reduced graphene oxide and graphene oxide. Adapted from reference 209.

IR spectroscopy is one of the preferred techniques to identify the presence of functional groups and has been widely used in graphene science. However, for low levels of functionalization of graphene, this technique is not the most convenient. Further information from other techniques, such as XPS could be necessary to support the analysis. Typical spectra of graphite, graphene oxide and reduced graphene oxide are illustrated in Figure 3.14. While the FTIR spectrum of graphite is flat due to the lack of polarity in the graphitic lattice, graphene oxide derivatives show more peaks due to the different functional groups introduced either during oxidation or through functionalization. As expected, graphene oxide shows typical oxygen-related vibrations: O-H stretching vibrations at ~3400 cm^{-1}, stretching vibrations from C=O at 1720 cm^{-1} and sp^2 C=C vibrations at 1600 cm^{-1} from unoxidized graphitic domains as well as C-OH and C-O stretching vibrations at 1220 cm^{-1} and 1060 cm^{-1}, respectively. On the other hand, typical spectra of reduced graphene oxide will show a significant reduction in the O-H peak but peaks coming from C=O and C-O bonds will still be detected because of the incomplete restoration from the sp^2 network.[210–212]

3.7 X-ray Photoelectron Spectroscopy (XPS)

XPS, also referred to as electron spectroscopy for chemical analysis (ESCA) is a technique that provides information from the outermost 10 nm from the surface of a sample. It is commonly used for elemental composition analysis assuming that the element of interest is present in at least 0.05 atomic%. Furthermore, it is also sensitive to the chemical environment of the atoms.[213]

During XPS the sample is irradiated with X-rays and the kinetic energy from the emitted electron is obtained for further analysis. The emitted electrons come from the core levels of the atom. This is expressed mathematically as:[214]

$$h\nu = BE + KE + \Phi_{spec} \qquad \text{Eq. 3.4}$$

where $h\nu$ is the energy of the incident X-rays, BE is the binding energy of the electron, KE is the kinetic energy measured with respect to the Fermi level, and Φ_{spec} is a constant value defined as the spectrometer work function, which correlates to the minimum energy required to eject an electron from an atom. It is noted that the binding energy is independent from the X-ray source, and any electron with a binding energy less than the X-ray source will be detected by XPS. The loss of one electron from the core will make one of the electrons from the valence band fill the vacancy and the relaxation process will create X-ray fluorescence and Auger electrons, the latter being the only ones detected by XPS (Figure 3.15a). Auger electrons are only used for qualitative analysis since their binding changes with the X-ray source (Figure 3.15b). However, they are helpful when spectral overlap is present.[214]

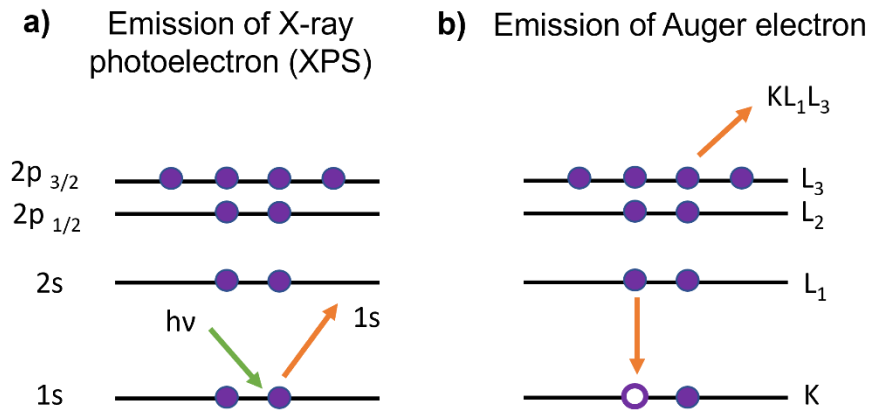

Figure 3.15 a) Emission process of a photoelectron upon X-Ray radiation. b) Auger electron emission process. KL_1L_3 means that the first ejected electron camos from K orbital, the electron that filled the core hole came from an L_1 orbital and the final Auger electron came from L_3 orbital. Adapted from reference 214.

In XPS, chemical environment sensitivity is influenced by factors like the nearest neighbours or the oxidation state of the element. For example, as neighbour atoms become more electronegative, the binding energy for the C 1s electron increases, so it can be distinguished between C-C, C-O, C=O and C-F_2 bonds (see Table 3.1). Also, the area under each peak is proportional to the number of carbon atoms in each environment. Therefore, XPS is an important technique to confirm the covalent functionalization of graphene-based materials, especially when functionalizing single monolayer graphene.[190,214–217]

Table 3.1 Binding energies for carbon in different chemical environments. Table adapted from reference 218.

Functional group	Chemical state	Binding energy (eV)
Hydrocarbon	C-C or C=C	285.0
Amine	C-N	286.0
Alcohol, ether	C-O-H, C-O-C	286.5
Carbonyl	C=O	288.0
Acid, ester	O-C=O	289.0
2 F bound to carbon	CF_2	292.0
3 F bound to carbon	CF_3	293-294

3.8 Thermogravimetric analysis (TGA)

TGA is a technique that records sample mass, temperature, and time. It is usually specified as a temperature program. To monitor the mass, a microbalance is connected to a sample pan inside a furnace with a temperature programmer and controller. Temperature is measured using a thermocouple near the pan while a purge gas passes over the sample. It can be normally air or any other inert gas such as nitrogen, argon, or helium. The thermogram obtained typically shows the mass change over time or temperature. Thermograms have different sections:[219]

1. Below 150 °C physisorbed water, low molecular volatile compounds, solvents, and trapped gases evolve.
2. Between 150 °C – 250 °C mass loss is due to chemisorbed water and low molecular weight compounds.
3. Above 250 °C decomposition begins between the onset and end set temperature. At this stage, multiple onset temperatures are possible and complex mechanisms take place.

Typically, the first derivative of the weight loss over temperature (DTG) readily identifies different stages since inflexion points will appear as peaks. Overall, TGA is a simple and robust technique widely used in the analysis of carbon materials such as carbon nanotubes, fullerenes, and graphene-based materials.

The International Organization for Standardization (ISO) reserved the term few-layer graphene (FLG) to a material that has between 3 and 10 layers of stacked graphene (ISO/TS 80004-13:2017).[220] DTG graphs have recently been used to assess the quality of bulk few-layer graphene. Graphite consists of many stacked layers of graphene and is the most thermodynamically stable material, due to the additional van der Waals forces that hold these honeycomb carbon lattice layers together. DTG peaks corresponding to maximum temperature values (T_{max}) can be linked to the number of stacked graphene layers (very high in graphite) and defects in carbon structures (very high in graphene oxide). Therefore, it is expected a higher T_{max} in graphite than in reduced graphene oxide (RGO) and FLG. In the case of GO, oxygen functionalities create a highly defective sp^3 carbon lattice. It also means a weaker interaction between the GO layers and thus, the degradation temperature is reached much faster (first DTG peak in Figure 3.16). On the other hand, since RGO is a derivative

of GO, it reveals a DTG peak shifted to higher temperatures since the sp^2 network was not fully recovered after the reduction step (Figure 3.16). The study concludes that the area under the peak for graphene oxide and graphite can be used to quantify their amount in industrial FLG batches.[221]

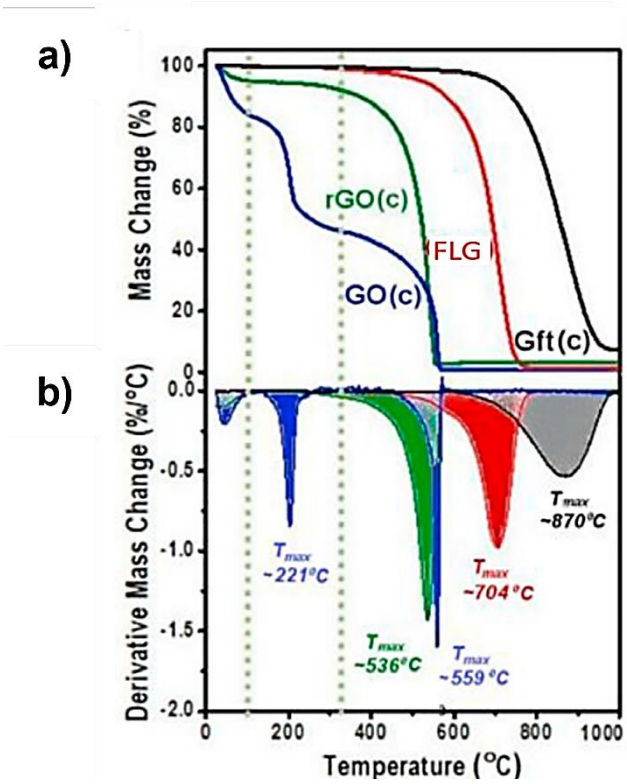

Figure 3.16 a) TGA of graphene oxide (GO), reduced graphene oxide (rGO), Few-Layer graphene (FLG), Graphite (Gft). b) DTG of GO, rGO, FLG and Gft. Adapted from reference 221.

3.9 Rheology

Rheology is the study of the deformation and flow of matter. Although the deformation of solids and the flow behaviour of liquids are classically explained by Hooke and Newton's law respectively, the behaviour of real materials can be thought of as a combination of an elastic and viscous part.[222]

The most common geometry in oscillatory experiments is the parallel plates or cone-plate geometries in which the upper plate rotates and the bottom remains stationary. The two parallel plates model is helpful to explain the main concepts and terminology. Two important assumptions must be met for the model to be valid: 1) there are no wall-slip effects and 2) the sample is deformed homogeneously.[222]

In oscillatory experiments a sinusoidal deformation $\gamma(t)$ with amplitude γ_0 and frequency ω (rad/s) is applied to the sample, as described by Eq. 3.5.

$$\gamma(t) = \gamma_0 \sin \omega t \qquad \text{Eq. 3.5}$$

when applying such a periodical deformation γ(t) on a purely elastic material, Hooke's law holds as in Eq. 3.6, where G^* is the complex modulus which could be considered as a measure of the resistance of the material against the deformation and $\tau(t)$ is the shear stress. Because G^* is a constant $\tau(t)$ and γ(t) must be in phase $(\delta = 0°)$ at all times.

$$\tau(t) = G^* \cdot \gamma(t) \qquad \text{Eq. 3.6}$$

A similar analysis can be performed for a purely viscous material, which will follow Newton's law (Eq. 3.7), when η^* is also a measurement of the resistance of the liquid to flow and is constant. Thereby, $\tau(t)$ as defined for a solid (Eq. 3.6) and $\tau(t)$ as defined for a Newtonian liquid (Eq. 3.7-Eq. 3.9) will be shifted by $\delta = 90°$ one respect to the other.

$$\tau(t) = \eta^* \cdot \frac{d\gamma(t)}{dt} \qquad \text{Eq. 3.7}$$

$$\tau(t) = \eta^* \cdot \gamma_0 \omega \cos \omega t \qquad \text{Eq. 3.8}$$

$$\tau(t) = \eta^* \cdot \sin(\omega t + \delta) \qquad \text{Eq. 3.9}$$

In general, for any viscoelastic material $0° < \delta < 90°$. Then, the complex modulus is measured in shear. G^* represents the contribution from the storage modulus (G") and the loss modulus (G"), which are responsible for the reversible deformation behaviour and the energy dissipated, respectively. The relationship between them is given by:

$$\tan\delta = \frac{G''}{G'} \qquad \text{Eq. 3.10}$$

$$|G^*| = \sqrt{(G')^2 + (G'')^2} \qquad \text{Eq. 3.11}$$

3.9.1 Small amplitude oscillation (SAOS) experiments

At low amplitude or strain values, both curves G'(γ) and G''(γ)will be constant and thus independent of the strain applied. This is called the linear viscoelastic region (LVE), in which the measurement is said to be non-destructive. However, out of this region, the structure of the sample is irreversibly changed. Such measurements are commonly named small amplitude oscillatory shear (SAOS) experiments.

There is interest in knowing the behaviour of a material under different time scales and frequency sweeps can test it. Since time is the reciprocal of the frequency, the short term is simulated at high frequencies and the long term is simulated at low frequencies.

SAOS experiments have become one of the most critical tools in analysing graphene-polymer blends. Thus, a significant number of papers have been published so far. When studying the impact of filler in immiscible polymer blends, it is desirable to get information about the interaction of fillers and polymers, especially regarding the rheological percolation, which can be considered as the minimum amount of filler needed to create an internal 3D-network within the polymer blend. Even when it can be visually identified as a plateau forming at lower frequencies, power-law approaches can also be used.[223] To illustrate the concept, Figure 3.17a shows the high amount of filler (20 wt% bentonite-graphene) needed to reach percolation in a polyethylene/ethyl vinyl acetate blend.[224] This is in contrast with the estimated ultralow percolation values (~0.028 vol% - 0.056 wt%) obtained due to the interfacial localization of graphene in the polystyrene/polylactic acid blend (Figure 3.17b).[154]

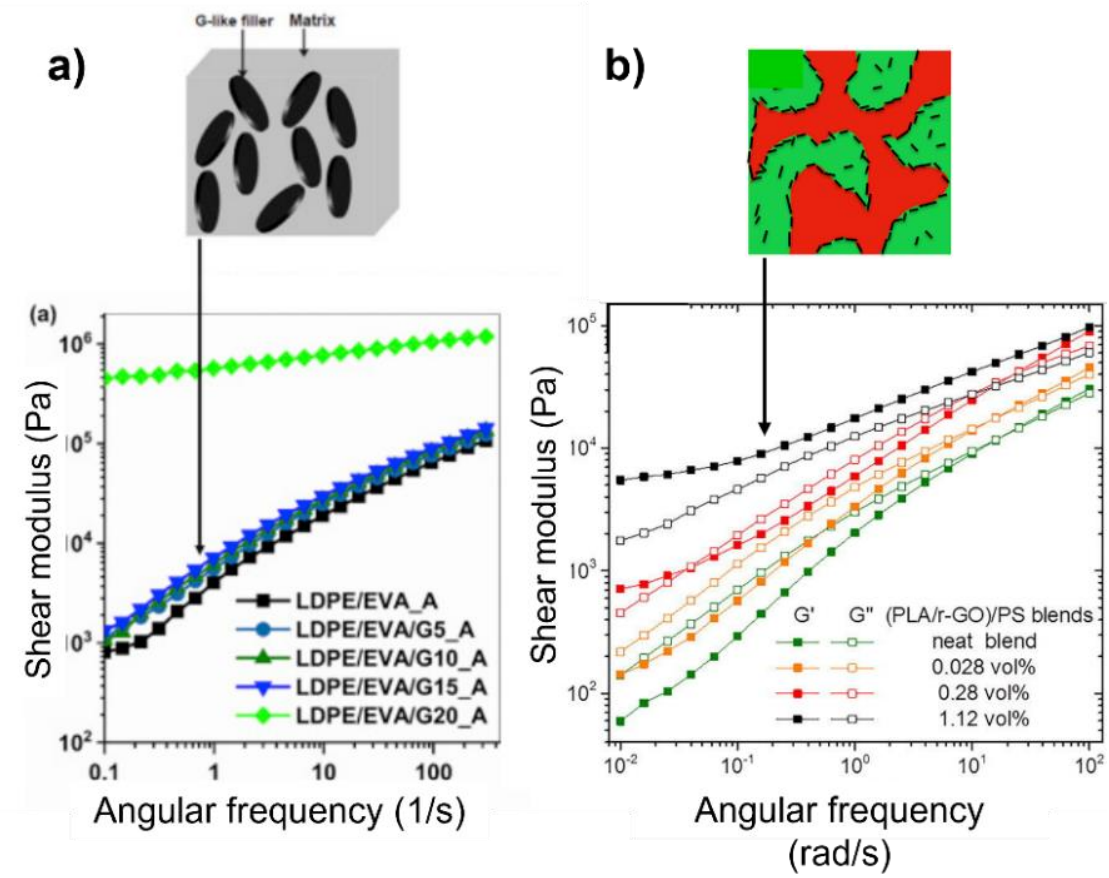

Figure 3.17 a) Frequency sweep from a low-density polyethylene/Ethyl vinyl acetate with different loadings of graphene-like filler ranging from 5 wt% to 20 wt%. b) Frequency sweep from a Polylactic acid/ Polystyrene blend with different graphene loadings ranging from 0.028 vol% (~0.06 wt%) to 1.12 vol% (~2.4 wt%). Adapted from references 154,224.

3.10 Sheet resistivity: Van der Paw method

Van der Paw method is popular in the electronics industry to determine material resistivity and has been used since its invention in 1958 by Johan van der Paw. The method is versatile since its derivation implicates four probes to be in contact at the periphery of an arbitrary shape material, which does not pose any strict constraint on the geometry of the probe, or the shape of the material tested. Apart from the previous condition, three more must be met to get accurate results. The contacts are as small as possible. Material is homogeneous in thickness and the samples do not contain any holes.[225]

The conditions mentioned above arise from physical constraints when posing the problem. Originally, the problem was solved using a conformal mapping theory of bidimensional electric field, deriving the following formula:[225]

$$e^{-\frac{\pi R_{vertical}}{R_s}} + e^{-\frac{\pi R_{horizontal}}{R_s}} = 1 \qquad \text{Eq. 3.12}$$

where R_s is the sheet resistance in Ω/sq, whose value is solved numerically. $R_{vertical}$ and $R_{horizontal}$ are average values that consider any anisotropic variation since ideally $R_{12,34} = R_{34,12}$ and $R_{23,41} = R_{41,23}$.[225]

$$R_{vertical} = \frac{R_{12,34} + R_{34,12}}{2} \qquad \text{Eq. 3.13}$$

$$R_{horizontal} = \frac{R_{23,41} + R_{41,23}}{2} \qquad \text{Eq. 3.14}$$

where $R_{AB,CD} = \frac{V_{34}}{I_{12}}$. Figure 3.18 shows the configurations used along with a source meter to estimate each value.

The Van der Paw methodology is a robust technique to measure the electrical conductivity of CVD-grown graphene on insulating substrates. Furthermore, it has been shown to provide results similar to those of terahertz time-domain spectroscopy, which is free of the ohmic contact restriction.[226] In the present work, the size of the pins is 1.5 mm in diameter and the interspace is 7 mm from centre to centre. It was sourced 100 μA which is well below the breakdown current for CVD-grown graphene which is 10^7 A/cm^2.[227] Further experimental details can be found in Section 8.23.

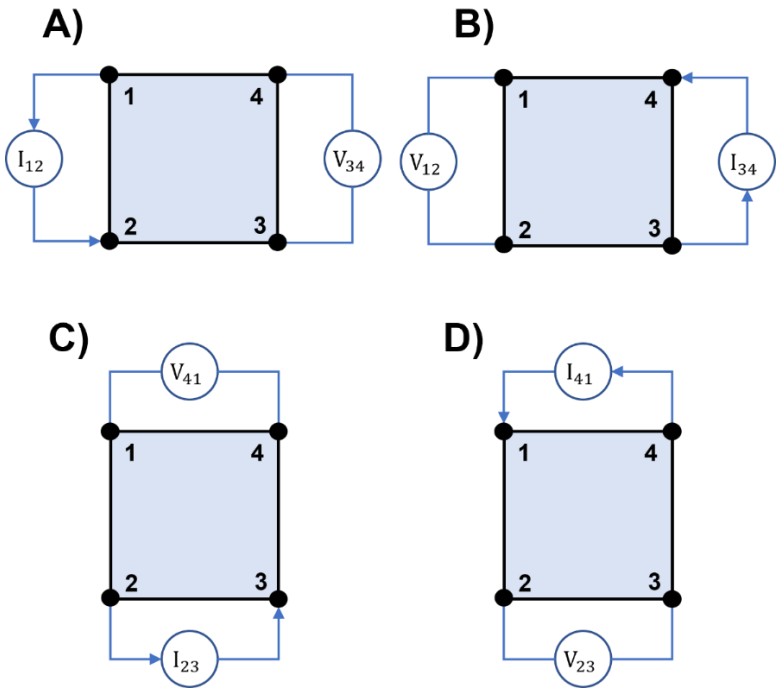

Figure 3.18 Van der Paw geometries used to calculate the sheet resistance.

3.11 Electroimpedance spectroscopy

The concept of impedance is simple, and it is governed by Ohm's law, in which the resistance R is expressed as input voltage V divided by the output current I. This is the usual definition when working with direct current. So, the impedance Z can be considered as the generalization of the resistance concept that applies in alternating current. Therefore:

$$Z = \frac{V}{I} \qquad \text{Eq. 3.15}$$

In general, when a sinusoidal voltage with amplitude V_0 and frequency ω (Eq. 3.16) is applied, the registered current signal I(t) with amplitude I_A will be out of phase and shifted ϕ degrees (Eq. 3.17):

$$V(t) = V_0 \sin \omega t \qquad \text{Eq. 3.16}$$

$$I(t) = I_A \sin(\omega t + \phi) \qquad \text{Eq. 3.17}$$

When working with EIS it is commonly expressed in complex notation where real and imaginary parts are split using Euler's relationship and related through the phase lag. Then, impedance can be expressed as:

$$Z = \frac{V}{I} = Z_0 (\cos\phi + j \sin\phi) = Z_{real} + j Z_{im} \quad \text{Eq. 3.18}$$

$$\tan\phi = \frac{Z_{im}}{Z_{real}}, \quad \phi - 90° < \phi < 0° \quad \text{Eq. 3.19}$$

Many real systems are represented by a combination of capacitive and resistive elements. One of the simplest models is the RC model which is represented by a resistance and a capacitor in a parallel configuration. For a pure resistor, the impedance will be independent of the frequency, that is $Z = R$. On the other hand, for a pure capacitor, the measured current signal will be completely out of phase with the applied voltage, and then the impedance will be given by $Z = -j (\omega C)^{-1}$. Applying Kirchhoff's law, the following relationship can be derived for the impedance in an RC model in which the real part represents the resistive part, and the imaginary part represents the capacitive part.

$$Z = \frac{R}{1 + (\omega RC)^2} - j \frac{\omega R^2 C}{1 + (\omega RC)^2} \quad \text{Eq. 3.20}$$

In this work the customized setup shown in Figure 3.19a was used to measure the complex volume resistivity of filled polymers. The setup shows a 4-wire configuration which reduced the influence of resistance of the leads. Whenever a two-wire configuration is used, it will be stated in the text and the experimental section.

As explained before, the simple RC model can provide information about the formation of conductive networks when low frequencies are applied. Thus, impedance measurements at low frequencies can be used as an approximation to the resistance value using direct current and resistivity can be estimated using the following relationship:[228,229]

$$\rho = R \frac{A}{t} \quad \text{Eq. 3.21}$$

Where R is the resistivity (Ω·cm), A is the cross-sectional area (cm^2) and t is the thickness of the sample. Also, the same electrical setup (Figure 3.19 b) was used to measure the skin-electrode impedance. In this case, the stage was substituted by a pair of electrodes and the corresponding modelling is more complicated than the RC model. Figure 3.19c) illustrates a prototypical model for the electrode-skin impedance response that consists of resistive and capacitive elements. Due to the complexity involved, the parameters for every model are estimated using a fitting procedure.[230]

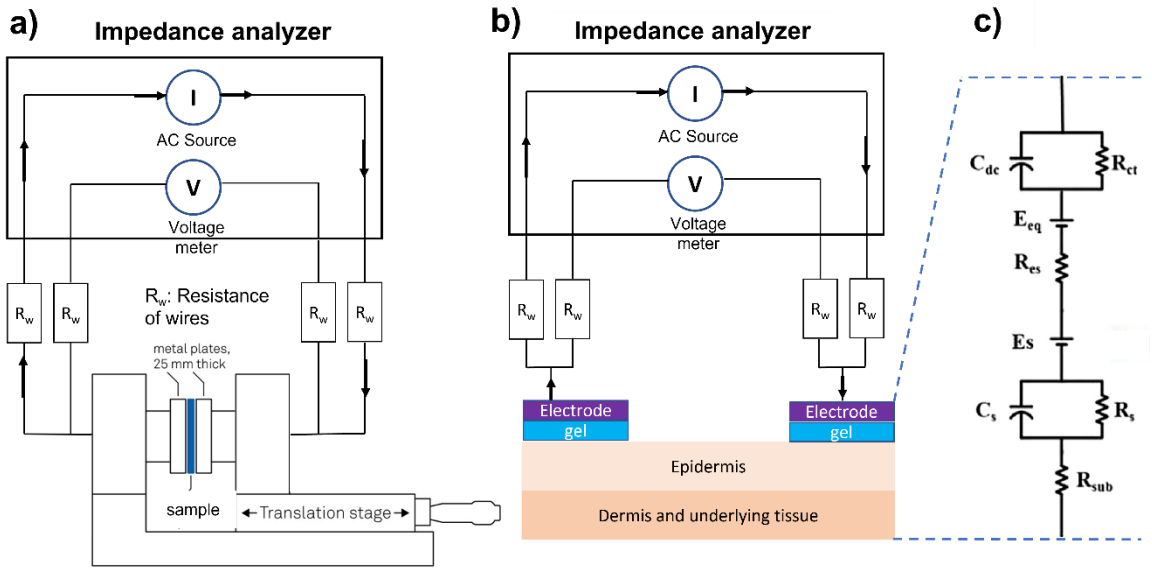

Figure 3.19 a) Setup to measure volume resistivity at room temperature. b) Adaption of the setup for electrode-skin impedance measurements. c) Equivalent circuit model proposed for a gel electrode where C_{dc} and R_{ct} are the elements from the electrode double layer, E_{eq} is the electrode-potential difference in the two electrode sets up, R_{es} is the contact resistance between the gel and the skin, E_s the potential drop for one pair of electrodes due to the semipermeable membrane and ion difference in the stratum corneum, C_s is represents the stratum corneum that works as a dielectric layer, R_s represents the contribution from sweat glands in the epidermis, and R_{sub} represents the resistance from the subcutaneous tissue. Adapted from: 230.

4 Graphene oxide production and functionalization

4.1 Introduction

Among the different precursors for graphene, graphene oxide (GO) is one of the most widely used. Even when its structure is significantly different from pristine graphene due to the oxygen functional groups and the limited efficiency of reduction methods, it is still used to explore potential applications of graphene in quite diverse areas such as catalysis,[231] energy storage devices,[232] flexible electrodes,[233] conductive inks,[234] filtration membranes,[235] just to name a few.

Furthermore, GO production uses low-cost raw materials, consumes low energy and the synthesis is relatively straightforward. Therefore, this approach offers a balanced solution in terms of cost-effectiveness and potential scaling-up.[236] However, it is not free of challenges as it involves a risk of explosion because of the exothermic oxidation process. It also involves the purification process to remove heavy metal ions, which is difficult. Furthermore, making concentrated dispersions is particularly difficult as it increases the viscosity of the solution.[236] While the risk of explosion can be solved by carefully controlling the temperature, the options for purification and water removal are still limited. The most common options for purification include washing in a centrifuge,[237] dialysis,[238] and filtration through a membrane.[239] However, these processes are affected by the gelation of the GO due to the pH decrease while residual acid is being removed. Moreover, dialysis requires days or weeks to be completed, and filtration through a membrane is hindered because of the inevitable blocking of the pores. Similarly, centrifugation can result in low yields due to the solubility of GO.[240]

Cross-flow filtration is a mature technology employed in many industries such as pharmaceutical and food. The key difference with conventional filtration is that the solutions flow tangentially across the porous membrane. This will minimize the clogging and fouling of the membrane. Although this technology is not new, it has just recently been considered as an attractive option to purify and concentrate graphene oxide solutions on larger scales.[240] Since 2014 there have been a small number of studies on the use of cross-flow filtration to purify graphene oxide.[240–244]

In this work, the method proposed by Marcano and Tour[2] will be used as a starting point. The synthetic procedure and modifications made are explained in Section 8.2. This method was demonstrated to be safer and even when it contains a larger fraction of oxidized areas, in general, the material obtained contained higher amounts of isolated aromatic areas. Overall, this method demonstrated that the electrical conductivity after reduction with hydrazine was similar to that obtained using the traditional Hummers' procedure.[52] Therefore, this method provided a platform for obtaining a conductive material after a reduction. Here, it was used as the synthesis procedure for GO followed by purification using a commercial cross-flow filtration system. The resulting material was characterized and used as a starting point to test different silanization conditions.

4.2 Results

4.2.1 X-ray diffraction

Graphene oxide used in this work was synthesized as explained in Section 8.2 starting from commercial graphite flakes (Sigma Aldrich, 99 %, 325 mesh). According to the crystallographic chart for graphite (JCPDS-Card no.75-1621), the peak at $2\theta = 26.6°$ corresponds to the [002] plane and d_{002} corresponds to the interlayer distance between graphene layers that conform the graphite. Figure 4.1 shows the XRD pattern of graphite and the well-defined [002] reflection plane around $2\theta = 26.6°$ corresponding to a d-spacing of 0.335 nm, according to Bragg's law (Eq. 3.3). Since the oxidation process of graphite will increase the interlayer distance between adjacent graphene planes, the [002] will exhibit a peak at $2\theta = 10.6°$ corresponding to an interlayer distance $d_{002} = 0.83$ nm, which agrees with previously reported values in the literature.[2,245,246] In graphene oxide, the broadening of the [002] peak happens as a result of the crystal size decrease, which is also explained by the Scherrer equation (Eq. 3.2). The increase in d-spacing is due to the oxygen functionalities introduced during the oxidation. Since oxidation disrupts the crystal lattice in graphite, the crystal size (D) decreases as it is expressed in the Scherrer equation, which accounts for broadening of the peak only due to the crystal size (Eq. 4.1):

$$D = \frac{K\lambda}{\beta \cos\theta} \qquad \text{Eq. 4.1}$$

where K is the Scherrer constant (0.91), λ is the wavelength of the X-ray beam (1.54 Å), β is the full width at half maximum (FWHM) of the peak corresponding to the [002] planes and θ is the Bragg diffraction angle.[247] A summary of these parameters can be found in Table 4.1. From Figure 4.1 it is shown that graphene oxide purified using the crossflow filtrations shows only a single peak which implies that no other crystalline structure is present apart from that of graphene oxide.

Table 4.1 Interlayer spacing and crystallite size of graphite and graphite oxide.

	Peak position [°]	d_{002} [nm]	FWHM	Crystallite size [nm]
Graphite	26.62	0.34	0.13	64.2
Graphene oxide	10.63	0.83	0.89	11.4

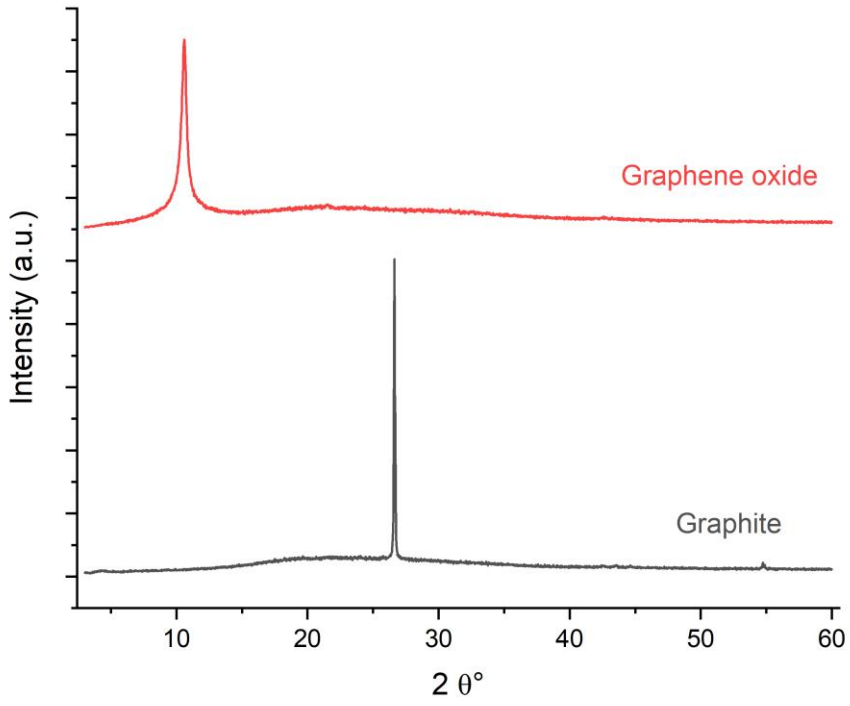

Figure 4.1 X-ray diffraction pattern of graphite and graphene oxide.

4.2.2 Raman spectroscopy of graphene oxide

Figure 4.2 shows the typical spectrum of graphite and graphene oxide (experimental details are given in Section 8.8). Graphite shows a peak at 1580 cm^{-1} corresponding to the G band associated with the vibration of the graphite lattice due to pairs of sp^2 carbon atoms. It

also shows the D band at 1351 cm^{-1} which is associated with the symmetry breaking at the edges. It also shows a small peak at 1618 cm^{-1} known as D', revealing a significant concentration of defects associated with edges. This is an expected phenomenon as the graphite used in this work has flakes ≤ 40 μm according to the manufacturer. Therefore, many graphite flakes will have a particle size less than the spot size of the laser beam (~1 μm) accounting for edge-associated defects observed in the spectrum.

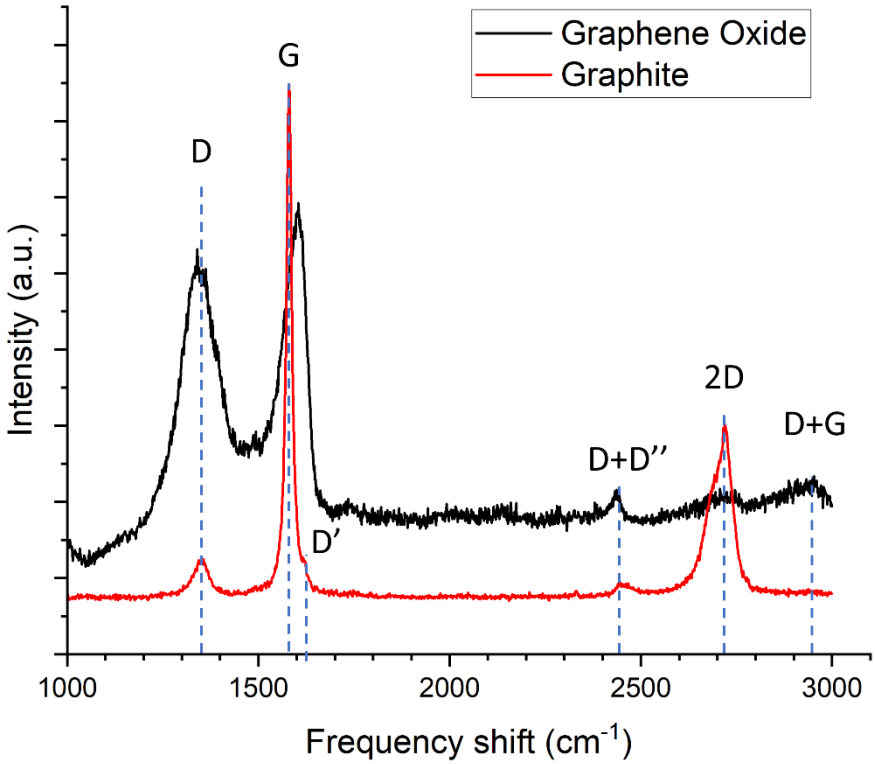

Figure 4.2 Normalized Raman spectra of graphite and graphene oxide measured at 532 nm and 1.2 mW.

It has been commonly observed that higher disorder in graphene oxide leads to a broader G band, as well as to a broad D band of higher relative intensity compared to that of the G band.[248,249] As explained in detail in Section 3.4 the D band is activated by defects, coming from anomalies in bond angle, bond length and sp^3 hybridization that disrupt the symmetry of the lattice. In the case of graphene oxide, the oxidation process disrupts the graphitic lattice by introducing oxygen functionalities causing the D band to appear. Therefore, it is expected that the Raman spectrum of graphene oxide appears similar to that of graphite transitioning to amorphous carbon showing a characteristic shift of the D band towards higher frequencies.[248] Also, since the 2D peak at 2720 cm^{-1} is a second-order phonon

of the D peak, its intensity decreases while the full width at half maximum broadens with increasing defect density.[248] As for the peak around 2450 cm^{-1}, it is assigned to an overtone of the D+D''.[250]

4.2.3 Infrared spectroscopy of graphene oxide

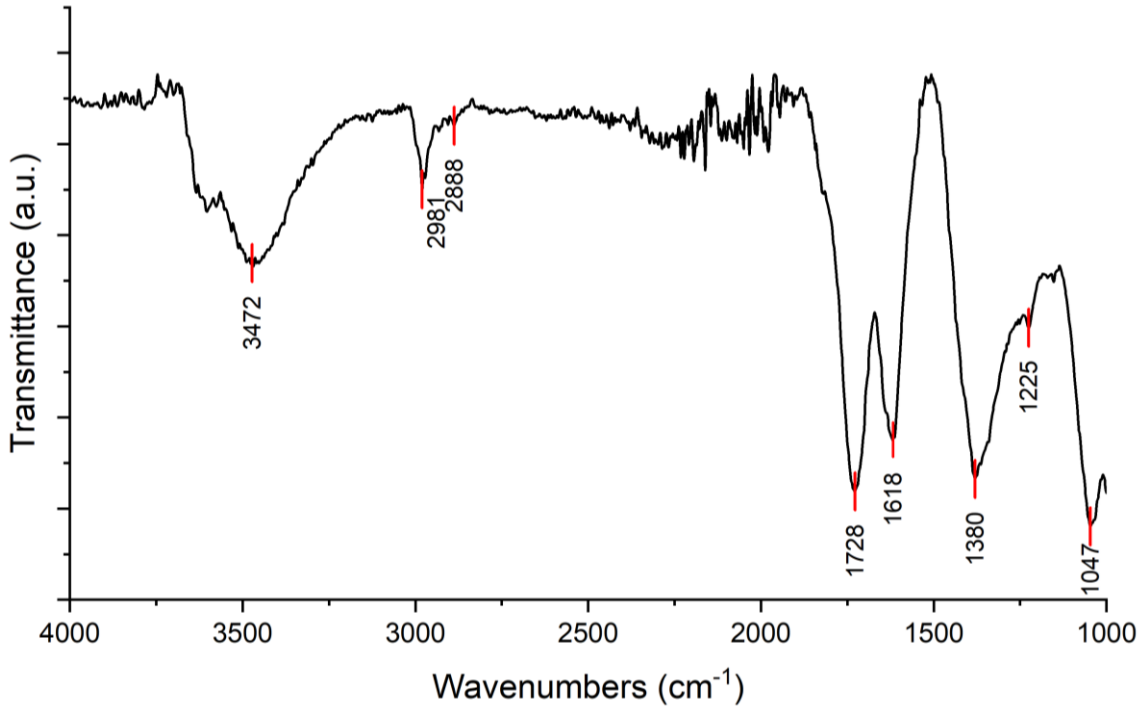

Figure 4.3 FTIR spectrum of the resulting graphene oxide.

Figure 4.3 shows a typical FTIR spectrum from the GO obtained. Due to the rich chemistry of graphene oxide (GO), it exhibits a complex spectrum and peak assignment. The characteristic region peaking at 3472 cm^{-1} comes from the stretching modes of hydroxyl groups (-OH), which theoretically come from -OH grafted to tertiary carbon atoms but most of the contributions come from water molecules adsorbed, as demonstrated in experiments with deuterated water.[251,252] The peaks around 2961 and 2888 cm^{-1} are ascribed to the asymmetric and symmetric stretching vibrations of $-CH_2$ bonds.[253] The pair of absorption bands at 1728 and 1618 cm^{-1} is the typical signature from GO and they are commonly reported. The first one is normally reported in the range of 1719-1734 cm^{-1} and has been assigned to the stretching mode of carbonyls (>C=O), coming from ketones and aldehydes moieties. Even when the peak at 1618 cm^{-1} is commonly assigned to C=C bonds stretching modes, it was demonstrated that it originated from the bending modes of water molecules adsorbed on GO. Assignment of peaks in the fingerprint region is more complicated as

overlapping from different vibration modes complicate it, therefore there is no consensus. However, the peaks around 1380 cm^{-1} have been assigned to the bending modes of tertiary C-OH bonds[251,252] while the peak at 1047 cm^{-1} has been attributed to stretching vibrations of C-O bonds presumably from epoxy or alkoxy groups.[253–255] Further XPS analysis will provide more information on the chemistry of graphene oxide.

4.2.4 XPS analysis of graphene oxide

To get more detailed information about the chemical environment of graphene oxide C 1s spectra were deconvoluted into asymmetric Lorentzian components (LA lineshape) after using a Shirley background correction using CASA XPS software for fitting the spectra.[256] Further details about the acquisitions of the data are given in Section 8.9. Graphene oxide typically contains a large proportion of oxygen functionalities. In this work, a C/O ratio of 2.2 was found, which is in agreement with other studies.[2,257,258] The C 1s spectrum was deconvoluted into 4 components, as shown in Figure 4.4. First, the peak at 284.5-285 eV was assigned to the sp^2 C=C bond which has been a common designation when working with graphene and multiwalled carbon nanotubes.[257,259–261] The peak at 286.9 eV was assigned to C-OH bonds which contribute minimally (0.05 at%). The peak at 287.1 eV was assigned to C-O-C epoxy bonds which is the main contribution to the spectra (60.9 at%). Theoretical approaches indicate that C-O-C bond must have a binding energy higher than C-OH bond but less than >C=O bond.[262] Moreover, it has been experimentally demonstrated that upon increasing the oxidation level, hydroxyl groups are converted into epoxy groups.[245] The peak at 288.4 was ascribed to >C=O accordingly. The peak at 289.2 eV was assigned to O=C-O bonds from carboxyl groups whose binding energy must be higher than C=O bonds.[246,263]

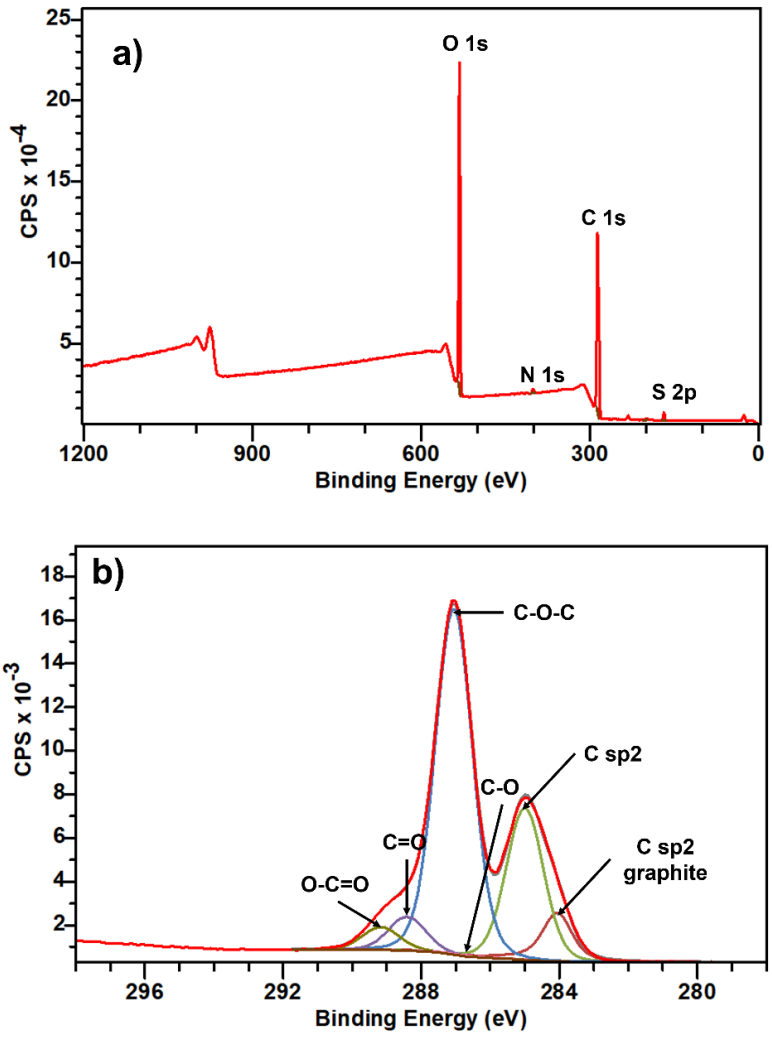

Figure 4.4 a) Survey spectra and b) high-resolution spectra of C1s of graphene oxide.

4.3 Exfoliation mechanism

Exfoliation of graphite oxide can occur because of shear forces when graphene oxide layers slide on each other. Therefore, it is expected that when graphite oxide passes through the hollow fibre membrane (1 mm inner diameter) exfoliation will happen if the critical shear rate is met. It has previously been described that exfoliation will occur whenever the shear rate associated with the flow is higher than the net energy of adhesion of two adjacent graphene oxide sheets in a solvent. The following equation was derived according to this analysis by Patton *et al.*:[31]

$$L\eta\gamma_{crit} = \left[\sqrt{E_{S,L}} - \sqrt{E_{S,G}}\right]^2 \qquad \text{Eq. 4.2}$$

where $E_{S,G}$, $E_{S,L}$ are the surface energy of water and graphene oxide. While the first one is a well-known value (72.8 mJ/m^2), the surface energy of graphene oxide was estimated according to contact angle measurements (see experimental Section 8.7). On the other hand, η, L are the viscosity of the solution ($\eta = 1.07 \times 10^{-2}$ Pa·s), and the average lateral size ($L = 16.2$ μm). Then, the critical shear rate estimated was 2450 s^{-1}. Graphene oxide solutions exhibit a shear thinning behaviour, that is, their viscosity decreases as the shear rate increases.[264,265] The relationship between the stress (σ) and the shear rate (γ) follows a power-law dependence:

$$\sigma = \gamma^n \qquad \text{Eq. 4.3}$$

where $n < 1$ for a shear thinning fluid, and can be obtained from the slope of the graph of log σ vs. log γ. From Figure 4.5 it can be observed that for a graphene oxide solution (8.05 mg/ml) $n = 0.63$. Therefore, it can be estimated the maximum shear rate reached in a hollow fibre (1 mm inner diameter) using Eq. 4.4 for a shear thinning fluid:[266]

$$\gamma_{max} = \frac{Q}{\pi r^3}\left(1 + \frac{1}{n}\right) \qquad \text{Eq. 4.4}$$

where Q is the flow rate, typically 50 ml/min and r is the radius of the hollow fibre. The estimated value of γ_{max} is 9533.4 s^{-1}. Because $\gamma_{max} > \gamma_{crit}$, exfoliation will occur during the cross-flow filtration step. This explains the considerably high amount of exfoliated graphene oxide before the sonication step. As seen from Table 4.3, 70% of the population of flakes have a thickness less than 1.4 nm, which is associated with monolayer graphene oxide, as explained later in Section 4.3.2.

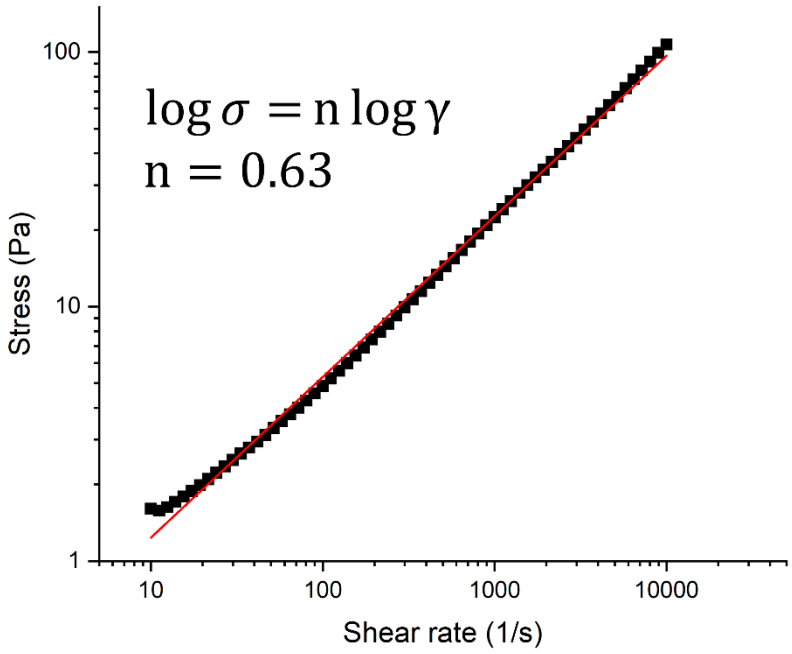

Figure 4.5 Graph of the shear rate vs. stress showing a power-law dependence. The red line corresponds to the straight line when least squares regression is applied.

4.3.1 Lateral size measurements

Figure 4.6 shows the distribution of the lateral sizes of graphene oxide and Table 4.2 summarizes the average lateral sizes and main percentiles obtained at different sonication times. In the case of graphene oxide without sonication treatment and the sample sonicated for 30 seconds, the average lateral size was measured from SEM images to account for large flakes as AFM is limited by the maximum area analysed in each scan (80 × 80 μm). Figure 4.7 shows typical SEM and AFM images of the graphene oxide sheets obtained at different sonication times. Samples sonicated for 60, 90 and 120 seconds were analysed by AFM only. Samples not treated with sonication exhibit a broad range of lateral sizes, averaging 16.2 ± 1.7 μm. A sharp decrease in lateral size can be obtained after 30 seconds of sonication, corresponding to an average lateral size of 5.0 ± 0.9 μm. Exfoliation for times above 90 seconds does not reduce the lateral size significantly as seen from Table 4.2.

Table 4.2 Summary of the lateral size distribution from at least 80 flakes of graphene oxide measured by AFM after different sonication times. P(k) stands for the k-th percentile, representing the percentage k of measured flakes that have a lateral size equal or less than the value stated.

	Percentiles and average lateral size [μm]					
	P90	P70	P50	P30	P10	Average
No sonication	23.7	20.1	15.3	12.4	8.59	16.2 ± 1.7
30 sec	8.6	6.0	3.8	3.1	2.33	5.0 ± 0.9
60 sec	3.4	2.5	1.8	1.4	0.86	2.1 ± 0.3
90 sec	3.3	2.6	1.7	1.2	0.73	1.9 ± 0.3
120 sec	2.6	1.9	1.3	1.1	0.9	1.6 ± 0.2

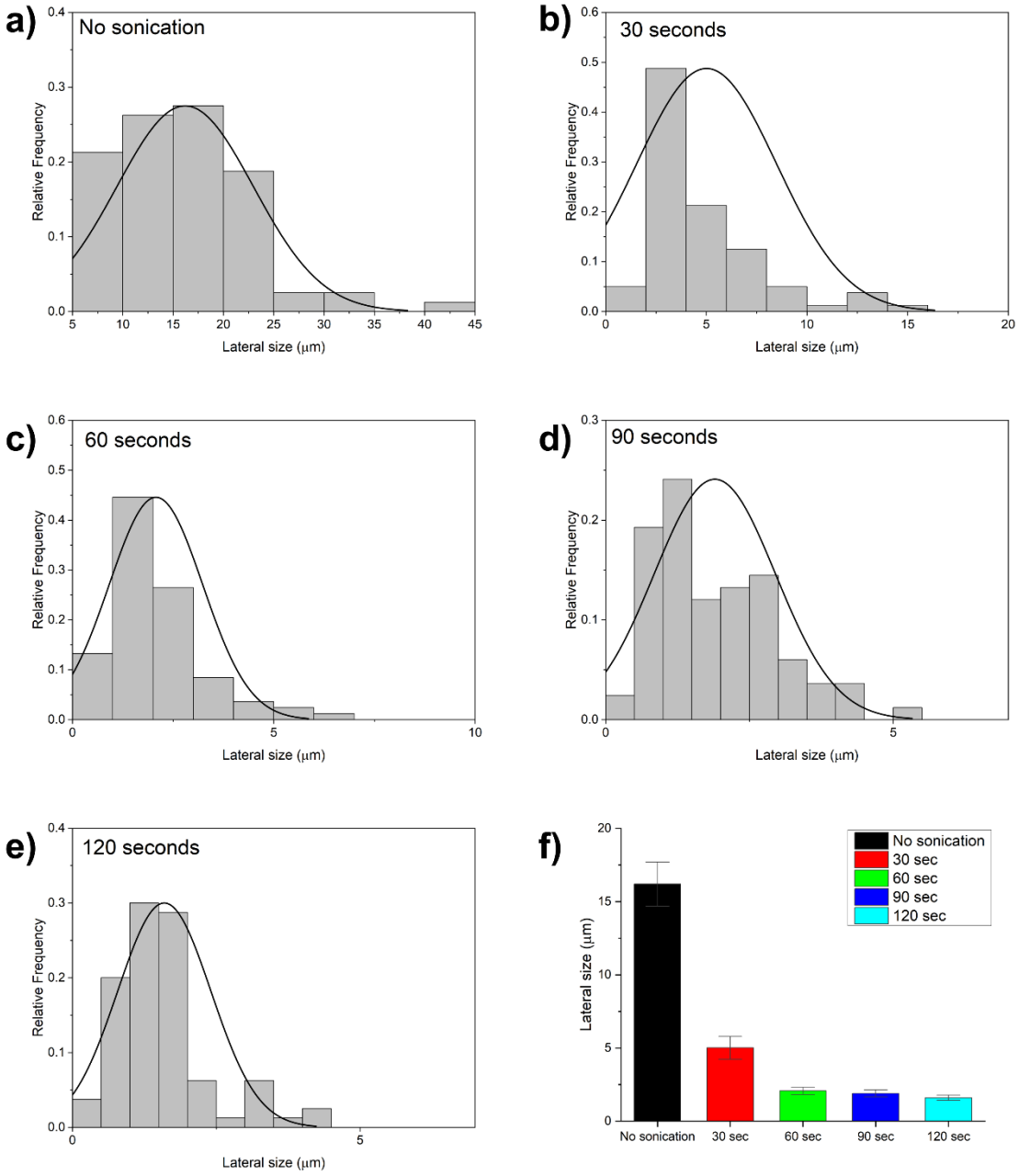

Figure 4.6 Lateral size distribution of graphene oxide solution (2 mg/ml) a) before sonication and after sonication at different times: a) 30 seconds, b) 60) seconds, c) 90 seconds and d)120 seconds. f) Summary of the lateral size distribution showing the average values and the 95% interval confidence. Data in a-e were fitted to a Gaussian distribution in OriginLab.[267]

4.3.2 Thickness measurements

As explained in Section 3.3, AFM can directly measure the thickness of graphene oxide sheets by measuring the height profiles. The degree of exfoliation can be directly assessed by the average thickness of the graphene oxide flakes obtained. Sample preparation details are given in Section 8.5. Figure 4.7 illustrates the typical profiles of graphene oxide sheets at different sonication times. Figure 4.8 and Table 4.3 summarize the average thickness obtained at different sonication times. Samples which were not sonicated showed an average thickness of 1.5 ± 0.3 nm. After sonication treatment there was no significant change, reaching a minimum value of 1.2 ± 0.1 nm for the longest sonication time (120 seconds). Due to the hydrophilic nature of graphene oxide, it can adsorb water under ambient conditions measurements, so monolayer graphene oxide is expected to show thickness values in the range of 0.8-1.5 nm for AFM measurements in the non-contact mode.[268–270] For samples that were not sonicated the average value is in the upper limit as it is also accounting for multilayer flakes. However, according to Table 4.3, the sample sonicated for 120 seconds shows that 90% of the flakes have a thickness less than 1.4 nm. As it will be explained in Section 4.3.3, TEM observations can confirm the presence of monolayer flakes.

Table 4.3 Summary of the thickness distribution from at least 80 flakes of graphene oxide measured by AFM after different sonication times. P(k) stands for the k-th percentile. P(k) stands for the k-th percentile, representing the percentage k of measured flakes that have a thickness equal or less than the value stated.

	Percentiles and average thickness [nm]					
	P90	P70	P50	P30	P10	Average
No sonication	2.8	1.4	1.2	0.9	0.6	1.5 ± 0.3
30 sec	1.8	1.5	1.4	1.3	1.1	1.5 ± 0.1
60 sec	1.8	1.4	1.2	1.1	0.9	1.3 ± 0.1
90 sec	1.4	1.3	1.1	1.0	0.9	1.2 ± 0.1
120 sec	1.4	1.3	1.2	1.1	0.9	1.2 ± 0.1

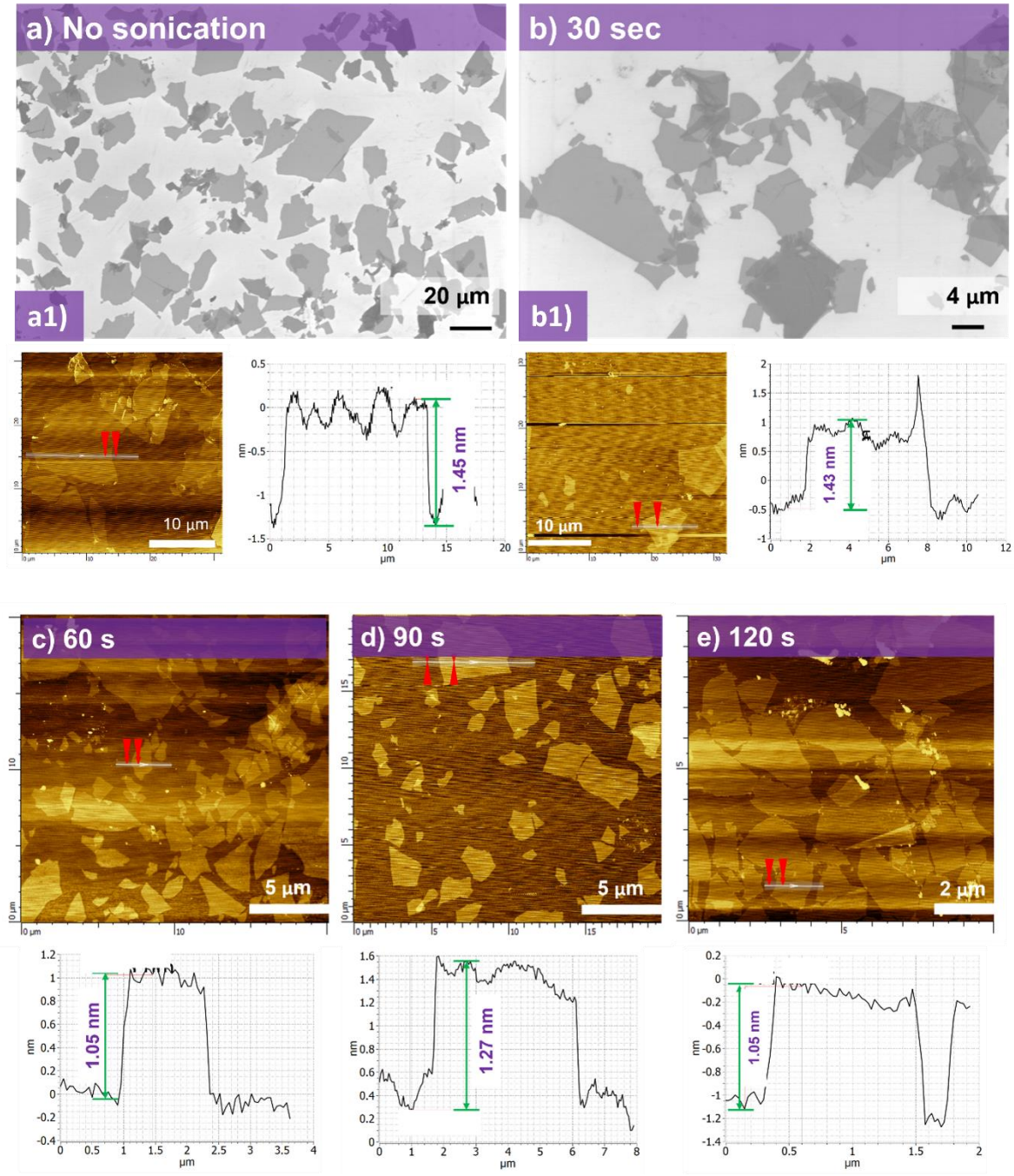

Figure 4.7 Typical images from graphene oxide deposited on a silicon substrate considered for thickness and lateral size measurements a) before sonication and after sonication at b) 30 seconds, c) 60) seconds, d) 90 seconds and e)120 seconds. All samples were treated using a sonication power of 14-17 W. Figures a1) and b1) are SEM images taken at 5 kV using an in-lens detector. The rest of them are AFM images where the plots show the profiles along the white lines and red arrows correspond to where the thickness was measured, as illustrated in the profiles.

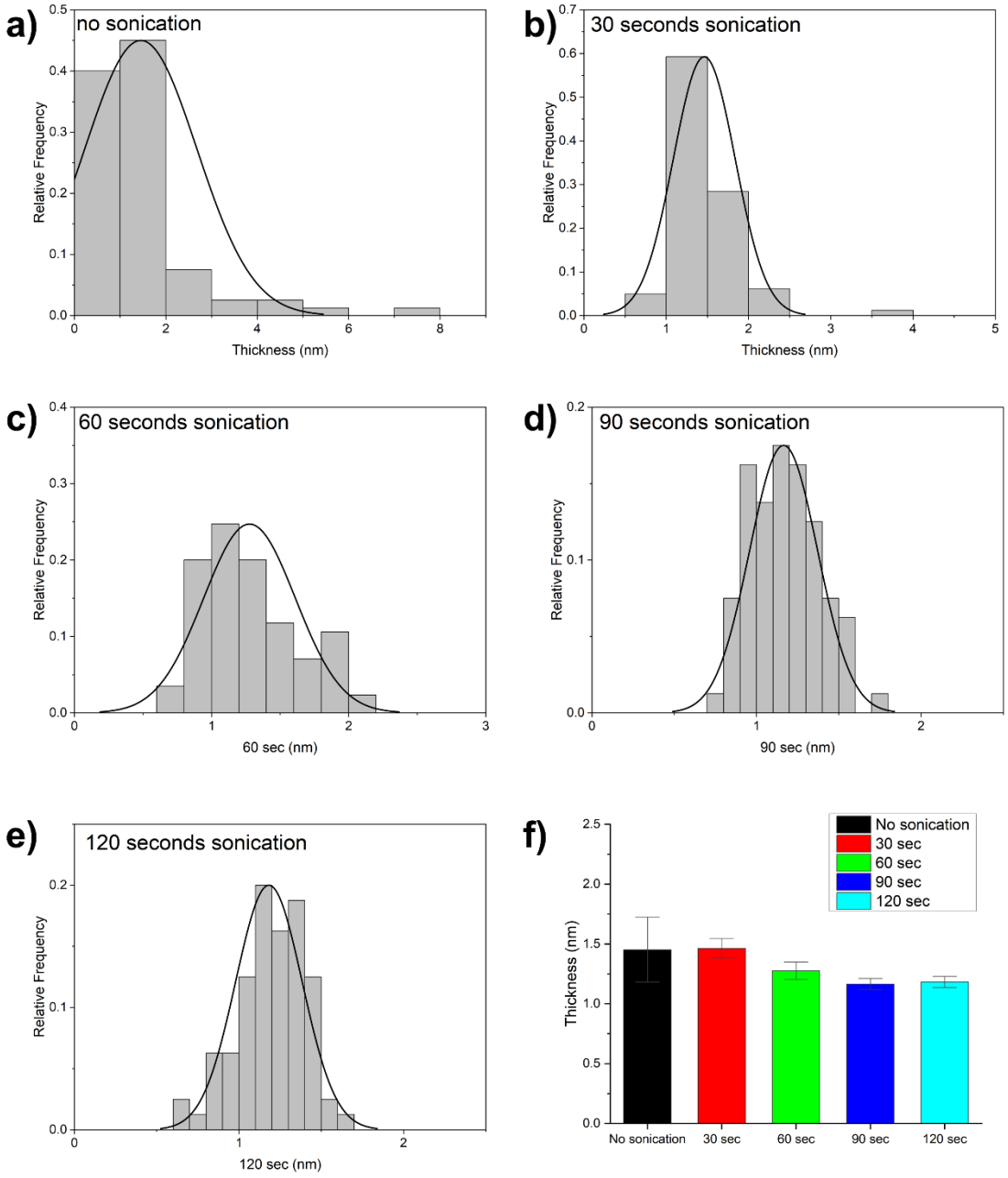

Figure 4.8 Thickness distribution of graphene oxide solution (2 mg/ml) a) before sonication and after sonication at different times: a) 30 seconds, b) 60) seconds, c) 90 seconds and d)120 seconds. f) Summary of the thickness distribution showing the average values and the 95% interval confidence. Data in a-e were fitted to a Gaussian distribution in OriginLab.[267]

4.3.3 TEM observations

AFM measurements suggest that the synthesized graphene oxide is predominantly monolayer after sonication for two minutes, having minimal variation in the thickness and lateral size. The monolayer nature was further confirmed by transmission electron microscopy (TEM). Sample preparation details are given in Section 8.4. Figure 4.9a shows a typical image of a graphene oxide flake after two minutes of sonication. The longest sonication time was selected because it provided a fully exfoliated material according to the thickness measurements in Table 4.3. High magnification on the circled section in Figure 4.9b shows the edge of the flake, showing no more than one layer, as has previously been observed in other studies. [271,272] Figure 4.9c shows the selected area electron diffraction (SAED) pattern, where the 6-fold pattern, consistent with the hexagonal graphene lattice, can be distinguished. The pattern was labelled according to the Miller-Bravais *hkil* notation.[273] It also suggests that graphene oxide sheets have some short-range crystalline order over a length scale of the coherence length of the electron beam which is a few nanometres. In addition, Meyer *et al.* showed that higher intensities of the inner reflections ($1\bar{1}00$ and $0\bar{1}00$) than those of outer reflections ($2\bar{1}\bar{1}0$ and $\bar{1}\bar{1}20$) are consistent with monolayer graphene structures or areas.[274] Furthermore, Figure 4.9 f shows a region where the graphene oxide is folded, creating a bilayer region where the mismatch corresponds to a 5.8° rotation. In Figure 4.9e it is observed another domain where the SAED pattern is not that sharp, reveals a state where the graphene oxide crystallinity has been compromised due to the functional groups that disrupt the lattice as it also has been reported previously.[275]

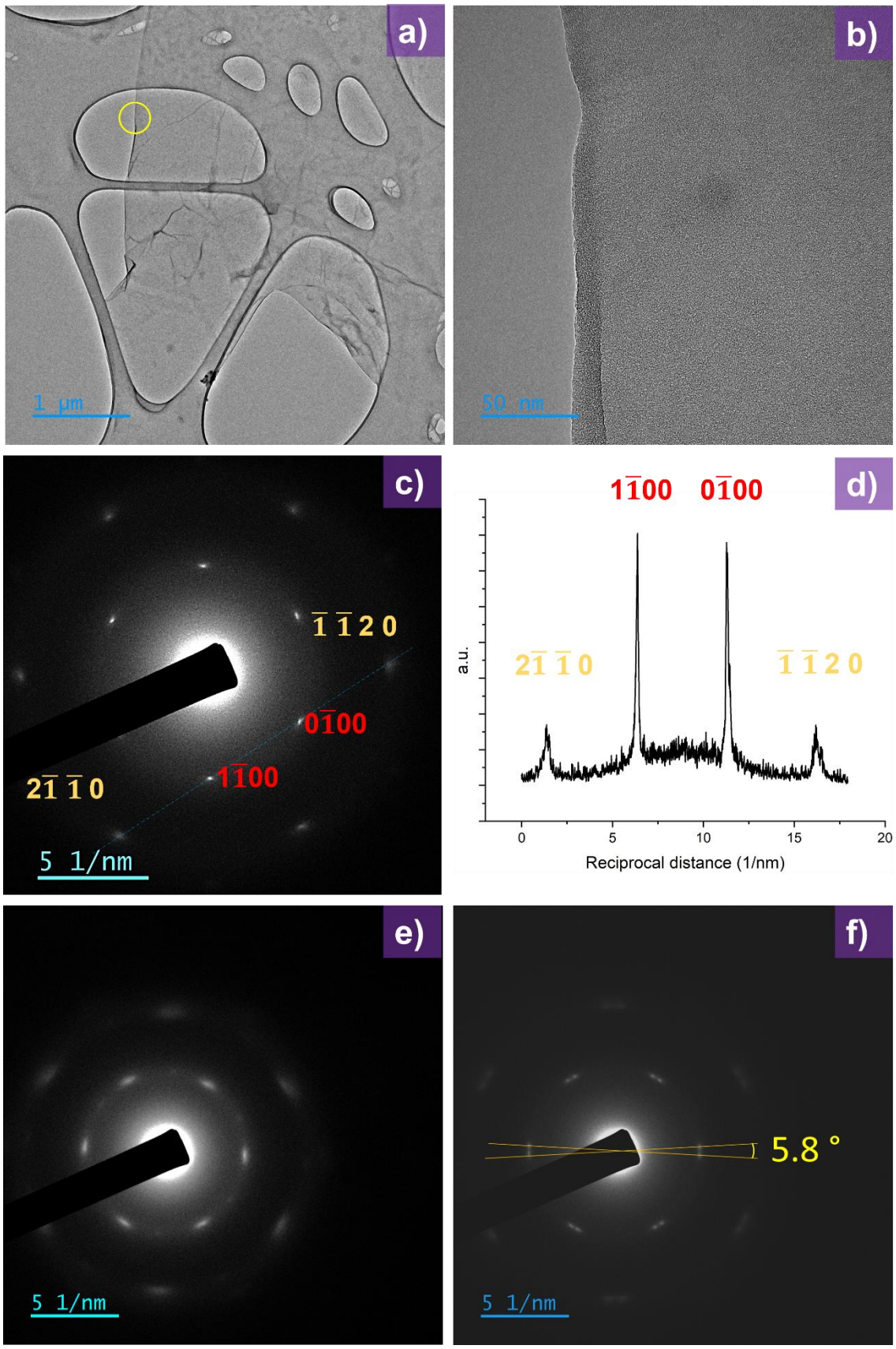

Figure 4.9 a) TEM image of a typical graphene oxide flake and b) high magnification image of the section circled. Typical SAED patterns of the graphene oxide flakes reveal c,d) single layer e) amorphous and single layer domains mixed and f) bilayer domains.

4.3.4 Synthesis and XPS analysis of hydroxylated chemically reduced graphene oxide

The surface of the chemically reduced graphene oxide (CRGO) was enriched with hydroxyl functional groups through a diazotization reaction using 1,4-aminophenyl ethanol. The synthetic procedure is schematically shown in Figure 4.10 and was adapted from Wang *et al.*[276] and experimental details are given in Section 8.10. In brief, once an aryldiazonium is formed *in situ* a delocalized electron is transferred from the chemically reduced graphene oxide to the aryldiazonium cation, which becomes a radical after releasing a nitrogen molecule.[277]

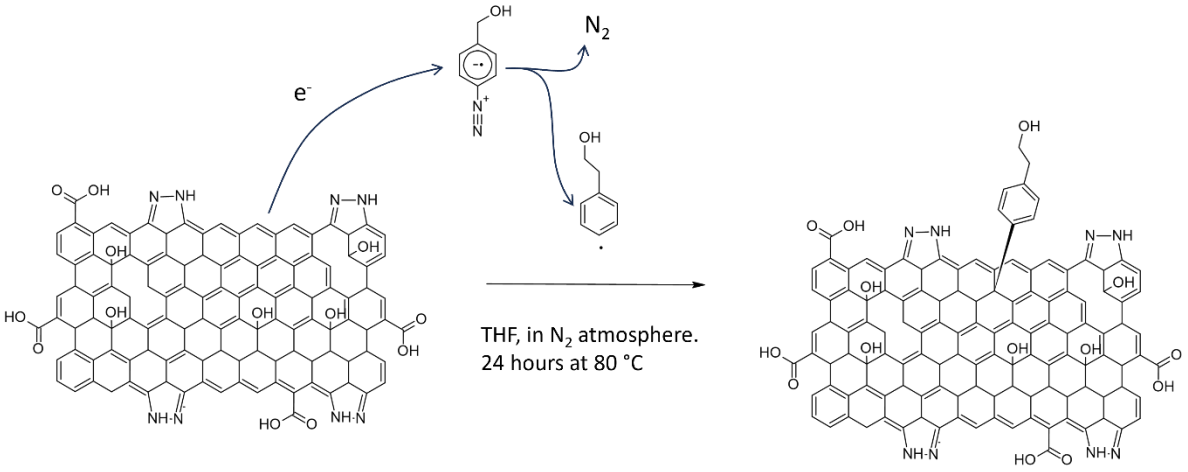

Figure 4.10 Schematic representation of the enrichment of hydroxyl groups on the surface of reduced graphene oxide through diazotization.

Chemically reduced graphene oxide was analysed similarly to graphene oxide. C 1s spectra were deconvoluted in 4 components as shown in Figure 4.11. First, the peak at 284.5 eV was assigned to sp^2 C=C bond.[257,259–261] The peak around 286.4 eV is assigned to C-OH bonds.[257,278] The peak at 288.1 was ascribed to >C=O accordingly.[246] Finally, the broad peak with a small contribution at 291.24 eV is assigned to plasmon corresponding to the to $\pi - \pi^*$ transitions in the sp^2 network.[279]

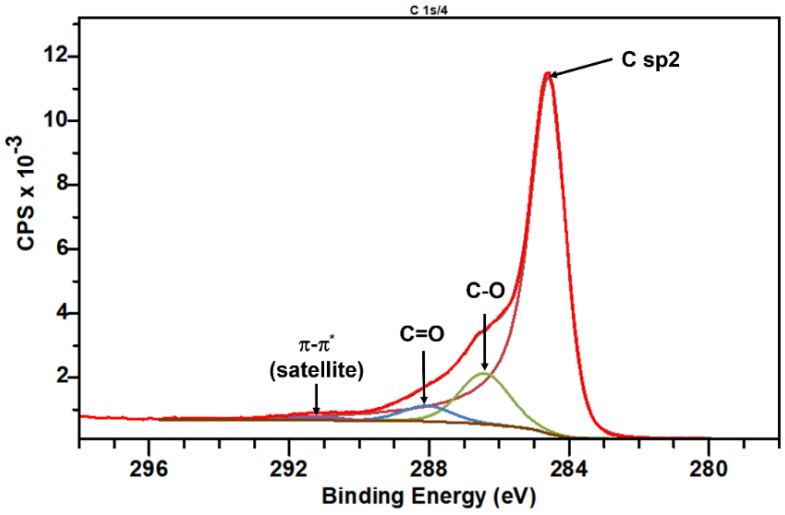

Figure 4.11 C1s spectrum of hydroxylated chemically reduced graphene oxide.

4.3.5 Silanization of hydroxylated chemically reduced graphene oxide

Silanization of hydroxylated surfaces can be achieved using a wide variety of protocols, most of them adapted from surface functionalization procedures. It is normally used as an alcoholic solution in acidic media to promote the formation of siloxane bonds. However, an alcoholic media and acid conditions promote the ring opening reaction of epoxy to form diols, which are desirable to keep intact for further use.[280] An alternative approach is the deposition in anhydrous conditions containing an adventitious amount of water that promotes the formation of silanol bonds (Si-OH).[281] In addition, higher temperatures (>100 °C) favour the condensation step of hydrogen-bonded silanols to form siloxane bonds.[282] Having said that, three different protocols were tested to introduce the silane coupling agent on the surface of the reduced graphene oxide containing hydroxyl groups. They are schematically depicted in Figure 4.12 and XPS analysis was used to assess the functionalization (see Section 8.12 for experimental details).

From Table 4.4 and Figure 4.13a1 and a2, it is observed that the same bonds in almost the same proportions remained after method 1, demonstrating that only stirring at room temperature was not enough to induce the reaction. However, procedures 2 and 3 showed changes in the C 1s spectra which are discussed as follows. The C1s shows a new peak around 287.6 eV which has higher energy than the C-OH bond but less than >C=O bond, which was ascribed to the C-O-C bond from epoxy groups and is in agreement with

theoretical calculations and experimental observations where they used the same silane coupling agent.[246,262,283,284] Moreover, for procedures 2 and 3, Figure 4.13b2-c2 shows a peak corresponding to the Si 2p region at 102.1 which is associated with the Si-O-C/Si-C bonds.[285] From Table 4.4 procedure 2 shows a higher C/O ratio when compared to procedure 3 suggesting a higher level of functionalization due to reaction with GPTMS molecules. It is also noted from Table 4.4 that all samples have nitrogen, which come from the reduction step using hydrazine. It has been demonstrated that using hydrazine for the reduction of graphene oxide causes insertion of aromatic N moieties in a five-membered ring at the platelet edges whilst also restoring the graphitic lattice in the basal plane.[286]

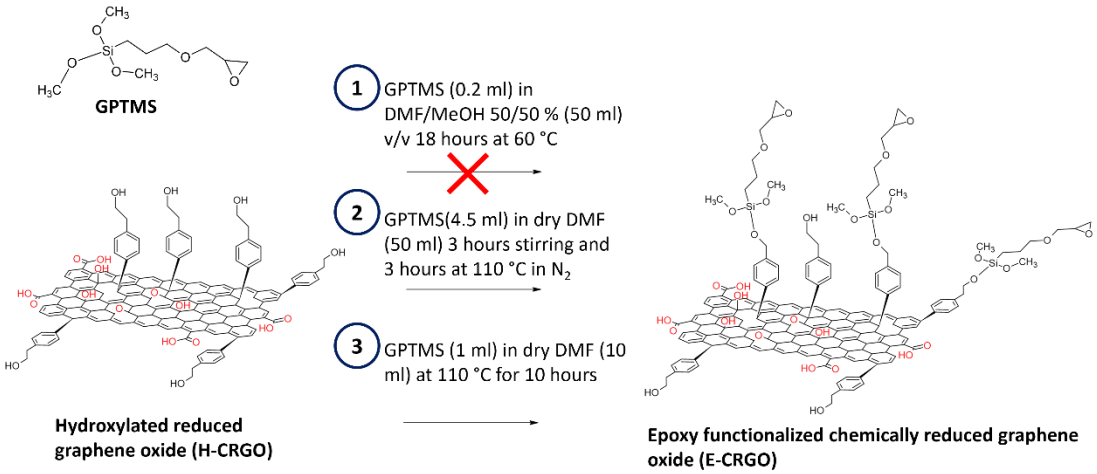

Figure 4.12 Synthetic routes for the silanization of hydroxy functionalized reduced graphene oxide.

Table 4.4 Elemental analysis from XPS analysis comparing the three silanization methods to the hydroxylated chemically reduced graphene oxide (CRGO-OH).

Sample	Concentration [at%]			
	O 1s	C 1s	N 1s	Si 2p
CRGO-OH	14.85	79.82	4.81	0.15
Method 1	14.52	80.13	4.82	0.42
Method 2	20.56	72.77	3.44	3.22
Method 3	18.55	75.12	4.15	2.18

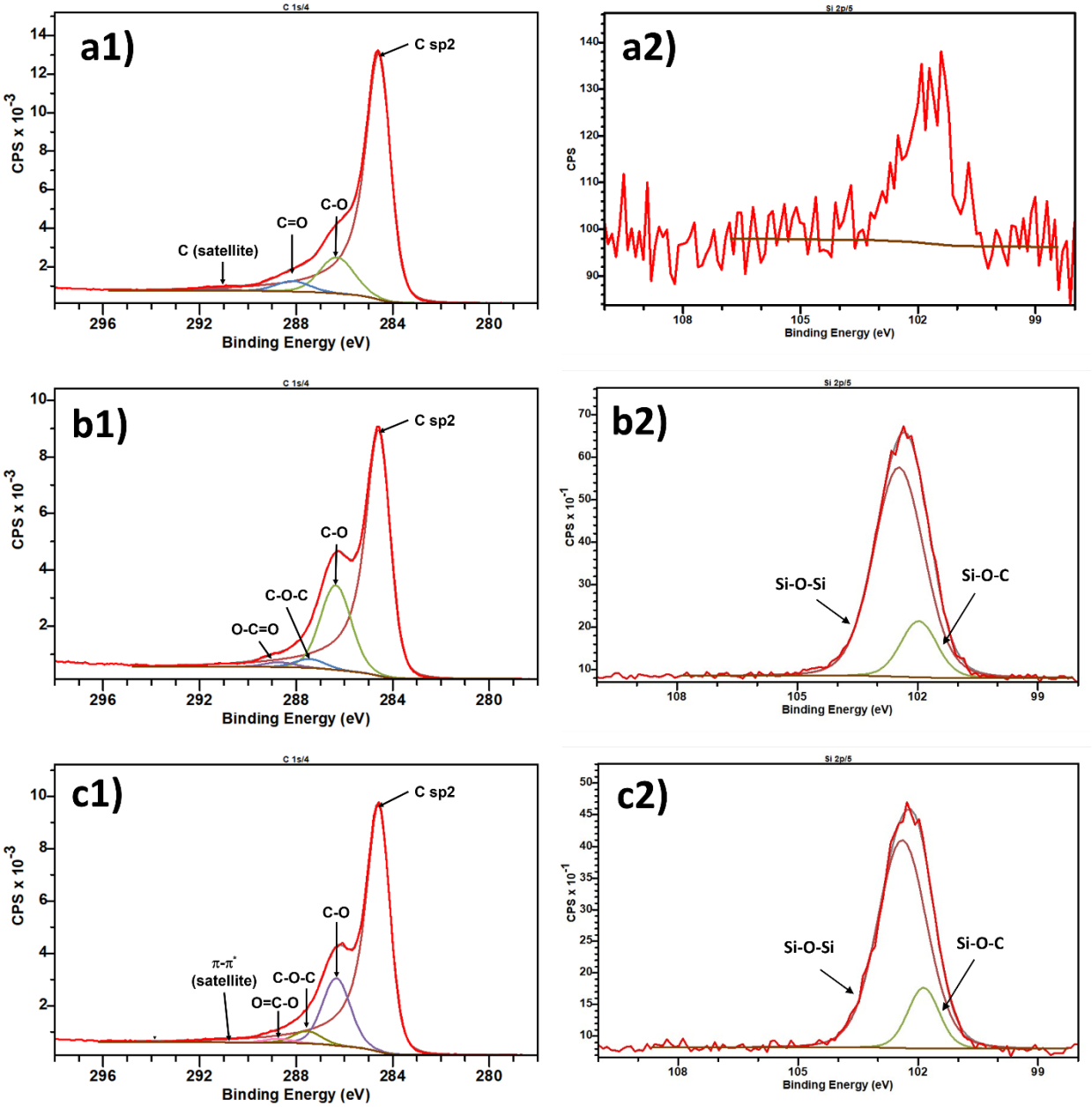

Figure 4.13 a1-a2) High-resolution C 1s and Si 2p spectra of epoxy functionalized CRGO from route synthesis 1. b1-b2) High-resolution C 1s and Si 2p of epoxy functionalized CRGO from route synthesis 2. c1-c2) High-resolution C 1s and Si 2p of epoxy functionalized CRGO from synthetic route 3.

4.4 Conclusion

Graphene oxide has long been considered one of the main precursors of graphene, which offers benefits such as scalability and dispersibility in a wide range of solvents due to the different functional groups on the surface. Therefore, careful control of the oxidation process is needed to produce less defective graphene oxide. The oxidation step of graphite leads to graphite oxide, an intercalated compound, and an exfoliation step is necessary to obtain the individual graphene oxide flakes. Here, the use of a cross-flow filtration system was explored to simultaneously remove the remaining manganese ions dissolved while exfoliating the graphite oxide at the same time. This is particularly useful due to the limitations of common purification techniques such as membrane filtration and dialysis, which are associated with difficulties such as long times and clogging of the membrane pores.

The model proposed by Paton *et al*.[31] for liquid phase exfoliation predicts a critical shear rate at which exfoliation of graphite oxide should happen. From rheological measurements and knowing the surface energy of graphene oxide, it is expected that when graphite oxide is forced to flow inside a tube, the shear can exceed the critical value, causing exfoliation and obtaining flakes as large as 16.2 ± 1.7 μm. Moreover, without sonication, it is possible to get 70% of graphene oxide flakes with a thickness less than or equal to 1.4 nm, consistent with values reported for monolayer graphene oxide. It is possible to tailor the lateral size of graphene oxide using brief sonication times (2 minutes was the longest sonication time), so the lateral size can be tailored in the range of 16.2 - 1.6 μm.

For the purpose of this project, it was desired to recover the electrical properties of graphene while introducing the epoxy groups. First, graphene oxide was chemically reduced, and the hydroxyl groups were introduced through a diazotisation reaction. Then, three procedures were tested to introduce epoxy groups. It was found that a high temperature (110 °C) was necessary to promote the reaction with the silane coupling agent. This methodology will be used in the next chapter to introduce epoxy groups on the surface of thermally reduced graphene oxide.

5 Compatibilizing immiscible polymer blends using reactive graphene

5.1 Introduction

As discussed in Section 1.5, polymer blending provides a way to intuitively improve the properties of polymers by creating a synergistic effect when mixing homopolymers. However, most pairs of homopolymers are thermodynamically immiscible and have a weak interface, leading to poor mechanical properties. Over the years, one of the most popular ways to tackle this problem was by introducing a copolymer or a reactive copolymer formed *in situ*.[287] Such an approach has its challenges, namely, the harsh flow conditions can remove the copolymers from the interface and form micelles.[288–290]

Alternative approaches range from using inorganic fillers like silica nanoparticles, [291,292] graphene derivatives,[148] and carbon nanotubes.[293,294] As explained in Section 1.5.3, the aspect ratio related to the geometry of these fillers plays an essential role in the transfer rate from the less thermodynamically compatible phase to the other. Therefore, it is expected that using carbon nanotubes and few layer graphene can improve the transfer rate. Macosko *et al.* have previously demonstrated that localising graphene nanoplatelets at the interface of the polystyrene and polylactic acid blend was possible. However, the authors showed that mixing for more than one minute had a detrimental effect on the conductivity of the blend, as a consequence of the continuous migration from the PLA to PS phase.[154,228] Furthermore, later research within the same group demonstrated that the same conditions did not work in a polylactic acid /ethyl vinyl acetate blend, highlighting the importance of approaches independent of the mixing time.[295] In Section 1.5.4, it was explained that the shear force distribution in the flow is related to the stress tensor $\boldsymbol{\tau}$ and will impact the localization of nanoparticles, but the intrinsic complexity makes it unknown.

A better option to improve the adhesion of the nanoparticles at the interface is by promoting entanglement with the polymer chains in both phases of the blend, preventing them from being detached due to shear forces from the blending process. Therefore, devising reactive compatibilization strategies could be a potential alternative to reach these goals. In reactive compatibilization, reactive functional groups in polymer chains react with other functional groups from either another polymer or groups on the surface of nanoparticles.[296]

For example, Yonjing, L. *et al.* have explored the reactive compatibilization of the polyvinylidene fluoride (PVDF) and polylactic acid blend using reactive silica nanoparticles, carbon nanotubes, silica nanoparticles, boehmite nanorods that contain both epoxy groups and polymethylmethacrylate chains.[156,297–301] They proposed that the polylactic acid, which has carboxylic groups at the end of the chains, can react with epoxy groups through a ring-opening reaction at high temperatures. However, polymers like PVDF are miscible with PMMA. Therefore, they suggested nanoparticles with epoxy groups and PMMA chains could be more easily driven to the interface.

The PLA/PS blend is a semi-biodegradable blend. Although PLA has a relatively high strength and stiffness, it has a low viscosity and high thermal stability; it is moisture sensitive and has a relatively high cost compared to other commodity polymers such as polystyrene.[302] Therefore, mixing PLA and PS can be a cost-effective way to improve PLA mechanical properties. Based on this previous research, a similar approach was adapted to compatibilize the polylactic acid/polystyrene blend using reduced graphene oxide. Furthermore, the high difference in surface energy can be harnessed as a driving force for selectively localising nanoparticles at the interface. Figure 5.1 shows a schematic representation of the proposed approach.

Given that nanoparticles' localisation depends on their size, first, it was necessary to control the size of the graphene oxide. To introduce epoxy groups, a silane coupling agent, 3-Glycidyloxypropyl trimethoxysilane, was used as it can be grafted to the hydroxyl groups available on the surface of thermally reduced graphene oxide (TRGO). Then, it was introduced to carboxyl-terminated polystyrene to react with the introduced epoxy groups. As a last step, a PLA masterbatch containing the functionalized TRGO was made and blended in a mini extruder where the reaction of the remaining epoxy groups with carboxyl group from PLA chains occurs. Due to the number of variables involved, it was used as a PLA masterbatch for two purposes: making a homogeneous dispersion of the functionalized TRGO in the PLA phase, and because it is presumably mixed with the less thermodynamically favourable phase, it will increase the driving force (difference in surface energy) to promote the migration from the PLA phase to the polystyrene phase. The following sections will discuss the synthesis process, microstructure, and the effect on the electrical and mechanical properties.

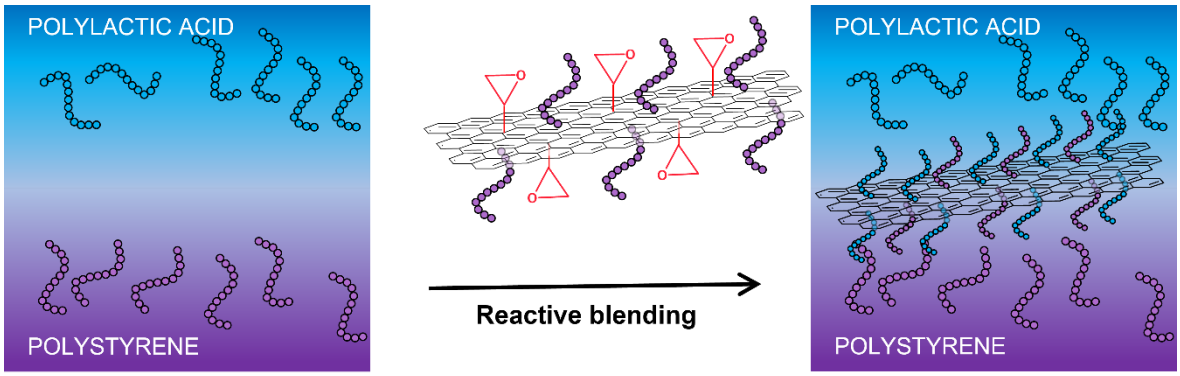

Figure 5.1 Schematic representation of the proposed reactive pathway.

5.2 Results

5.2.1 Synthesis sequence of reactive graphene

5.2.1.1 Synthesis of carboxy terminated polystyrene

Synthesis of carboxyl terminated polystyrene (PS-COOH) was done using radical polymerization using TEMPO (2,2,6,6-tetramethyl-1-piperidyloxyl as initiator and AIBN'$(COOH)_2$ 4,4′ azobis [4-cyanopntanecarboxylic acid]). Figure 5.2a shows the synthetic route followed adapted from reference 303. Since the ring-opening reaction requires that carboxylic groups are available, steric hindrance may result in high molecular weight PS-COOH formation. Previous works also suggested using low molecular weight carboxy terminated polymer chains.[297–301,304] One and two hours reactions resulted in carboxy terminated polystyrene with a molecular weight M_w = 11374 g/mol and M_w = 16348 g/mol as determined by gel permeation chromatography (Figure 5.2b).

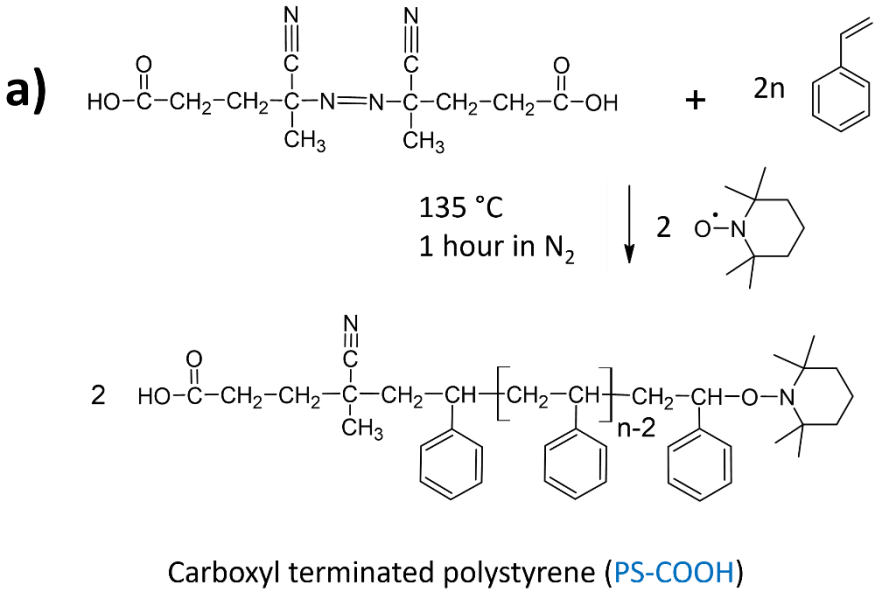

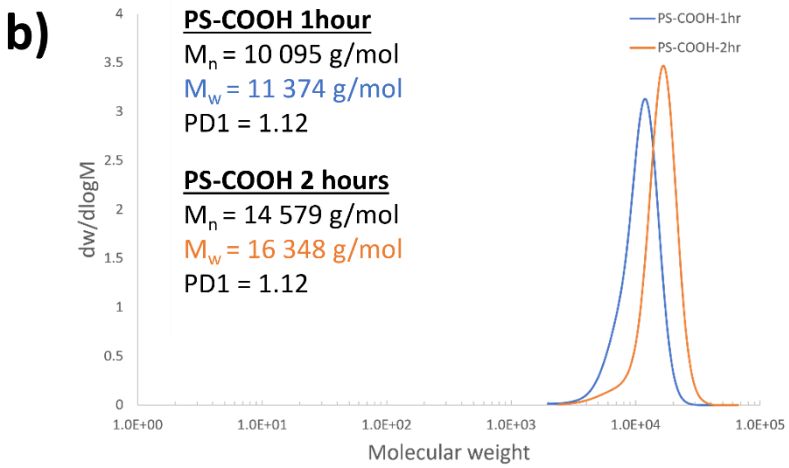

Figure 5.2 Synthesis of carboxy terminated polystyrene (a) and molecular weight distribution at different times (b)

5.2.1.2 Synthesis of epoxy functionalized thermally reduced graphene oxide (Epoxy-TRGO)

Epoxy-terminated polystyrene-Thermally reduced graphene oxide (Epoxy-TRGO) was synthesised using a silane coupling agent 3-Glycidyloxylpropyl trimethoxysilane (GPTMS) in anhydrous conditions. Figure 4.3 illustrates the reaction between hydroxyl groups in the thermally reduced graphene oxide (TRGO) and the GPTMS. The mechanism is the same as that explained in Section 4.3.5.

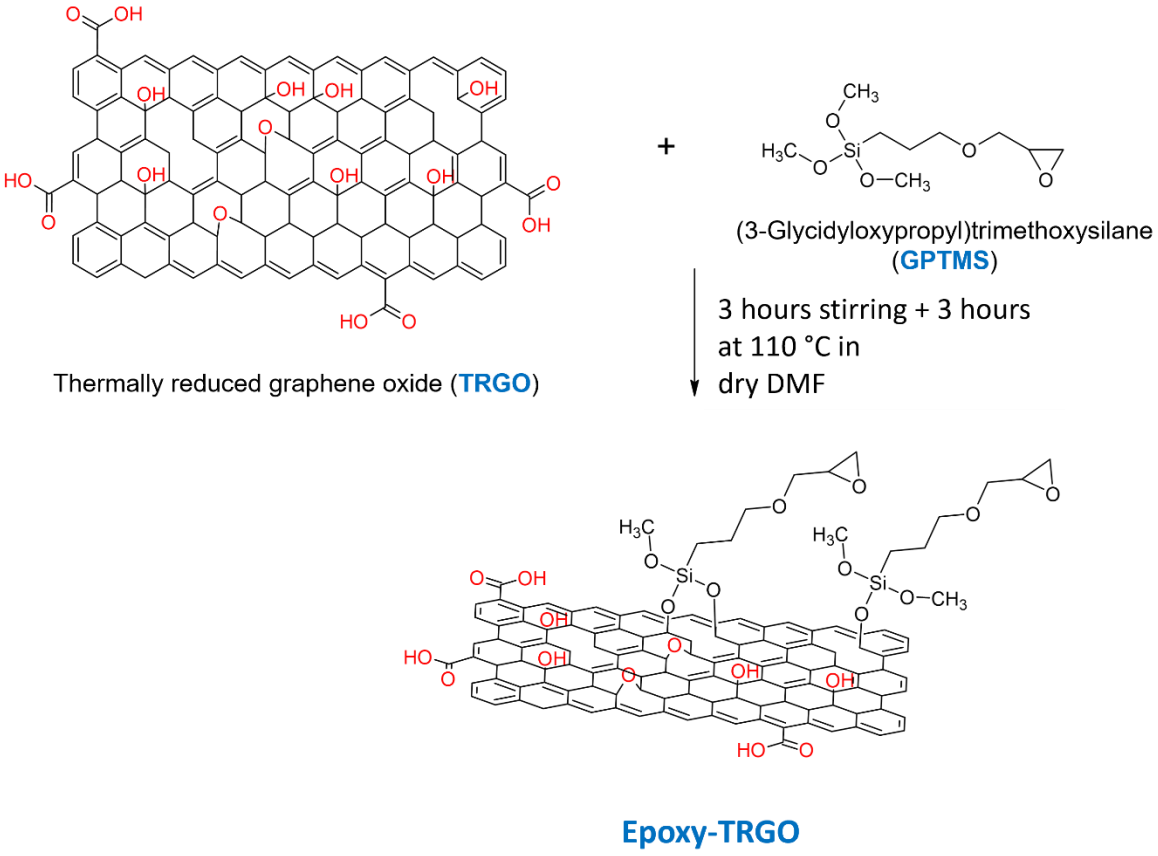

Figure 5.3 Synthesis of epoxy functionalized thermally reduced graphene oxide.

5.2.1.3 Synthesis of Polystyrene grafted Epoxy-TRGO

Grafting carboxy terminated polystyrene (PS-COOH) can occur through a ring-opening reaction with epoxy groups grafted on TRGO (Figure 5.4). Since this is an equilibrium reaction, it is expected that there will be remaining epoxy groups and grafted PS-COOH chains, and equilibrium is favoured by higher temperatures.[305] Based on previous research conditions, we used a temperature of 135 °C and 24 hr using a base catalyst. [297–301,304]

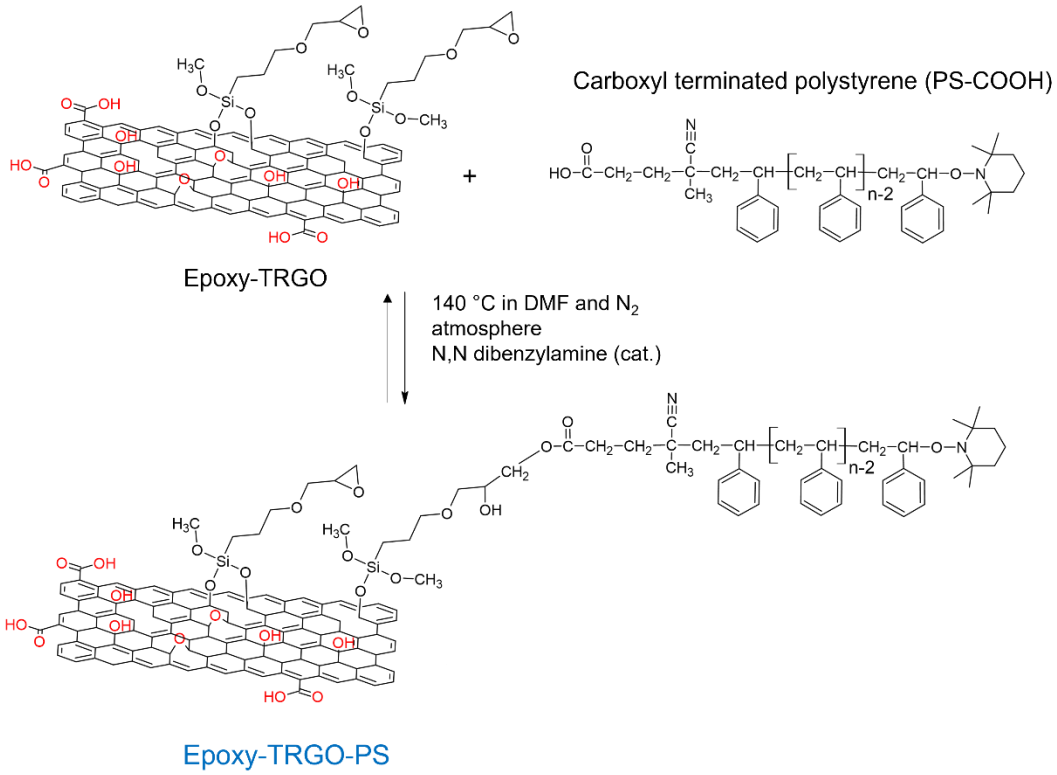

Figure 5.4 Synthesis of Epoxy-TRGO-PS.

5.2.2 Thermal gravimetric analysis (TGA) of the synthesized graphene platelets.

Thermal gravimetric analysis provides a valuable and straightforward way to get information about introducing different chemical moieties attached to the graphene surface since they are all degraded in a particular way. It is commonly accepted that the weight loss for T < 100 °C is due to water moisture adsorbed. Due to the high porosity of the graphene-based materials, it will only be considered where the regions of temperature are higher than 100 °C. Figure 5.5a and b show the thermograms from TRGO, Epoxy-TRGO and Epoxy-TRGO-PS. Figure 5.5c and d show the graphs corresponding to the first derivative of the weight (DTG graph), so each decomposition step can be visualized as a peak corresponding to the maximum rate of the decomposition. From Figure 5.5d, it is observed that Epoxy-TRGO-PS show three regions of decomposition. The first one from 100 – 300 °C, the second one from 300 – 500 °C, and the third from 500 – 800 °C.

From Figure 5.5d, TRGO mainly shows decomposition in regions 1 and 3. In the first region going from 100 °C to 300 °C no significant change occurred for the TRGO, but for

the Epoxy-TRGO, there is a 7.6 wt% loss at 300 °C suggesting the loss of more labile groups coming from the GPTMS. Also, in region 1 the Epoxy-TRGO-PS showed a 5.6 wt% loss, which is smaller when compared to the Epoxy-TRGO which can be explained by the thermal stability imparted by the grafted polystyrene chains (PS-COOH) as they minimally decomposed at 300 °C, showing only 1.9 wt% loss at this temperature.

In the second region, from 300 °C to 400 °C it is observed that polystyrene starts decomposing at 315 °C showing a pronounced peak at T = 425.8 °C in the DTG graph (Figure 5.5c). In the DTG graph, only the Epoxy-TRGO-PS has a peak in this region, confirming the presence of PS chains. This is also supported by the fact that at the end of the experiment, both Epoxy-TRGO and Epoxy-TRGO-PS had almost the same amount of remaining material (66.6 wt% and 67.4 wt% respectively) attributed to the full decomposition of the polystyrene. Table 5.1 summarizes the onset temperatures and the temperature at the maximum rate of weight loss.

Table 5.1 Summary of the start decomposition temperature (onset temperature), the temperature at the inflexion point from the DTG graph in Figure 5.5 and the corresponding remaining weight percent.

	Onset temperature / Temperature and weight (%) at the inflexion point		
	Region 1 100-300 °C	Region 2 300-500 °C	Region 3 500-800 °C
PS-COOH Carboxyl terminated polystyrene	222 °C /237.7 °C (99.6%)	398 °C /425.8 °C (37.4%)	-
TRGO Thermally reduced graphene oxide	216.3 °C /263.3 °C (97.9%)	-	667 °C /684.7 °C (85.4%)
Epoxy-TRGO Epoxy functionalized-TRGO	202.0 °C /240.2 °C (96%)	-	628.7 °C /696.8 °C (75.4%)
Epoxy-TRGO-PS Epoxy functionalized TRGO grafted with polystyrene chains	185.8 °C /214.6 °C (97.9%)	350.4 °C /392.7 °C (87.8%)	593.2 °C /700.8 °C (72.3%)

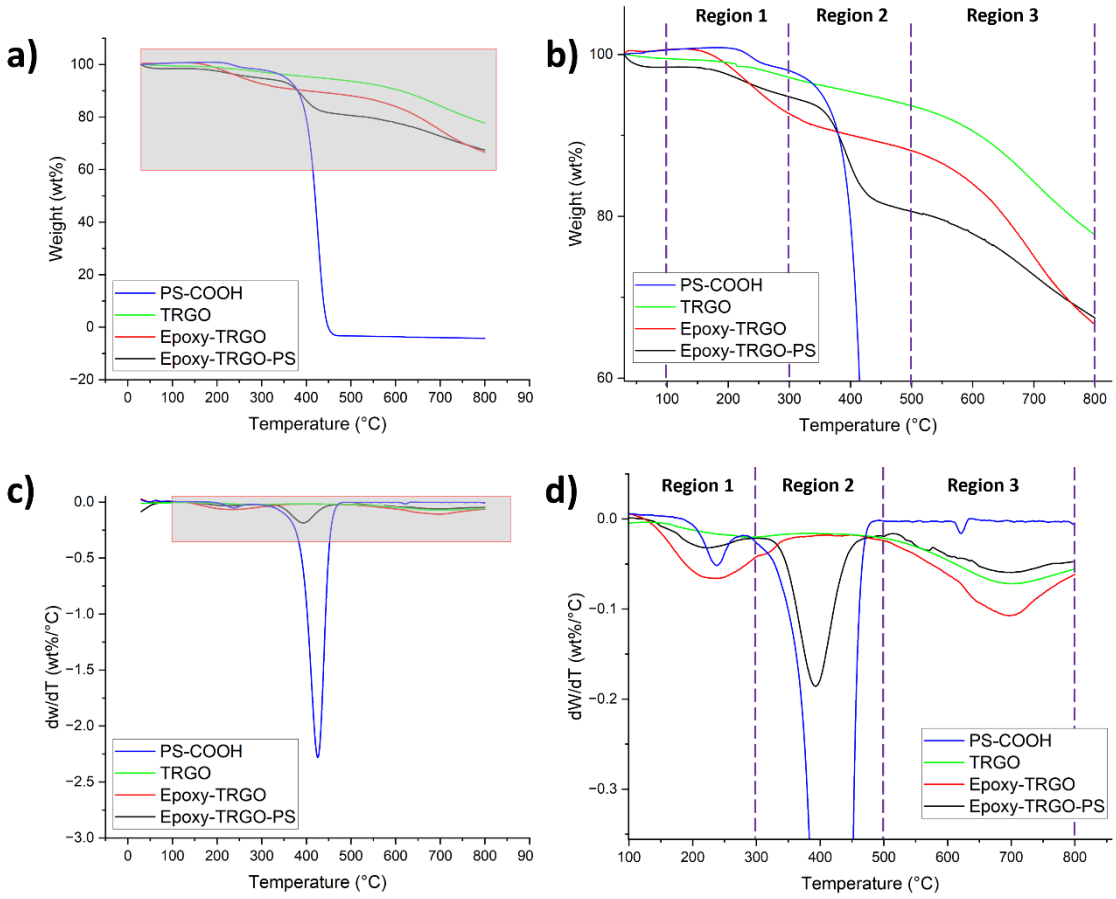

Figure 5.5 a) Thermograms from the decomposition of PS-COOH, TRGO, Epoxy-TRGO and Epoxy-TRGO-PS in argon atmosphere using a temperature rate of 10 °C/min, b) Zoom in on the area of the grey box in a), c)First derivative of the data (DTG graph) from a), d) Zoom in on the area of the grey box in c).

5.2.3 XPS analysis

5.2.3.1 Thermally reduced graphene oxide

Peak assignment for thermally reduced graphene oxide (TRGO) was done similarly to for graphene oxide (Section 4.2.4). Figure 5.6 shows the survey spectra and high resolution in the C1s region. TRGO shows a peak at 285 eV corresponding to sp^2 C=C estimated as 67.7 at%, which is expected because of the partial restoration of the sp^2 network.[257,259–261] Assignation of the remaining peaks was done according to the previous discussion. The peak at 286.4 eV was assigned to C-OH bonds, and the peak at 289 eV was assigned to O=C-O bonds as they must have higher energy than C=O.[262]

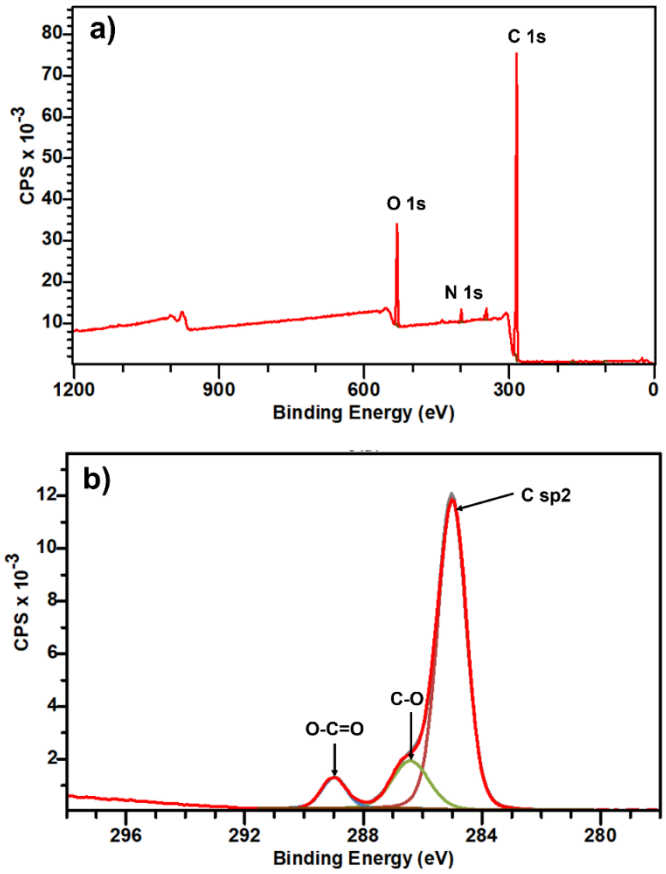

Figure 5.6 a) Survey spectra and b) high resolution spectra of C1s of thermally reduced graphene oxide (TRGO)

5.2.3.2 Epoxy-TRGO and Epoxy-PS-TRGO

To get more information about the chemical state of the graphene-based nanoparticles, XPS C1s spectra were fitted to Gaussian-Lorentizan functions using CASA XPS software for fitting.[256] Peaks in the C 1s region were assigned according to reported values in the literature. First, sp^2 (C=C) bonds were assigned to the peak around 284.3 eV as it usually has been assigned to graphene and multiwalled carbon nanotubes.[257,259–261] In principle, similar carbon-oxygen species are expected to be found in graphene oxide and reduced graphene oxide. Therefore, we assigned the peak around 286.2 eV to C-O bonds. C-O-C bonds from epoxy groups were ascribed to the peak around 287.9 eV. The peak around 289 eV was assigned to O-C=O from carboxyl groups, and the peak at 291 eV was assigned to π - π^* transitions.[246,263,279] Figure 5.7e also shows the deconvoluted Si 2p peak, and the assignment was done according to a previous report on the silanization of multiwall carbon nanotubes (MWCNTs) with 3-Glycidyloxypropyl trimethoxysilane.[306] The peak at 101.8 eV

is assigned to Si-O-C from the bond formed from hydroxyl groups on the surface of TRGO and the coupling agent, while the one at 102.2 eV corresponds to siloxane partial hydrolysis, coming from remaining moisture on the TRGO and from the washing step.

Upon grafting of polystyrene chains, the C/O ratio increases from 5.66 in the epoxy-functionalized graphene to 9.64, which is supported by the fact that each polystyrene chain grafted introduces a significant amount of carbon and a minimum amount of oxygen. This is further supported by the significant increase in the peak around 284.3 eV associated with the sp^2 aromatic carbons and a new broad peak around 294 eV associated with the shake-up due to π - π^*transitions in the polystyrene aromatic system.[307]

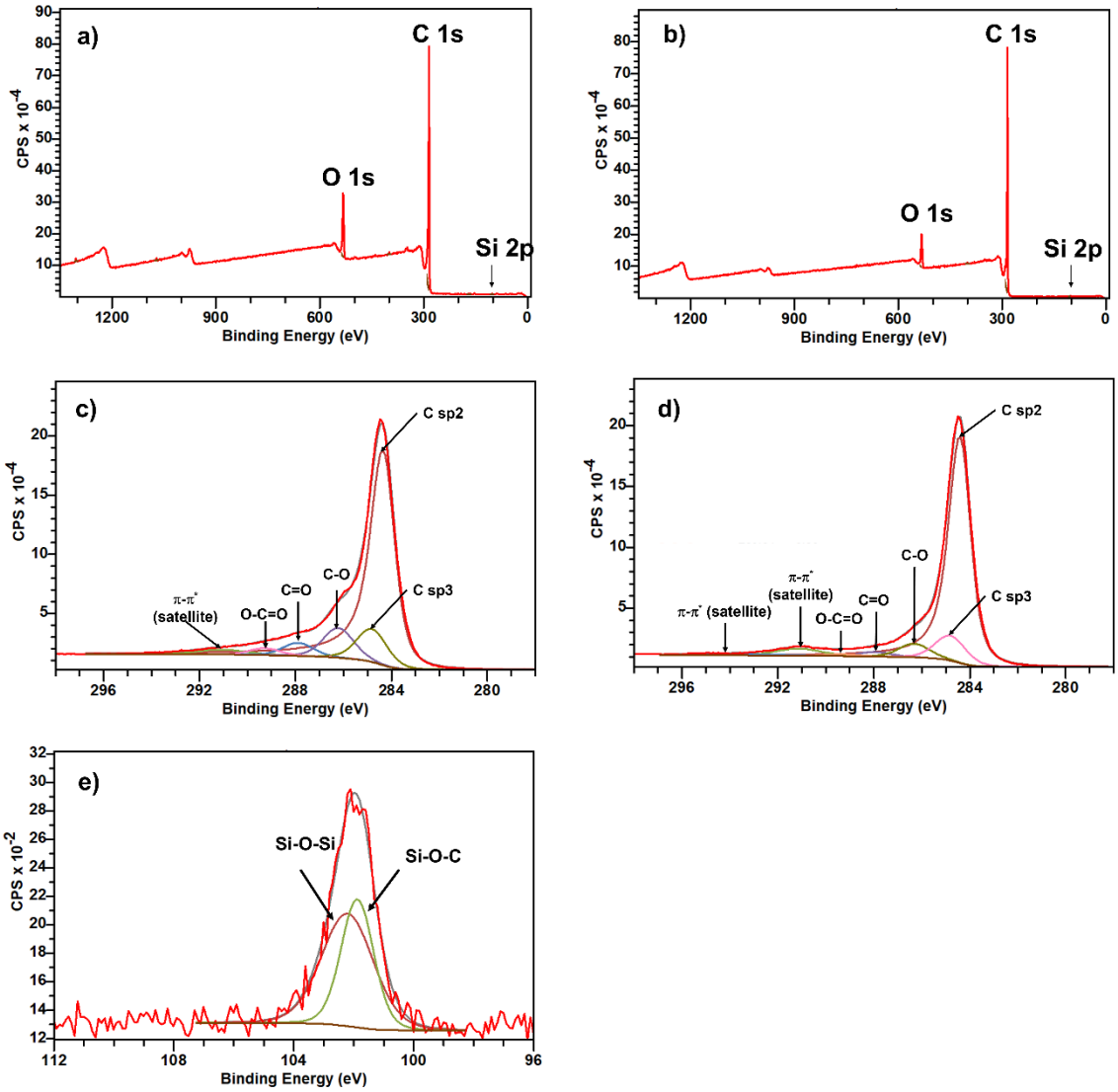

Figure 5.7 Survey spectra of Epoxy-TRGO (a) and Epoxy-PS-TRGO (b). High-resolution spectra of C1s of Epoxy-TRGO (c) and Epoxy-PS-TRGO (d). High-resolution spectra of Si 2p for Epoxy-TRGO (e).

5.2.4 Stability of the reactive functionalized graphene platelets

When different moieties or functional groups are attached to the surface of nanoparticles, their colloidal stability is expected to change. It is commonly accepted that zeta potential values represent the colloidal stability as follows: highly stable (> 30 mV), moderately stable (20-30 mV), relatively stable (10-20 mV) and unstable (0-10 mV).[308] Then, zeta potential measurements were used to infer whether functionalization occurred. Two solvents were chosen: methanol and tetrahydrofuran. Table 5.2 shows the stability of

solutions after settling for 30 minutes and the corresponding zeta potential values. Since polystyrene is insoluble in methanol but quite soluble in tetrahydrofuran, it was expected a low zeta potential value in methanol but not in tetrahydrofuran. Furthermore, thermally reduced graphene oxide (TRGO) showed low stability corresponding to low zeta potential values. However, upon introducing epoxy groups, the stability significantly improved.

Table 5.2 Zeta (ζ) potential measurements of the stability of 1 mg/ml solutions of TRGO, Epoxy-TRGO and Epoxy-TRGO-PS in methanol and tetrahydrofuran.

	ζ potential [mV]	
	Methanol	Tetrahydrofuran
TRGO	16.2	11.8
Epoxy-TRGO	25.1	51.8
Epoxy-TRGO-PS	2.1	39.4

5.2.5 Predicting the localization of the graphene functionalized graphene platelets

Calculation of the surface energy of the nanoparticles was estimated using the contact angle method using Image J.[309] Although the method works well for macroscopic surfaces, it is technically challenging for nanoparticles since it could imply using drops of the testing liquids smaller than the nanoparticles.[310] In this work, the surface energy was approximated using thin films of graphene-based nanoparticles deposited on a PTFE membrane as substrates. Diiodomethane and deionized water were used as testing liquids, for which polar and dispersive parts are known. Figure 5.8 shows a typical image of the surface energy measurement for commercial graphene nanoplatelets. The surface energy is calculated by minimizing the error using γ^d and γ^p as fitting parameters. Full details about sample preparation are given in Section 8.7. To validate the accuracy of this method, the values obtained were compared to those reported in the literature for graphene oxide and reduced graphene oxide.

Table 5.3 Surface energies estimated using the geometric mean and harmonic mean.

	Surface energy $\gamma_s = \gamma_p + \gamma_d$ $[mJ/m^2]$	γ_p $[mJ/m^2]$	γ_d $[mJ/m^2]$	Polarity $[mJ/m^2]$
Testing liquids				
Water[311]	72.8	50.7	22.1	0.7
Diiodomethane [311]	50.8	1.8	49	0.03
Graphene based materials	**Calculations based on the geometric mean equation**			
Graphene oxide	61.7 ± 1.1	33.3 ± 1.0	28.5 ± 0.1	0.54
Chemically reduced graphene oxide	38.5 ± 1.6	12.6 ± 2.0	25.9 ± 2.7	0.33 ± 0.1
GNPs	41.6 ± 2.3	0.33 ± 0.3	41.2 ± 2.6	~ 0.0
Thermally reduced graphene oxide	44.6 ± 1.9	17.3 ± 4.7	27.3 ± 2.8	0.38 ± 0.1
TRGO-Epoxy	46.6 ± 2.8	16.2 ± 2.2	30.4 ± 2.7	0.35 ± 0.0
TRGO-Epoxy-PS	46.4 ± 3.2	10.5 ± 2.9	35.9 ± 4.0	0.23 ± 0.1
	Calculations based on the harmonic-mean equation			
Graphene oxide	67.6 ± 1.0	31.3 ± 0.8	36.3 ± 0.3	0.46 ± 0.01
Chemically reduced graphene oxide	45.2 ± 1.4	15.6 ± 1.2	29.7 ± 1.6	0.34 ± 0.1
GNPs	42.4 ± 1.8	2.6 ± 2.0	39.8 ± 3.6	0.1 ± 0.1
Thermally reduced graphene oxide	51.4 ± 1.5	19.2 ± 1.6	32.2 ± 3.1	0.37 ± 0.1
TRGO-Epoxy	53.7 ± 3.0	18.9 ± 2.3	34.8 ± 1.6	0.35 ± 0.04
TRGO-Epoxy-PS	53.3 ± 3.5	14.9 ± 3.2	38.4 ± 2.3	0.28 ± 0.1
	$[mJ/m^2]$			
Graphite	54.8	Values from reference 312		
Graphene oxide	62.1			
Chemically Reduced graphene oxide	46.7			

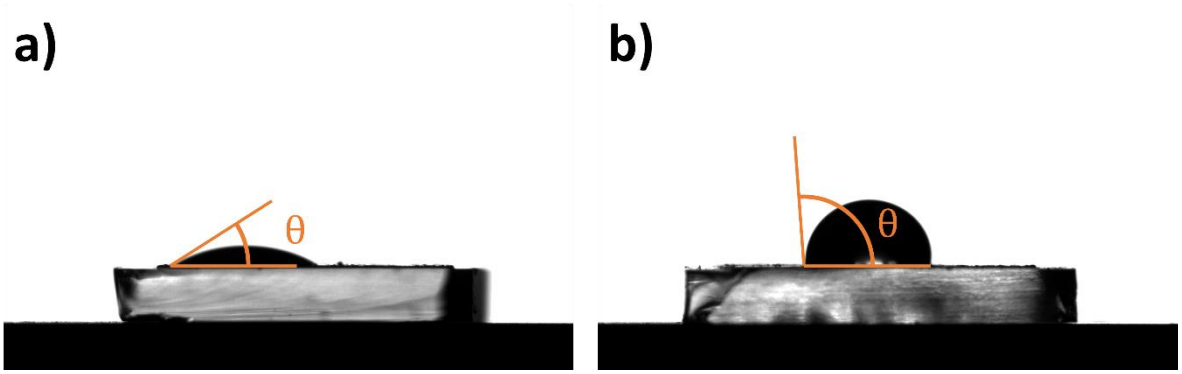

Figure 5.8 Example of typical contact angle measurements for surface energy calculations of graphene nanoplatelets (GNPs) using a 5μL drop of a) diiodomethane and b) deionized water as testing liquids. Similar measurements were done for GO, CRGO, TRGO, Epoxy-TRGO and Epoxy-TRGO-PS.

The geometric mean and harmonic mean were used to estimate the surface energy of the graphene-based nanoparticles, as explained in detail in Section 1.5.1**,** and values are reported in Table 5.3. The values estimated using the geometric mean for graphene oxide (GO) and thermally reduced graphene oxide (RGO) were 61.7 and 44.6 mJ/m^2, respectively. These are in good agreement with those reported previously by Wang *et al.,* which were reported as 62.1 and 46.7 mJ/m^2 for GO and RGO, respectively.[313] Therefore, these values, along with polar and dispersive parts (γ^d and γ^p) were used to estimate the preferential localization of the graphene-based particles before reacting with PLA. From the discussion in 1.5.1it can be established that the wetting coefficient is given by:

$$\omega = \frac{\gamma_{PS/G} - \gamma_{PLA/G}}{\gamma_{PS/PLA}} \qquad \text{Eq. 5.1}$$

where $\gamma_{i/j}$ is the surface energy estimated by the geometric mean between each pair formed by polystyrene (PS), polylactic acid (PLA) and the graphene-based nanoparticle (G). Estimations of the wetting coefficient are given in Table 5.4**.** Using the geometric or harmonic mean approximation does not change the result. It is then predicted that graphene-based nanoparticles preferred to stay in the polylactide acid phase. Although these calculations are only, based on a simple thermodynamic approach based on the minimization of the surface energy of the system. This method can predict the preferable localization of carbon-based nanoparticles with different geometries from a sphere, such as carbon black, carbon nanotubes and graphene in different immiscible polymer systems.[142,154,314–319]

Therefore, it is reasonable to infer that if there is a preferential interfacial localization of the reactive graphene, another factor must be influencing the localization.

Table 5.4 Estimations of the reactive graphene localization-based on wetting coefficient calculations.

	Surface energy $\gamma_s = \gamma_p + \gamma_d$ $[mJ/m^2]$	γ_p $[mJ/m^2]$	γ_d $[mJ/m^2]$	Reference
Polystyrene	42.6	1.4	41.2	311
Polylactic acid	43.5	3.9	39.6	320,321
TRGO-Epoxy-PS	46.4	10.5	35.9	

Geometric mean estimation		Harmonic mean estimation	
Wetting coefficient	Localization	Wetting coefficient	Localization
4.2	PLA phase	6.4	PLA phase

5.2.6 Rheological properties of PLA/PS composites modified with reactive graphene platelets.

Figure 5.9 shows the starting morphologies of the blends right after the extrudate was quenched in liquid nitrogen and the polystyrene phase was etched in cyclohexane. It shows that conditions applied during extrusion are enough to get a good mixing of the PLA and PS phases, and this will be the starting point from which the morphology will start evolving during an annealing step, as described next.

The morphology evolution of the blends at different loadings was followed in a time-dependant experiment by applying a 1 % strain at 1 rad/s and 180 °C for 1 hour in a nitrogen atmosphere. Samples were prepared as explained in Section 8.18. Since the strain is small and within the linear viscoelastic region, any change in the microstructure will only be because of temperature. Figure 5.10a reveals that the morphology remains stable after around 250 seconds. Furthermore, since the tan δ is the ratio of the loss modulus G'' and the storage modulus G', a constant value over time will indicate that the microstructure remains unchanged (Figure 5.10b). On the other hand, the elastic modulus of the neat blend decays over time while tan δ keeps on increasing, making clear that there are changes in the microstructure of the blend during the thermal annealing.

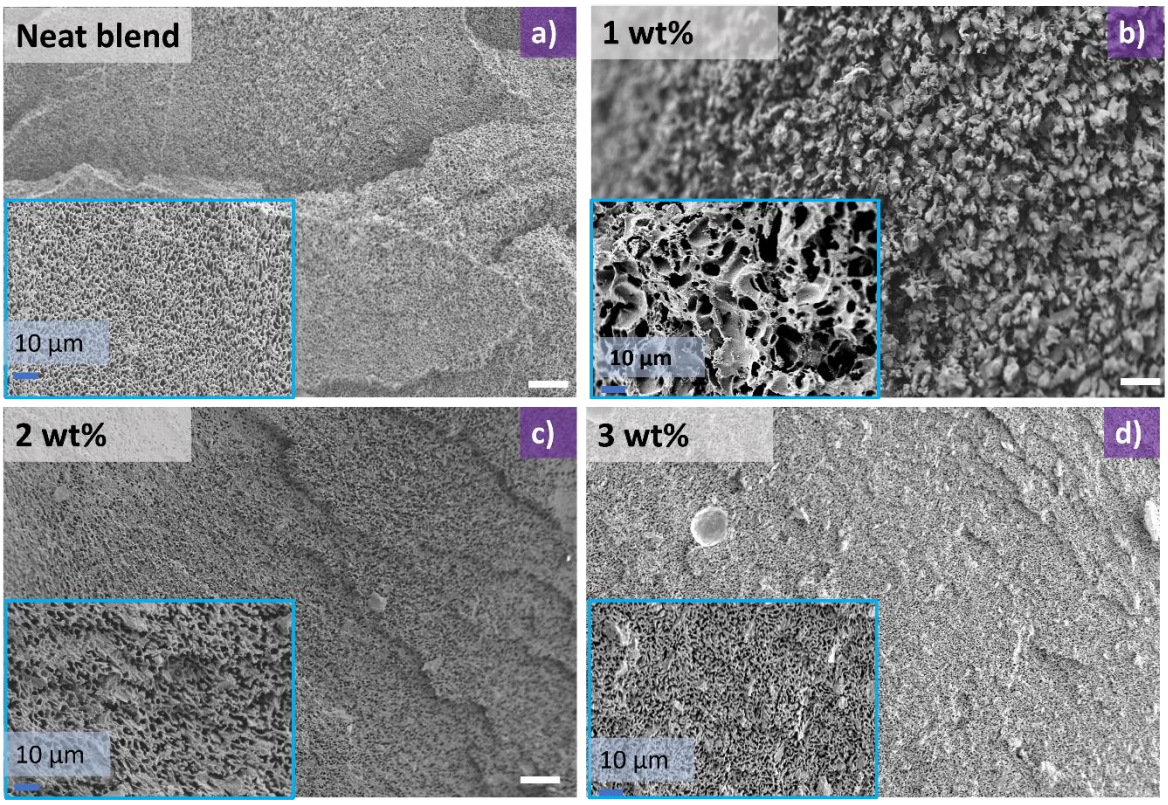

Figure 5.9 Initial morphologies of neat blend a) using different loadings of the reactive graphene: b) 1 wt% c) 2 wt%, and d) 3 wt% right after the extrusion. To preserve the morphology, samples were quenched in liquid nitrogen immediately after coming out from the extruder, and the polystyrene phase was etched in cyclohexane. White scale bars are 40 µm.

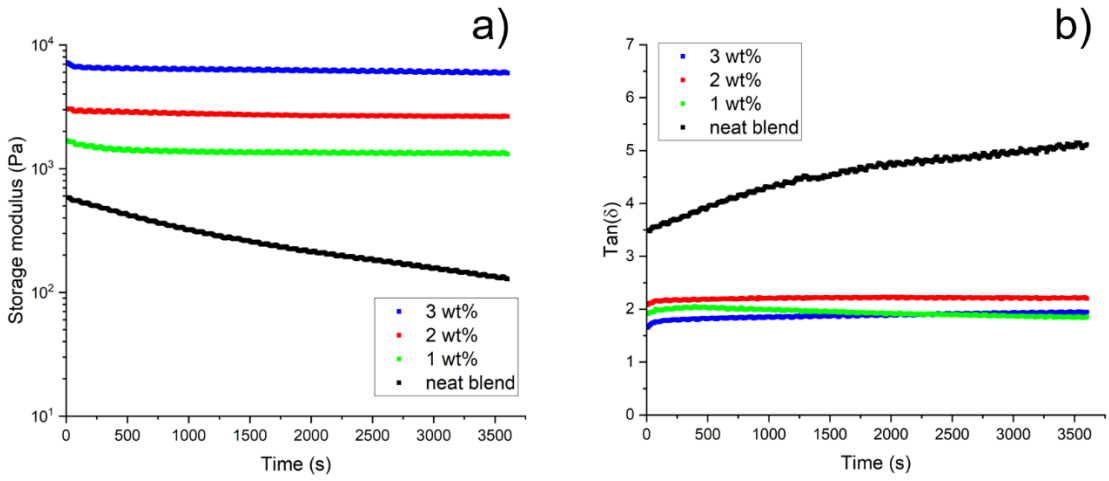

Figure 5.10 a) Storage modulus G' and b) tan δ evolution in an annealing experiment at 180 °C using a 25 mm parallel plate setup.

It was suggested by Lee *et al*. that the storage modulus of a blend (G'_{blend}) can be decomposed in the contribution from the components of the blend ($G'_{components}$) and the interface ($G'_{interface}$). Since the contribution from the components was demonstrated to remain constant, only the interfacial contribution will cause the change during an annealing experiment.[322] In a bicontinuous polymer blend, a decrease in the interfacial storage modulus ($G'_{interface}$) is expected due to the contribution to the stress tensor from the interfacial area, surface tension and curvature from the interface. These factors are responsible for the phase coarsening during the annealing process.[323] Therefore, the decrease in G'_{blend} from Figure 5.10a indicates that the morphology is coarsening over time. On the other hand, samples loaded with the reactive graphene reached a plateau, suggesting that the morphology stopped evolving.

From the discussion above, it was considered that 30 minutes was sufficient time to reveal the equilibrium morphology of the blend during annealing. To replicate the conditions in the rheometer, a small piece of the sample was placed in the mini extruder's channel, followed by annealing for 30 minutes at 180 °C without any applied external pressure. Therefore, changes in the morphology will only be due to the annealing temperature. Furthermore, the polystyrene phase was etched with cyclohexanone to reveal the microstructure of the blend at different loadings of reactive graphene. (More details are given in Section 8.17).

A bicontinuous morphology is formed when two polymer phases are connected, forming an interpenetrated network. This morphology can be rationalized using the model proposed by Yu *et al.*[324] Figure 5.11a shows the simplest element proposed that constitutes a bicontinuous blend, so the microstructure can be constructed by continuously adding the same element over again, that is, by taking the element in Figure 5.11a the whole PLA domain can be constructed. Since the polystyrene phase was etched, the PLA domain can be directly observed and d_{PLA} measurements can be done as seen in Figure 5.11 c-f.

When two immiscible polymer blends are mixed, the system will minimize the energy by decreasing the interfacial area, that is, by increasing d_{PLA} corresponding to the neat blend. Therefore, d_{PLA} can be used as a characteristic length linked to the coarsening process. Figure 5.11b shows that by increasing the amount of reactive graphene, d_{PLA} is reduced. For comparison, for the neat blend d_{PLA} = 58.5 ± 7.8 μm and by adding 3 wt% of reactive graphene d_{PLA} = 5.7 ± 0.5 μm, which is a decrease in the d_{PLA} around ten times. Therefore,

it can be suggested that finer microstructures could be because of compatibilization caused by the reactive graphene.

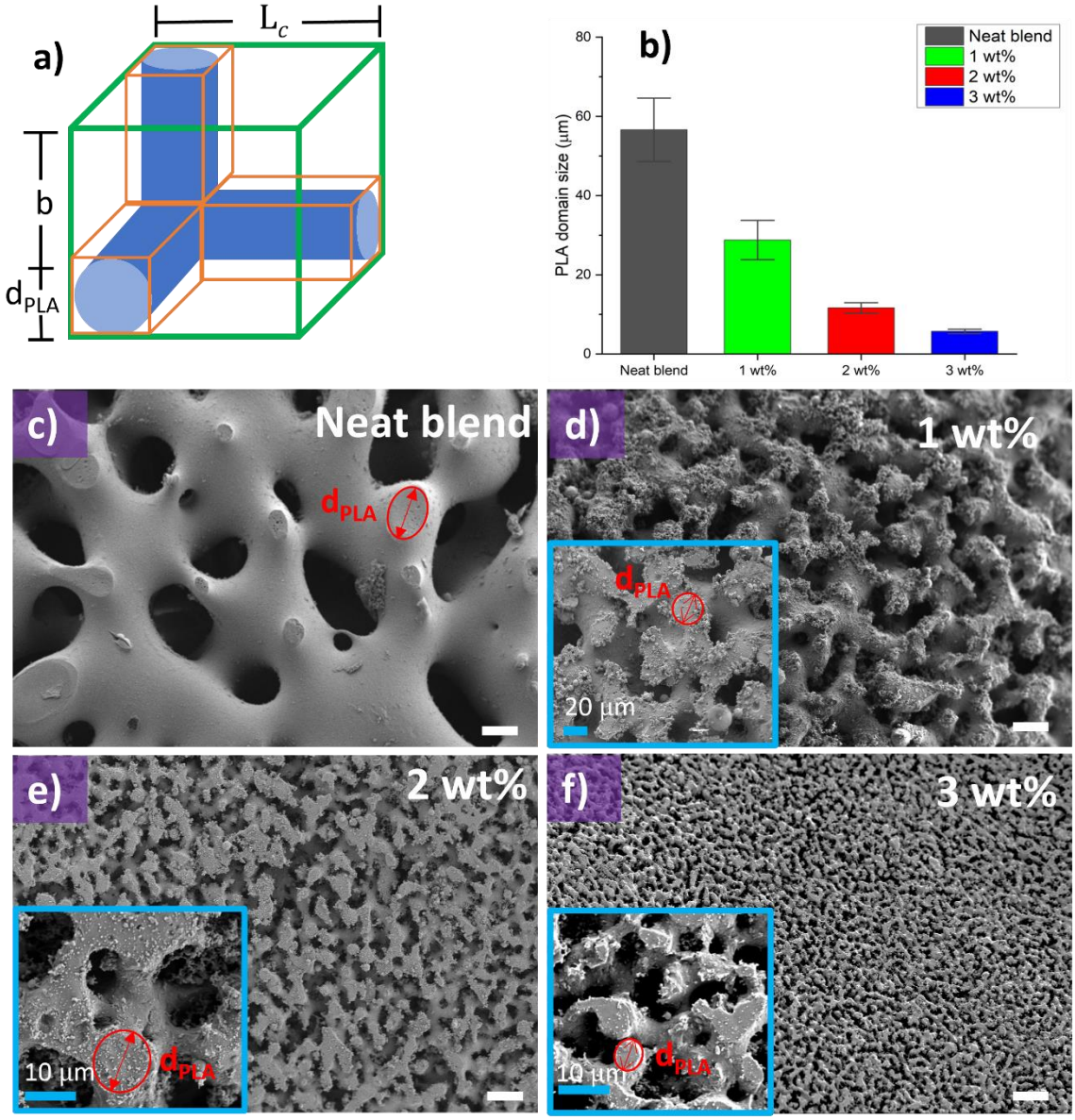

Figure 5.11 a) Simplest element constituting a bicontinuous blend adapted from the model proposed by Yu *et al.*[324] b)Dependence of the characteristic length d_{PLA} with the loading of reactive graphene. Microstructures of the polylactic acid /polystyrene blend after 30 minutes annealing at 180 °C and etching the polystyrene phase using different loadings of reactive graphene: c) neat blend d)1 wt%, e) 2 wt% and f) 3 wt%. White scale bar is 40 µm in all images. In images c-f it the red circle shows the characteristic length d_{PLA} used for measurements.

To provide more information about the microstructure of the blend, small amplitude oscillatory experiments were carried out after annealing at 180 °C for 30 minutes to guarantee the tested microstructure is stable. Figure 5.12a shows the storage modulus of the neat and compatibilized blends. An increase in the storage modulus over the frequency range is observed, which is more visible in the low-frequency range. In the model proposed by Yu *et al*., they suggested that for bicontinuous immiscible blends in the linear viscoelastic regime, the elastic modulus as a function of the ω frequency, G'(ω), can be decomposed into a contribution from the interface and one from the components of the blend.[324] The model was applied to a wide range of polymer blends with a broad range of viscosity differences, including the PLA/PS blend. The model revealed that at low frequencies, the interfacial contribution will overtake that of the components. Furthermore, the elastic modulus G′(ω) at low frequencies will be proportional to the specific area (S_V) given by the ratio of the interfacial area to the volume of the unit cell as shown in Figure 5.11 a. Furthermore, it has been demonstrated by Vinckier *et al*. that for an immiscible blend with island morphology in the low-frequency region:[325]

$$G'_{interface}(\omega) \propto \frac{\eta_m^2 \omega^2 R}{\Gamma} \qquad \text{Eq. 5.2}$$

where η_m^2, R, and Γ are the matrix viscosity, R is the radius of the droplet, and Γ is the interfacial tension, respectively. Because R is related to larger interfacial areas, then $R \propto S_V$. Therefore, this model reveals that the interface is reinforced by increasing the interfacial area and reducing the interfacial tension between the polymer phases. Considering the neat blend where the contribution from the components is constant and all parameters in Eq. 5.2 are fixed except S_V, the decay in G' over time could be associated with the decrease in the interfacial area driven by the high interfacial tension as the system tries to minimize its energy. Therefore, our experimental observations for the filled blends could suggest a synergistic effect where a decrease in the interfacial tension by the selective localization of reactive graphene increases the surface area.

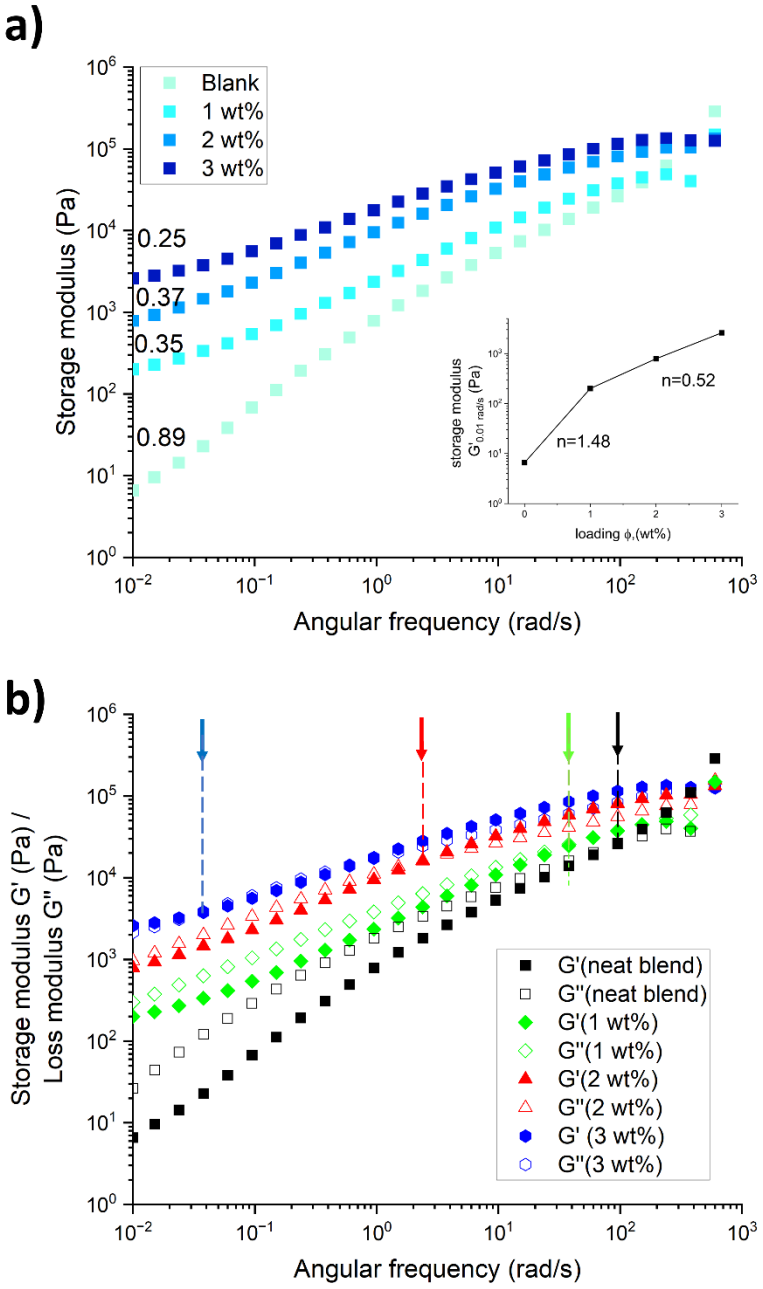

Figure 5.12 a) Frequency sweep of the storage modulus G' (ω) of the neat blend and blends containing reactive graphene b) Frequency sweep of G' (ω) and G"(ω) pointing out with arrows the cross over frequency point, that is when G' (ω) = G" (ω).

As explained before, analysis in the low-frequency region can provide information about interfacial phenomena happening in the immiscible blends. Experimental observations have associated the reduction in the terminal slope at low frequencies to the formation of elastic networks.[228,291,295,326–329] Here the terminal slope was estimated as 0.89 (from the last 4 points as it was been previously estimated in other work[291]). On the other hand, the compatibilized blends showed a plateau forming at lower frequencies, given by the reduction

in the slope, estimated as 0.35, 0.37 and 0.25 for 1, 2 and 3 wt%, respectively (Figure 5.12a). The significant decrease in the terminal slopes can be attributed to the transition from the liquid to the solid state and the creation of an elastic network because of the improved interfacial interactions promoted by the reactive graphene at the interface.[291] The compatibilized blends showed a power law dependency at low frequencies with respect to the loading of reactive graphene ϕ; therefore $\log G'_{(\omega,\phi)} \propto \phi^n$ and $n = 0.52$ as shown in Figure 5.12a. For $\phi \leq 1$ wt%, n=1.45, meaning that in this study 1 wt% is considered as the rheological percolation. Moreover, from Figure 5.12b a shift of the crossover frequency, $G'(\omega) = G''(\omega)$, is observed towards lower values, which means that the elastic character of the blend, $G'(\omega)$, is overtaking the viscous behaviour $G''(\omega)$. Another way to visualize it is from Figure 5.13, which shows the graph of $\tan\delta = G''(\omega)/G'(\omega)$, which illustrates that for $\tan\delta < 1$, the elastic behaviour overtakes the viscous behaviour. For the sample containing 3 wt% of reactive graphene its behaviour is predominantly elastic, which is in contrast with the neat blend that exhibits a typical viscous behaviour over almost the whole frequency sweep. Even the use of 1 wt% of reactive graphene dramatically improved the elastic response at $\omega < 1$ rad/s.

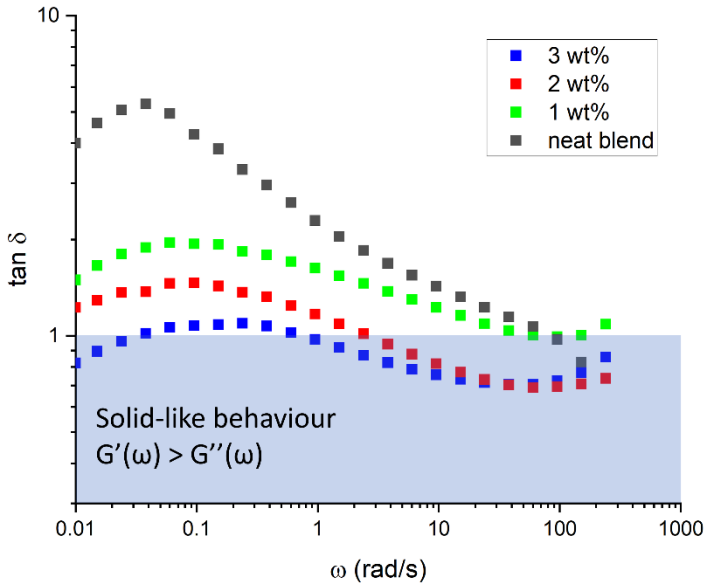

Figure 5.13 Tan δ graph of neat blend and filled polymer blends.

5.2.7 Rheoimpedance measurements

Rheoimpedance spectroscopy can assist in getting information about the formation of an electrical network. Polymers themselves are not conductive, and typically, they display a pure capacitive behaviour. In contrast, graphene platelets in a polymer can form conductive networks, showing a dominant resistive behaviour. Therefore, the RC model described by Eq. 3.19 and Eq. 3.20 in Section 3.11 can be suitable to describe graphene dispersed into a polymer matrix. The model predicts that at lower frequencies, the behaviour must be predominantly resistive ($Z \approx Z_{real}$), and exhibit a phase ϕ close to zero. Therefore, the electrical network was monitored by choosing a low frequency of 20 Hz during the experiments.

First, the effect of adding the reactive graphene on the impedance and the phase response was investigated. In brief, a piece of the polymer sample was placed between the two plates of a rheometer at 170 °C while a sinusoidal signal at 20 Hz was applied between the plates, and the impedance was recorded (see Figure 5.14a). Figure 5.14b shows that for the sample with 1 wt% the phase significantly oscillates because of the incomplete formation of the network, which is also reflected in a high impedance value around 4.3×10^8 Ω at the end of the experiment. On the other hand, for the blend with 2 wt% of reactive graphene the phase shows a steady value over the whole experiment around 5 degrees, accompanied by a decreased in the impedance reaching a final value of 5.2×10^5 Ω, which is almost two orders of magnitude lower than that of the blend with 1wt%. The abrupt decrease in the impedance and the phase shows that an already percolated network has been formed (Figure 5.14c). By increasing the loading to 3 wt% the phase remains around 5 degrees, and the impedance decreases to 2.3×10^5 Ω, which is a small decrease with respect to the blend filled with 2 wt%. (Figure 5.14d). These results can be interpreted from the percolation theory, which states that a minimum critical value (the percolation threshold) of reactive graphene is needed to form a network, that in this case corresponds to 2 wt%. Below this threshold, minimal conductive properties are shown in the case of the blend filled with 1 wt%, and above this point little improvement is observed in polymer systems involving carbon particles, MWCNTs and graphene.[330,331]

Since it is already known that the sample with 3wt% is forming a network, we are interested to know if it can recover. To determine this, first we need the microstructure to reach an equilibrium point (point a in Figure 5.15), then this initial microstructure needs to

be destroyed by shearing the sample (point b in Figure 5.15), that is by rotating the upper plate in the rheometer. Once the shearing stops, the structure will start to recover and 85 minutes later at the end of the experiment (point c in Figure 5.15) the network recovered 74.5% with respect to the value after the annealing step (point a in Figure 5.15).

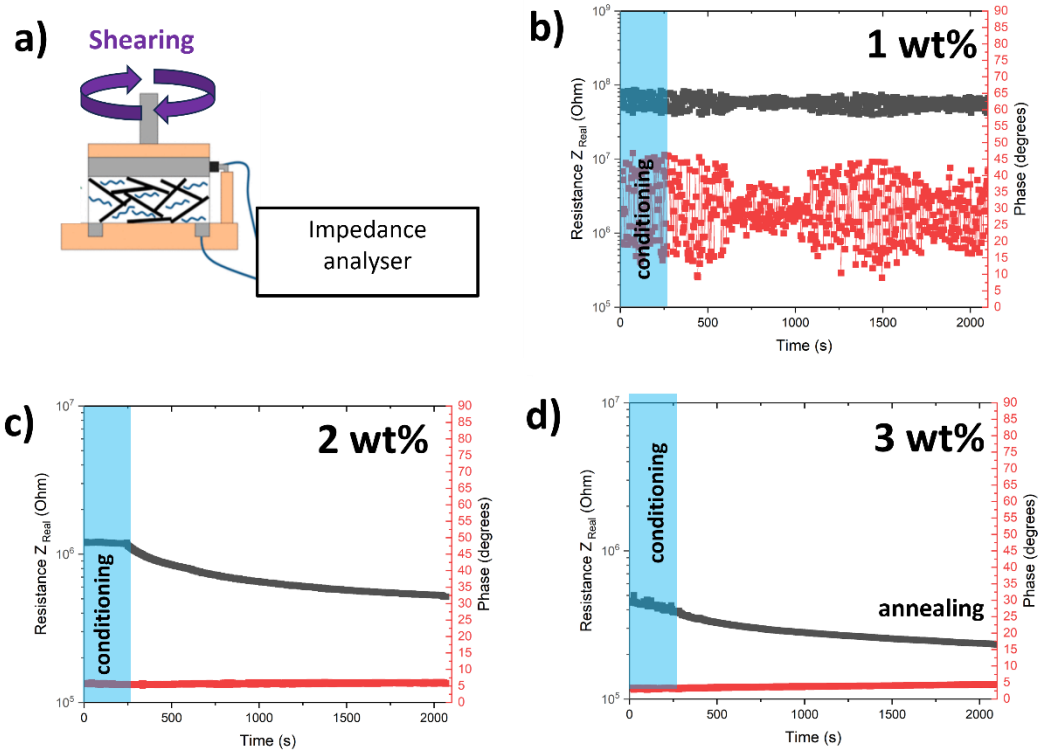

Figure 5.14 a) Experimental setup adapted from reference 332 b-d) Rheoimpedance response recorded at 20 Hz and 180 °C at different loadings (1, 2 and 3 wt%). Conditioning step: shearing at 0.01 s^{-1} and 180 °C for 5 minutes followed by static annealing. Black points correspond to the real part of the resistivity and the red points correspond to the phase shift.

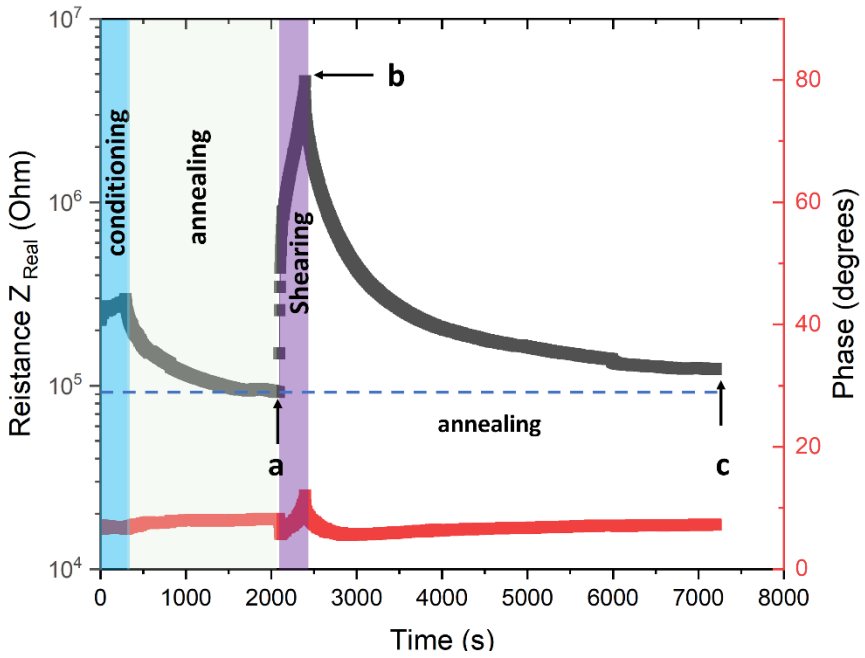

Figure 5.15 Rheoimpedance response recorded at 20 Hz and 180 °C). Conditioning step: shearing at 0.01 s^{-1} and 180 °C. shearing step: 0.1 s^{-1} for 5 minutes followed by static annealing. Black points correspond to the real part of the resistivity and the red points correspond to the phase shift.

5.2.8 Dynamical mechanical analysis

DMA is a technique sensitive to transitions associated with molecular motion. It can provide insight into reactive graphene's compatibilization effect on the blend. From all characteristic transitions, the analysis of the glass transition temperature (T_g) associated with PLA and the rubbery region can provide further evidence of the compatibilization effect. Glass transition temperature can be considered as the temperature where the loss modulus or tan δ graphs peak.[333]

Figure 5.16a shows the loss modulus graph having two peaks. The first one 72.9 °C corresponds to the T_g of PLA and the one at 120.2 C° corresponds to the T_g of PS. In all the blends, it is observed that for both the elastic and loss modulus at lower temperatures the storage modulus remains constant because the movement of all the polymeric chains is restricted to backbone stretching and bending. As temperature increases and approaches the $T_{g,\,PLA,}$ the elastic modulus starts dropping as the PLA domains relax, showing a peak in the loss modulus. From Figure 5.16b it is observed that tan δ at the corresponding PLA peak decreased with increasing the loading of the reactive graphene, which can be explained by a

more constrained movement of the PLA chains. Such restriction in motion can be attributed to the remaining epoxy groups that have reacted with the carboxylic groups on the surface of graphene to induce an effect similar to that of a crosslinker. The tan δ graph (Figure 5.16b) also showed that $T_{g,\,PLA}$ shifted towards lower values starting from 72.9 °C for the neat blend and reaching a minimum of 69.8 °C for the sample containing 3 wt % of reactive graphene. These two combined effects have also been observed in a system of thermoplastic polyurethane (TPU) and PLA that was extruded with reactive polyhedral oligomeric silsesquioxane (POSS) containing epoxy groups and the effects attributed to the compatibilization of the blend.[334]

This effect was studied in PLA/RGO systems by Ferreira and Tristão and was attributed to the reduction in crystallinity in the PLA phase and the increased mobility of the PLA chains in the amorphous regions as studied by DMA and time-domain nuclear magnetic resonance.[335] In another study by Yang *et al*., it was demonstrated that crosslinking of PLA chains with triallyl isocyanurate shifted minimally $T_{g,\,PLA}$ towards lower values. However, this effect was more noticeable when adding a plasticizer (dioctyl phthalate), in which crystallization significantly increased compared with the crosslinked sample. The increase in crystallinity was accompanied by an increase in the elastic modulus right after $T > T_{g,\,PLA,}$ caused by the shift of the onset crystallization temperature to lower temperatures and the increase in the rubbery plateau.[336] This is the same effect observed here and shown in Figure 5.16c for the filled samples. Therefore, given the nature of the synthesised nanoparticles, it could be expected that both plasticizing and crystallinity effects occur, with a net reinforcing effect on the blend.

Furthermore, the elastic and loss modulus showed higher magnitudes around the polystyrene glass transition temperature ($T_{g,\,PS}$). Since reactive graphene was only mixed with the PLA phase and only interacts through the interface, it may suggest a compatibilization effect due to the interfacial localization of graphene.

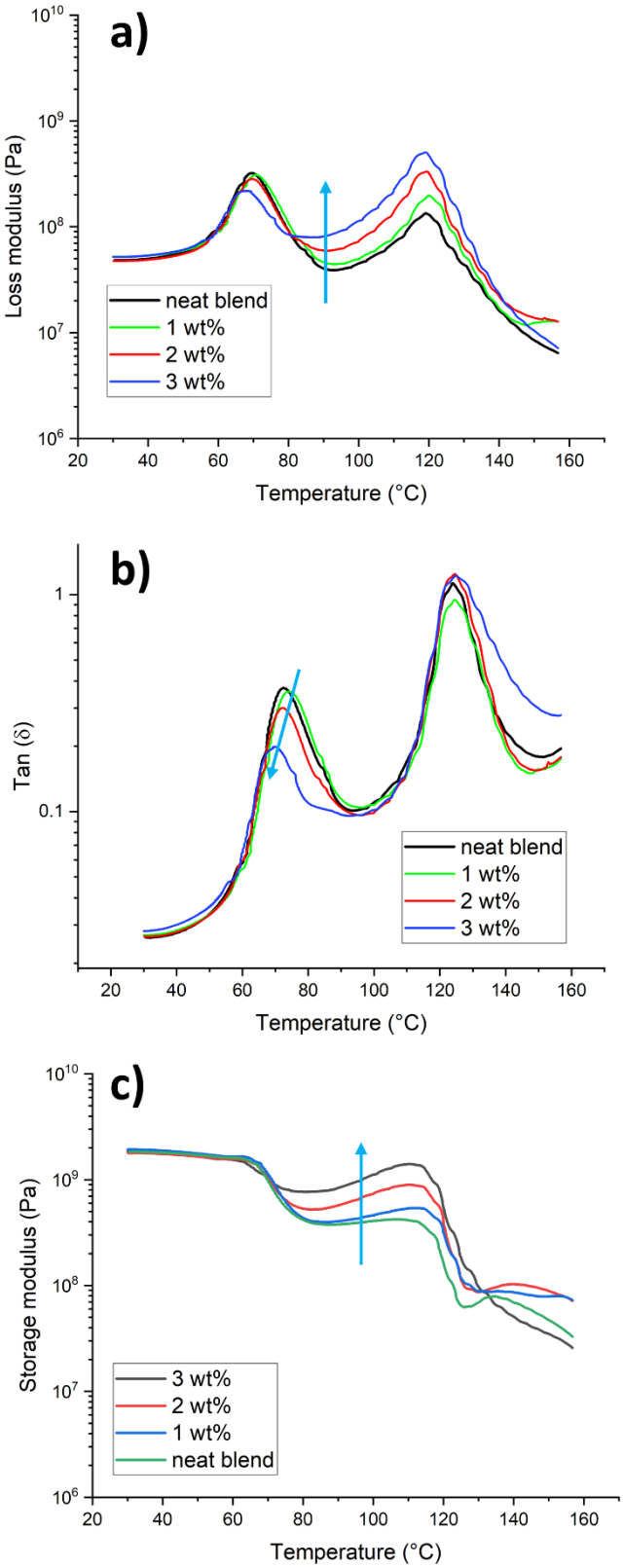

Figure 5.16 a) Storage modulus, b) loss modulus and tan δ graphs of the neat blend and blends containing reactive graphene.

5.2.9 Mechanism for localization of reactive graphene

To further investigate the localization of the reactive graphene, the sample containing 3 wt% was cross-sectioned in an ultra-microtome and imaged in a TEM. It is known that PS will not degrade under irradiation, but PLA will. Therefore, the mass loss will induce contrast and make the PLA phase look brighter than the PS phase.[337] Figure 5.17a shows the typical image from the neat blend, confirming the bicontinuous nature also observed in the TEM. It is important to highlight a few features commonly found in the neat blend to identify better the features in the blend containing the reactive nanoparticles.

Figure 5.17a shows a straight scar produced by the cutting process, some droplets of the PS phase in the PLA phase, and drops of PLA in the PS phase, which naturally occur due to the blending process. Figure 5.17b illustrates a high magnification area of the interface that is smooth and free of particles.

Figure 5.17c and d illustrates typical images of the blend with 3 wt% reactive graphene. It is confirmed that the smaller domain size of the PLA phase compared to the neat blend, agrees with observations from the SEM images. It is observed from Figure 5.17b and c that some reactive graphene remained in the PLA phase. However, most of them are preferentially located at the interface. Figure 5.18d1-d4 are high-magnification images of Figure 5.17. It is clearly shown that reactive graphene platelets remained adhered to the interface, and the presence of any of the nanoparticles in the PS phase was not observed. These observations agree well with measurements from rheology and dynamic mechanical analysis regarding the formation of an interfacial network. In the appendix A1 it is shown more supporting TEM images. Figures A1-A4 in Appendix A also make clear that thick unexfoliated reactive graphene ~ 20-50 nm thickness tends to detach from the interface and remain in the PLA phase, possibly due to the relatively high stiffness of the platelets that make them impossible to adapt to curvature changes during the interfacial coarsening process. Moreover, predictions on the possible localization of the reactive graphene indicate that reactive graphene should be dispersed in the PLA phase. Therefore, there must be an additional effect to make the graphene remain attached to the interface.

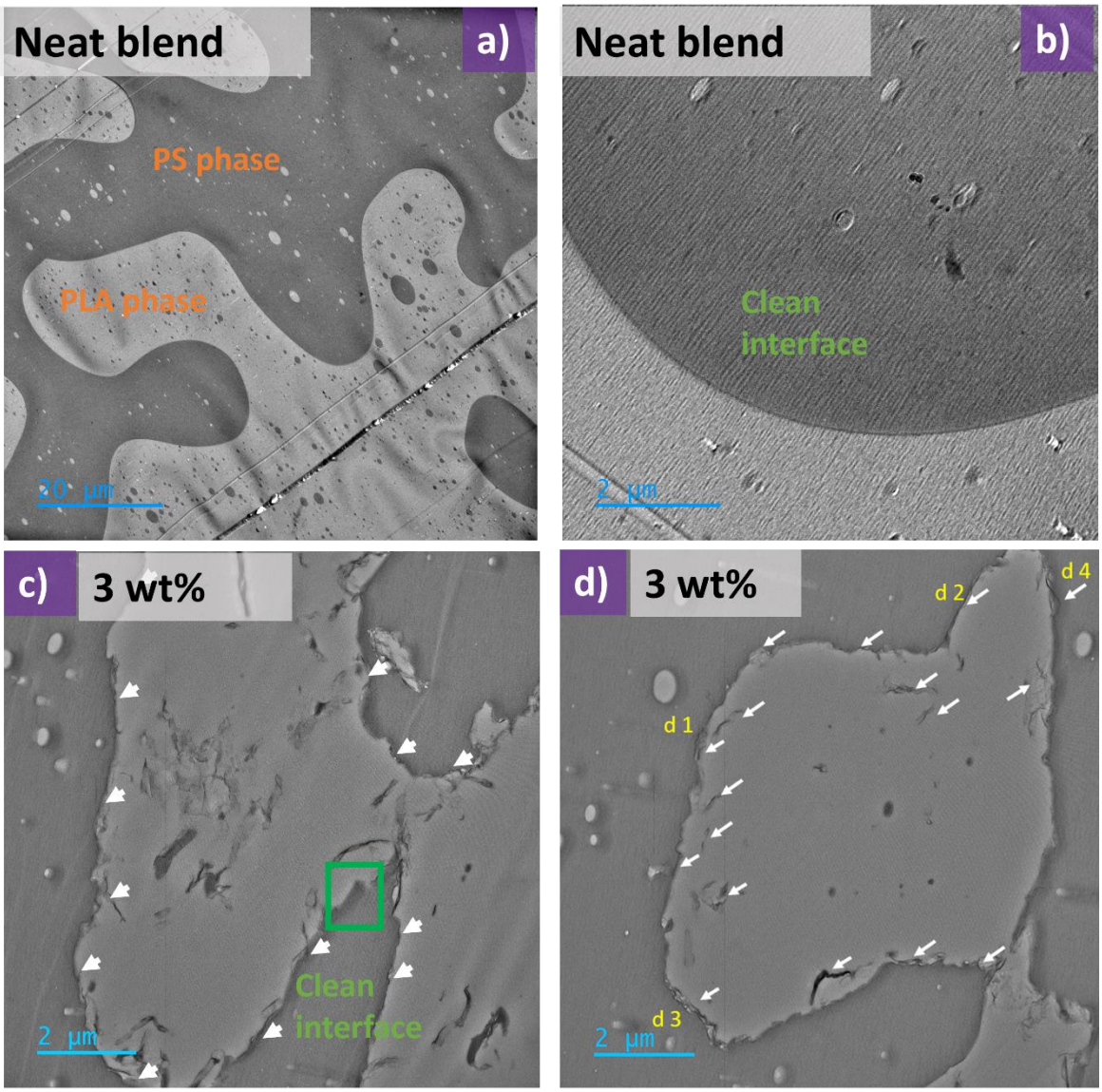

Figure 5.17 a,b) TEM images of the neat blend showing a clean interface. c,d) Typical images of the blend with 3 wt% reactive graphene. White arrows show reactive graphene trapped at the interface or in the PLA phase.

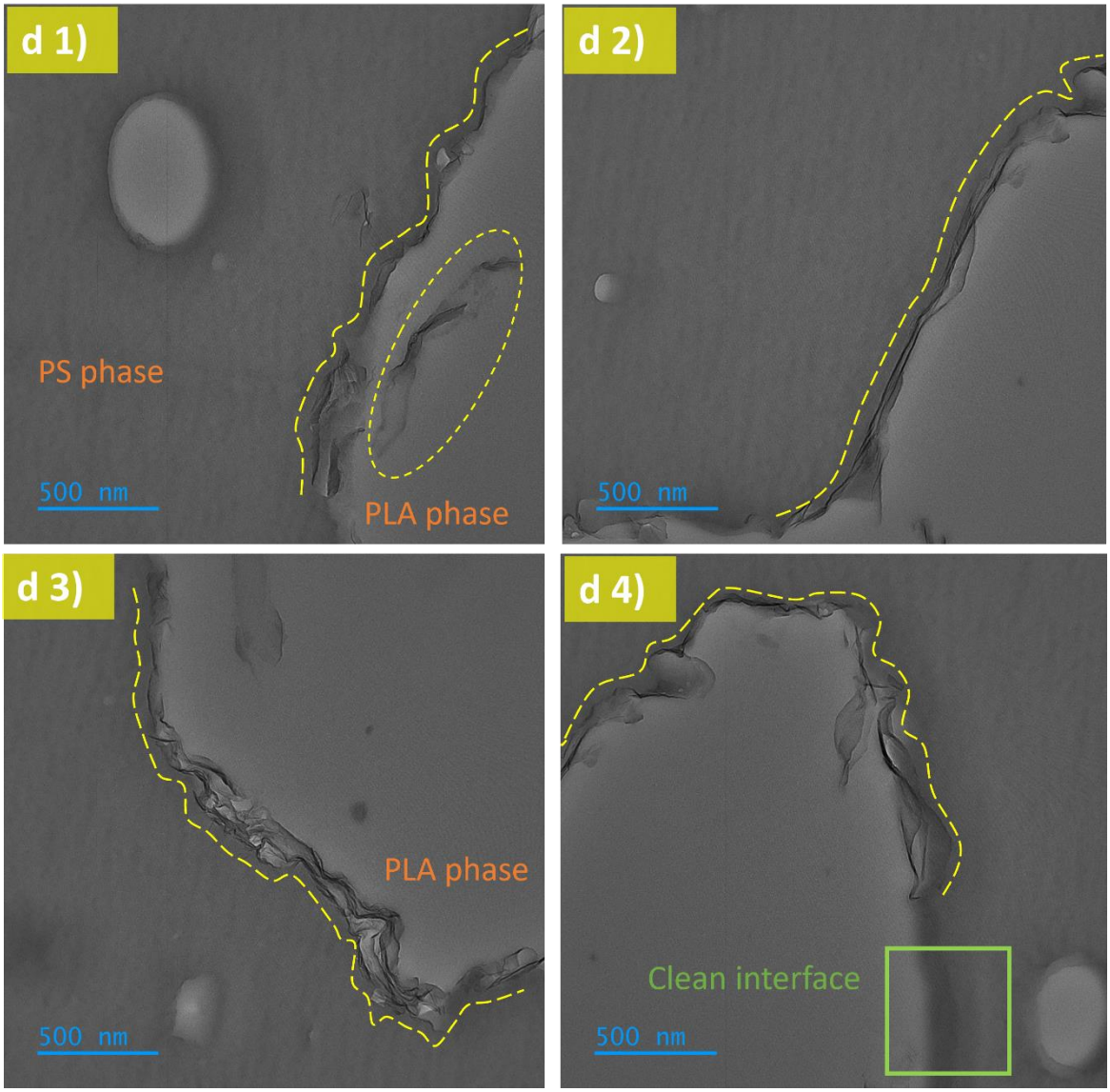

Figure 5.18 d1-d4) High magnification TEM images from selected areas in Figure 5.17d showing the reactive graphene localized at the PS/PLA interface. Contours of the reactive graphene are highlighted with dashed yellow lines. The green box is in d4) shows a clean area free of reactive graphene.

Our experimental observation agrees well with the mechanism proposed by Kou *et al*. for the localization of graphene nanoplatelets in polylactic acid/ethyl vinyl acetate.[295] A similar mechanism is proposed here to explain our observations. The mechanism proposed here is illustrated in Figure 5.19 where the selective localization at the interface is described in three stages. First, the remaining epoxy groups on the graphene react with terminal carboxyl groups in the PLA phase. Several previous studies have reported the reaction of terminal carboxyl terminated PLA with epoxy groups through glycidyl esterification during reactive extrusion.[334,338–346]

During this first stage, the reactive graphene platelets are also transported closer to the interface by convection from the bulk PLA phase, due the internal momentum gradients within the blend, so that reactive graphene aligns parallel to the interface. Figure 5.20 shows a high magnification image of the sample containing 3 wt% of reactive graphene quenched right after extrusion in liquid nitrogen. This structure is formed by lamellae around 100 nm thickness or less. In a previous study by Boothroyd *et al.* it was demonstrated that when graphene platelets are subject to high shear forces they align to the shear flow.[332] Therefore, it is expected that during extrusion, reactive graphene platelets flow parallel to the interface. Moreover, TEM observations (Figure 5.18 d1-d4) reveal that the length of the interfacial localized graphene is in the micron scale, which agrees with the average lateral size of graphene oxide starting material as determined from lateral size measurements in Section 4.3.1. In the second stage, film drainage of the departing PLA phase at the interface is induced by attractive forces from the PS phase, which is promoted by PS chains grafted on the surface of reactive graphene.

In the mechanism proposed by Kou *et al*., a third stage is related to the displacement of the three-phase contact line, which eventually leads to the migration of the reactive graphene to the other phase.[295] However, even when a long mixing time was used (10 minutes), no reactive graphene was found in the PS phase (see images provided in Appendix A), which is in contrast with previous studies that have reported the migration of carbon black, carbon nanotubes and graphene nanoplatelets in different immiscible blends to happen in a stretch window of time during the early few minutes of blending.[136,154,316,319,347,348] This suggests that the reactive graphene is stable at the interface and resistant to static annealing and the high shear forces, even when we used a long blending time (10 minutes), suggesting high adhesion energies.

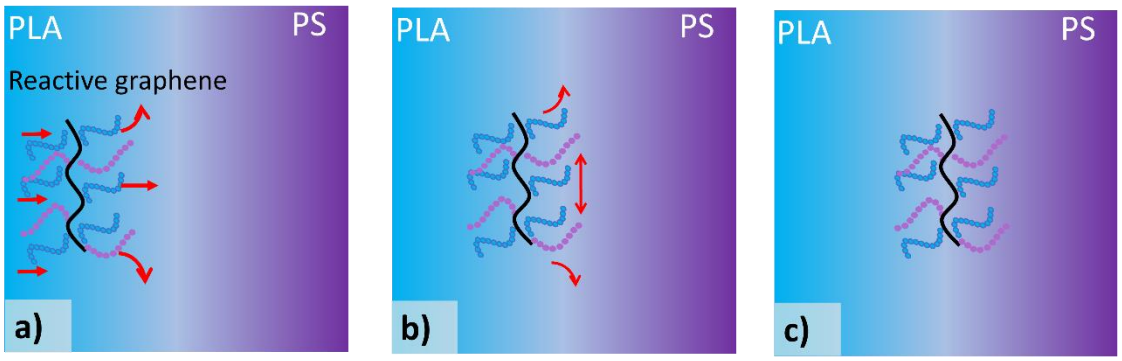

Figure 5.19 Schematic representation of the localization of reactive graphene. a) Remaining epoxy groups react with carboxyl groups on PLA chains aided by high shear forces. Those forces also transport reactive graphene by convection to a zone near the interface. b) Film drainage of reactive graphene driven by surface energy difference. c) Graphene is localized at the interface.

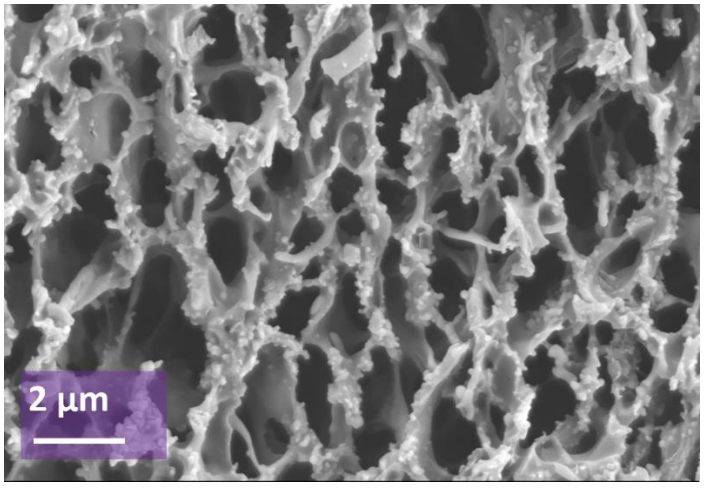

Figure 5.20 SEM image of sample containing 3 wt% of reactive graphene right after it was extruded and quenched in liquid nitrogen PS phase was etched in cyclohexane.

5.3 Conclusion

Polymers are generally immiscible due to the low entropy of mixing. So, when two polymers are mixed, they form microstructures. From the range of microstructures, the bicontinuous one has the property of creating a doubly interpenetrated network, which finds applications in developing blends with improved barrier properties, thermomechanical resistance and electrical conductivity. The thermodynamical immiscibility and high interfacial tension between the components of the blend result in weak interfacial adhesion, leading to poor mechanical properties of the blend. Moreover, bicontinuous morphologies are unstable, so when subjected to an annealing process, the morphology will minimise the system's energy by reducing the interfacial area. From the alternatives available to compatibilised immiscible blends, using graphene-based materials as nanofillers has emerged as an attractive option to improve the mechanical and electrical properties of the blends.

Here, the PLA/PS immiscible blend was used as a model to test the use of reactive graphene to improve the compatibilisation of the blend. As a first step, graphene oxide was thermally reduced, leaving hydroxyl groups on the surface, which reacted with a silane coupling agent to introduce epoxide groups. Next, carboxyl-terminated polystyrene chains were introduced through a base-catalysed ring-opening reaction. As a result, the reactive graphene had remaining epoxy groups and polystyrene chains grafted. Then, a master batch containing the reactive graphene was prepared and mixed with polystyrene in a mini extruder.

Calculations based on the contact angle predicted that the reactive graphene should have remained in the PLA phase; however, our TEM observations showed that most of it was localised at the PLA/PS interface. SEM observations revealed that phase coarsening was significantly decreased upon adding reactive graphene, and small amplitude oscillatory experiments showed that the microstructure was stable against static annealing. Moreover, rheoimpedance measurements showed that the addition of 2 wt% formed an electrically conductive network that, even when it was destroyed by shearing, could recover around 75% of its initial resistance.

From experimental observations, a mechanism was suggested in which first, the remaining epoxy groups on the platelets reacted with the terminal carboxyl groups from the PLA chains. Then, the graphene was transported close to the interface, and polystyrene chains attached to the reactive graphene drag it to the polystyrene phase driven by a local surface energy difference, leading to the final localisation of the graphene at the interface. Due to the high number of variables involved related to the blending process and the polymer system, further research must be done to explore the applicability and limits of this approach in more depth.

6 A conformability approach for graphene transfer

6.1 Introduction

Chemical Vapor Deposition (CVD) remains the production method to obtain high-quality graphene. In this process, a copper sheet is heated, and the chamber is fed with a mixture of methane and hydrogen. The thermal decomposition of methane on the metallic catalyst makes possible graphene growth on the surface of it. Further relevant information can be found in Section 1.3.4. The simplicity, low-cost and advances in the process optimisation have positioned graphene production by CVD as the most promising one for large-scale production.

Since graphene is grown on copper, transferring it to a desired substrate is necessary. This step is critical to develop applications such as electrochemical sensors, acoustic devices, and gas sensors, to name a few.[349–352] From the range of methods available, the most typical process involves coating the graphene on copper with a polymer supporting layer and then etching the copper, washing the film, and transferring it to a desired substrate as illustrated in Figure 1.10. From a broad perspective, this last step relies on how well the supported graphene conforms to the topography of the substrate. Here, we will refer to this concept as conformability. For practical purposes, it is of uttermost importance to develop wearable devices for electrophysiological sensing, such as electroencephalography (EEG), electrocardiography (ECG), electromyography (EMG), and biomarker monitors, among others. The thickness of the films is closely related to the conformability shown in Figure 6.1. Experiments and theoretical calculations showed that higher conformality leads to lower contact impedance and higher signal-to-noise ratio while decreasing random impedance changes due to deformation.[350,353–355]

The conformability concept can also help simplify the transfer of graphene to silicon oxide, which is widely used for electronic purposes. When transferring graphene onto Si/SiO_2 using a polymer supporting layer, lack of adhesion can cause delamination, which produce holes and tears in the graphene film. Although the transfer process is described in many papers, it is common to find papers where commercial enterprises do this step.[352]

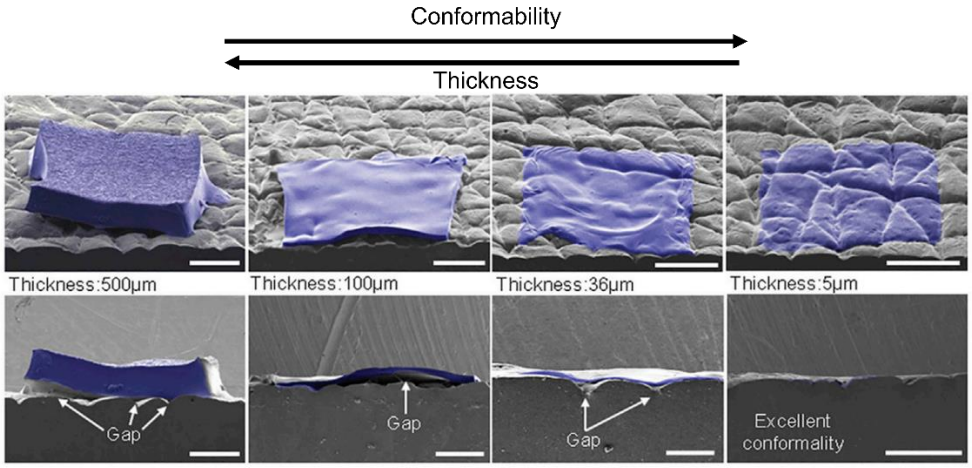

Figure 6.1 Relationship between film (shaded in blue) thickness and conformability to skin. Reproduced from reference 356.

Generally, the transfer of the graphene/supporting layer to a substrate with a known roughness can be rationalized from the conformality point of view. The model described next has been previously reported, and here it will be briefly described.[354,357,358] First, let us consider a more general case where an elastic substrate with plane strain modulus E_s is described by a sinusoidal wave described by the wavelength λ and amplitude h_0 as in Eq. 6.1:

$$w_0(x) = h_0\left(1 + \cos\frac{2\pi x}{\lambda}\right) \qquad \text{Eq. 6.1}$$

Due to the membrane-substrate interaction in the contact section ($0 \leq x \leq x_c$) the substrate deforms, preserving the same sinusoidal shape but different amplitude h_1 (Eq. 6.2):

$$w_1(x) = h_1\left(1 + \cos\frac{2\pi x}{\lambda}\right) \qquad \text{Eq. 6.2}$$

On the other hand, the membrane with elastic modulus E_m can be described as a piecewise function (Eq. 6.3), which is formed by a function that describes the section where the graphene/supporting polymer is in contact with the substrate and a section where graphene is pending and not in contact. In the contact section, it is described by $w_1(x)$ and in the non-contact zone ($x_c \leq x \leq \lambda/2$) it adopts a parabolic profile in agreement with a case where a pure bending condition is assumed.[357,359]

$$w_2(x) = \begin{cases} h_1\left(1 + \cos\frac{2\pi x}{\lambda}\right), & 0 \le x \le x_c \\ a\left(x - \frac{\lambda}{2}\right)^2 + b, & x_c \le x \le \lambda/2 \end{cases} \qquad \text{Eq. 6.3}$$

At the point x_c the function must be continuous, that is $w_2(x) = w_1(x)$ and $dw_2(x)/dx = dw_1(x)/dx$. Therefore, solving for unknown constants a and b, $w_2(x)$ can be expressed as a continuous function:

$$w_2(x) = h_1\left[\frac{\pi}{\lambda\left(\frac{\lambda}{2} - x_c\right)}\sin\left(\frac{2\pi x_c}{\lambda}\right)\left[\left(x - \frac{\lambda}{2}\right)^2 - \left(x_c - \frac{\lambda}{2}\right)^2 + 1 + \cos\left(\frac{2\pi x_c}{\lambda}\right)\right]\right] \quad x_c \le x \le \lambda/2 \qquad \text{Eq. 6.4}$$

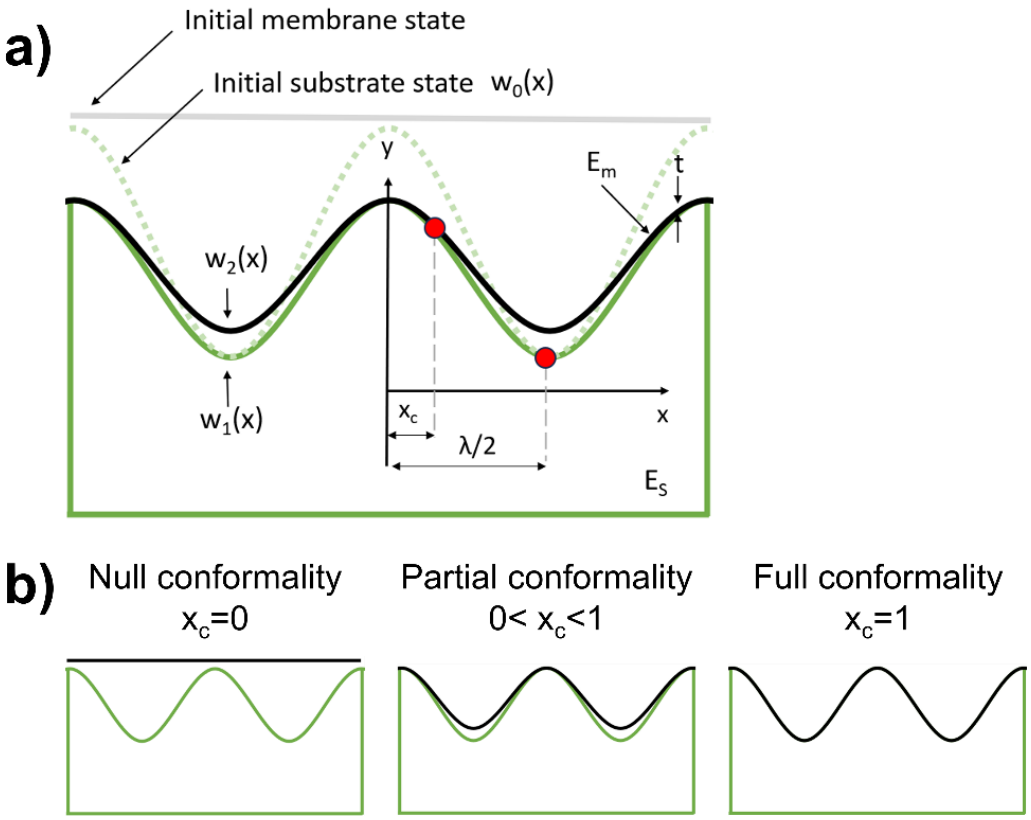

Figure 6.2 a) Illustration of partial conformality showing the geometrical parameters that defines the equilibrium state. b) Three possible scenarios spanning from null conformality to full conformality.

To solve for the unknown variables x_c and h_1 will be used as variables that minimize the energy of the system formed by the substrate and the membrane. It can be expressed as:

$$U_{total} = U_{bending} + U_{membrane} + U_{adhesion} + U_{substrate} \qquad \text{Eq. 6.5}$$

where $U_{bending}$ is the bending energy of the membrane, $U_{membrane}$ is the energy associated with the tensile strain in the membrane, $U_{adhesion}$ is the energy of adhesion between the membrane and the substrate in the contact zone and $U_{substrate}$ is the elastic energy stored in the substrate. The bending energy can be expressed as:

$$U_{bending} = \frac{2}{\lambda}\left[\frac{1}{2}\int_0^{x_c} E_m I t \kappa_1^2 \, ds + \frac{1}{2}\int_{x_c}^{\lambda/2} E_m I t \kappa_2^2 \, ds\right] \qquad \text{Eq. 6.6}$$

where $E_mI = E_mt^3/12$ is the plane bending stiffness of the membrane κ_i is the curvature associated, and ds is the arc length. From Eq. 6.6 the first term represents the part of the membrane in contact with the substrate, and the second term represents the membrane suspended in the non-contact zone. Similarly, the energy membrane (Eq. 6.7) can be decomposed in a contribution from the tensile strains ϵ_i in the contact (ϵ_1) zone and non-contact zone (ϵ_2).

$$U_{membrane} = \frac{2}{\lambda}\left[\frac{1}{2}\int_0^{x_c} E_m t\epsilon_1^2\, ds + \frac{1}{2}\int_{x_c}^{\lambda/2} E_m t\epsilon_2^2\, ds\right] \qquad \text{Eq. 6.7}$$

The adhesion mechanism provides stability to the system; therefore, this term must be negative. Then, the energy of adhesion per arc length is just the product of the work of adhesion between the substrates and the membrane times the arc length of the contact zone, as in Eq. 6.8.

$$U_{adhesion} = -\frac{2}{\lambda}\int_0^{x_c} \gamma ds \qquad \text{Eq. 6.8}$$

Because, in a more general case, the substrate is compliant, and the energy of the substrate must equal the work done by the surface traction forces on the substrate as in Eq. 6.9 where $u(x) = w_1(x) - w_0(x)$ is the surfaces displacement, and $P(x)$ is the surface traction that induces the displacement.[358]

$$\begin{aligned} U_{substrate} &= \frac{2}{\lambda}\int_0^{x_c} \frac{1}{2}u(x)P(x)dx \\ &= \frac{E_s\pi(h_1 - h_0)^2}{4\lambda}\sin^4\left(\frac{\pi x_c}{L}\right) \end{aligned} \qquad \text{Eq. 6.9}$$

In order to make computations simpler, the arc length is described as $ds = \sqrt{1+\left(\frac{dw_i}{dx}\right)^2}\,dx$ and can be approximated as a first-order Taylor series approximation;

therefore $ds \approx 1+\frac{1}{2}\left(\frac{dw_i}{dx}\right)^2 dx$. This same approximation can be applied to the calculation of the tensile strains ϵ_i which are expressed as $\epsilon_i=(ds - dx)/dx$. On the other hand, the full description of the curvature κ_i is given by Eq. 6.10. However, using it significantly increases the computation time, so it can be assumed that for a small deflection, that is, small roughness $\left(\frac{h_0}{\lambda} \ll 1\right)$ then $ds \approx dx$ and curvature can be simplified to $\kappa_i \approx d^2w_i/dx^2$. Observe that this assumption cannot be made for the energy of the membrane since ϵ_i would be zero.

$$\kappa_i = \frac{d^2w_i/dx^2}{\left[1+\left(\frac{dw_i}{dx}\right)^2\right]^{3/2}} \qquad \text{Eq. 6.10}$$

6.2 Results

6.2.1 Graphene characterization

Graphene was synthesized on a copper substrate using low-pressure chemical vapour deposition (LPCVD). See Section 1.3.4 for more information on LPCVD process. Figure 6.4a shows graphene films transferred on Si/SiO_2 substrate using a wet transfer procedure using PMMA as a supporting layer (see experimental Section 8.19). Figure 6.4b shows SEM images of the graphene transferred, showing no significant cracks and tears. Also, TEM imaging (Figure 6.4c) shows that the graphene layer is continuous and self-standing, which is critical to developing applications where electrical conductivity is needed. Although SEM imaging reveals it exhibits some adlayer regions, it is predominantly monolayer. This is further supported by the typical Selected Area Electron Diffraction (SAED) pattern (Figure 6.4d), showing higher intensities of the inner reflections ($1\bar{1}00$ and $0\bar{1}00$) than those of outer reflections ($2\bar{1}\bar{1}0$ and $\bar{1}\bar{1}20$), which is consistent with monolayer graphene structures.[274]

Raman spectroscopy was used to assess the quality of the graphene. It shows typical features of graphene, the G peak around 1585 cm^{-1} and the 2D peak around 2678 cm^{-1}. The 2D peak can be fitted to a single Lorentzian peak, a characteristic feature of monolayer graphene.[171,360] Monolayer nature is also supported by intensities ratio $I_{2D}/I_G \sim 2$, which has

been proposed as a parameter to define graphene quality by the National Physical Laboratory (NPL), UK.[182] Also, the D peak around 1350 cm^{-1} associated to defects in the graphitic lattice is minimal.

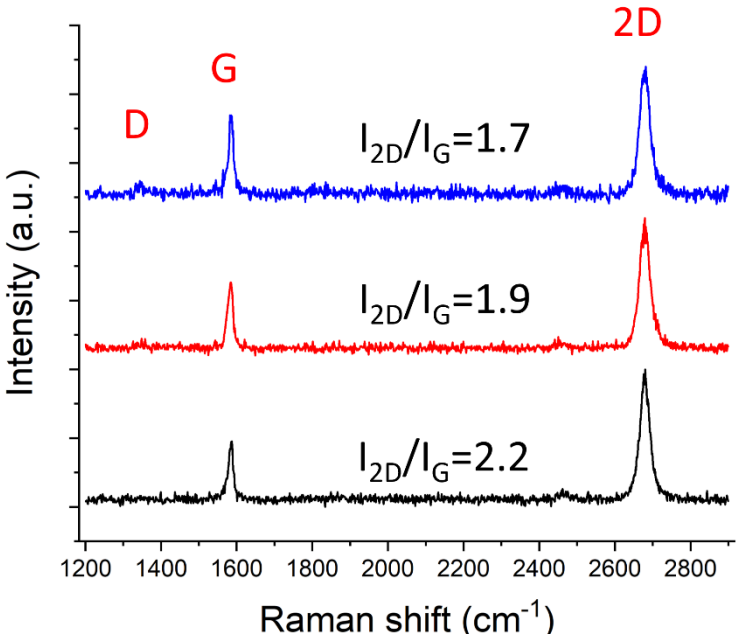

Figure 6.3 Graphene spectra of three random points over the figure shown in Figure 6.4a. Spectra were recorded using a laser excitation wavelength of 532 nm.

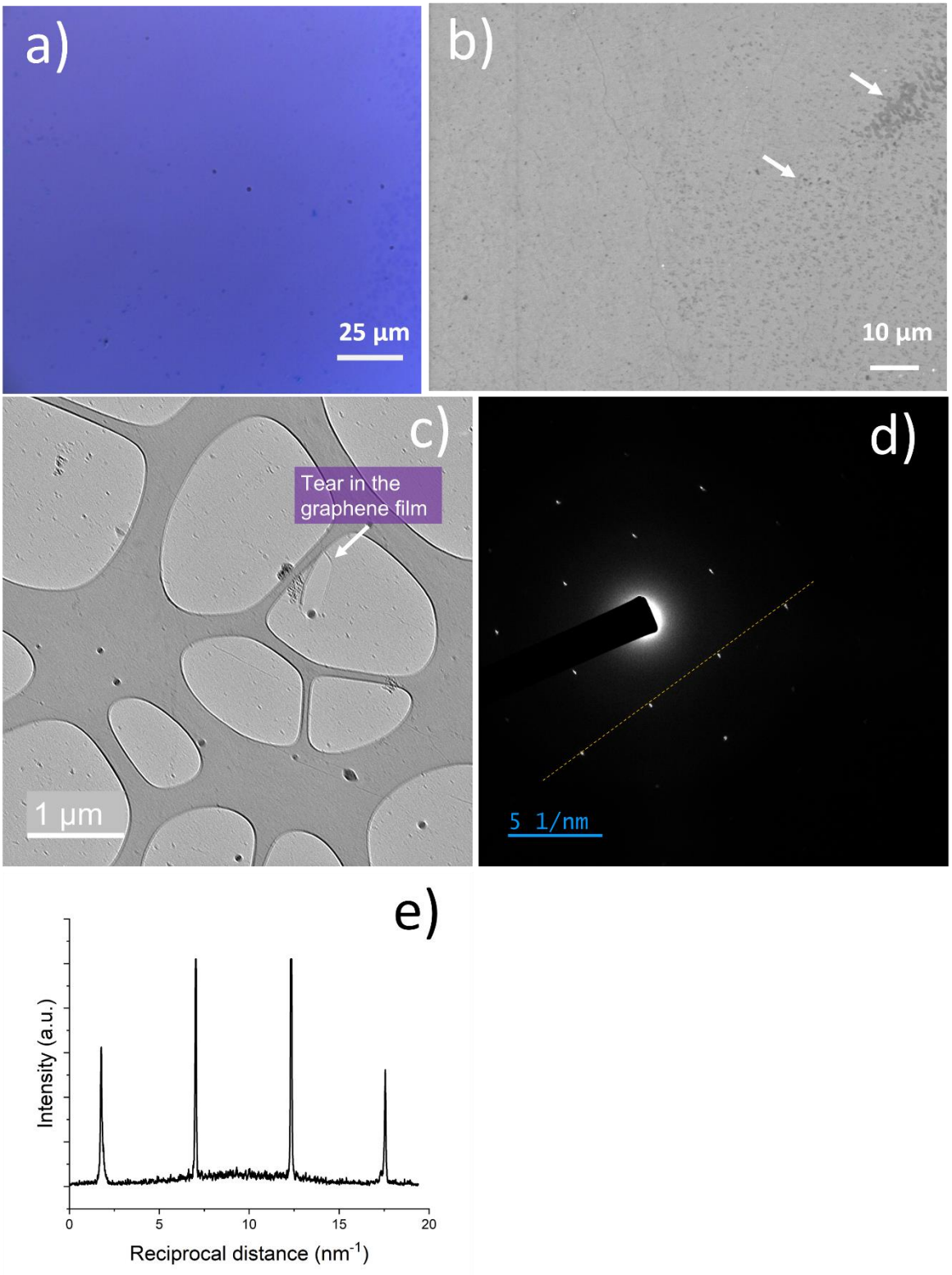

Figure 6.4 a) Optical and b) SEM image of graphene on Si/SiO_2.(arrows point out at adlayer domains) c) Self standing graphene film on TEM grid and d) corresponding selected area diffraction pattern and e) intensity profile along the line.

6.2.2 Graphene transfer on Si/SiO_2

Graphene deposited on Si/SiO_2 has become the preferred choice when developing graphene-based electronic devices such as transistors. Although extensive research has been done on the adhesion of graphene on SiO_2 using different techniques such as AFM, nanoindentation, fracture and scratch tests, very different results have been obtained. A study by Koenig *et al.* showed a higher energy of adhesion of 0.45 J/m^2 for single-layer graphene, which decreased for multilayer graphene to 0.31 J/m^2.[361] This study concluded that the difference was caused by the higher conformability of the monolayer graphene to the topography of the silicon oxide than the multilayer counterpart.

It has been experimentally demonstrated that poor contact between graphene and SiO_2 substrates causes cracks and tears during a wet transfer process.[112] During the wet transfer process, the last step involves transferring the PMMA/graphene film floating on water onto a SiO_2 substrate, leaving a thin film of water between the graphene and silicon oxide. Therefore, easier ways to remove the water between the graphene and SiO_2 include heating at temperatures above the saturation temperature of water, using vacuum, or even more sophisticated methods like applying a high electric field between graphene on copper and the substrate.[362] Recently, it has been demonstrated that annealing at high temperatures of 450 °C increased almost three times the energy of adhesion measurements. It was attributed to an improved conformal contact between the graphene and the SiO_2 substrate.[363]

Therefore, the lack of conformality between the Si/SiO_2 substrates reduces the energy of adhesion. However, from a macroscopic point of view, since graphene is transferred using a PMMA layer, the transfer is also influenced by the PMMA mechanical properties. The conformality concept can assist in finding a rational way to transfer large areas of graphene.

The model previously described in Section 6.1 can be simplified by making a few assumptions. First, the Si/SiO_2 substrate is assumed to be flat and does not store any elastic energy, thus $U_s = 0$. Second, because the copper foil has an associated roughness coming from the rolling process during its production, the PMMA film will also conform to that morphology (Figure 6.5). Therefore, the elastic energy of the PMMA/graphene stack will be defined by PMMA properties only. Since U_m and U_b are always positive, and the adhesion term U_a is always negative, the adhesion mechanism must compensate for the energy for bending the membrane (U_b) and the energy associated with the normal strains within it (U_m).

Figure 6.5 illustrates the system proposed and its parameters where E_m is the Young's modulus of the PMMA t_{PMMA} is the thickness of the PMMA supporting layer, whose topographical properties are defined by $2h_0$ and λ which are the average height and wavelength describing the wavy nature of the PMMA film (Eq. 6.12). The energy balance is expressed as:

$$U_m + U_b = U_a \qquad \text{Eq. 6.11}$$

Now the set of equations to be solved is given by:

$$w_0 = h_0\left(1 + \cos\frac{2\pi x}{\lambda}\right) \qquad \text{Eq. 6.12}$$

$$U_{bending} = \frac{1}{\lambda_{copper}}\int_0^{\lambda_{copper}} E_m I t \kappa^2 \, ds \qquad \text{Eq. 6.13}$$

$$U_{membrane} = \frac{1}{\lambda_{copper}}\int_0^{\lambda_{copper}} E_m t \epsilon^2 \, ds \qquad \text{Eq. 6.14}$$

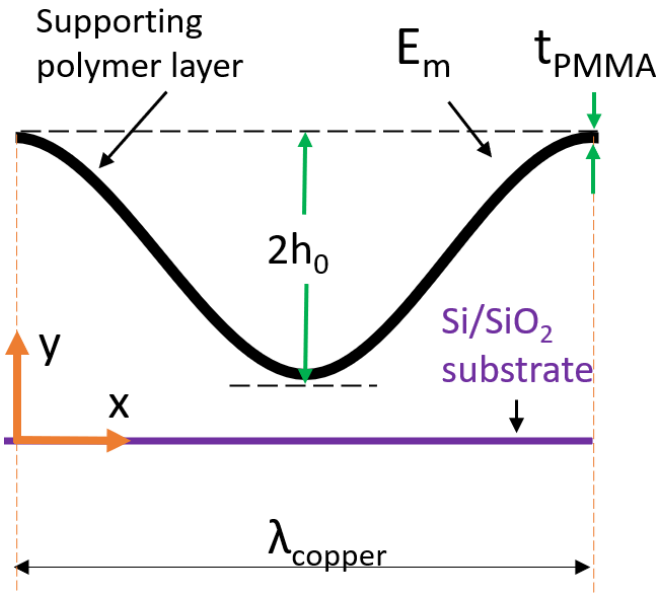

Figure 6.5 Model where a wavy PMMA film with thickness t_{PMMA} and Young's modulus E_m adopts the roughness features from copper represented by λ, h_0.

The set of equations is solved using the same assumptions stated in Section 6.1. $ds \approx 1+\frac{1}{2}\left(\frac{dw_0}{dx}\right)^2 dx$, $\kappa \approx d^2w_0/dx^2$ and $E_mI=\frac{E_mt^3}{12}$. The parameters from the roughness of the copper surface λ_{copper} and h_{copper} are determined as follows. Figure 6.6 shows that the surface topography of copper is wavy and irregular, having regions as high as $2h_{copper} = 841$ nm and some others as low as $2h_{copper} = 270$ nm. For this analysis, we can extract the mean value of h_{copper} from the relationship between the random mean square (RMS) of the surface and a sinusoidal wave:

$$h_{copper} = \sqrt{2}\,\mathrm{RMS} \qquad \text{Eq. 6.15}$$

The average RMS value is 210 ± 30 nm, so $h_{copper} = 296 \pm 42$ nm . The average wavelength of the copper surface λ_{copper} is estimated from the average peak-to-peak distance. The average measured value is $\lambda_{copper} = 19.3 \pm 3.4$ μm . As for the energy of adhesion it can be considered as twice the surface tension of water, then $\gamma = 0.144$ J/m^2. Figure 6.5 shows the relationship between height h_0 and thickness t_{PMMA}.

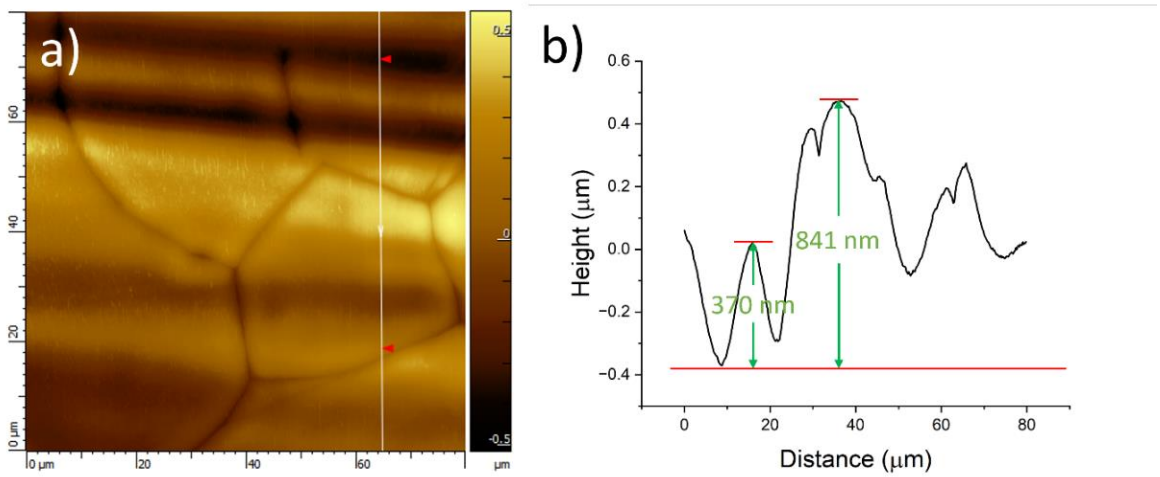

Figure 6.6 Topography of graphene on copper (a) and a typical profile showing arbitrary heights ($2h_0$) measured from the lowest points.

In the equations that account for the storage of the elastic energy in the membrane (Eq. 6.11-Eq. 6.14), assuming the thickness of the PMMA film is 415 nm, and the rest of parameters are known except for h_0. Then, there must be an h_0 value that satisfies Eq. 6.11, so the elastic energy stored in the film equals the adhesion energy between the graphene and the Si/SiO_2. Because the elastic energy increases with the thickness ($U_{bending} \propto t^3$ and $U_{membrane} \propto t$), solving Eq. 6.11 will give the maximum value of h_0 allowable. Calculations were done in Matlab.[364] Figure 6.7a and b show the image of the film and the measured profile. It was not considered a measurement near the edge as the film was carefully torn and lack of contact might have led to an overestimation of the thickness. Figure 6.7c shows the graphical solution of the equations for the maximum h_0. It was estimated that for a PMMA film ~415 nm the maximum value of h_0 is 387.5 nm. Using the average value h_0 estimated from RMS of the copper surface, it could be concluded that all the PMMA will adhere to the SiO_2. As seen in Figure 6.6, there are regions where $h_0 > 387.5$ nm, where the film will not fully adhere, making these regions prone to come off.

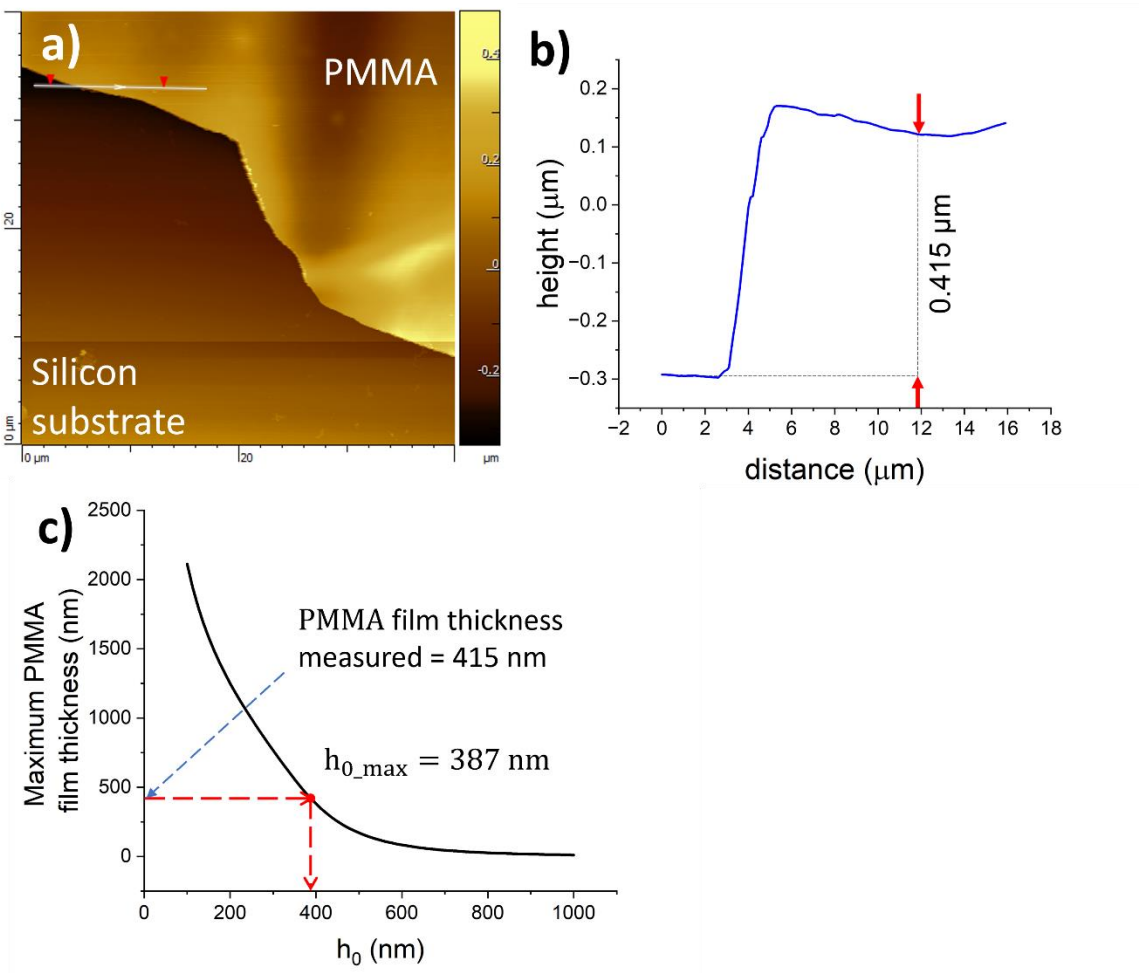

Figure 6.7 a) AFM image of the PMMA film on a silicon substrate. b) Height profile from the line in a) and the thickness measurement of the film. c) Graph of the maximum thickness of the PMMA film for a given h_0 for full conformability. $h_{0\ max}$ is the maximum value for a PMMA film of 415 nm thickness.

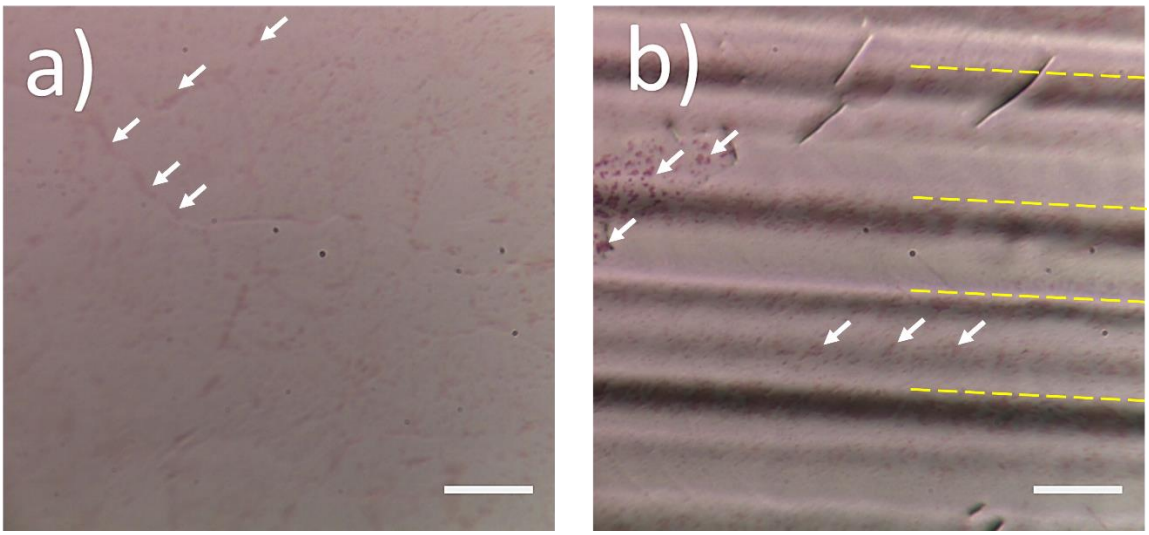

Figure 6.8 Graphene on copper stored at ambient conditions: a) Sample from a commercial brand and b)From the graphene used in this work. White arrows in a) and b) point at copper(I) oxide and yellow dashed lines in b) represent the marks from the rolling process. The scale bar in both images is 25 μm.

Here, a reproducible method is reported to transfer a centimetre scale sample of graphene on Si/SiO_2 substrates using a polymer supporting layer. Figure 1.10a illustrates that during the last step of this process the supporting polymer/graphene stack is floating on a deionized water bath and needs to be fished out on a desired substrate, typically Si/SiO_2. Hence a thin film of water will remain trapped between the graphene and the Si/SiO_2. Therefore, a strategy is needed to remove the water and improve the adhesion with the Si/SiO_2 substrate. So, after transferring the samples onto SiO_2 substrates, they were gently heated at 35 – 37 °C on a hot plate to remove as much water as possible. Although graphene is theoretically impermeable to water, PMMA, on the other hand, has a higher permeability of $P = 1.7 \frac{g \cdot mm_{film\ thickness}}{m^2\ day}$. Recent studies on the breathability of PMMA/graphene films showed that it is possible because of micro-defects, cracks, and holes. This implies that apart from the edges, the surface of the graphene/PMMA stack can actively remove water.[365] Figure 6.8 shows graphene on copper exposed to air for a long time. It reveals that graphene from a commercial brand and the one used in this work have red areas where copper (I) oxide is formed, meaning there are areas not fully covered with graphene so water can be transpired. It was reported that for a film around 200 nm thickness, the permeability coefficient was $P = 1400 \frac{g}{m^2\ day}$ at 50 °C.[355,365] Using this value, we can roughly estimate the amount of water that can be evaporated through the surface per hour to be $5.8 \times 10^{-3} \frac{g_{water}}{cm^2\ hr}$. Although permeability coefficients exhibit an Arrhenius-like dependence, it has been shown

that the water permeability of PMMA does not change significantly. Therefore, we can still use this value as an estimation.[366] Since typical sizes of the graphene were 1 cm^2, the equivalent thickness of a layer of water that could be potentially evaporated in 1 hour would be 58 μm, which is clearly more than that trapped during the transfer process. Therefore, it can be inferred that a gentle heating can remove most of the water trapped.

It is expected that not all water can be expelled from heating at low temperatures, and there will be regions where graphene effectively prevents water evaporation. However, there will be regions where graphene effectively adheres to the SiO_2 substrate. Furthermore, the PMMA/graphene stack also has a roughness associated with the copper surface. This presumably creates blisters of water. Samples were tilted and heated at temperatures above the saturation temperature of water at atmospheric conditions to improve the adhesion by removing residual water.

Figure 6.9 illustrates that when samples were tilted at lower angles of ~30° and heated at the lowest temperature 100 °C, the size of the area where graphene was detached was considerably larger than for samples tilted at higher angles at the same temperature (70° and 90°). This suggests that tilting the sample allows water to redistribute and migrate to zones where it can transpire through defects in the graphene film. When heating at higher temperatures (130 °C or 160 °C), all water will be in the vapour phase.

Figure 6.9 also shows that heating at higher temperatures (130 °C or 160 °C) suppressed the formation of holes. This can be explained due to the increased conformability of the PMMA film to the Si/SiO_2 substrate. Since the PMMA film initially has the rough topography of the copper substrate, at lower temperatures, the high elastic modulus of the PMMA film will make it sufficiently stiff to prevent full conformality in some areas. However, upon increasing the temperature the Young's modulus is expected to decrease significantly at temperatures higher than the glass transition temperature (T_g = 134.6 °C as estimated from dynamic mechanical analysis, see Appendix B).

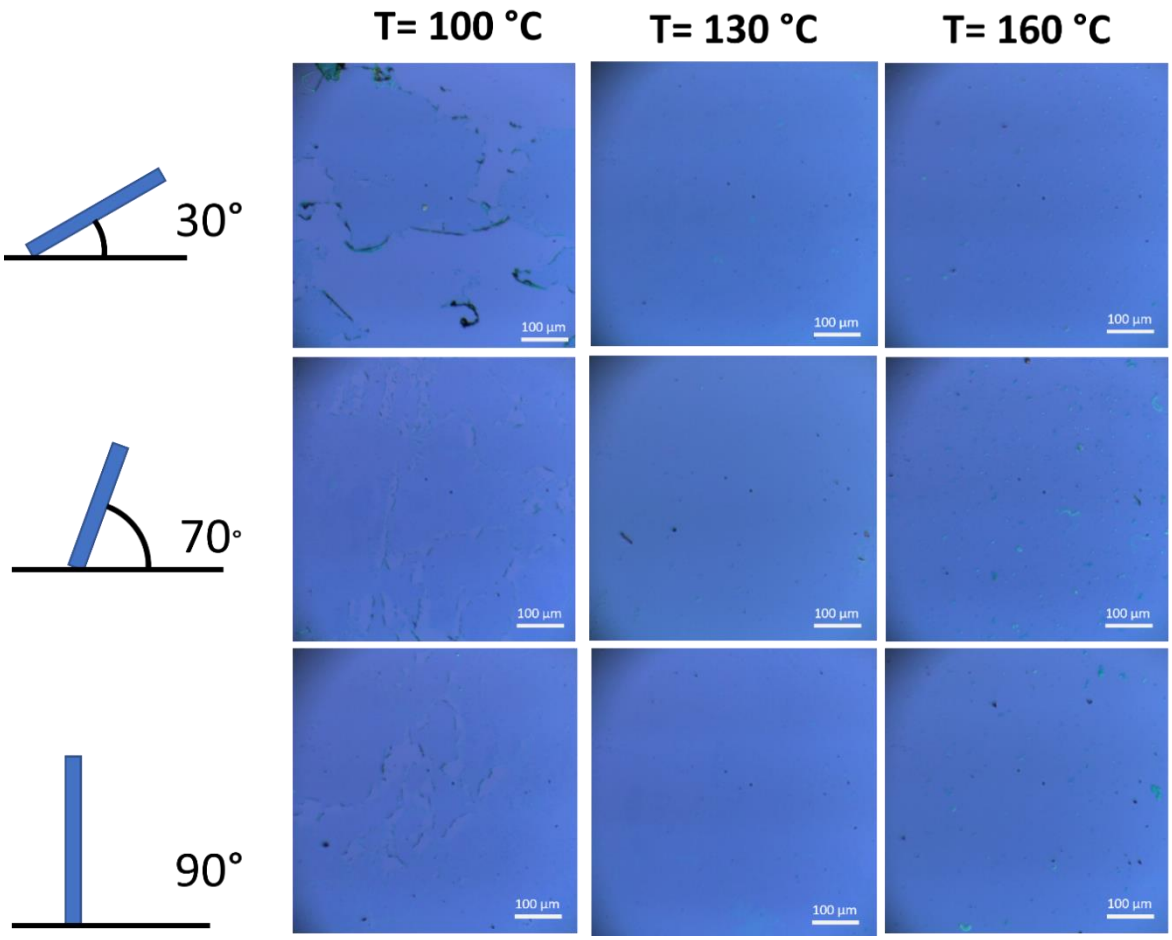

Figure 6.9 Graphene transferred on Si/SiO_2. Residual water was evaporated at different titling and temperature conditions.

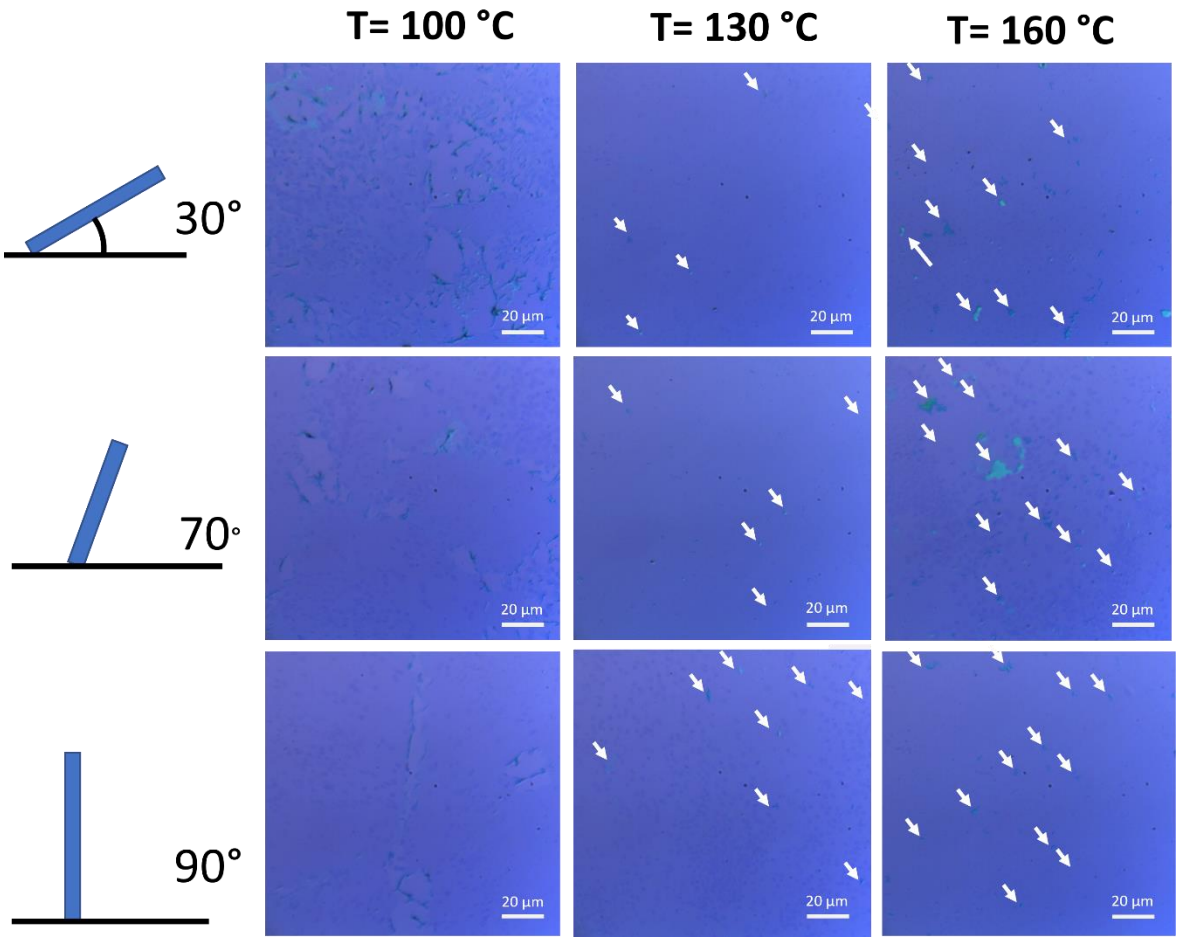

Figure 6.10 Optical images of the graphene on Si/SiO_2 at higher magnifications. White arrows show residual PMMA after dissolving the PMMA and rinsing with acetone.

Although the graphene film was transferred with few defects by annealing it at 130 °C or 160 °C, they showed differences in residual PMMA. Figure 6.10 shows that annealing the film at 160 °C significantly increased the amount of PMMA residues left. PMMA residuals pointed out with white arrows in Figure 6.10 have also been previously observed in other studies by optical microscopy.[367,368] This is also shown in Figure 6.11 from SEM images, where PMMA residues are pointed out with blue arrows. It has been experimentally demonstrated that annealing a graphene film with PMMA residues at 160 °C promotes its decomposition, which explains the significantly more residues left on the graphene surface.[369]

Figure 6.11 and Figure 6.12 show average images and the worst images obtained under the conditions mentioned. Figure 6.11 shows images with more defects under the different conditions mentioned. When annealing at 130 °C and a tilting angle of 30°, sporadic submicron holes appeared, presumably from micro-regions where water remained trapped

(this is more evident in Figure 6.12). This effect seems to be suppressed by increasing the tilting angle to 70° or 90°; even in the worst images, only sporadic defects were observed (Figure 6.12). It is important to highlight that samples annealed at 100 °C and tilted at 90° show areas fully transferred with no defects (Figure 5.11) as well as areas transferred with big cracks (Figure 6.12). Overall, annealing the film at 130 °C and tilting the sample in the range of 70 - 90° provides a balanced way for transferring graphene on Si/SiO_2 with few defects and minimal PMMA residues.

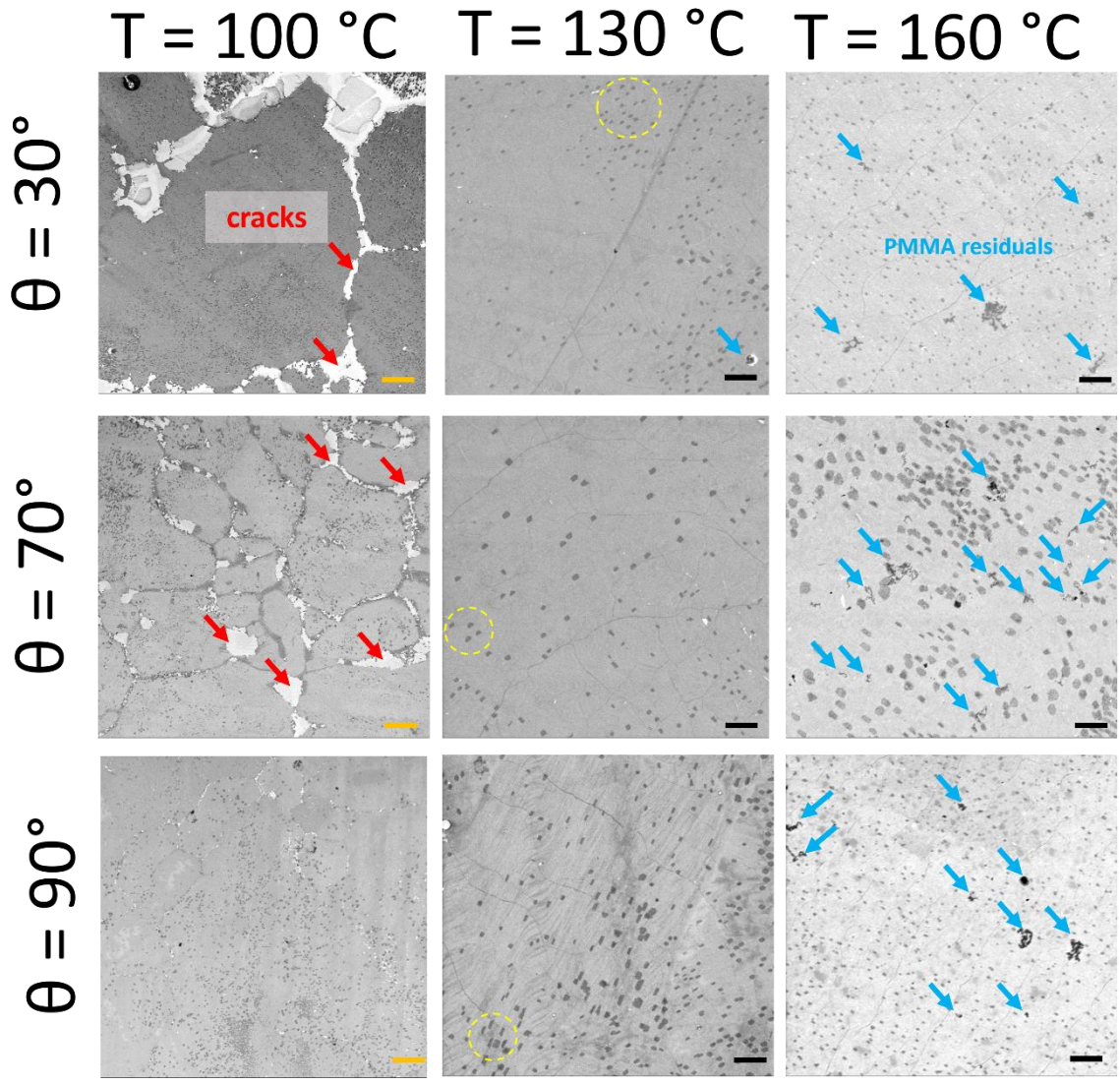

Figure 6.11 Average SEM images of the graphene transferred on Si/SiO_2. Blue arrows point out small residuals of PMMA. Red arrows point at cracks domains where graphene came off leaving voids. Yellow dashed circles show regions with graphene adlayers. The yellow scale bar is 40 μm, and the black scale bar is 10 μm.

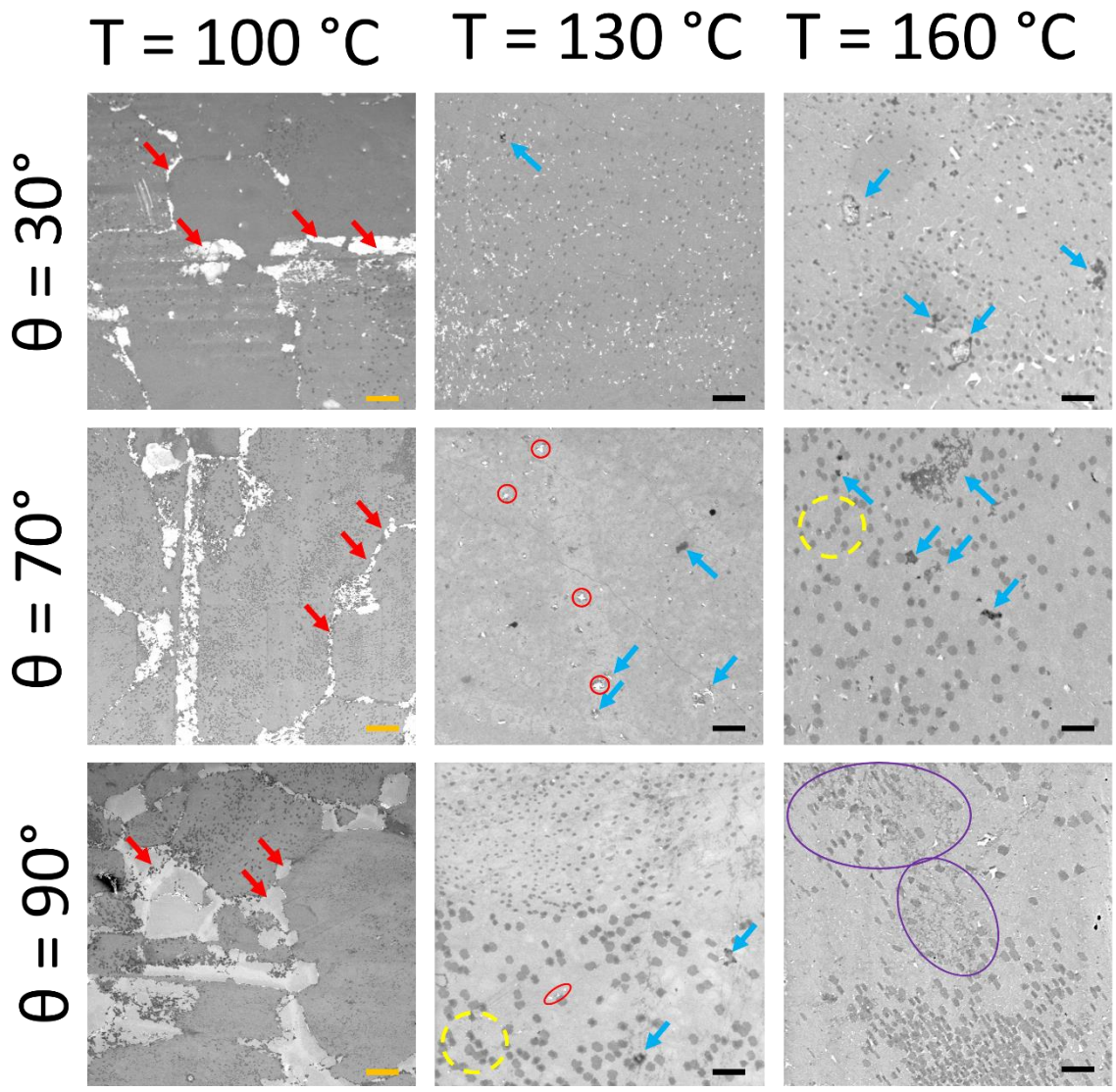

Figure 6.12 The worst images obtained from the graphene on Si/SiO_2.The yellow scale bar is 40 μm and the black scale bar is 10 μm. Red arrows point at cracks domains where graphene came off leaving voids. Yellow dashed circles show regions with graphene adlayers. Red circles enclose submicron holes, purple ovals highlight areas full of polymer residue, and blue arrows point out small residuals of PMMA.

Optical and SEM images are helpful to identify residues at the microscopic scale. However, it has been demonstrated the presence of residues at the nanometric scale on the surface of graphene.[114] Therefore, TEM and AFM observations would be more suitable to assess how free of residues graphene is at the nanometric scale. Also, it has been reported that replacing PMMA with poly bisphenol A carbonate (PC) is a better supporting layer than PMMA.[115] Considering that PC has a lower Young's modulus (E_m = 2.34 GPa) than PMMA and a similar permeability coefficient $P = 2.3 \frac{g \cdot mm_{film\ thickness}}{m^2\ day}$,[370] we adapted the transfer procedure from that of PMMA. Figure 6.13a and b show the polycarbonate film on a silicon

substrate and the thickness of it to be 346 nm. From Figure 6.13, the maximum h_0 allowable given a thickness of 346 nm. Full details of the transfer process for PMMA can be found in experimental Section 8.19c, which shows a TEM image from a sample transferred using PMMA, showing typical residues as those observed in SEM. A high-magnification image (Figure 6.14d) reveals a significant residual of PMMA. On the other hand, the sample transferred using polycarbonate proved to be cleaner on the micron scale (Figure 6.15d) and had a higher proportion of area free of polymer residue when compared to the one transferred using PMMA (Figure 6.14d). Also, AFM observations can provide information on the roughness of the sample, which is increased by the presence of residues and topography-related features such as wrinkles, bubbles and cracks.[106] By comparing AFM images from the two transfer processes (Figure 6.14 and Figure 6.15), the PC transfer process showed a less rough surface (RMS = 1.75 nm) than that for PMMA (RMS = 2.15 nm). Figure 6.14 and Figure 6.15 illustrate typical height profiles from the corresponding AFM images for PMMA and PC transfer processes, respectively, showing that PMMA has a topography with more kinks from wrinkles and residues. On the other hand, the process corresponding to PC shows a flatter profile with less pronounced wrinkles. Figure 6.16a shows the electrical sheet resistance for both PMMA and PC optimized transfer processes. The average sheet resistance for films transferred using PC was 737 ± 85 Ω/sq and 1016 ± 219 Ω/sq when using PMMA. Therefore, PC instead of PMMA is a better supporting material for a cleaner transfer process.

It was compared the transfer process using PC with graphene transferred on Si/SiO_2 from a commercial brand (Figure 6.17). Optical and SEM images showed no apparent residuals; however, TEM images showed the presence of residual polymer in both cases. Roughness measurements from AFM showed that RMS values are comparable, 1.45 nm for the commercial brand and 1.75 nm for the sample transferred using PC. All the samples under test were done using pieces of 1 × 1 cm^2, but it can be used to transfer larger areas up to 2 × 2 cm^2 (Figure 6.16b).

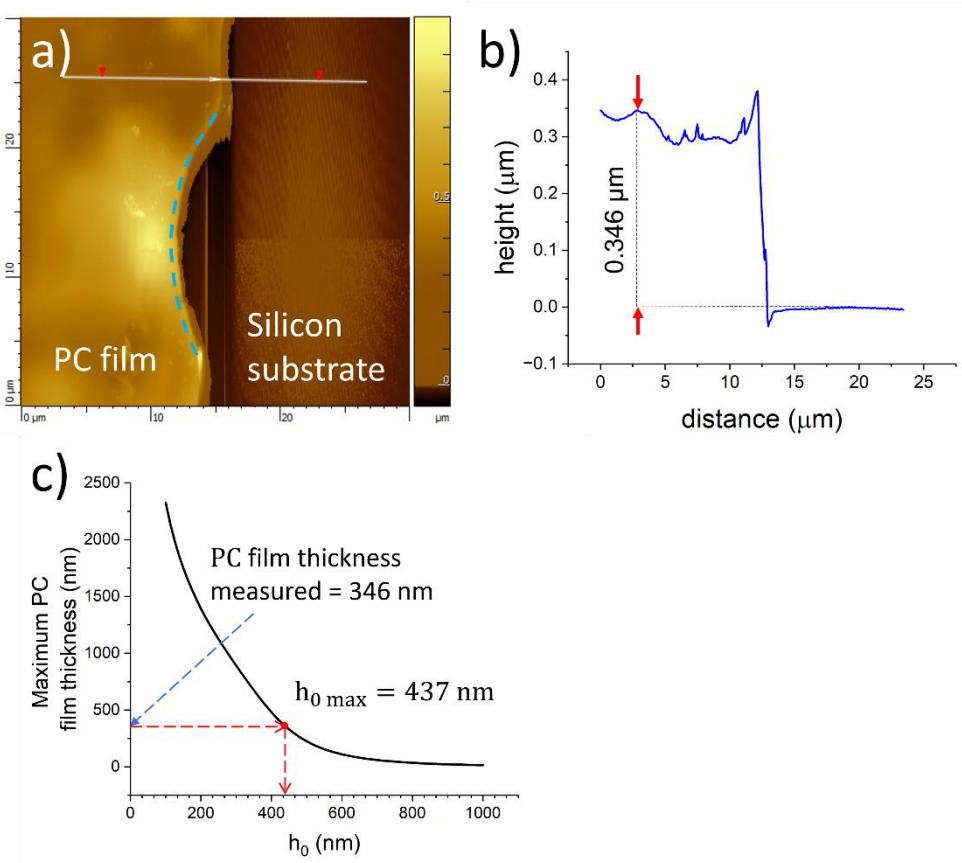

Figure 6.13 a) AFM image of a polycarbonate film on a silicon substrate b) Profile of the thickness of a PC film deposited on a silicon substrate. The dashed blue line represent a part of the film that came off as a result of the sample preparation c) Graphical solution of the model relating the maximum PC film thickness and average h_0.

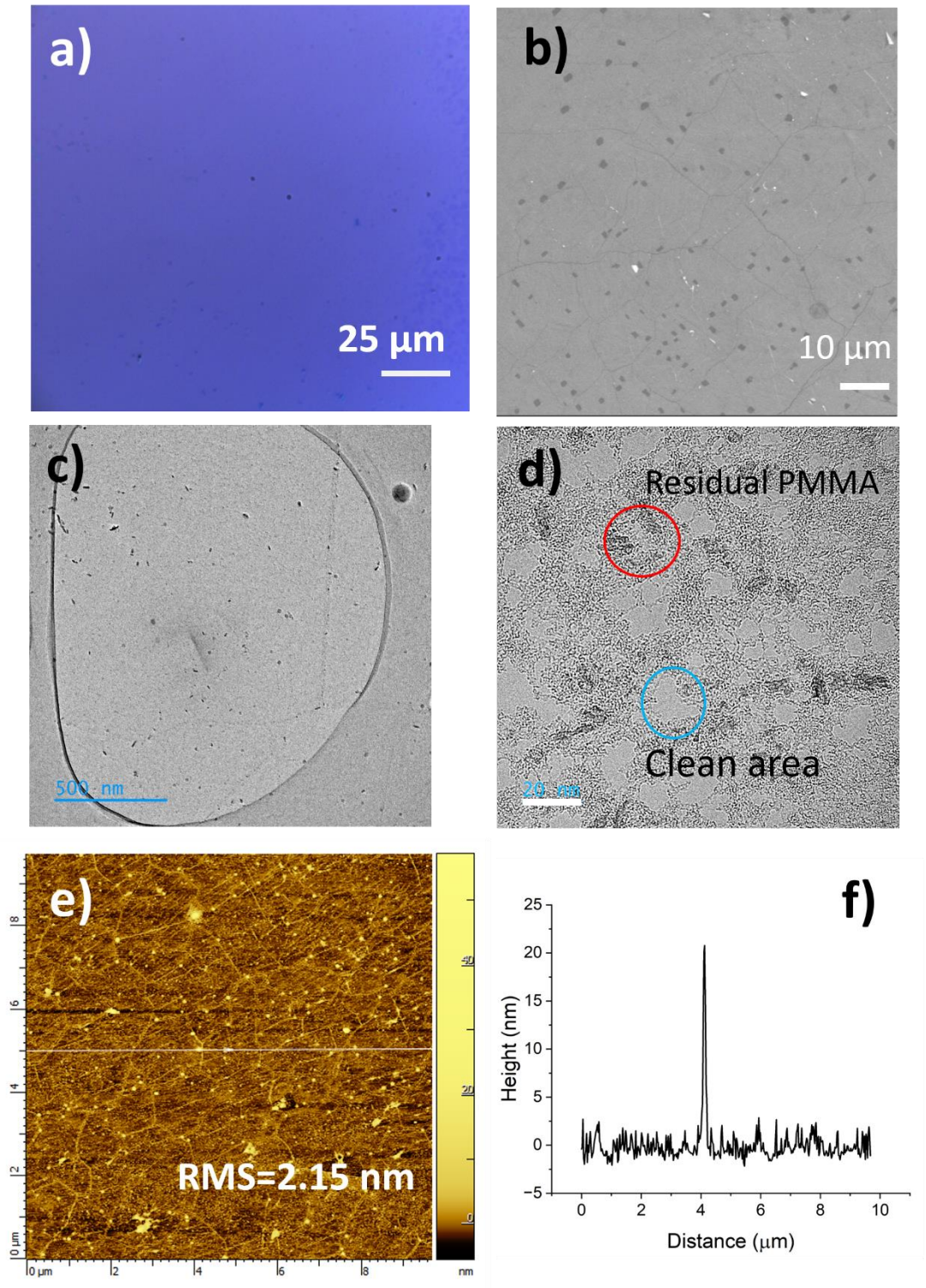

Figure 6.14 Typical images from the transfer process using PMMA annealing at 130 °C and tilting at 70°: a) Optical, b) SEM,c,d)TEM and high magnification TEM (scale bar = 20 nm), e) AFM and f) Profile along the line in e).

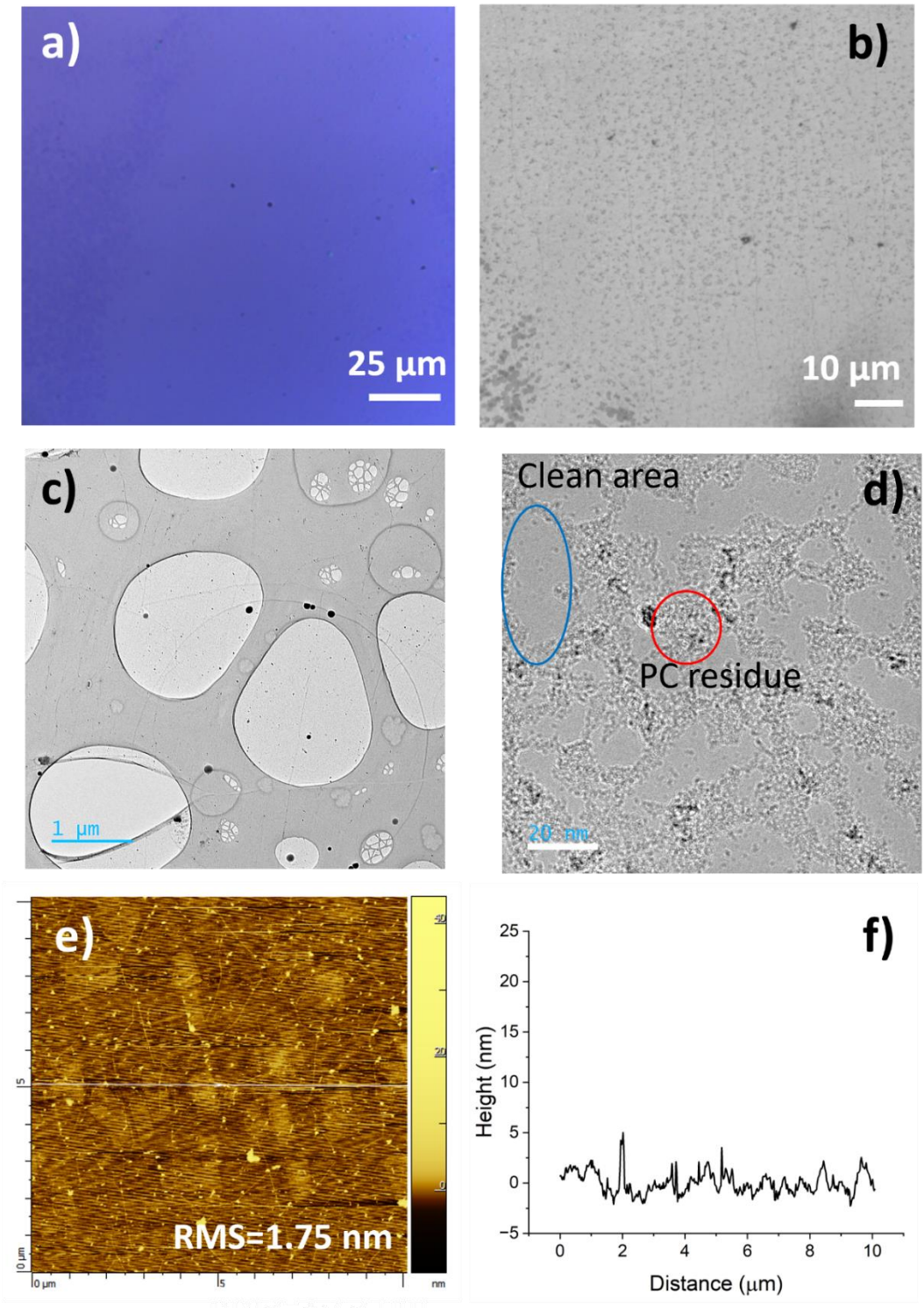

Figure 6.15 Typical images from the transfer process using poly bisphenol A carbonate (PC) annealing at 130 °C and tilting at 70°: a) Optical, b) SEM, c,d)TEM and high magnification TEM (scale bar = 20 nm), e) AFM and f) Profile along the line in e).

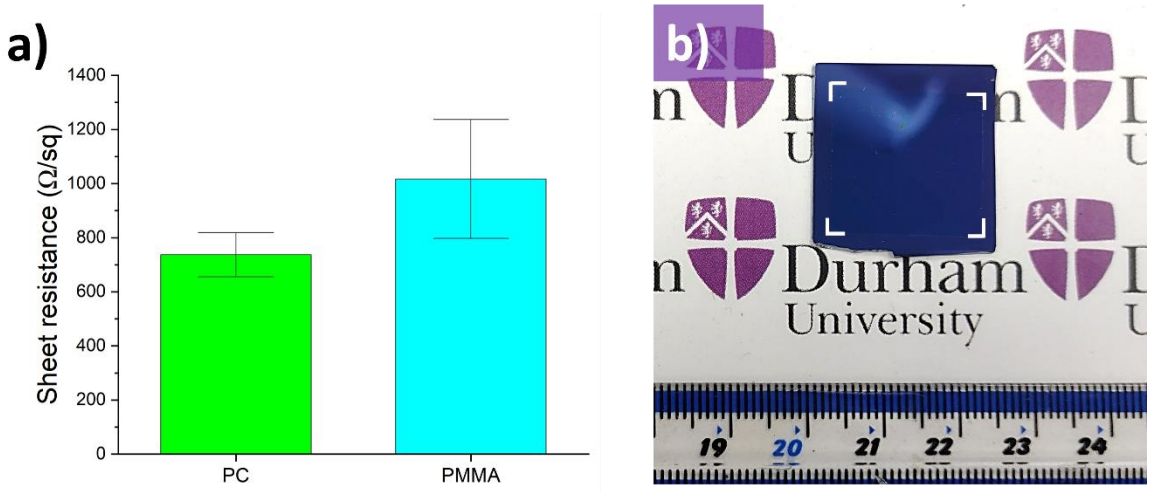

Figure 6.16 a) 2 x 2 cm^2 of graphene transferred on Si/SiO_2 using PC b) comparison of the sheet resistance measurements for PMMA and PC transfer process.

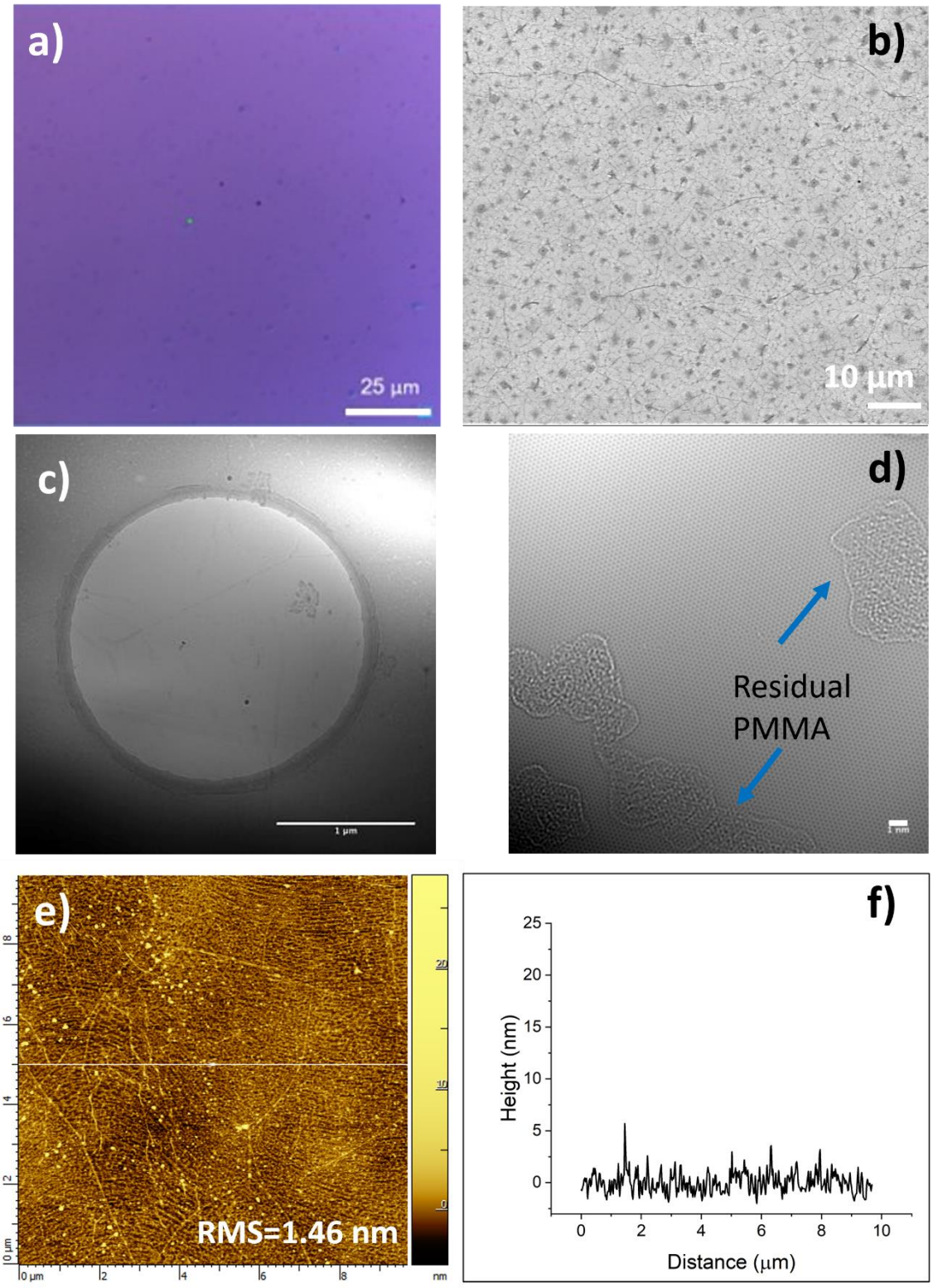

Figure 6.17 Typical images from a commercial graphene sample on Si/SiO_2. a) Optical image b) SEM, c,d)TEM and high magnification TEM (scale bar = 1 nm), e) AFM and f) Profile along the line in e) Note: Images c and d were reproduced from the webpage of the same supplier (https://www.graphenea.com/collections/graphene-tem-grids). Images a,b) and e) are from the analysis in this work from the sample of graphene on Si/SiO_2 supplied from Graphenea.

6.2.3 Graphene transfer on soft substrates for wearable electronics

One of the key elements to improve the signal-to-noise ratio is having a highly conductive element such as graphene, which has a high charge carrier density. Although rigid commercial Ag/AgCl have good conductivity, they cannot fulfil a wearable function, while flexible or stretchable electrodes show lower conductivities.[371] Another requirement is the conformal contact between the electrode and the skin, which can be achieved by controlling the thickness of the electrodes or tailoring their mechanical properties. Graphene is a material with atomic thickness and outstanding electrical properties. It can be supported on a polymeric material whose thickness can be controlled. Therefore, it provides a way to make electrodes for electrophysiological sensing.

The contact between the electrode and the skin can be represented by the most straightforward model (Figure 6.18), where the skin is represented by an RC component corresponding to the epidermis (R_{Ep} and C_{Ep}) and a resistive component corresponding to the dermis (R_D), which are fixed parameters. The contact between the skin and the electrodes can also be represented by an RC component where the resistive part (R_C) represents the contribution from all areas in direct contact with the skin. On the other hand, the capacitive part (C_c) accounts for those regions where an air gap is formed due to the imperfect contact of the electrode with the skin. Therefore, when the electrode fully conforms to the skin, the overall electrical impedance is decreased.[372]

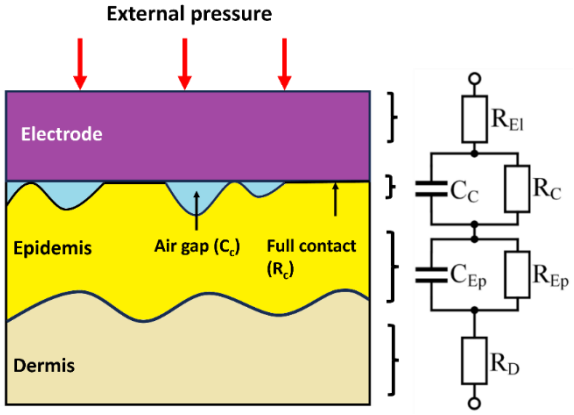

Figure 6.18 Electrical model of an electrode/skin system where the contact is imperfect, forming air gaps. The model was adapted from reference 372.

As preliminary experiments, first, graphene was transferred to commercial EVA/PET laminating pouches having 80 μm thickness. This procedure was the simplest one as it provided a thick enough material for the electrical contacts. Moreover, the EVA (ethyl vinyl acetate) is a soft and elastic material as given by their small Young's modulus (150 MPa) and high elongation at break. It means that EVA film can deform upon applying light pressure, providing better electrode contact to the skin.

The graphene-EVA/PET electrode preparation is briefly described, and full experimental details are given in Section 8.21. First, graphene was laminated in an office laminator, the copper was etched in 1M $FeCl_3$, and the film was washed three times in deionized water. Figure 6.19b shows the network formed by silver nanowires (AgNWs) on graphene/copper once transferred to EVA/PET substrates. Figure 6.19a shows that even when graphene was conductive, the variation in the sheet resistance was considerably high. Such variation can be a side effect of lamination, as compression strains in the graphene film defects can induce cracks and their propagation. Laminating two layers of graphene reduced the variation; however, it made the process more complicated. An attractive way is to encapsulate silver nanowires (AgNWs) between graphene and the EVA/PET substrate. Encapsulation was done by spin-coating AgNWs on the graphene on copper before lamination. Thus, this process provided a more balanced and practical solution in terms of reduced variation.

The electrodes were assessed according to the impedance measurement on the skin and its ability to capture ECG signals. Briefly, electroimpedance measurements were done using a potentiostat in a 2-wire configuration and a scan range of 1 - 10^6 Hz. The set up is similar to that shown in Figure 6.22b. On the other hand, electrocardiogram (ECG) signals were collected using a Ganglio board from OpenBCI and raw signals were processed using a fourth-order Butterworth filter from 5 - 50Hz as implemented in Origin Lab.[267]

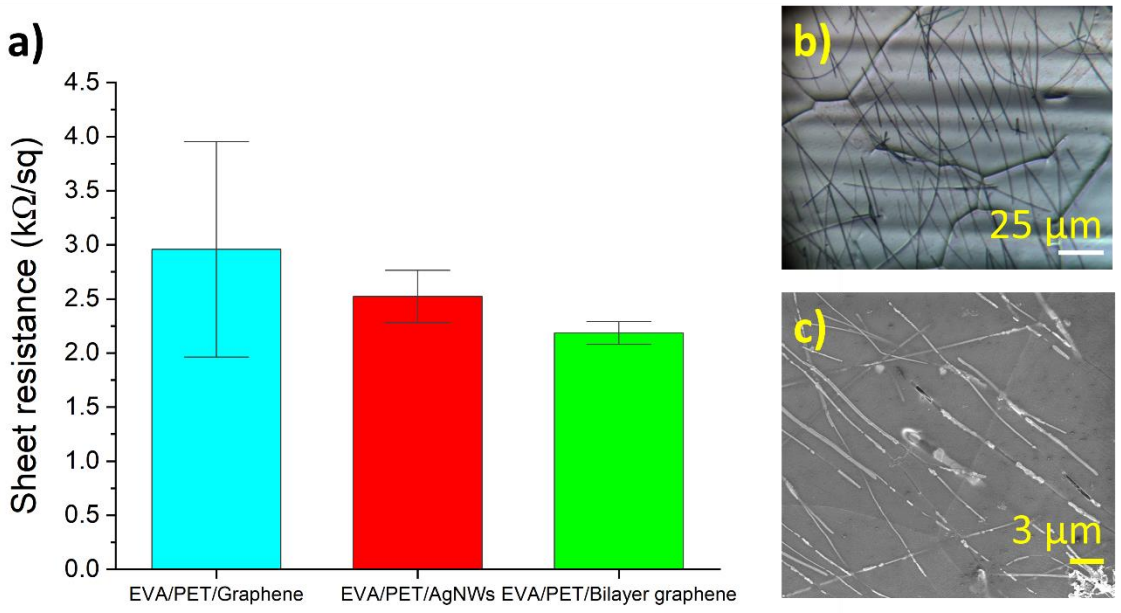

Figure 6.19 Sheet resistance values for graphene supported on EVA/PET using a single layer, encapsulated AgNWs and two graphene layers. b) Optical image of graphene on copper covered with AgNWs. c) SEM image of AgNWs encapsulated between graphene and EVA/PET film

Figure 6.20 shows that the graphene laminated on EVA/PET with and without AgNWs showed similar impedance responses. The ECG signals collected looked very similar but clearly showed the QRS component. To highlight the importance of conformality, strips of aluminium foil and conductive copper tape were used as electrodes. While aluminium is very conductive, copper tape has a conductive adhesive, and both are considerably stiff and thick. As observed from Figure 6.21a, measurements have a considerable amount of noise below 4000 Hz, highlighting the role of conformability.

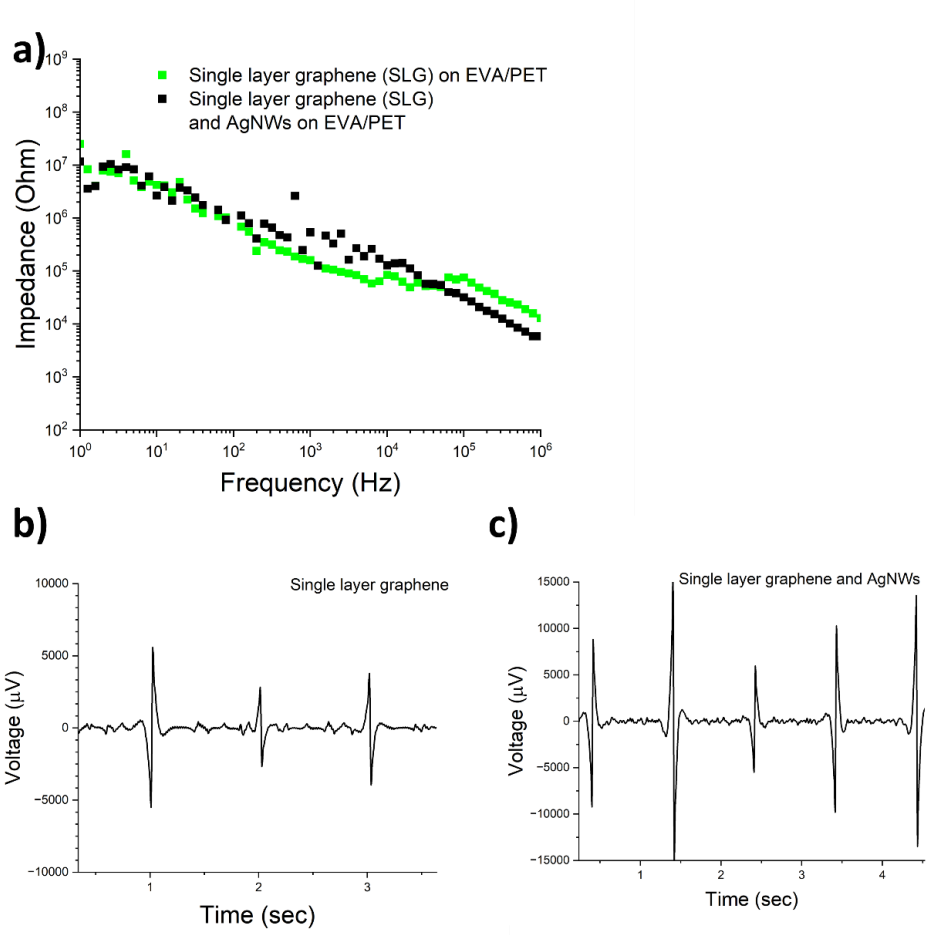

Figure 6.20 a) Frequency sweep response of the impedance of single-layer graphene (SLG) and graphene/silver nanowires(SLG/AgNWs) supported on EVA/PET substrates and ECG signals collected from b) EVA/PET/SLG and c) EVA/PET/SLG/AgNWs.

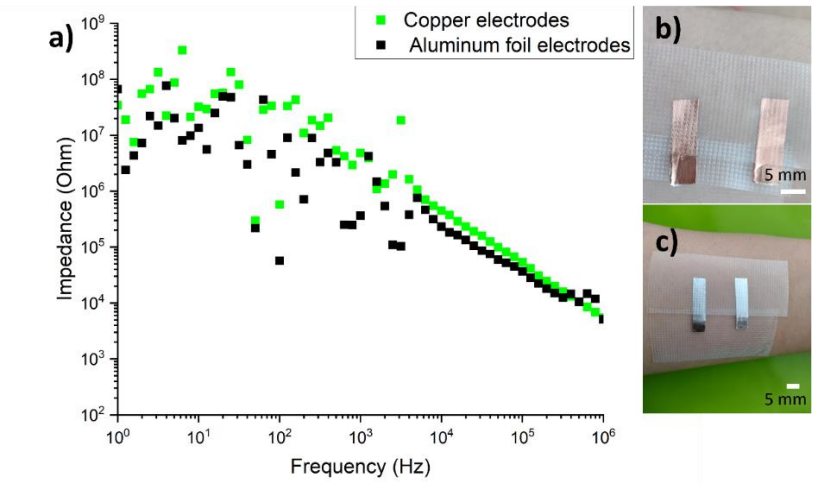

Figure 6.21 a) Impedance frequency sweeps measured on the forearm using b) conductive adhesive copper tape strips and c) aluminium foil strips held by adhesive tape to ensure the best contact.

6.2.3.1 Graphene-based temporary tattoos

<u>Ethical Disclaimer and Risk Assessment:</u> Please refer to Section 8.22.2 for full assessment and justification on risk assessment associated with these following sections.

Following the conformability analysis described in Section 6.2.3 it is expected that by tailoring the thickness of the supporting PMMA, full adhesion of the graphene can be achieved, diminishing the contribution from air gaps where the electrodes are detached. While EVA/PET electrodes rely on tape to hold the electrodes, using submicron-thickness electrodes can also lead to more wearable devices whose use can be expanded in principle to the design of skin-based sensors. For this section, ECG measurements will be used to assess the performance of submicron-electrodes where AgNWs were added to improve the stability of the electro-impedance response.

To transfer the PMMA/graphene film onto the skin, first, it is necessary to have it on a suitable substrate like temporary tattoo paper. It consists of a sub-micrometric film of polyurethane/allyl resin attached to a paper sheet through a sacrificial water-soluble PVA layer. When moistened, the resin film loses its tackiness and can slide onto the skin, transferring the tattoo effectively to the skin.[373] This material has become popular for developing on-skin sensors for various sensing applications such as pH and detecting analytes such as sodium ions, ammonium, lactate, and glucose, to name a few.[374] In this work, we will use temporary tattoo paper to transfer thin PMMA/graphene films that can be used to collect ECG signals.

Briefly, graphene-based tattoos were made as follows. First, graphene on copper (2×2 cm^2) was coated with a thin layer of PMMA. The copper was etched in a 1 M ferric chloride solution (Figure 6.22a). The film was fished out on a piece of Kapton film and transferred on tattoo paper. The PVA film was previously removed in water, so the graphene faces up on the tattoo paper/PMMA/graphene stack (Figure 6.22b). It was cut into four equal strips of 0.5×2 cm^2 that were used for transferring onto the skin. Before making measurements, a piece of Tegaderm was used to isolate the contacts from the skin, so the signal acquired only corresponded to the effect of graphene. The contacts were made of Au/Pd sputter-coated tape and conductive copper tape to reduce the noise from measurements. This way, the alligator clips did not scratch the surface of the tape, while on

the opposite side, Tegaderm/Au/Pd tape would be thin enough so the graphene/PMMA would not break. More details are given in Section 8.22.

Figure 6.23 shows that the impedance response is more stable over the whole range of frequencies when compared to the response of EVA/PET based electrodes, even if only a single layer is present. Furthermore, adding a thin layer of silver nanowires promotes a higher stability of the electrodes, like commercial electrodes, over the whole range of frequencies. Figure 6.23 also shows the ECG signals, revealing that the PQRST segment is distinguishable just as in commercial electrodes, and it can capture more details from the signal than the corresponding electrode with just one single layer of graphene.

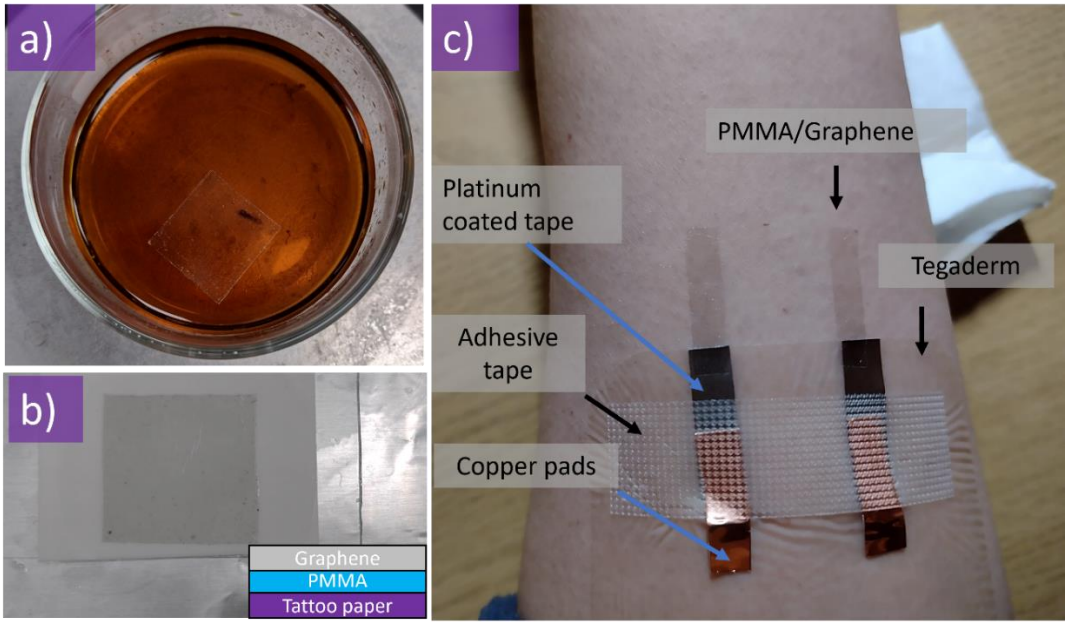

Figure 6.22 a) Graphene on copper square (2 x 2 cm^2) etching in 1 M Ferric chloride b) PMMA/graphene on tattoo paper c) Typical setup for impedance measurements.

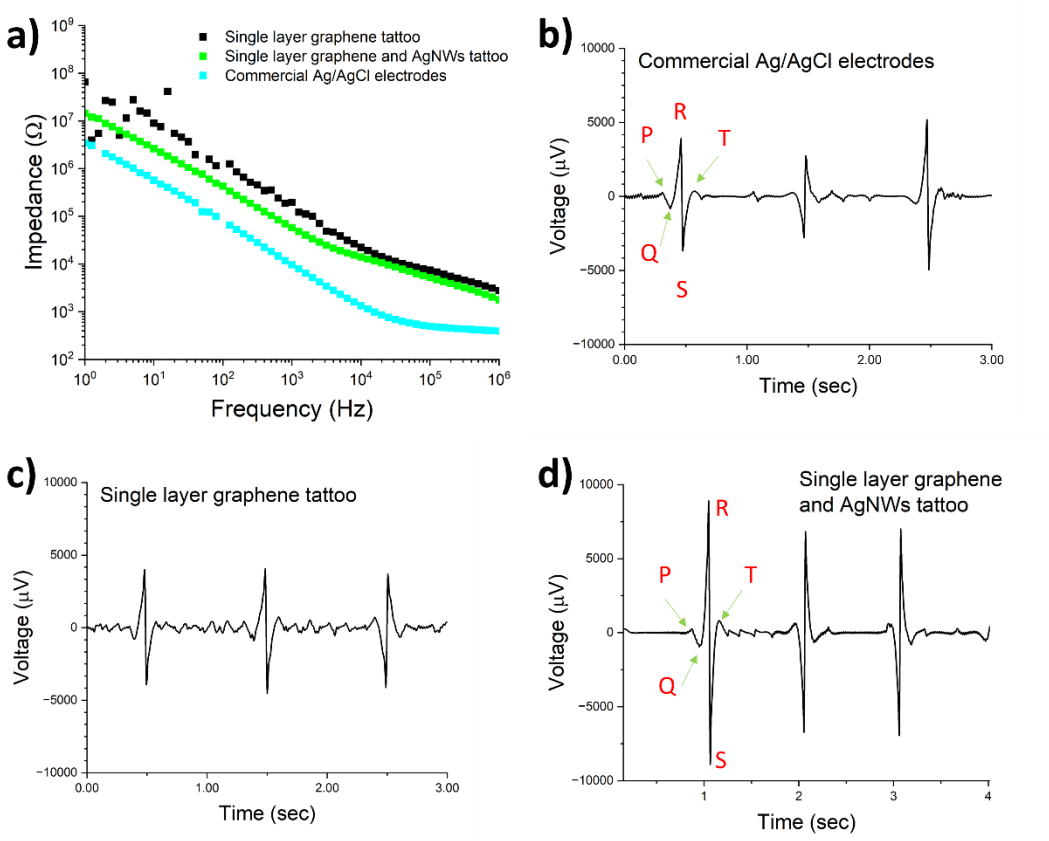

Figure 6.23 Comparison of the frequency sweep impedance response and their corresponding ECG signals acquired for a) commercial electrodes, b) single-layer graphene tattoos and d) single-layer graphene and AgNWs tattoos.

The model described in Section 6.1 can be numerically solved using MATLAB[364] to estimate the PMMA film's maximum thickness to achieve complete skin conformability. The parameters used are given in Table 6.1. Since the PMMA/graphene stack is transferred in wet conditions and the skin transpires moisture, $\gamma_{skin/tattoo}$ can be approximated as twice the surface tension of water $2\gamma_{water} = 0.14$ J/m^2. A value of 0.21 J/m^2 for the adhesion of silicone membranes to the skin has been reported, making our assumption reasonable.[375] Figure 6.24c shows the graphical solution so that for a thickness of less than 450 nm, the PMMA/graphene films will fully adhere to the skin ($x_c = 1$). The thickness of the PMMA film measured by AFM was around 415 nm (Figure 6.7b), which guarantees the full adhesion of it, explaining in part why tattoos behave better than thicker electrodes.

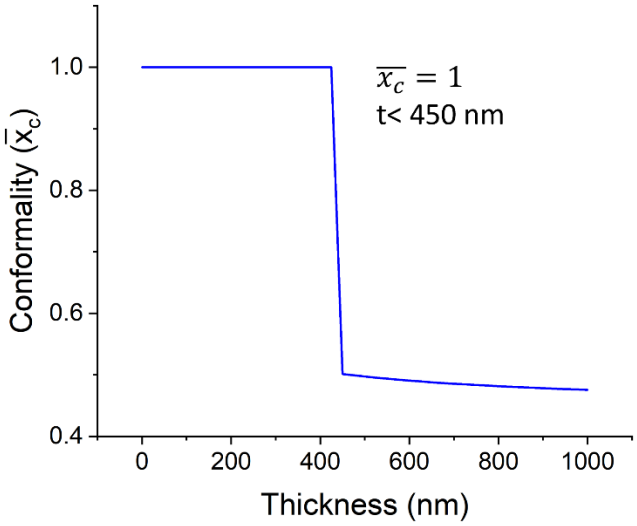

Figure 6.24 Graphical solution for maximum PMMA thickness to reach full conformality $\overline{x_c}$=1.

Table 6.1 Parameters used as input for the conformability model.

Parameter		Reference
Skin roughness	λ=250 μm h_0=20 μm	354,376
Skin in plane Young's modulus	E_s=100 kPa	377
work of adhesion	$\gamma_{skin/tattoo}$= 0.14 J/m^2	
PMMA Young's modulus	E_m=3.2 GPa	378

6.3 Conclusion

Chemical vapour deposition has become the most popular method for growing high-quality single-layer graphene, but it is grown on a metal catalyst such as copper. Therefore, a transfer step is unavoidable and not trivial since it must be in contact with a substrate depending on the desired application. For example, graphene must first be transferred onto a flat Si/SiO_2 chip to develop next-generation chips. However, graphene must be transferred onto a soft and rough substrate for developing neural interfaces. Hence, a common aspect of these two examples is that graphene must adapt to the shape of the substrate; that is, it must conform to the topography of the substrate. In this work, a conformality approach was applied to transfer graphene onto a flat substrate, such as Si/SiO_2 and onto a rough substrate, such as the skin.

Using PMMA as a supporting layer is the most popular method for transferring graphene onto Si/SiO_2 and is used by enterprises. Moreover, the PMMA film will adopt the topography of the copper substrate, which has a roughness in the submicron range, while Si/SiO_2 has a roughness of a few nanometers. So, the success of the transfer process will rely on the ability of the PMMA film to adapt to the shape of the flat substrate. In this procedure, graphene is supported by a PMMA film while floating in a water bath. In the next step, graphene is picked up using a Si/SiO_2 substrate, leaving a thin layer of water trapped. The model described here relies on the balance between the adhesion energy between the graphene and Si/SiO_2 and the elastic energy stored by the membrane. A consequence of the model developed here is that the flatter the copper substrate is, the more it will conform to the Si/SiO_2. Otherwise, given an average roughness on the copper surface, there will be a maximum thickness of the PMMA film to conform fully to the Si/SiO_2. Most commonly, the PMMA/graphene film is heated at high temperatures, creating high-pressure zones and causing holes and tears in the film. Because there are regions on the copper where graphene growth is incomplete, the PMMA/graphene can transpire water. It was found that gentle heating removed most of the excess water, and adhesion improved if it was followed by heating at a high temperature due to a combined effect of reducing Young's modulus of PMMA and removing the remaining water. Moreover, tears and holes are significantly reduced if samples are tilted.

In summary, to succeed in transfer, the water trapped must be removed in two steps: gently heating ~37 °C for 30 minutes followed by annealing at 130 °C and the sample tilted

> 70°. Overall, the graphene transfer proved to be competitive compared to graphene acquired from a commercial brand in terms of cleanness and coverage. Based on previous research, it has been suggested that using polycarbonate instead of PMMA left less residuals. Applying the same procedure proved that complete transfer was achieved, and a cleaner graphene surface could be obtained according to TEM observations.

Similarly, PMMA/graphene can be transferred onto rough substrates such as the skin. In this case, the roughness of the skin is bigger than the PMMA/graphene, and the substrate can also store elastic energy. In this case, the PMMA film should not exceed a maximum thickness to achieve full conformity to the skin. From a general perspective, novel applications of graphene rely on the conformal contact of graphene, such as the development of on-skin chemical sensors and neural interfaces. This approach can provide guidelines for selecting the supporting polymer layer and the maximum thickness given the roughness of the substrate.

7 Conclusions and Outlook

In this work, graphene oxide, one of the most popular precursors of graphene, was synthesised. Using a cross-flow filtration system avoids some of the problems associated with the purification process of graphene. For example, membrane filtration is limited because graphene oxide forms a gel at high concentrations, clogging the membrane pores. On the other hand, dialysis is limited by the amount of graphene and the prolonged time (typically a week) it takes. In cross-flow filtration, graphene oxide solution flows tangentially across the hollow fibre, preventing the membrane from blocking. Even when the primary goal of using a cross-flow filtration system was the removal of residual manganese ions, we found that the average lateral size was 16.2 ± 1.7 μm and 70 % of graphene oxide flakes had a thickness equal to or less than 1.4 nm, which is consistent with reported values of monolayer graphene oxide. We attributed this effect to the shear forces caused by the flow of graphite oxide inside the tube. Moreover, reduction of the lateral size of graphene oxide was possible using brief sonication times (up to 2 minutes).

The graphene oxide was used to synthesise reactive graphene nanoparticles. First, graphene was thermally reduced to partially restore its electrical properties and functionalised with a silane coupling agent to enrich the surface with epoxy groups. This was followed by grafting polystyrene chains through a ring-opening reaction. The reactive nanoparticles were introduced in an immiscible blend (PS/PLA) that formed a double-percolated network and was used as a scaffold for localising the reactive graphene at the interface. It was demonstrated by TEM observations and rheoimpedance measurements that a network formed along the interface of the polymer blend. Moreover, the polymer blend was shown to be stable under thermal annealing, demonstrating the ability of the reactive graphene to stop the phase separation of the polymer blend.

Since the reactive graphene remains stable at the interface, the mechanical properties of the blend are expected to be improved. Therefore, tensile strength measurements are suggested to test the mechanical performance of the blend. Also, since reactive graphene is demonstrated to stabilise the morphology of the bicontinuous blend, it creates a scaffold for other particles to form a percolated network. It opens the possibility to include more conductive particles, such as multi-walled carbon nanotubes or highly reduced graphene, which can create a conductive network in the PLA domain. For example, from our

observations, we know that when adding 3 wt% of reactive graphene to the blend, the PLA domain has an average $d_{PLA} = 5.7 \pm 0.5$ μm, so adding carbon nanotubes with an average length the same magnitude a d_{PLA} could be a potential route to make highly conductive polymer composites. Although this concept has been demonstrated to work in principle, further investigation is needed on the applicability to other polymer blends and devising more straightforward ways to functionalise the graphene to make the process more attractive for scale-up.

This work also explored the transfer of graphene grown by chemical vapour deposition onto substrates with different roughness. Here, it was considered that the conformal contact between graphene and the substrate was crucial for developing a method to transfer it onto Si/SiO_2 and develop conformable electrodes for on-skin applications. In the model described here, the elastic energy stored by the polymer films must be compensated by the energy of adhesion between the graphene and the Si/SiO_2. We concluded that the transfer of graphene onto a flat substrate such as Si/SiO_2 using PMMA as a supporting layer was governed by the thickness of the supporting polymer film and the roughness of the copper substrate. Therefore, the flatter the copper substrate is, the more it will conform to the Si/SiO_2. It also implies that given an average roughness of the copper substrate, there will be a maximum thickness for the supporting polymer film beyond which full conformality will not be possible.

A very common problem when transferring graphene onto Si/SiO_2 is the formation of holes, cracks, and tears, which originate from residual water trapped between the graphene and the Si/SiO_2 when picking up the sample from the water bath. It was found that excess water could be removed by gently heating the sample at 35 - 37 °C, which was explained by the permeability of the supporting polymer and the incomplete stitching of the graphene domains. Moreover, tears and cracks are significantly reduced when samples are annealed in a tilted position, as it improves the adhesion. Using PMMA is the standard methodology to transfer graphene onto Si/SiO_2, and even when polycarbonate has been suggested as a cleaner alternative, it is not widely used. Here, we applied the same procedure to transfer onto Si/SiO_2 using polycarbonate instead of PMMA, and it was proven to be a cleaner method in terms of residual polymer and exposed area of graphene, as observed from SEM and TEM images.

This conformality concept can also be applied to rough and compliant substrates such as leather substrates or skin. From a mathematical point of view, a new term needs to be introduced to account for the elastic energy stored by the substrate. Similarly, the model gives an estimate of the maximum thickness of the film so full conformality can be achieved. In this work, we considered conformal graphene electrodes as a starting point to develop on-skin sensors for future work. For example, it has been found that some metabolites present in blood, such as glucose and lactate, correlate with the concentration of these metabolites in sweat. As an example, cortisol detection in real-time is a current topic of research since it is associated with anxiety, depression, and cardiovascular diseases. All these applications could benefit from graphene as it offers an interesting alternative for conformal between the sensor and the skin. Also, the functionalisation of its surface can enable it to selectively detect a wide range of biomarkers, with the goal of monitoring them in real-time in a non-invasive way.

8 Experimental details

8.1 Materials

All chemicals used in the synthesis process were used without further purification. Sulfuric acid (98 %, Fisher Scientific), phosphoric acid (85 %, Fisher Scientific), hydrochloric acid (37 %, Fischer Scientific), hydrogen peroxide (37 %, Sigma Aldrich), diiodomethane (99 %, Sigma Aldrich), hydrazine monohydrate (98 %, Sigma Aldrich), graphite flakes (99 %, 325 mesh, Sigma Aldrich), graphene nanoplatelets (XG Sciences, grade M5), (3-Glycidyloxypropyl)trimethoxysilane (98% Sigma Aldrich), dry N,N-Dimethylformamide (99.8 % Fisher Scientific), styrene (99.9 % Sigma Aldrich), 2,2,6,6-Tetramethyl-1-piperidinyloxy (TEMPO 98%, Sigma Aldrich). 4,4′-Azobis(4-cyanovaleric acid) (98% Sigma Aldrich). Methanol (AR for analysis, > 99.8 %), dibenzylamine (97% Sigma Aldrich), ferric chloride anhydrous (> 99.9 %, Alfa Aesar), chloroform (99 %, Fischer Scientific), polybisphenol A carbonate (M_w = 45 000, Sigma Aldrich), polymethyl methacrylate (M_w ~ 120 000), polystyrene (M_w ~ 192 000) and polylactic acid (GoodFellow).

8.2 Synthesis of Graphene oxide

The procedure has been previously reported in the literature[2] with a few modifications, as it will be explained next. Typically, a 9:1 mixture of concentrated H_2SO_4/H_3PO_4 (360:40 ml) was added to 3 g of graphite flakes and stirred a few minutes in a three neck round bottom flask and a thermometer was coupled to one of the necks. Then, 18 g of $KMnO_4$ were added slowly. The mixture was stirred for 30 minutes at room temperature, after which it was immersed in an oil bath. The temperature was increased in steps of 2 °C/5 min to keep control of the exothermic reaction and avoid overheating. Once the reaction flask had an inner temperature about 58 - 60 °C, it was left to react for 12 h. Then, the reaction was cooled to room temperature and poured onto 400 ml of ice and 8 ml of H_2O_2 (37% vol/vol) to quench the reaction and was left until it reached room temperature. The mixture was split in two equal volumes and centrifuged at 4000 rpm for 30 minutes to remove most of the residual acid and manganese ions. This step was repeated two times more, adding 500 ml of deionized water and 5 ml of H_2O_2 (37% vol/vol) each time and stirring for 30 minutes before centrifuging again. Next, the sample was transferred to a

conical flask and the solution was treated with a 10 vol% HCl solution to solubilize residual manganese ions. This solution was passed through a cross-flow filtration system and water was constantly added to keep the volume of the solution constant. The flow rate was fixed at 50 ml/min. The workup procedure finished once the pH from the permeate was ~6.5-7.0. To calculate the concentration of the graphene oxide solution, 3 ml were freeze-dried, and the remaining solid-like sponge was weighted. It was repeated 3 times, and the average value was reported as the concentration of the solution. Typically, the values obtained were in the range of 7.5 - 8.5 mg/ml.

8.3 Sample preparation for SEM and imaging details

A scanning electron microscope (Zeiss 360 VP) was used for imaging. Using an in-lens detector, the accelerating voltage was 5 kV and the working distance was 6 mm. Samples of graphene oxide for SEM imaging were deposited in a Langmuir-Blodgett setup to avoid overlapping of flakes, and distinguishing them individually. This procedure was also used for sample preparation for AFM imaging, and it is described next. A solution of 0.1 mg/ml of graphene oxide in deionized water was prepared. The solution was vigorously agitated using a vortex mixer. To prepare a uniform film and avoid overlapping of the flakes, samples for SEM were deposited using the Langmuir-Blodgett trough. The solution was added drop by drop on the trough, and the film was compressed at the rate of 20 cm^2/min until it reached a pressure of 5 mN/m. This pressure was kept constant through the deposition process. Then, a piece of silicon (0.5 × 1.5 cm^2) was lifted up at the rate of 2 mm/min. The sample was dried on a hot plate at 80 °C for 5 minutes and kept for further characterization. **Note**: Values with errors in image Figure 4.6f and Table 4.2 were calculated using the 95% interval confidence.

8.3.1 Preparation of Si/SiO_2 substrates

Before using the substrates, they were put into a 50 ml glass beaker with isopropanol, cleaned for 5 minutes using a bath sonicator, rinsed with fresh isopropanol and dried with a nitrogen gun.

8.4 Sample preparation for TEM and imaging details

TEM imaging was done using a JEOL 2100F FEG TEM operating at 200 kV. A solution of 0.01 mg/ml of graphene oxide was prepared in deionized water and one drop was deposited on a 300-mesh holey carbon TEM grid. The sample was left to dry overnight and kept for further analysis.

For CVD graphene samples, the procedure stated in Section 8.19 was followed to etch the copper and to wash the PMMA/graphene film, but when it was floating on the last deionized water bath, it was taken out on a holey carbon TEM grid.. It was left to dry overnight at room temperature before dissolving the protective polymer film in an appropriate solvent: acetone for PMMA and chloroform for PC.

8.5 AFM measurements

AFM measurement was performed on a Scanning Probe Microscope (SPM) SmartSPM-1000 in non-contact mode. Samples for AFM measurements were deposited on a Si/SiO_2 substrate supplied by PI-KEM UK Ltd. (WAFER-SILI-0476W1). Deposition of the graphene oxide flakes were done as explained in Section 8.3.

Note 1: Errors in image Figure 4.8f and Table 4.3 were calculated using the 95% interval confidence.

Note 2: RMS error values were calculated using the 95% interval confidence. RMS was obtained from 3 different areas and the value reported was obtained from the AIST software. h copper was obtained from Eq. 6.15 once RMS in known.

8.6 X-Ray diffraction

Diffractograms were obtained using a Bruker D8 Venture diffractometer Cu $K_{\alpha 1}$ source (λ = 1.54 Å) operated in Braggs Beta mode. The sample was prepared by pressing a small amount of graphene oxide into a pellet and it was stuck to PMMA sample holder using a small amount of Vaseline to keep the sample in place during the measurement.

8.7 Contact angle measurements

Thin films of each material were deposited by vacuum filtration over a PTFE membrane, transferred to a glass substrate, and dried overnight at room temperature. Two

liquid testing liquids were used: water and diiodomethane. Each measurement was done 3 times using a 5 µl drop of the testing liquid to avoid gravity effects. Images were processed in ImageJ, using the contact angle plugin. **Note**: Errors were calculated using the 95% interval confidence from 3 different samples.

8.8 Raman spectroscopy

Raman spectra were acquired using a Horiba Jobin Ybon LabRam Evolution HR spectrometer equipped with a CCD detector and in a backscattered confocal configuration using a 532 nm laser with a power of 1.2 mW (according to the laser calibration curve). and a long working distance objective lens 50×. The instrument was calibrated against the 520.7 cm^{-1} Raman signal of silicon. Every single spectrum was collected over an area around 1 μm^2. For powders, such as graphene oxide, they were pressed between two glass slides and the sample was placed on a piece of silicon. For samples from graphene deposited by chemical vapour deposition the transfer process stated in Section 8.19 was followed.

8.9 XPS analysis

A Kratos Axis Ultra DLD system was used to collect XPS spectra using a monochromatic Al K_α X-ray source operating at 120 W (10 mA × 12 kV). Data was collected with pass energies of 80 eV for survey spectra and 20 eV for the high-resolution scans with step sizes of 1 eV and 0.1 eV, respectively. The system was operated in the hybrid mode, using a combination of magnetic immersion and electrostatic lenses, and acquired over an area of approximately 300 × 700 μm^2. A magnetically confined charge compensation system using low energy electrons was used to minimize charging of the sample surface, and all spectra were taken with a 90° take off angle. A pressure of ca. 3×10^{-9} Torr was maintained during the collection of the spectra. All samples were pressed into recesses of a modified Kratos Axis Ultra standard sample bar and pressed flat with isopropyl alcohol cleaned glass slides before insertion into the spectrometer. All data was analysed using CasaXPS (v2.3.24)[256] after subtraction of a Shirley background and using modified Wagner sensitivity factors as supplied by the instrument manufacturer. Curve fits were performed using an asymmetric Lorentzian form (LA Lineshape in CasaXPS), whereas the lineshape for graphitic, sp^2 carbon, was based on a clean highly ordered pyrolytic graphite sample. Note: All fittings were assessed based on the residual standard deviation, which in all cases was minimized to be close to unity.

8.10 Chemically reduced graphene oxide (CRGO)

The procedure used was previously reported in the literature.[258] Typically, a colloidal suspension of individual graphene oxide sheets (3 mg/ml) was prepared in a bath sonicator for 40 minutes. Hydrazine monohydrate (1 μl for 3 mg of graphene oxide) was subsequently added to the suspension, and the mixture was heated at 80 °C for 12 h. After cooling, the mixture was filtered through a fritted glass filter and rinsed with deionized water. The resulting black material was freeze-dried for further use.

8.11 Thermally reduced graphene oxide (TRGO)

Around 50 mg of freeze-dried graphene oxide was introduced in the centre of a quartz tube. The tube was placed in a tube furnace (MTI OTFX12000) and flushed with 20 ml/min of argon for 10 minutes to remove the remaining air. The program of the furnace controller is as it follows: 1) A ramp from room temperature to 400 °C in 20 minutes, 2) dwelling at 350 °C for 30 minutes 3) Stop and wait for it to reach room temperature. The thermally reduced graphene oxide was transferred into a bottle and kept under vacuum for further use.

8.12 Salinization of thermally reduced graphene oxide (Epoxy-TRGO)

For method 2 described in Chapter 3: In a glovebox, 300 mg of thermally reduced graphene oxide were mixed with 9 ml of (3-Glycidyloxypropyl)trimethoxysilane and 100 ml of dry N,N-Dimethylformamide. The mixture was stirred for 3 hours in a nitrogen atmosphere and then the solution was heated at 110 °C for 3 hours. It was left to reach room temperature before filtering over a PTFE membrane and washed with 75 ml of acetone. The residue on the filter was dissolved in acetone and filtered again. This process was repeated two time more. The residue on the filter was transferred into a sample vial and left to dry under vacuum at 40 °C. A similar methodology was used for method 1 and method 3 by adjusting the amount to GPTMS, DMF and the temperature.

8.13 Carboxy terminated polystyrene (PS-COOH)

The methodology described here was adapted from reference [303]. Styrene was passed through a silica column (Brockman) to remove stabilizers and 8 ml were collected and transferred to a Schlenk tube with a stir bar. Then, 45.3 mg of TEMPO and 81.3 mg of ACVA

were added to the tube. The mixture was frozen, and the atmosphere was evacuated under vacuum and then it was left to thaw. The cycle was repeated three times and in the last cycle the tube was refilled with argon. The tube was then transferred into an oil bath preheated at 135 °C and the reaction proceeded for 1 hour, after which the tube was placed into a cool water bath and opened to the atmosphere to quench the reaction. The synthesized polymer was precipitated in 200 ml of methanol and vacuum filtered over a nylon membrane. The synthesized polymer was washed three more times with 50 ml methanol. The residue on the filter was collected in a sample vial and dried under vacuum for 12 hours before use.

8.14 Synthesis of Reactive graphene (Epoxy-TRGO-PS)

1 gram of carboxy terminated polystyrene (PS-COOH) and 1 gram of epoxy functionalized graphene (Epoxy-TRGO) were transferred into a round bottom flask. Then, 350 ml of dry N,N-Dimethylformamide and 1.5 ml of N,N-dibenzylamine as catalyst were added. The mixture was stirred for 30 minutes at 140 °C for 24 hours. The flask was cooled to room temperature before vacuum filtration over a PTFE membrane. The filter cake was washed three times with 75 ml of tetrahydrofuran to remove residual polymer. The solid residue was collected and dried under vacuum at 40 °C for further use.

8.15 Preparation of the PLA and reactive graphene masterbatch

A 2 mg/ml solution of Epoxy-TRGO-PS was previously prepared and mixed for 1 hour. Polylactic acid was mixed with N,N-Dimethylformamide in a proportion of 2 mg/ml and mixed at 80 °C for 2 hours using a shear mixer (IKA EURO-ST P CV S2). The two solutions were combined and mixed 2 hours more and it was precipitated in 400 ml of methanol. The polymer precipitated was washed with 200 ml of methanol in a vacuum filtration setup. The polymer masterbatch was dried under vacuum at 40 °C.

8.16 Preparation of the polystyrene with the PLA masterbatch

A certain amount of the PLA masterbatch was grinded with a pestle and mortar until a fine powder was obtained. Then it was introduced into a mini extruder HAAKE microconical twin extruder compounder under a nitrogen atmosphere followed by the

introduction of the polystyrene pellets (90k) and it was mixed for 10 minutes at 100 rpm. The extrudate was immediately quenched in liquid nitrogen to preserve the morphology.

8.17 Sample preparation of polymer simples for SEM and TEM observation

A piece of the extruded polymer quenched in nitrogen were placed in a sample vial with cyclohexanone at 50 °C and was left overnight to etch the polystyrene phase. The samples were mounted on an aluminium stub and fixed with carbon tape. Samples were sputter coated with 20 nm of Au/Pd to avoid charging effects during imaging.

Note: Errors in Figure 5.11b were calculated using the 95% interval confidence.

8.18 Sample preparation for rheological measurements and rheoimpedance

The experiments for rheological measurements were done using a rheometer Discovery HR-2 (TA instruments). Frequency sweeps instruments were done using a strain of 1% at 180 °C. To prepare the samples around 500 mg of the (PLA-Reactive graphene)/PS was hot pressed using 5 tons at 180 °C in a 25 mm diameter mould and 1 mm thickness. After 7 minutes the pressure was removed.

8.18.1 Rheoimpedance experiments

The rheometer used for these measurements was a AR 2000 (TA Instruments). Samples were prepared as in the previous section. The samples were placed in a rheometer using an setup similar to that previously reported in reference 332 using a temperature of 180 °C during the whole experiment. The signal was recorded using a potentiostat in a two-wire configuration. The program run in the rheometer is as follows: 1) annealing the sample for 30 minutes 2) shearing at 0.01 s^{-1} for 5 minutes and then followed by a static annealing step. The electrical signal was collected using a potentiostat (Palmsense 4) over the whole experiment. It was injected a sinusoidal signal of 20 Hz and an amplitude of 0.1 V.

8.19 CVD transfer on Si/SiO_2 substrate using PMMA

The process illustrates the typical transfer of 1 cm^2 of graphene. A piece of graphene on copper is placed on Thermal release tape (Nitto Denko) and 50 µl of a solution of 8 wt% PMMA in anisole is spin-coated at 2000 rpm for 1 min. Then, the thermal release tape is removed by heating at 110 °C for one minute. The graphene on the back (the side not coated with PMMA) is removed by floating it on an oxidizing solution of $HCl:H_2O_2:H_2O$ (3:2:20 ml) for 2 minutes after which it is transferred into a crystallizer with deionized water and left for 5 minutes. The copper remaining is removed in a 1 M $FeCl_3$ solution at 55 °C and left for 10 minutes. Then the graphene film was washed three times in deionized water and taken out on a Si/SiO_2 substrate and left it for 30 minutes at around 37 °C and then it was baked at 130 °C for 30 minutes and the PMMA was removed in an acetone bath at 55 °C and left there for 2 hours. The graphene on Si/SiO_2 was rinsed with fresh acetone and dried with a nitrogen gun.

8.20 CVD transfer on SiO_2 substrate using polycarbonate

First, a polycarbonate solution 1wt% in chloroform was prepared and stirred at room temperature overnight to fully dissolve it. The same protocol as the one previously described in Section 8.19 was adapted to transfer using a polycarbonate film. The following steps were changed: the spin coating step and the polycarbonate removal. Spin coating step: 50 µl of 1 wt% polycarbonate in chloroform and is spin-coated at 2000 rpm for 1 min. Polycarbonate removal: After fishing out the film on the silicon substrate it is placed on a hot plate at 37 °C for 30 minutes. Then sample is immersed in a chloroform bath at 50 °C for two hours. Finally, it was rinsed with fresh chloroform and dried with a nitrogen gun.

8.21 Flexible electrodes using EVA/PET laminating pouches

A piece of 2 × 2 cm^2 of graphene on copper was laminated onto a 80 µm thickness EVA/PET laminating pouch using an office laminator. The graphene on one of the sides of the copper was removed using an oxidizing solution of $HCl:H_2O_2:H_2O$ (3:2:20 ml) as previously explained in Section 8.19. Then the stack was laminated onto a piece of EVA/PET pouch of the same size (2 × 2 cm^2). The copper was etched in a solution of ferric chloride 1 M for 20 minutes after which the samples were placed in a water bath to clean the film. This

process was repeated 2 more times. Then, the piece was divided into 4 equal pieces of 0.5 × 2 cm^2. The electrodes were contacted with electrically conductive adhesive copper tape and kept for further use.

8.21.1 Deposition of silver nanowires on the graphene on copper

When silver nanowires (AgNWs) are required, a solution of 0.5 mg/ml of AgNWs was deposited at 3000 rpm using a spin coater, followed by spin coating of the PMMA solution, as explained in Section 8.19.

8.22 Process for making PMMA/graphene based tattoos

Graphene on copper (2 × 2 cm^2) was coated with a thin layer of PMMA by spin coating a solution of 8 wt% PMMA (M_w ~ 120 000) at 2000 rpm. The back of the graphene on copper was etched with a solution of HCl:H_2O_2:H_2O (3:2:20 ml), as previously explained in Section 8.19. Then it was rinsed in a water bath and the copper was etched in a 1 M ferric chloride solution for 20 minutes. The films were fished out and transferred into a deionized water bath and left 10 minutes. This process was repeated 2 more times, after which it was fished out two times more. The film was fished out using a polyimide film (Kapton) and it was immediately placed in contact with the tattoo paper previously prepared as described in the Section 8.22.1. Then the Kapton film was carefully lifted up, leaving the PMMA/graphene on the tattoo paper. The PMMA/graphene on tattoo paper was cut into 4 equal pieces of 0.5 cm × 2 cm and kept in a humid atmosphere for further use. This same procedure was used when AgNWs were needed, as detailed in Section 8.21.1.

8.22.1 Preparation of the tattoo paper

A piece of 2.5 × 2.5 cm^2 was placed in a petri dish with water for 10 seconds. Then the PVA film covering the paper was carefully removed with tweezers. The paper was removed from water and left to partially dry.

8.22.2 Preparation of the contacts and transferring the PMMA/graphene onto the skin

Ethical disclaimer and Risk Assessment: For the following experiments ethical checklist was completed, and no formal ethical approval was necessary. All associated scientific protocol used have been fully risk assessed. The published work of Ferrari *et al.* (reference 373) has been studied and followed. This paper has also confirmed that the proposed non-invasive, skin contact experiments using commercially available non-hazardous materials (graphene, tattoo transfer paper and electrodes) techniques can safely be carried out and falls under low-risk environment category. Hence, no formal ethical approval is needed. This was based on the following: a) the researcher in the publication has used his own skin as a background, with the objective to check the sensor performance only; b) did not take any samples of human skin; c) relied on a non-invasive, harmless procedure to attach the sensor; d) did not require any analysis regarding potential health implications, with the sensor data reported anonymously in the paper and the thesis.

As an extra additional measure for safety scientific evidence was gathered by the researcher, prior to application of the sensor, using X ray Photoelectron Spectroscopy (XPS, Figure 8.1) to confirm that the graphene electrodes did not include any harmful contaminants. The risk assessment carried out as per above has deemed the overall experiment and associated process low risk and rendered it not needing formal ethical approval.

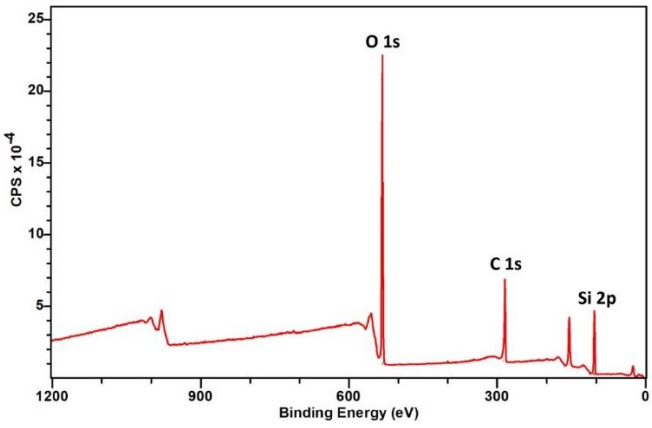

Figure 8.1 XPS survey mode of graphene on silicon oxide, the silicon and oxygen signals come from the silicon oxide substrate.

Commercial magic tape was spin coated with 100 nm thickness of Au/Pd. As part of the preparation, a piece of Tegaderm was put onto the skin and the electrodes (~7 mm × 2 cm) were place on top of them, avoiding contact with the skin. The humid PMMA/graphene on tattoo paper was placed on top of the electrodes and a few drops of water was added on top while gently pressing while sliding to one side leaving the PMMA/graphene onto the skin.

8.22.3 Setup for ECG measurements

ECG measurements were done using a Ganglio board. From Figure 6.22 the copper electrodes were connected to one of the channels of the board and the reference electrode was a commercial Ag/AgCl electrode connected to the elbow. Raw data were collected from the OpenBCI software and processed in OriginLab using a fourth-order Butterworth filter from 5-50Hz as implemented in Origin Lab.[267]

8.23 Sheet resistance measurements

To measure the sheet resistance of EVA/PET electrodes or graphene deposited on Si/SiO_2 substrates, it was used a Keithley 2602 Source Measure Unit (SMU) in four-wire configuration sourcing 100 μA are recording the resulting resistances. For each sample, the four configurations shown in Section 3.10 were tested and calculation of the final sheet resistance was done by fitting according to the set of the equation in section 3.10.

References

1 H. P. Boehm, R. Setton and E. Stumpp, *Carbon.*, 1986, **24**, 241–245.

2 D. C. Marcano, D. V. Kosynkin, J. M. Berlin, A. Sinitskii, Z. Sun, A. Slesarev, L. B. Alemany, W. Lu and J. M. Tour, *ACS Nano*, 2010, **4**, 4806–4814.

3 P. R. Wallace, *Phys. Rev.*, 1947, **71**, 622–634.

4 K. S. Novoselov, A. K. Geim, S. V. Morozov, D. Jiang, Y. Zhang, S. V. Dubonos, I. V. Grigorieva and A. A. Firsov, *Science.*, 2004, **306**, 666–669.

5 A. K. Geim and K. S. Novoselov, *Nat. Mater.*, 2007, **6**, 183–191.

6 W. Lu, P. Soukiassian and J. Boeckl, *MRS Bull.*, 2012, **37**, 1119–1124.

7 S. Eigler, *Angew. Chemie Int. Ed.*, 2016, **55**, 5122–5122.

8 Y. Cao, V. Fatemi, S. Fang, K. Watanabe, T. Taniguchi, E. Kaxiras and P. Jarillo-Herrero, *Nature*, 2018, **556**, 43–50.

9 E. Codecido, Q. Wang, R. Koester, S. Che, H. Tian, R. Lv, S. Tran, K. Watanabe, T. Taniguchi, F. Zhang, M. Bockrath and C. N. Lau, *Sci. Adv.*, 2019, **5**, eaaw9770.

10 R. Bistritzer and A. H. MacDonald, *Proc. Natl. Acad. Sci.*, 2011, **108**, 12233–12237.

11 C. Lee, X. Wei, J. W. Kysar and J. Hone, *Science.*, 2008, **321**, 385–388.

12 A. A. Balandin, S. Ghosh, W. Bao, I. Calizo, D. Teweldebrhan, F. Miao and C. N. Lau, *Nano Lett.*, 2008, **8**, 902–907.

13 W. Cai, A. L. Moore, Y. Zhu, X. Li, S. Chen, L. Shi and R. S. Ruoff, *Nano Lett.*, 2010, **10**, 1645–1651.

14 H. Chien-Te, L. Cheng-En, C. Yu-Fu, C. Jeng-Kuei and T. Hsi-sheng, *Nanoscale*, 2015, **7**, 18663.

15 J. Oliva, A. I. Mtz-Enriquez, A. I. Oliva, R. Ochoa-Valiente, C. R. Garcia and Q. Pei, *J. Phys. D. Appl. Phys.*, 2019, **52**, 025103.

16 G. Kalita, M. Masahiro, H. Uchida, K. Wakita and M. Umeno, *Mater. Lett.*, 2010, **64**, 2180–2183.

17 S. Bae, H. Kim, Y. Lee, X. Xu, J.-S. Park, Y. Zheng, J. Balakrishnan, T. Lei, H. Ri Kim, Y. Il Song, Y.-J. Kim, K. S. Kim, B. Özyilmaz, J.-H. Ahn, B. H. Hong and S. Iijima, *Nat. Nanotechnol.*, 2010, **5**, 574–578.

18 J. Krupka and W. Strupinski, *Appl. Phys. Lett.*, 2010, **96**, 82101.

19 S. De and J. N. Coleman, *ACS Nano*, 2010, **4**, 2713–2720.

20 H. Lee, K. Paeng and I. S. Kim, *Synth. Met.*, 2018, **244**, 36–47.

21 H. Liu, Y. Liu and D. Zhu, *J. Mater. Chem.*, 2011, **21**, 3335–3345.

22 K. K. Kim, A. Reina, Y. Shi, H. Park, L.-J. Li, Y. H. Lee and J. Kong, *Nanotechnology*, 2010, **21**, 285205.

23 Z.-S. Wu, W. Ren, L. Xu, F. Li and H.-M. Cheng, *ACS Nano*, 2011, **5**, 5463–5471.

24 Q. Bin Zheng, M. M. Gudarzi, S. J. Wang, Y. Geng, Z. Li and J.-K. Kim, *Carbon.*, 2011, **49**, 2905–2916.

25 K. S. Novoselov and A. H. Castro Neto, *Phys. Scr.*, 2012, **T146**, 014006.

26 S. Das, J. A. Robinson, M. Dubey, H. Terrones and M. Terrones, *Annu. Rev. Mater. Res.*, 2015, **45**, 1–27.

27 M. Yi and Z. Shen, *J. Mater. Chem. A*, 2015, **3**, 11700–11715.

28 T. Skaltsas, X. Ke, C. Bittencourt and N. Tagmatarchis, *J. Phys. Chem. C*, 2013, **117**, 23272–23278.

29 G. M. Rutter, J. N. Crain, N. P. Guisinger, T. Li, P. N. First and J. A. Stroscio, *Science.*, 2007, **317**, 219–222.

30 M. Yi, Z. Shen, S. Liang, L. Liu, X. Zhang and S. Ma, *Chem. Commun.*, 2013, **49**, 11059–11061.

31 K. R. Paton, E. Varrla, C. Backes, R. J. Smith, U. Khan, A. O'Neill, C. Boland, M.

Lotya, O. M. Istrate, P. King, T. Higgins, S. Barwich, P. May, P. Puczkarski, I. Ahmed, M. Moebius, H. Pettersson, E. Long, J. Coelho, S. E. O'Brien, E. K. McGuire, B. M. Sanchez, G. S. Duesberg, N. McEvoy, T. J. Pennycook, C. Downing, A. Crossley, V. Nicolosi and J. N. Coleman, *Nat. Mater.*, 2014, **13**, 624–630.

32 L. Liu, Z. Shen, M. Yi, X. Zhang and S. Ma, *RSC Adv.*, 2014, **4**, 36464–36470.

33 E. Varrla, K. R. Paton, C. Backes, A. Harvey, R. J. Smith, J. McCauley and J. N. Coleman, *Nanoscale*, 2014, **6**, 11810–11819.

34 S. Biccai, S. Barwich, D. Boland, A. Harvey, D. Hanlon, N. McEvoy and J. N. Coleman, *2D Mater.*, 2019, **6**, 15008.

35 Y. Arao, Y. Mizuno, K. Araki and M. Kubouchi, *Carbon.*, 2016, **102**, 330–338.

36 S. Lund, J. Kauppila, S. Sirkiä, J. Palosaari, O. Eklund, R.-M. Latonen, J.-H. Smått, J. Peltonen and T. Lindfors, *Carbon.*, 2021, **174**, 123–131.

37 Y. Chen and M. Sun, *Nanoscale*, 2021, **13**, 5594–5619.

38 Y. Hernandez, V. Nicolosi, M. Lotya, F. M. Blighe, Z. Sun, S. De, I. T. McGovern, B. Holland, M. Byrne, Y. K. Gun'Ko, J. J. Boland, P. Niraj, G. Duesberg, S. Krishnamurthy, R. Goodhue, J. Hutchison, V. Scardaci, A. C. Ferrari and J. N. Coleman, *Nat. Nanotechnol.*, 2008, **3**, 563–568.

39 A. Kozbial, Z. Li, C. Conaway, R. McGinley, S. Dhingra, V. Vahdat, F. Zhou, B. D'Urso, H. Liu and L. Li, *Langmuir*, 2014, **30**, 8598–8606.

40 C. D. van Engers, N. E. A. Cousens, V. Babenko, J. Britton, B. Zappone, N. Grobert and S. Perkin, *Nano Lett.*, 2017, **17**, 3815–3821.

41 Y. Hernandez, M. Lotya, D. Rickard, S. D. Bergin and J. N. Coleman, *Langmuir*, 2010, **26**, 3208–3213.

42 S. D. Bergin, V. Nicolosi, P. V. Streich, S. Giordani, Z. Sun, A. H. Windle, P. Ryan, N. P. P. Niraj, Z. T. Wang, L. Carpenter, W. J. Blau, J. J. Boland, J. P. Hamilton and J. N. Coleman, *Adv. Mater.*, 2008, **20**, 1876–1881.

43 J. N. Coleman, *Acc. Chem. Res.*, 2013, **46**, 14–22.

44 A. O'Neill, U. Khan, P. N. Nirmalraj, J. Boland and J. N. Coleman, *J. Phys. Chem. C*, 2011, **115**, 5422–5428.

45 X. Zhang, A. C. Coleman, N. Katsonis, W. R. Browne, B. J. van Wees and B. L. Feringa, *Chem. Commun.*, 2010, **46**, 7539.

46 K. Parvez, S. Yang, X. Feng and K. Müllen, *Synth. Met.*, 2015, **210**, 123–132.

47 M. Lotya, Y. Hernandez, P. J. King, R. J. Smith, V. Nicolosi, L. S. Karlsson, F. M. Blighe, S. De, Z. Wang, I. T. McGovern, G. S. Duesberg and J. N. Coleman, *J. Am. Chem. Soc.*, 2009, **131**, 3611–3620.

48 R. Hao, W. Qian, L. Zhang and Y. Hou, *Chem. Commun.*, 2008, 6576.

49 S. Vadukumpully, J. Paul and S. Valiyaveettil, *Carbon.*, 2009, **47**, 3288–3294.

50 C. Schafhaeutl, *London, Edinburgh, Dublin Philos. Mag. J. Sci.*, 1840, **16**, 570–590.

51 B. C. Brodie, *Philos. Trans. R. Soc. London*, 1859, **149**, 249–259.

52 W. S. Hummers and R. E. Offeman, *J. Am. Chem. Soc.*, 1958, **80**, 1339–1339.

53 Y. Hou, S. Lv, L. Liu and X. Liu, *Ceram. Int.*, 2020, **46**, 2392–2402.

54 J. Zhao, S. Pei, W. Ren, L. Gao and H.-M. Cheng, *ACS Nano*, 2010, **4**, 5245–5252.

55 M. Hirata, T. Gotou, S. Horiuchi, M. Fujiwara and M. Ohba, *Carbon.*, 2004, **42**, 2929–2937.

56 N. I. Kovtyukhova, P. J. Ollivier, B. R. Martin, T. E. Mallouk, S. A. Chizhik, E. V. Buzaneva and A. D. Gorchinskiy, *Chem. Mater.*, 1999, **11**, 771–778.

57 Z.-S. Wu, W. Ren, L. Gao, B. Liu, C. Jiang and H.-M. Cheng, *Carbon.*, 2009, **47**, 493–499.

58 D. R. Dreyer, S. Park, C. W. Bielawski and R. S. Ruoff, *Chem. Soc. Rev.*, 2010, **39**, 228–240.

59 A. L. Higginbotham, D. V Kosynkin, A. Sinitskii, Z. Sun and J. M. Tour, *ACS Nano*, 2010, **4**, 2059–2069.

60 S. Pei and H.-M. Cheng, *Carbon.*, 2012, **50**, 3210–3228.

61 A. Lerf, H. He, M. Forster and J. Klinowski, *J. Phys. Chem. B*, 1998, **102**, 4477–4482.

62 H. He, J. Klinowski, M. Forster and A. Lerf, *Chem. Phys. Lett.*, 1998, **287**, 53–56.

63 W. Cai, R. D. Piner, F. J. Stadermann, S. Park, M. A. Shaibat, Y. Ishii, D. Yang, A. Velamakanni, S. J. An, M. Stoller, J. An, D. Chen and R. S. Ruoff, *Science.*, 2008, **321**, 1815–1817.

64 W. Gao, L. B. Alemany, L. Ci and P. M. Ajayan, *Nat. Chem.*, 2009, **1**, 403–408.

65 A. B. Kaiser, *Reports Prog. Phys.*, 2001, **64**, 1–49.

66 Y. Kopelevich and P. Esquinazi, *Adv. Mater.*, 2007, **19**, 4559–4563.

67 V. Agarwal and P. B. Zetterlund, *Chem. Eng. J.*, 2021, **405**, 127018.

68 Q. Su, S. Pang, V. Alijani, C. Li, X. Feng and K. Müllen, *Adv. Mater.*, 2009, **21**, 3191–3195.

69 Y. Chen, X.-L. Gong and J.-G. Gai, *Adv. Sci.*, 2016, **3**, 1500343.

70 P.-G. Ren, D.-X. Yan, X. Ji, T. Chen and Z.-M. Li, *Nanotechnology*, 2010, **22**, 55705.

71 R. Wang, Y. Wang, C. Xu, J. Sun and L. Gao, *RSC Adv.*, 2013, **3**, 1194–1200.

72 D. Li, M. B. Müller, S. Gilje, R. B. Kaner and G. G. Wallace, *Nat. Nanotechnol.*, 2008, **3**, 101–105.

73 J. Zhang, H. Yang, G. Shen, P. Cheng, J. Zhang and S. Guo, *Chem. Commun.*, 2010, **46**, 1112–1114.

74 G. Shruthi, G. Baishali, V. Radhakrishna and P. Verma, *Graphene Technol.*, 2020, **5**, 19–25.

75 H. A. Becerril, J. Mao, Z. Liu, R. M. Stoltenberg, Z. Bao and Y. Chen, *ACS Nano*, 2008, **2**, 463–470.

76 X. Li, W. Cai, J. An, S. Kim, J. Nah, D. Yang, R. Piner, A. Velamakanni, I. Jung, E.

Tutuc, S. K. Banerjee, L. Colombo and R. S. Ruoff, *Science*, 2009, **324**, 1312–1314.

77 L. Banszerus, M. Schmitz, S. Engels, J. Dauber, M. Oellers, F. Haupt, K. Watanabe, T. Taniguchi, B. Beschoten and C. Stampfer, *Sci. Adv.*, 2015, **1**, e1500222.

78 Z. Yan, Z. Peng and J. M. Tour, *Acc. Chem. Res.*, 2014, **47**, 1327–1337.

79 T. Wu, X. Zhang, Q. Yuan, J. Xue, G. Lu, Z. Liu, H. Wang, H. Wang, F. Ding, Q. Yu, X. Xie and M. Jiang, *Nat. Mater.*, 2016, **15**, 43–47.

80 X. Li, W. Cai, L. Colombo and R. S. Ruoff, *Nano Lett.*, 2009, **9**, 4268–4272.

81 Y. Wu, H. Chou, H. Ji, Q. Wu, S. Chen, W. Jiang, Y. Hao, J. Kang, Y. Ren, R. D. Piner and R. S. Ruoff, *ACS Nano*, 2012, **6**, 7731–7738.

82 S. Bhaviripudi, X. Jia, M. S. Dresselhaus and J. Kong, *Nano Lett.*, 2010, **10**, 4128–4133.

83 R. Muñoz and C. Gómez-Aleixandre, *Chem. Vap. Depos.*, 2013, **19**, 297–322.

84 L. Lin, B. Deng, J. Sun, H. Peng and Z. Liu, *Chem. Rev.*, 2018, **118**, 9281–9343.

85 N. N. Greenwood and A. Earnshaw, *Chemistry of the Elements*, Elsevier, 2012.

86 G. A. López and E. J. Mittemeijer, *Scr. Mater.*, 2004, **51**, 1–5.

87 A. Reina, X. Jia, J. Ho, D. Nezich, H. Son, V. Bulovic, M. S. Dresselhaus and J. Kong, *Nano Lett.*, 2009, **9**, 30–35.

88 X. Zhang, H. Li and F. Ding, *Adv. Mater.*, 2014, **26**, 5488–5495.

89 D. R. Lenski and M. S. Fuhrer, *J. Appl. Phys.*, 2011, **110**, 13720.

90 M. Losurdo, M. M. Giangregorio, P. Capezzuto and G. Bruno, *Phys. Chem. Chem. Phys.*, 2011, **13**, 20836–20843.

91 I. Vlassiouk, M. Regmi, P. Fulvio, S. Dai, P. Datskos, G. Eres and S. Smirnov, *ACS Nano*, 2011, **5**, 6069–6076.

92 S. Choubak, P. L. Levesque, E. Gaufres, M. Biron, P. Desjardins and R. Martel, *J.*

Phys. Chem. C, 2014, **118**, 21532–21540.

93 A. M. Lewis, B. Derby and I. A. Kinloch, *ACS Nano*, 2013, **7**, 3104–3117.

94 S. Chaitoglou and E. Bertran, *J. Mater. Sci.*, 2017, **52**, 8348–8356.

95 S. Chaitoglou, E. Pascual, E. Bertran and J. L. Andujar, *J. Nanomater.*, 2016, **2016**, 9640935.

96 S. Chaitoglou and E. Bertran, *J. Mater. Sci.*, 2017, **52**, 8348–8356.

97 A. Alnuaimi, I. Almansouri, I. Saadat and A. Nayfeh, *RSC Adv.*, 2017, **7**, 51951–51957.

98 J. Sun, H. O. Finklea and Y. Liu, *Nanotechnology*, 2017, **28**, 125703.

99 M. Chen, D. Stekovic, W. Li, B. Arkook, R. C. Haddon and E. Bekyarova, *Nanotechnology*, 2017, **28**, 255701.

100 H. H. Kim, B. Kang, J. W. Suk, N. Li, K. S. Kim, R. S. Ruoff, W. H. Lee and K. Cho, *ACS Nano*, 2015, **9**, 4726–4733.

101 M. Jang, T. Q. Trung, J.-H. Jung, B.-Y. Kim and N.-E. Lee, *Phys. Chem. Chem. Phys.*, 2014, **16**, 4098–4105.

102 Y. Wang, Y. Zheng, X. Xu, E. Dubuisson, Q. Bao, J. Lu and K. P. Loh, *ACS Nano*, 2011, **5**, 9927–9933.

103 L. G. P. Martins, Y. Song, T. Zeng, M. S. Dresselhaus, J. Kong and P. T. Araujo, *Proc. Natl. Acad. Sci.*, 2013, **110**, 17762–17767.

104 N. Hong, D. Kireev, Q. Zhao, D. Chen, D. Akinwande and W. Li, *Adv. Mater.*, 2022, **34**, 2106615.

105 K. L. Johnson, K. Kendall, A. D. Roberts and D. Tabor, *Proc. R. Soc. London. A. Math. Phys. Sci.*, 1997, **324**, 301–313.

106 A. J. Watson, W. Lu, M. H. D. Guimarães and M. Stöhr, *2D Mater.*, 2021, **8**, 32001.

107 N. Liu, Z. Pan, L. Fu, C. Zhang, B. Dai and Z. Liu, *Nano Res.*, 2011, **4**, 996–1004.

108 K.-S. Kim, C., Yoon, M.-A., Jang, B., Kim, J.-H., & Kim, *Tribol. Lubr.*, 2020, **36**, 1–10.

109 A. Reina, H. Son, L. Jiao, B. Fan, M. S. Dresselhaus, Z. Liu and J. Kong, *J. Phys. Chem. C*, 2008, **112**, 17741–17744.

110 C. R. Dean, A. F. Young, I. Meric, C. Lee, L. Wang, S. Sorgenfrei, K. Watanabe, T. Taniguchi, P. Kim, K. L. Shepard and J. Hone, *Nat. Nanotechnol.*, 2010, **5**, 722–726.

111 X. Liang, B. A. Sperling, I. Calizo, G. Cheng, C. A. Hacker, Q. Zhang, Y. Obeng, K. Yan, H. Peng, Q. Li, X. Zhu, H. Yuan, A. R. H. Walker, Z. Liu, L.-M. Peng and C. A. Richter, *ACS Nano*, 2011, **5**, 9144–9153.

112 X. Li, Y. Zhu, W. Cai, M. Borysiak, B. Han, D. Chen, R. D. Piner, L. Colombo and R. S. Ruoff, *Nano Lett.*, 2009, **9**, 4359–4363.

113 Y.-C. Lin, C. Jin, J.-C. Lee, S.-F. Jen, K. Suenaga and P.-W. Chiu, *ACS Nano*, 2011, **5**, 2362–2368.

114 Y.-C. Lin, C.-C. Lu, C.-H. Yeh, C. Jin, K. Suenaga and P.-W. Chiu, *Nano Lett.*, 2012, **12**, 414–419.

115 J. D. Wood, G. P. Doidge, E. A. Carrion, J. C. Koepke, J. A. Kaitz, I. Datye, A. Behnam, J. Hewaparakrama, B. Aruin, Y. Chen, H. Dong, R. T. Haasch, J. W. Lyding and E. Pop, *Nanotechnology*, 2015, **26**, 55302.

116 Y. Jia, X. Gong, P. Peng, Z. Wang, Z. Tian, L. Ren, Y. Fu and H. Zhang, *Nano-micro Lett.*, 2016, **8**, 336–346.

117 A. A. Murthy, T. K. Stanev, J. D. Cain, S. Hao, T. LaMountain, S. Kim, N. Speiser, K. Watanabe, T. Taniguchi, C. Wolverton, N. P. Stern and V. P. Dravid, *Nano Lett.*, 2018, **18**, 2990–2998.

118 J. M. Mativetsky, H. Wang, S. S. Lee, L. Whittaker-Brooks and Y.-L. Loo, *Chem. Commun.*, 2014, **50**, 5319–5321.

119 Y.-J. Chen, J. D. Cain, T. K. Stanev, V. P. Dravid and N. P. Stern, *Nat. Photonics*, 2017, **11**, 431–435.

120 D. Daw, R. Sebait and C. Biswas, *J. Korean Phys. Soc.*, 2020, **77**, 884–887.

121 S. Bae, S. J. Kim, D. Shin, J.-H. Ahn and B. H. Hong, *Phys. Scr.*, 2012, **2012**, 14024.

122 J. Du and H. Cheng, *Macromol. Chem. Phys.*, 2012, **213**, 1060–1077.

123 S. Thomas, R. Shanks and S. Chandrasekharakurup, *Nanostructured Polymer Blends*, 2014.

124 M. Sumita, K. Sakata, Y. Hayakawa, S. Asai, K. Miyasaka and M. Tanemura, *Colloid Polym. Sci.*, 1992, **270**, 134–139.

125 M. Sumita, S. Kazuya, S. Asai, K. Mayasaka and H. Nakagawa, *Polym. Bull.*, 1991, **25**, 265–271.

126 T. Young, *Philos. Trans. R. Soc. London*, 1805, **95**, 65–87.

127 F. M. Fowkes, *J. Adhes.*, 1972, **4**, 155–159.

128 F. M. Fowkes, *Ind. Eng. Chem.*, 1964, **56**, 40–52.

129 D. K. Owens and R. C. Wendt, *J. Appl. Polym. Sci.*, 1969, **13**, 1741–1747.

130 S. Wu, *J. Polym. Sci. Part C Polym. Symp.*, 1971, **34**, 19–30.

131 S. Levine, B. D. Bowen and S. J. Partridge, *Colloids and Surfaces*, 1989, **38**, 325–343.

132 B. P. Binks, *Curr. Opin. Colloid Interface Sci.*, 2002, **7**, 21–41.

133 D. J. French, P. Taylor, J. Fowler and P. S. Clegg, *J. Colloid Interface Sci.*, 2015, **441**, 30–38.

134 B. Krasovitski and A. Marmur, *J. Adhes.*, 2005, **81**, 869–880.

135 A. Göldel, A. Marmur, G. R. Kasaliwal, P. Pötschke and G. Heinrich, *Macromolecules*, 2011, **44**, 6094–6102.

136 F. Gubbels, R. Jerome, E. Vanlathem, R. Deltour, S. Blacher and F. Brouers, *Chem. Mater.*, 1998, **10**, 1227–1235.

137 A. E. Zaikin, R. R. Karimov and V. P. Arkhireev, 2001, **63**, 57–63.

138 J. Plattier, L. Benyahia, M. Dorget, F. Niepceron and J. F. Tassin, *Polymer.*, 2015, **59**, 260–269.

139 A. Göldel, G. R. Kasaliwal, P. Pötschke and G. Heinrich, *Polymer.*, 2012, **53**, 411–421.

140 L. Elias, F. Fenouillot, J.-C. Majesté, G. Martin and P. Cassagnau, *J. Polym. Sci. Part B Polym. Phys.*, 2008, **46**, 1976–1983.

141 A. Taghizadeh and B. D. Favis, *Carbohydr. Polym.*, 2013, **98**, 189–198.

142 X. Zhao, J. Zhao, J. Cao, D. Wang, G. Hu, F. Chen and Z. Dang, *J. Mater.*, 2014, **56**, 807–815.

143 M. P. Stevens, *Polymer Chemistry: An Introduction*, Oxford University Press, New York, USA, Second edi., 1990.

144 N. O. Jaensson, C. Mitrias, M. A. Hulsen and P. D. Anderson, *Langmuir*, 2018, **34**, 1795–1806.

145 J. Yang, C. Feng, J. Dai, N. Zhang, T. Huang and Y. Wang, *Polym. Int.*, 2013, **62**, 1085–1093.

146 S. K. Tiwari, G. Hatui, R. Oraon, A. De Adhikari and G. C. Nayak, *Curr. Appl. Phys.*, 2017, **17**, 1158–1168.

147 T. H. Kim, H. Kim, K. I. Choi, J. Yoo, Y. S. Seo, J. S. Lee and J. Koo, *Langmuir*, 2016, **32**, 12741–12748.

148 Y. Tan, L. Fang, J. Xiao, Y. Song and Q. Zheng, *Polym. Chem.*, 2013, **4**, 2939–2944.

149 G. P. Kar, S. Biswas and S. Bose, *Phys. Chem. Chem. Phys.*, 2015, **17**, 1811–1821.

150 A. Paydayesh, F. Pashaei Soorbaghi, A. Aref Azar and A. Jalali-Arani, *Polym. Compos.*, 2019, **40**, 704–715.

151 Y. Lan, H. Liu, X. Cao, S. Zhao, K. Dai, X. Yan, G. Zheng, C. Liu, C. Shen and Z. Guo, *Polymer.*, 2016, **97**, 11–19.

152 R. S. Kurusu, E. Helal, N. Moghimian, E. David and N. Demarquette, *Macromol. Mater. Eng.*, 2018, **303**, 1–9.

153 M. Liebscher, M. O. Blais, P. Pötschke and G. Heinrich, *Polymer.*, 2013, **54**, 5875–5882.

154 L. Bai, S. He, J. W. Fruehwirth, A. Stein, C. W. Macosko and X. Cheng, *J. Rheol.*, 2017, **61**, 575–587.

155 H. Wang, X. Yang, Z. Fu, X. Zhao, Y. Li and J. Li, *Macromolecules*, 2017, **50**, 9494–9506.

156 X. Zhao, H. Wang, Z. Fu and Y. Li, *ACS Appl. Mater. Interfaces*, 2018, **10**, 8411–8416.

157 A. Ul-Hamid, *A Beginners' Guide to Scanning Electron Microscopy*, Springer Cham, Cham, Switzerland, First Edit., 2019.

158 A. Ul-Hamid, *A Beginners' Guide to Scanning Electron Microscopy*, Springer International Publishing, Cham, 2018.

159 J. I. Goldstein, D. E. Newbury, J. R. Michael, N. W. M. Ritchie, J. H. J. Scott and D. C. Joy, *Scanning Electron Microscopy and X-Ray Microanalysis*, Springer New York, New York, NY, 2018.

160 V. Kochat, A. Nath Pal, E. S. Sneha, A. Sampathkumar, A. Gairola, S. A. Shivashankar, S. Raghavan and A. Ghosh, *J. Appl. Phys.*, 2011, **110**, 14315.

161 Z. Luo, *A Practical Guide to Transmission Electron Microscopy: Fundamentals*, Momentum Press, New York, USA, First Edit., 2016.

162 A. W. Robertson and J. H. Warner, *Nanoscale*, 2013, **5**, 4079.

163 Y. Kim, J. Ihm, E. Yoon and G.-D. Lee, *Phys. Rev. B*, 2011, **84**, 075445.

164 J. Kotakoski, A. V. Krasheninnikov, U. Kaiser and J. C. Meyer, *Phys. Rev. Lett.*, 2011, **106**, 105505.

165 J. Kotakoski, J. C. Meyer, S. Kurasch, D. Santos-Cottin, U. Kaiser and A. V.

Krasheninnikov, *Phys. Rev. B*, 2011, **83**, 245420.

166 J. C. Meyer, C. Kisielowski, R. Erni, M. D. Rossell, M. F. Crommie and A. Zettl, *Nano Lett.*, 2008, **8**, 3582–3586.

167 P. Y. Huang, C. S. Ruiz-Vargas, A. M. van der Zande, W. S. Whitney, M. P. Levendorf, J. W. Kevek, S. Garg, J. S. Alden, C. J. Hustedt, Y. Zhu, J. Park, P. L. McEuen and D. A. Muller, *Nature*, 2011, **469**, 389–392.

168 C. O. Girit, J. C. Meyer, R. Erni, M. D. Rossell, C. Kisielowski, L. Yang, C.-H. Park, M. F. Crommie, M. L. Cohen, S. G. Louie and A. Zettl, *Science.*, 2009, **323**, 1705–1708.

169 P. Koskinen, S. Malola and H. Häkkinen, *Phys. Rev. B*, 2009, **80**, 073401.

170 Z. Liu, K. Suenaga, P. J. F. Harris and S. Iijima, *Phys. Rev. Lett.*, 2009, **102**, 015501.

171 A. C. Ferrari, J. C. Meyer, V. Scardaci, C. Casiraghi, M. Lazzeri, F. Mauri, S. Piscanec, D. Jiang, K. S. Novoselov, S. Roth and A. K. Geim, *Phys. Rev. Lett.*, 2006, **97**, 187401.

172 J. C. Meyer, A. K. Geim, M. I. Katsnelson, K. S. Novoselov, T. J. Booth and S. Roth, *Nature*, 2007, **446**, 60–63.

173 G. Haugstad, *Atomic Force Microscopy: Understanding Basic Modes and Advanced Applications*, JohnWiley & Sons, Inc., New Jersey, USA, First edit., 2012.

174 P. Nemes-Incze, Z. Osváth, K. Kamarás and L. P. Biró, *Carbon.*, 2008, **46**, 1435–1442.

175 K. S. Novoselov, D. Jiang, F. Schedin, T. J. Booth, V. V. Khotkevich, S. V. Morozov and A. K. Geim, *Proc. Natl. Acad. Sci. U. S. A.*, 2005, **102**, 10451–10453.

176 C. J. Shearer, A. D. Slattery, A. J. Stapleton, J. G. Shapter and C. T. Gibson, *Nanotechnology*, 2016, **27**, 125704.

177 K. Xu, P. Cao and J. R. Heath, *Science.*, 2010, **329**, 1188–1191.

178 M. Ishigami, J. H. Chen, W. G. Cullen, M. S. Fuhrer and E. D. Williams, *Nano Lett.*,

2007, **7**, 1643–1648.

179 R. Jalili, S. H. Aboutalebi, D. Esrafilzadeh, K. Konstantinov, S. E. Moulton, J. M. Razal and G. G. Wallace, *ACS Nano*, 2013, **7**, 3981–3990.

180 J. I. Paredes, S. Villar-Rodil, P. Solís-Fernández, A. Martínez-Alonso and J. M. D. Tascón, *Langmuir*, 2009, **25**, 5957–5968.

181 E. Smith and G. Dent, *Modern Raman spectroscopy : a practical approach*, John Wiley & Sons Ltd, Chichester, UK, First Edit., 2005.

182 P. Turner, K. R. Paton, E. J. Legge, A. de Luna Bugallo, A. K. S. Rocha-Robledo, A.-A. Zahab, A. Centeno, A. Sacco, A. Pesquera, A. Zurutuza, A. M. Rossi, D. N. H. Tran, D. L Silva, D. Losic, F. Farivar, H. Kerdoncuff, H. Kwon, J. Pirart, J. L. E. Campos, K. M. Subhedar, L.-L. Tay, L. Ren, L. G. Cançado, M. Paillet, P. Finnie, P. L. Yap, R. Arenal, S. R. Dhakate, S. Wood, S. Jiménez-Sandoval, T. Batten, V. Nagyte, Y. Yao, A. R. Hight Walker, E. H. Martins Ferreira, C. Casiraghi and A. J. Pollard, *2D Mater.*, 2022, **9**, 035010.

183 M. M. Lucchese, F. Stavale, E. H. M. Ferreira, C. Vilani, M. V. O. Moutinho, R. B. Capaz, C. A. Achete and A. Jorio, *Carbon.*, 2010, **48**, 1592–1597.

184 L. G. Cançado, A. Jorio, E. H. M. Ferreira, F. Stavale, C. A. Achete, R. B. Capaz, M. V. O. Moutinho, A. Lombardo, T. S. Kulmala and A. C. Ferrari, *Nano Lett.*, 2011, **11**, 3190–3196.

185 J. E. Proctor, E. Gregoryanz, K. S. Novoselov, M. Lotya, J. N. Coleman and M. P. Halsall, *Phys. Rev. B*, 2009, **80**, 073408.

186 M. Huang, H. Yan, T. F. Heinz and J. Hone, *Nano Lett.*, 2010, **10**, 4074–4079.

187 M. Mohr, J. Maultzsch and C. Thomsen, *Phys. Rev. B*, 2010, **82**, 201409.

188 C. Casiraghi, S. Pisana, K. S. Novoselov, A. K. Geim and A. C. Ferrari, *Appl. Phys. Lett.*, 2007, **91**, 233108.

189 D. C. Elias, R. R. Nair, T. M. G. Mohiuddin, S. V. Morozov, P. Blake, M. P. Halsall, A. C. Ferrari, D. W. Boukhvalov, M. I. Katsnelson, A. K. Geim and K. S. Novoselov,

Science., 2009, **323**, 610–613.

190 J. E. Johns and M. C. Hersam, *Acc. Chem. Res.*, 2013, **46**, 77–86.

191 C. Faugeras, M. Amado, P. Kossacki, M. Orlita, M. Sprinkle, C. Berger, W. A. de Heer and M. Potemski, *Phys. Rev. Lett.*, 2009, **103**, 186803.

192 T. Ando, *J. Phys. Soc. Japan*, 2007, **76**, 024712.

193 R. J. Nemanich, G. Lucovsky and S. A. Solin, *Solid State Commun.*, 1977, **23**, 117–120.

194 A. Grüneis, J. Serrano, A. Bosak, M. Lazzeri, S. L. Molodtsov, L. Wirtz, C. Attaccalite, M. Krisch, A. Rubio, F. Mauri and T. Pichler, *Phys. Rev. B*, 2009, **80**, 085423.

195 J. Maultzsch, S. Reich, C. Thomsen, H. Requardt and P. Ordejón, *Phys. Rev. Lett.*, 2004, **92**, 075501.

196 A. C. Ferrari and D. M. Basko, *Nat. Nanotechnol.*, 2013, **8**, 235–246.

197 F. Tuinstra and J. L. Koenig, *J. Chem. Phys.*, 1970, **53**, 1126–1130.

198 A. C. Ferrari and J. Robertson, *Phys. Rev. B*, 2000, **61**, 14095–14107.

199 C. Thomsen and S. Reich, *Phys. Rev. Lett.*, 2000, **85**, 5214–5217.

200 R. J. Nemanich and S. A. Solin, *Phys. Rev. B*, 1979, **20**, 392–401.

201 R. P. Vidano, D. B. Fischbach, L. J. Willis and T. M. Loehr, *Solid State Commun.*, 1981, **39**, 341–344.

202 P. Lespade, A. Marchand, M. Couzi and F. Cruege, *Carbon.*, 1984, **22**, 375–385.

203 A. J. Pollard, B. Brennan, H. Stec, B. J. Tyler, M. P. Seah, I. S. Gilmore and D. Roy, *Appl. Phys. Lett.*, 2014, **105**, 253107.

204 C. Suryanarayana and M. G. Norton, *X-Ray Diffraction: A Practical Approach*, Springer Science and Business Media, New York, USA, First Edit., 1998.

205 A. M. Dimiev, G. Ceriotti, N. Behabtu, D. Zakhidov, M. Pasquali, R. Saito and J. M. Tour, *ACS Nano*, 2013, **7**, 2773–2780.

206 J. Cao, P. He, M. A. Mohammed, X. Zhao, R. J. Young, B. Derby, I. A. Kinloch and R. A. W. Dryfe, *J. Am. Chem. Soc.*, 2017, **139**, 17446–17456.

207 A. M. Dimiev and J. M. Tour, *ACS Nano*, 2014, **8**, 3060–3068.

208 D. L. Pavia, G. M. Lampman and G. S. Kriz, *Introduction to spectroscopy. A guide for students for organic chemistry*, Thomson Learning, Inc., Toronto, Ontario, Canada, Thrid edit., 2001.

209 C. H. Manoratne, S. R. . Rosa and I. R. . Kottegoda, *Mater. Sci. Res. India*, 2017, **14**, 19–30.

210 Y. Xu, H. Bai, G. Lu, C. Li and G. Shi, *J. Am. Chem. Soc.*, 2008, **130**, 5856–5857.

211 S. Stankovich, R. D. Piner, S. T. Nguyen and R. S. Ruoff, *Carbon.*, 2006, **44**, 3342–3347.

212 U. K. Sur, A. Saha, A. Datta, B. Ankamwar, F. Surti, S. D. Roy and D. Roy, *Bull. Mater. Sci.*, 2016, **39**, 159–165.

213 P. van der Heide, *X-ray photoelectron spectroscopy : an introduction to principles and practices*, WILEY, Hoboken, New Jersey, USA, First edit., 2012.

214 F. A. Stevie and C. L. Donley, *J. Vac. Sci. Technol. A*, 2020, **38**, 063204.

215 P. Kovaříček, V. Vrkoslav, J. Plšek, Z. Bastl, M. Fridrichová, K. Drogowska and M. Kalbáč, *Carbon.*, 2017, **118**, 200–207.

216 A. Criado, M. Melchionna, S. Marchesan and M. Prato, *Angew. Chemie Int. Ed.*, 2015, **54**, 10734–10750.

217 V. Mishyn, T. Rodrigues, Y. R. Leroux, P. Aspermair, H. Happy, J. Bintinger, C. Kleber, R. Boukherroub, W. Knoll and S. Szunerits, *Nanoscale Horizons*, 2021, **6**, 819–829.

218 B. D. Ratner and D. G. Castner, in *Surfaces Analysis - The Principal Thecniques*, eds.

J. C. Vickerman and I. S. Gilmore, Wiley, Chichester, UK, Second edi., 2009, p. 56.

219 N. Saadatkhah, A. Carillo Garcia, S. Ackermann, P. Leclerc, M. Latifi, S. Samih, G. S. Patience and J. Chaouki, *Can. J. Chem. Eng.*, 2020, **98**, 34–43.

220 ISO, *ISO Geneva, Switz.*

221 F. Farivar, P. L. Yap, K. Hassan, T. T. Tung, D. N. H. Tran, A. J. Pollard and D. Losic, *Carbon.*, 2021, **179**, 505–513.

222 T. G. Mezger, *The Rheology Handbook*, Vincentz Network, Hannover, Germany, 2019.

223 C. Penu, G.-H. Hu, A. Fernandez, P. Marchal and L. Choplin, *Polym. Eng. Sci.*, 2012, **52**, 2173–2181.

224 S. Azizi, C. M. Ouellet-Plamondon, P. Nguyen-Tri, M. Fréchette and E. David, *Compos. Part B Eng.*, 2019, **177**, 107288.

225 L. J. Van der Paw, *Philips Res. Reports*, 1958, **13**, 1–9.

226 C. Melios, N. Huang, L. Callegaro, A. Centeno, A. Cultrera, A. Cordon, V. Panchal, I. Arnedo, A. Redo-Sanchez, D. Etayo, M. Fernandez, A. Lopez, S. Rozhko, O. Txoperena, A. Zurutuza and O. Kazakova, *Sci. Rep.*, 2020, **10**, 3223.

227 M. Dragoman, D. Neculoiu, A. Cismaru, A. A. Muller, G. Deligeorgis, G. Konstantinidis, D. Dragoman and R. Plana, *Appl. Phys. Lett.*, 2011, **99**, 033112.

228 L. Bai, R. Sharma, X. Cheng and C. W. Macosko, *Langmuir*, 2018, **34**, 1073–1083.

229 L. Bai, 2017.

230 G. Li, S. Wang and Y. Y. Duan, *Sensors Actuators B Chem.*, 2018, **277**, 250–260.

231 C. Su and K. P. Loh, *Acc. Chem. Res.*, 2013, **46**, 2275–2285.

232 T. Kuila, A. K. Mishra, P. Khanra, N. H. Kim and J. H. Lee, *Nanoscale*, 2013, **5**, 52–71.

233 Z. Yin, S. Sun, T. Salim, S. Wu, X. Huang, Q. He, Y. M. Lam and H. Zhang, *ACS*

Nano, 2010, **4**, 5263–5268.

234 L. Huang, Y. Huang, J. Liang, X. Wan and Y. Chen, *Nano Res.*, 2011, **4**, 675–684.

235 R. K. Joshi, P. Carbone, F.-C. Wang, V. G. Kravets, Y. Su, I. V Grigorieva, H. A. Wu, A. K. Geim and R. R. Nair, *Science.*, 2014, **343**, 752–754.

236 A. M. Dimiev and S. Eigler, *Graphene Oxide*, John Wiley & Sons, Ltd, Chichester, UK, 2016.

237 J. P. Rourke, P. A. Pandey, J. J. Moore, M. Bates, I. A. Kinloch, R. J. Young and N. R. Wilson, *Angew. Chemie Int. Ed.*, 2011, **50**, 3173–3177.

238 C. Petit, M. Seredych and T. J. Bandosz, *J. Mater. Chem.*, 2009, **19**, 9176–9185.

239 O. Akhavan and E. Ghaderi, *ACS Nano*, 2010, **4**, 5731–5736.

240 F. J. Tölle, K. Gamp and R. Mülhaupt, *Carbon.*, 2014, **75**, 432–442.

241 A. T. Abdel-Motagaly, W. M. A. El Rouby, S. I. El-Dek, I. M. El-Sherbiny and A. A. Farghali, *Diam. Relat. Mater.*, 2018, **86**, 20–28.

242 P. Bhunia, M. Kumar and S. De, *Sep. Purif. Technol.*, 2019, **209**, 103–111.

243 C. Li, Y. Guo, L. Shen, C. Ji and N. Bao, *Chem. Eng. Sci.*, 2019, **200**, 127–137.

244 Y. Shi, X. Ye, L. Shen and N. Bao, *Chem. Eng. Sci.*, 2022, **248**, 117143.

245 K. Krishnamoorthy, M. Veerapandian, K. Yun and S.-J. Kim, *Carbon.*, 2013, **53**, 38–49.

246 L. Stobinski, B. Lesiak, A. Malolepszy, M. Mazurkiewicz, B. Mierzwa, J. Zemek, P. Jiricek and I. Bieloshapka, *J. Electron Spectros. Relat. Phenomena*, 2014, **195**, 145–154.

247 M. S. Seehra and A. S. Pavlovic, *Carbon.*, 1993, **31**, 557–564.

248 X. Díez-Betriu, S. Álvarez-García, C. Botas, P. Álvarez, J. Sánchez-Marcos, C. Prieto, R. Menéndez and A. de Andrés, *J. Mater. Chem. C*, 2013, **1**, 6905–6912.

249 K. N. Kudin, B. Ozbas, H. C. Schniepp, R. K. Prud'homme, I. A. Aksay and R. Car, *Nano Lett.*, 2008, **8**, 36–41.

250 J.-B. Wu, M.-L. Lin, X. Cong, H.-N. Liu and P.-H. Tan, *Chem. Soc. Rev.*, 2018, **47**, 1822–1873.

251 T. Szabó, O. Berkesi and I. Dékány, *Carbon.*, 2005, **43**, 3186–3189.

252 T. Szabó, O. Berkesi, P. Forgó, K. Josepovits, Y. Sanakis, D. Petridis and I. Dékány, *Chem. Mater.*, 2006, **18**, 2740–2749.

253 C. Liu, K. Wang, S. Luo, Y. Tang and L. Chen, *Small*, 2011, **7**, 1203–1206.

254 M. Seredych and T. J. Bandosz, *Langmuir*, 2010, **26**, 5491–5498.

255 S. Y. Toh, K. S. Loh, S. K. Kamarudin and W. R. W. Daud, *Chem. Eng. J.*, 2014, **251**, 422–434.

256 N. Fairley, V. Fernandez, M. Richard-Plouet, C. Guillot-Deudon, J. Walton, E. Smith, D. Flahaut, M. Greiner, M. Biesinger, S. Tougaard, D. Morgan and J. Baltrusaitis, *Appl. Surf. Sci. Adv.*, 2021, **5**, 100112.

257 D. Yang, A. Velamakanni, G. Bozoklu, S. Park, M. Stoller, R. D. Piner, S. Stankovich, I. Jung, D. A. Field and C. A. Ventrice Jr, *Carbon.*, 2009, **47**, 145–152.

258 S. Park, J. An, J. R. Potts, A. Velamakanni, S. Murali and R. S. Ruoff, *Carbon.*, 2011, **49**, 3019–3023.

259 S. Rey and F. Le Normand, *Thin Solid Films*, 2011, **519**, 4426–4428.

260 L.-Z. Fan, J.-L. Liu, R. Ud-Din, X. Yan and X. Qu, *Carbon.*, 2012, **50**, 3724–3730.

261 S. Kundu, Y. Wang, W. Xia and M. Muhler, *J. Phys. Chem. C*, 2008, **112**, 16869–16878.

262 A. Ganguly, S. Sharma, P. Papakonstantinou and J. Hamilton, *J. Phys. Chem. C*, 2011, **115**, 17009–17019.

263 Y. C. G. Kwan, G. M. Ng and C. H. A. Huan, *Thin Solid Films*, 2015, **590**, 40–48.

264 I. Malnarič, B. Alič, M. Krajnc, A. Vesel and U. Šebenik, *Colloids Surfaces A Physicochem. Eng. Asp.*, 2023, **675**, 132012.

265 M. A. Haruna, S. Pervaiz, Z. Hu, E. Nourafkan and D. Wen, *J. Appl. Polym. Sci.*, 2019, **136**, 47582.

266 H. A. Barnes, J. F. Hutton and K. Walters, *An Introduction to Rheology*, Elsevier Science \& Technology, 1989.

267 OriginLab Corporation, 2022.

268 C. Gómez-Navarro, R. T. Weitz, A. M. Bittner, M. Scolari, A. Mews, M. Burghard and K. Kern, *Nano Lett.*, 2007, **7**, 3499–3503.

269 S. Gilje, S. Han, M. Wang, K. L. Wang and R. B. Kaner, *Nano Lett.*, 2007, **7**, 3394–3398.

270 Z. Luo, Y. Lu, L. A. Somers and A. T. C. Johnson, *J. Am. Chem. Soc.*, 2009, **131**, 898–899.

271 C. Wu, G. Dong and L. Guan, *Phys. E Low-dimensional Syst. Nanostructures*, 2010, **42**, 1267–1271.

272 J. Geng, B.-S. Kong, S. B. Yang and H.-T. Jung, *Chem. Commun.*, 2010, **46**, 5091–5093.

273 N. R. Wilson, P. A. Pandey, R. Beanland, R. J. Young, I. A. Kinloch, L. Gong, Z. Liu, K. Suenaga, J. P. Rourke, S. J. York and J. Sloan, *ACS Nano*, 2009, **3**, 2547–2556.

274 J. C. Meyer, A. K. Geim, M. I. Katsnelson, K. S. Novoselov, D. Obergfell, S. Roth, C. Girit and A. Zettl, *Solid State Commun.*, 2007, **143**, 101–109.

275 G. Wang, J. Yang, J. Park, X. Gou, B. Wang, H. Liu and J. Yao, *J. Phys. Chem. C*, 2008, **112**, 8192–8195.

276 A. Wang, W. Yu, Z. Huang, F. Zhou, J. Song, Y. Song, L. Long, M. P. Cifuentes, M. G. Humphrey and L. Zhang, *Sci. Rep.*, 2016, **6**, 23325.

277 G. L. C. Paulus, Q. H. Wang and M. S. Strano, *Acc. Chem. Res.*, 2013, **46**, 160–170.

278 H.-K. Jeong, H.-J. Noh, J.-Y. Kim, M. H. Jin, C. Y. Park and Y. H. Lee, *Europhys. Lett.*, 2008, **82**, 67004.

279 D.-Q. Yang and E. Sacher, *Langmuir*, 2006, **22**, 860–862.

280 V. Bennevault-Celton, O. Maciejak, B. Desmazières and H. Cheradame, *Polym. Int.*, 2010, **59**, 1273–1281.

281 M. Mousavi and E. Fini, *ACS Sustain. Chem. Eng.*, 2020, **8**, 3231–3240.

282 M. Zhu, M. Z. Lerum and W. Chen, *Langmuir*, 2012, **28**, 416–423.

283 H. Hu, S. Zhao, G. Sun, Y. Zhong and B. You, *Prog. Org. Coatings*, 2018, **117**, 118–129.

284 C. Tang, Y. Jiang, L. Chen, J. Sun, Y. Liu, P. Shi, J. Y. Aguilar-Hurtado, A. Rosenkranz and L. Qian, *ACS Nano*, 2023, **17**, 2497–2505.

285 S. S. Abbas, G. J. Rees, N. L. Kelly, C. E. J. Dancer, J. V Hanna and T. McNally, *Nanoscale*, 2018, **10**, 16231–16242.

286 S. Park, Y. Hu, J. O. Hwang, E.-S. Lee, L. B. Casabianca, W. Cai, J. R. Potts, H.-W. Ha, S. Chen, J. Oh, S. O. Kim, Y.-H. Kim, Y. Ishii and R. S. Ruoff, *Nat. Commun.*, 2012, **3**, 638.

287 Y. Xu, J. Loi, P. Delgado, V. Topolkaraev, R. J. McEneany, C. W. Macosko and M. A. Hillmyer, *Ind. Eng. Chem. Res.*, 2015, **54**, 6108–6114.

288 P. Charoensirisomboon, T. Inoue and M. Weber, *Polymer.*, 2000, **41**, 6907–6912.

289 A. Adedeji, S. Lyu and C. W. Macosko, *Macromolecules*, 2001, **34**, 8663–8668.

290 H. Zhao and B. Huang, *J. Polym. Sci. Part B Polym. Phys.*, 1998, **36**, 85–93.

291 S. Huang, L. Bai, M. Trifkovic, X. Cheng and C. W. Macosko, *Macromolecules*, 2016, **49**, 3911–3918.

292 S. S. Ray, S. Pouliot, M. Bousmina and L. A. Utracki, *Polymer.*, 2004, **45**, 8403–8413.

293 E. Cohen, L. Zonder, A. Ophir, S. Kenig, S. McCarthy, C. Barry and J. Mead, *Macromolecules*, 2013, **46**, 1851–1859.

294 T. Gegenhuber, M. Krekhova, J. Schöbel, A. H. Gröschel and H. Schmalz, *ACS Macro Lett.*, 2016, **5**, 306–310.

295 Y. Kou, A. T. Cote, J. Liu, X. Cheng and C. W. Macosko, *J. Rheol.*, 2021, **65**, 1139–1153.

296 C. W. Macosko, H. K. Jeon and T. R. Hoye, *Prog. Polym. Sci.*, 2005, **30**, 939–947.

297 X. Zhang, X. Xue, Q. Yin, H. Jia, J. Wang, Q. Ji and Z. Xu, *Compos. Part B Eng.*, 2017, **111**, 243–250.

298 H. Wang, Z. Fu, X. Zhao, Y. Li and J. Li, *ACS Appl. Mater. Interfaces*, 2017, **9**, 14358–14370.

299 Z. Fu, H. Wang, X. Zhao, X. Li, X. Gu and Y. Li, *J. Mater. Chem. A*, 2019, **7**, 4903–4912.

300 X. Li, Z. Fu, X. Gu, H. Liu, H. Wang and Y. Li, *Compos. Part B Eng.*, 2020, **198**, 108153.

301 Z. Fu, H. Wang, X. Zhao, S. Horiuchi and Y. Li, *Polymer.*, 2017, **132**, 353–361.

302 X. Zuo, Y. Xue, L. Wang, Y. Zhou, Y. Yin, Y.-C. Chuang, C.-C. Chang, R. Yin, M. H. Rafailovich and Y. Guo, *Macromolecules*, 2019, **52**, 7547–7556.

303 M. Baumert and R. Mülhaupt, *Macromol. Rapid Commun.*, 1997, **18**, 787–794.

304 B. Wei, Q. Lin, X. Zheng, X. Gu, L. Zhao, J. Li and Y. Li, *Polymer.*, 2019, **185**, 121952.

305 H. Kakiuchi and Y. Tanaka, *J. Org. Chem.*, 1966, **31**, 1559–1564.

306 P. C. Ma, J.-K. Kim and B. Z. Tang, *Carbon.*, 2006, **44**, 3232–3238.

307 C. Girardeaux and J.-J. Pireaux, *Surf. Sci. Spectra*, 1996, **4**, 130–133.

308 S. Bhattacharjee, *J. Control. Release*, 2016, **235**, 337–351.

309 C. A. Schneider, W. S. Rasband and K. W. Eliceiri, *Nat. Methods*, 2012, **9**, 671–675.

310 A. Honciuc and O.-I. Negru, *Nanomaterials*, 2023, **13**, 1246.

311 S. Wu, *Polymer interface and adhesion*, Marcel Dekker, New York, First edit., 2017.

312 S. Wang, Y. Zhang, N. Abidi and L. Cabrales, *Langmuir*, 2009, **25**, 11078–11081.

313 S. Wang, Y. Zhang, N. Abidi and L. Cabrales, *Langmuir*, 2009, **25**, 11078–11081.

314 S. L. Scherzer, E. Pavlova, J. D. Esper and Z. Starý, *Compos. Sci. Technol.*, 2015, **119**, 138–147.

315 K. Dai, X.-B. Xu and Z.-M. Li, *Polymer.*, 2007, **48**, 849–859.

316 A. Göldel, G. Kasaliwal and P. Pötschke, *Annu. Tech. Conf. - ANTEC, Conf. Proc.*, 2009, **5**, 2662–2669.

317 P. Pötschke, S. Pegel, M. Claes and D. Bonduel, *Macromol. Rapid Commun.*, 2008, **29**, 244–251.

318 L. Xu, B. Y. Zhang, Z. Y. Xiong, Z. X. Guo and J. Yu, *J. Appl. Polym. Sci.*, 2015, **132**, 1–8.

319 C. J. Lee, R. Salehiyan, D. S. Ham, S. K. Cho, S. J. Lee, K. J. Kim, Y. Yoo, K. Hyun, J. H. Lee and W. J. Choi, *Polymer.*, 2016, **84**, 198–208.

320 C. Ringard-Lefebvre and A. Baszkin, *Langmuir*, 1994, **10**, 2376–2381.

321 G. Biresaw and C. J. Carriere, *J. Polym. Sci. Part B Polym. Phys.*, 2002, **40**, 2248–2258.

322 H. M. Lee and O. O. Park, *J. Rheol.*, 1994, **38**, 1405–1425.

323 C. R. López-Barrón and C. W. Macosko, *J. Rheol.*, 2012, **56**, 1315–1334.

324 W. Yu, W. Zhou and C. Zhou, *Polymer.*, 2010, **51**, 2091–2098.

325 I. Vinckier, P. Moldenaers and J. Mewis, *J. Rheol.*, 1996, **40**, 613–631.

326 X. Zhao, H. Wang, Z. Fu and Y. Li, *ACS Appl. Mater. Interfaces*, 2018, **10**, 8411–

8416.

327 H. Kim, A. A. Abdala and C. W. Macosko, *Macromolecules*, 2010, **43**, 6515–6530.

328 J. Vermant, S. Ceccia, M. K. Dolgovskij, P. L. Maffettone and C. W. Macosko, *J. Rheol.*, 2007, **51**, 429–450.

329 A. Paydayesh, A. Arefazar and A. Jalaliarani, *J. Appl. Polym. Sci.*, 2016, **133**, 1–12.

330 T. Gong, S.-P. Peng, R.-Y. Bao, W. Yang, B.-H. Xie and M.-B. Yang, *Compos. Part B Eng.*, 2016, **99**, 348–357.

331 T. Khan, M. S. Irfan, M. Ali, Y. Dong, S. Ramakrishna and R. Umer, *Carbon.*, 2021, **176**, 602–631.

332 S. C. Boothroyd, D. W. Johnson, M. P. Weir, C. D. Reynolds, J. M. Hart, A. J. Smith, N. Clarke, R. L. Thompson and K. S. Coleman, *Chem. Mater.*, 2018, **30**, 1524–1531.

333 K. P. Menard and N. Menard, *Dynamic mechanical analysis*, CRC press, Boca Ratón, Florida, 3rd Editio., 2020.

334 N. T. Kilic, B. N. Can, M. Kodal and G. Özkoç, *Prog. Rubber, Plast. Recycl. Technol.*, 2021, **37**, 301–326.

335 W. H. Ferreira and C. T. Andrade, *J. Therm. Anal. Calorim.*, 2021, **143**, 3107–3115.

336 S.-L. Yang, Z.-H. Wu, B. Meng and W. Yang, *J. Polym. Sci. Part B Polym. Phys.*, 2009, **47**, 1136–1145.

337 E. L. Thomas and Y. Talmon, *Polymer.*, 1978, **19**, 225–227.

338 R. Al-Itry, K. Lamnawar and A. Maazouz, *Polym. Degrad. Stab.*, 2012, **97**, 1898–1914.

339 L. Quiles-Carrillo, N. Montanes, J. M. Lagaron, R. Balart and S. Torres-Giner, *J. Polym. Environ.*, 2019, **27**, 84–96.

340 J. C. Lee, M.-C. Choi, D.-H. Choi and C.-S. Ha, *Polym. Degrad. Stab.*, 2019, **160**, 195–202.

341 E. Martínez-Mercado, F. A. Ruiz-Treviño, A. González-Montiel, L. E. Lugo-Uribe and L. Flores-Santos, *J. Polym. Res.*, 2019, **26**, 260.

342 A. Mirzadeh, H. Ghasemi, F. Mahrous and M. R. Kamal, *J. Appl. Polym. Sci.*, 2015, **132**, 42664.

343 B. Xue, H. He, Z. Zhu, J. Li, Z. Huang, G. Wang, M. Chen and Z. Zhan, *Polymers.*, 2018, **10**, 1401.

344 J. Cailloux, O. Santana, M. L. Maspoch, J. J. Bou and F. Carrasco, *J. Rheol.*, 2015, **59**, 1191–1227.

345 X. Yu, X. Wang, Z. Zhang, S. Peng, H. Chen and X. Zhao, *Polym. Test.*, 2019, **78**, 105980.

346 J.-C. Lee, D.-H. Choi, J.-Y. Choi and C.-S. Ha, *Macromol. Res.*, 2020, **28**, 327–335.

347 F. Gubbels, R. Jérôme, P. Teyssié, E. Vanlathem, R. Deltour, A. Calderone, V. Parenté and J. L. Brédas, *Macromolecules*, 1994, **27**, 1972–1974.

348 J. Huang, C. Mao, Y. Zhu, W. Jiang and X. Yang, *Carbon.*, 2014, **73**, 267–274.

349 H. Tian, T.-L. Ren, D. Xie, Y.-F. Wang, C.-J. Zhou, T.-T. Feng, D. Fu, Y. Yang, P.-G. Peng and L.-G. Wang, *ACS Nano*, 2011, **5**, 4878–4885.

350 S. Kabiri Ameri, R. Ho, H. Jang, L. Tao, Y. Wang, L. Wang, D. M. Schnyer, D. Akinwande and N. Lu, *ACS Nano*, 2017, **11**, 7634–7641.

351 Y. Yang, X. Yang, X. Zou, S. Wu, D. Wan, A. Cao, L. Liao, Q. Yuan and X. Duan, *Adv. Funct. Mater.*, 2017, **27**, 1604096.

352 N. S. S. Capman, X. V Zhen, J. T. Nelson, V. R. S. K. Chaganti, R. C. Finc, M. J. Lyden, T. L. Williams, M. Freking, G. J. Sherwood, P. Bühlmann, C. J. Hogan and S. J. Koester, *ACS Nano*, 2022, **16**, 19567–19583.

353 S. Liu, Y. Rao, H. Jang, P. Tan and N. Lu, *Matter*, 2022, **5**, 1104–1136.

354 L. Wang and N. Lu, *J. Appl. Mech.*, 2016, **83**, 41007.

355 D. Kireev, S. K. Ameri, A. Nederveld, J. Kampfe, H. Jang, N. Lu and D. Akinwande,

Nat. Protoc., 2021, **16**, 2395–2417.

356 J.-W. Jeong, W.-H. Yeo, A. Akhtar, J. J. S. Norton, Y.-J. Kwack, S. Li, S.-Y. Jung, Y. Su, W. Lee, J. Xia, H. Cheng, Y. Huang, W.-S. Choi, T. Bretl and J. A. Rogers, *Adv. Mater.*, 2013, **25**, 6839–6846.

357 S. Qiao, J.-B. Gratadour, L. Wang and N. Lu, *IEEE Trans. Components, Packag. Manuf. Technol.*, 2015, **5**, 1237–1243.

358 L. Wang, S. Qiao, S. Kabiri Ameri, H. Jeong and N. Lu, *J. Appl. Mech.*, 2017, **84**, 111003.

359 T. J. W. Wagner and D. Vella, *Appl. Phys. Lett.*, 2012, **100**, 233111.

360 D. Yoon, H. Moon, H. Cheong, J. S. Choi, J. A. Choi and B. H. Park, *J. Korean Phys. Soc*, 2009, **55**, 1299–1303.

361 S. P. Koenig, N. G. Boddeti, M. L. Dunn and J. S. Bunch, *Nat. Nanotechnol.*, 2011, **6**, 543–546.

362 W. Jung, D. Kim, M. Lee, S. Kim, J.-H. Kim and C.-S. Han, *Adv. Mater.*, 2014, **26**, 6394–6400.

363 Y. T. Megra, S. Lim, T. Lim, S. R. Na and J. W. Suk, *Appl. Surf. Sci.*, 2021, **570**, 151243.

364 The MathWorks Inc., 2022.

365 D. Kireev, J. Kampfe, A. Hall and D. Akinwande, *npj 2D Mater. Appl.*, 2022, **6**, 46.

366 J. A. Barrie and D. Machin, *Trans. Faraday Soc.*, 1971, **67**, 244–256.

367 M. Wang, E. H. Yang, R. Vajtai, J. Kono and P. M. Ajayan, *J. Appl. Phys.*, 2018, **123**, 195103.

368 X. Yang and M. Yan, *Nano Res.*, 2020, **13**, 599–610.

369 L. H. Karlsson, J. Birch, A. Mockute, A. S. Ingason, H. Q. Ta, M. H. Rummeli, J. Rosen and P. O. Å. Persson, *Carbon.*, 2016, **100**, 345–350.

370 P. E. Keller and R. T. Kouzes, *Water vapor permeation in plastics*, Pacific Northwest National Lab.(PNNL), Richland, WA (United States), 2017.

371 H. Wu, G. Yang, K. Zhu, S. Liu, W. Guo, Z. Jiang and Z. Li, *Adv. Sci.*, 2021, **8**, 2001938.

372 R. Kusche, S. Kaufmann and M. Ryschka, *Biomed. Phys. Eng. Express*, 2018, **5**, 15001.

373 L. M. Ferrari, K. Keller, B. Burtscher and F. Greco, *Multifunct. Mater.*, 2020, **3**, 32003.

374 A. J. Bandodkar, W. Jia and J. Wang, *Electroanalysis*, 2015, **27**, 562–572.

375 S. Wang, M. Li, J. Wu, D.-H. Kim, N. Lu, Y. Su, Z. Kang, Y. Huang and J. A. Rogers, *J. Appl. Mech.*, 2012, **79**, 031022.

376 L. Tchvialeva, H. Zeng, I. Markhvida, D. I. McLean, H. Lui and T. K. Lee, *New Dev. Biomed. Eng.*, 2010, 341–358.

377 X. Liang and S. A. Boppart, *IEEE Trans. Biomed. Eng.*, 2010, **57**, 953–959.

378 C. Ishiyama and Y. Higo, *J. Polym. Sci. Part B Polym. Phys.*, 2002, **40**, 460–465.

Appendix A

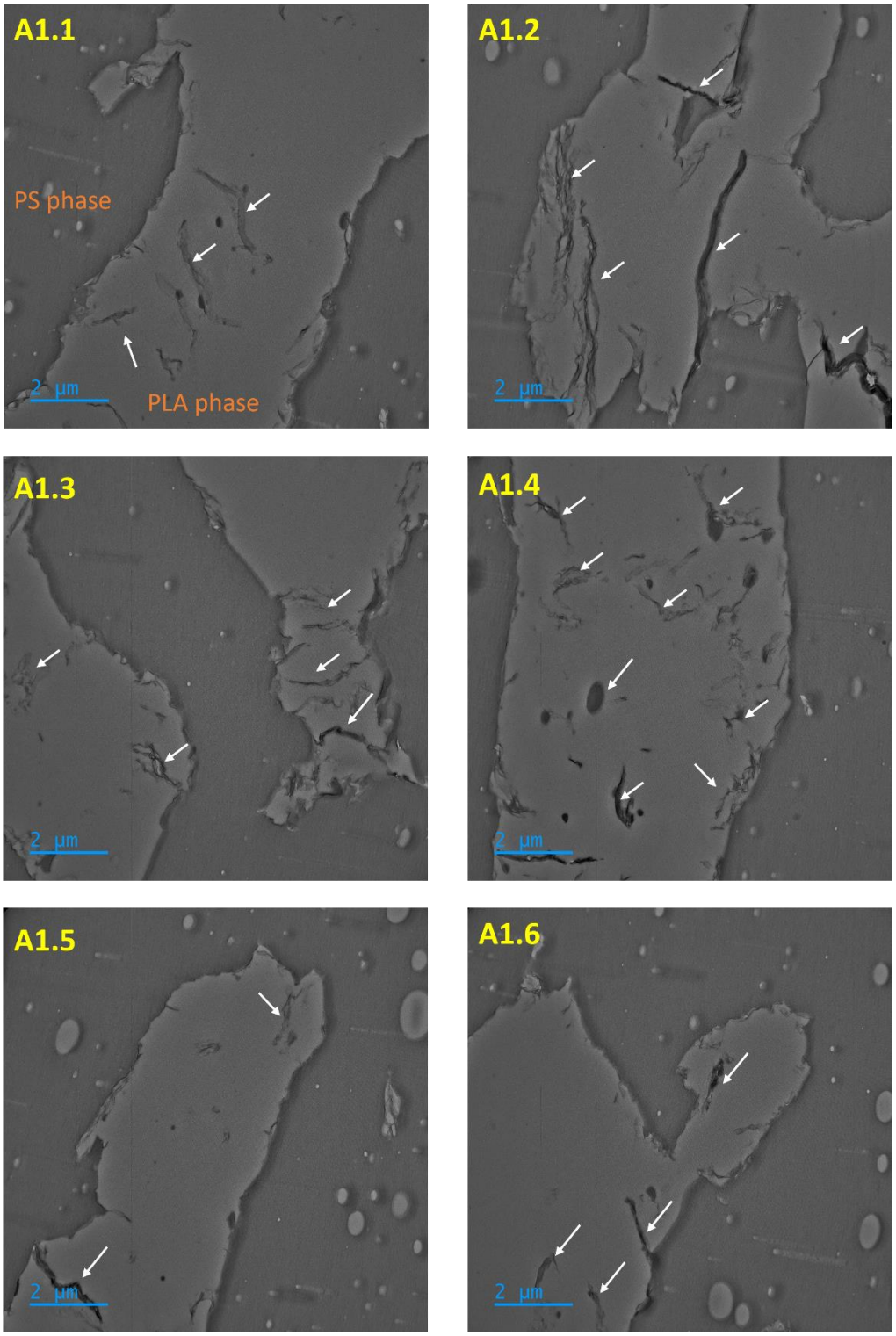

A1.1-A1.6 TEM images showing the reactive graphene platelets localized at the interface between PLA and PS. As explained in section 5.2.9 darker regions correspond to the PS phase and brighter ones correspond to the PLA phase. White arrows point at platelets that remained in the PLA phase.

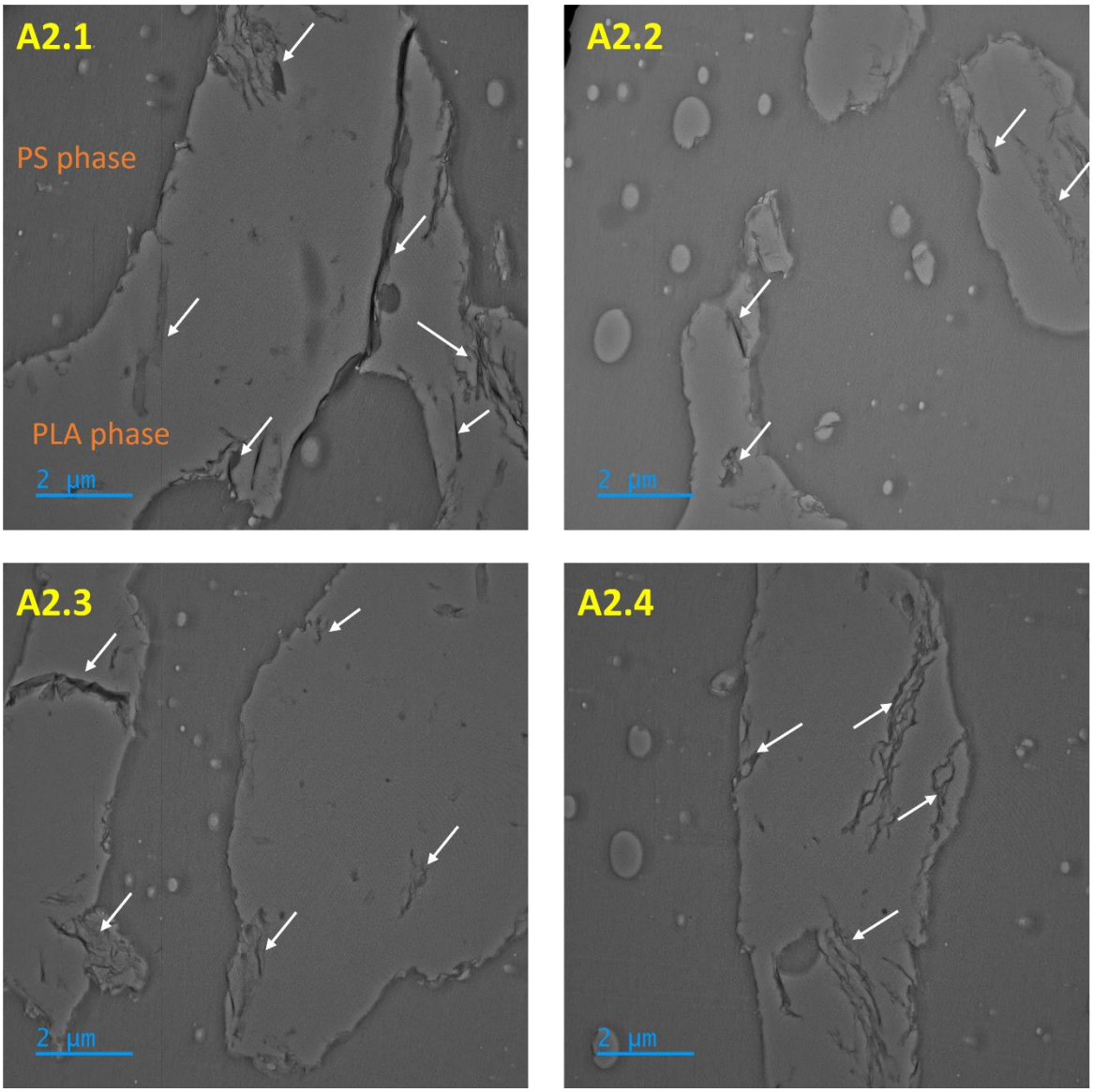

A2.1-A2.4 TEM images showing the reactive graphene platelets localized at the interface between PLA and PS. As explained in section 5.2.9 darker regions correspond to the PS phase and brighter ones correspond to the PLA phase. White arrows point at platelets that remained in the PLA phase.

.

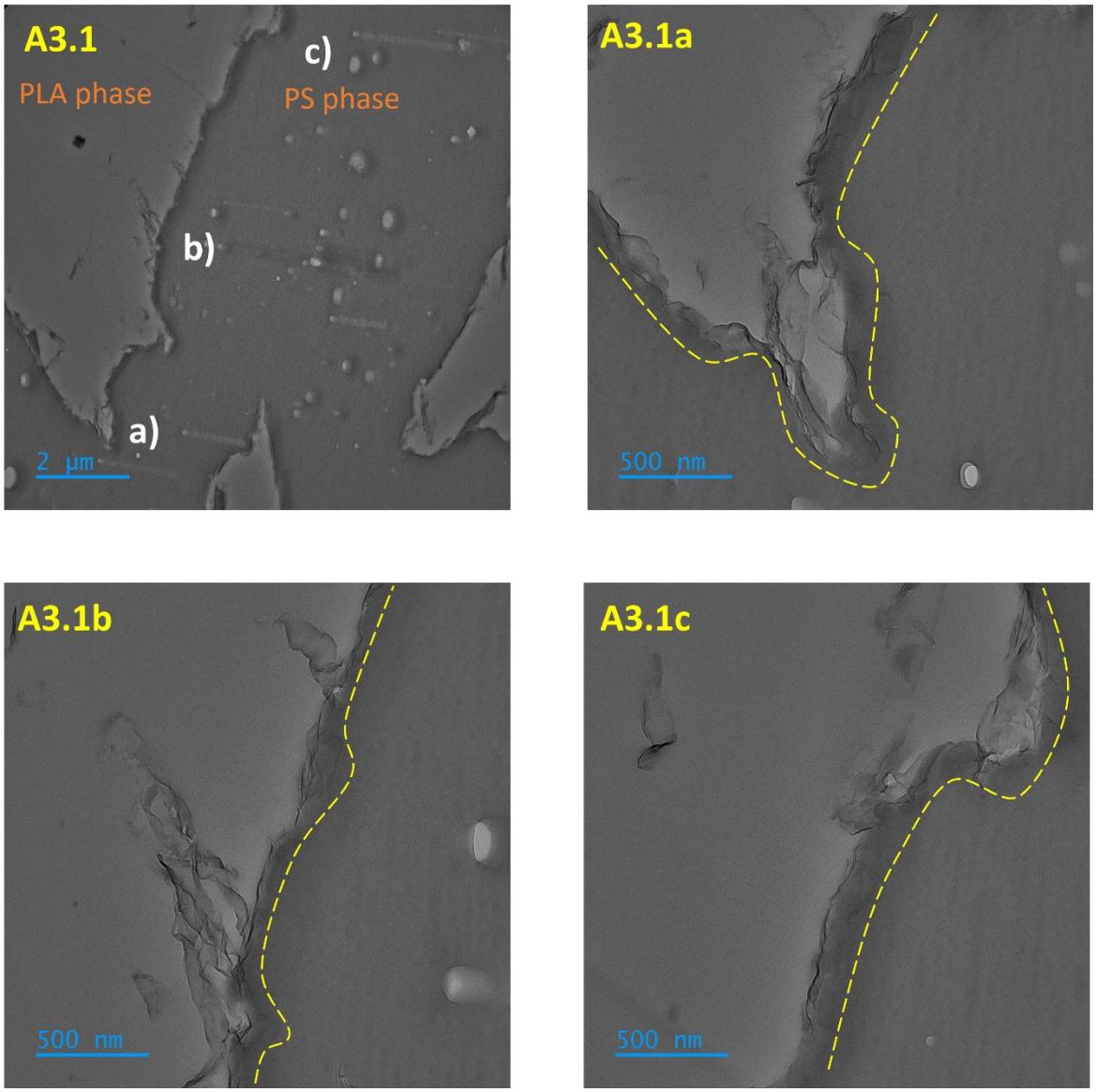

A3.1 TEM image showing regions where the reactive graphene platelets is localized at the interface between PLA and PS. A3.1a-c) Higher magnification on the areas shown in a,b and c. Yellow dashed lines highlight regions where graphene is interfacially located.

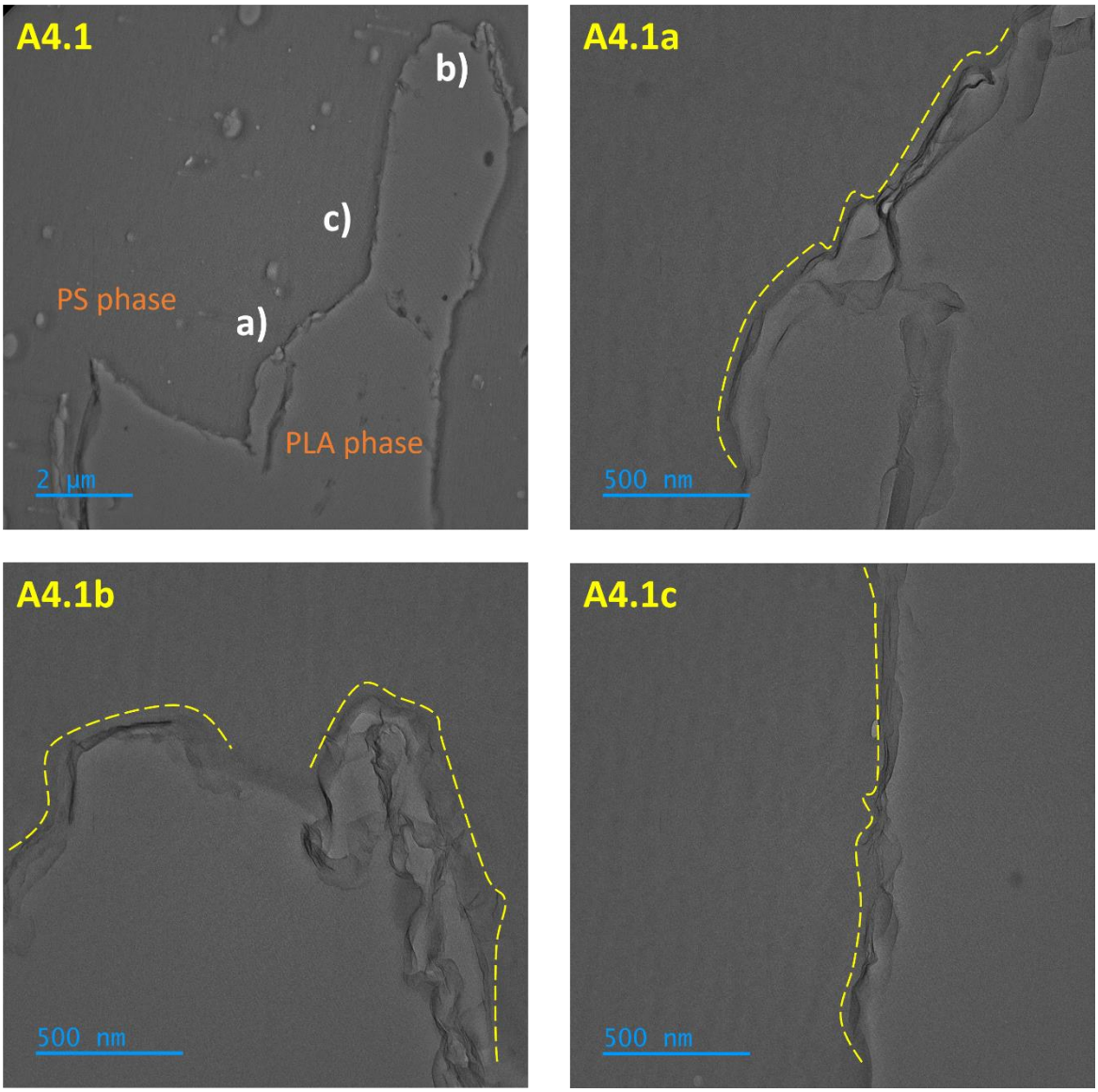

A4.1 TEM image showing regions where the reactive graphene platelets is localized at the interface between PLA and PS. A4.1a-c) Higher magnification on the areas shown in a,b and c. Yellow dashed lines highlight regions where graphene is interfacially located.

Appendix B

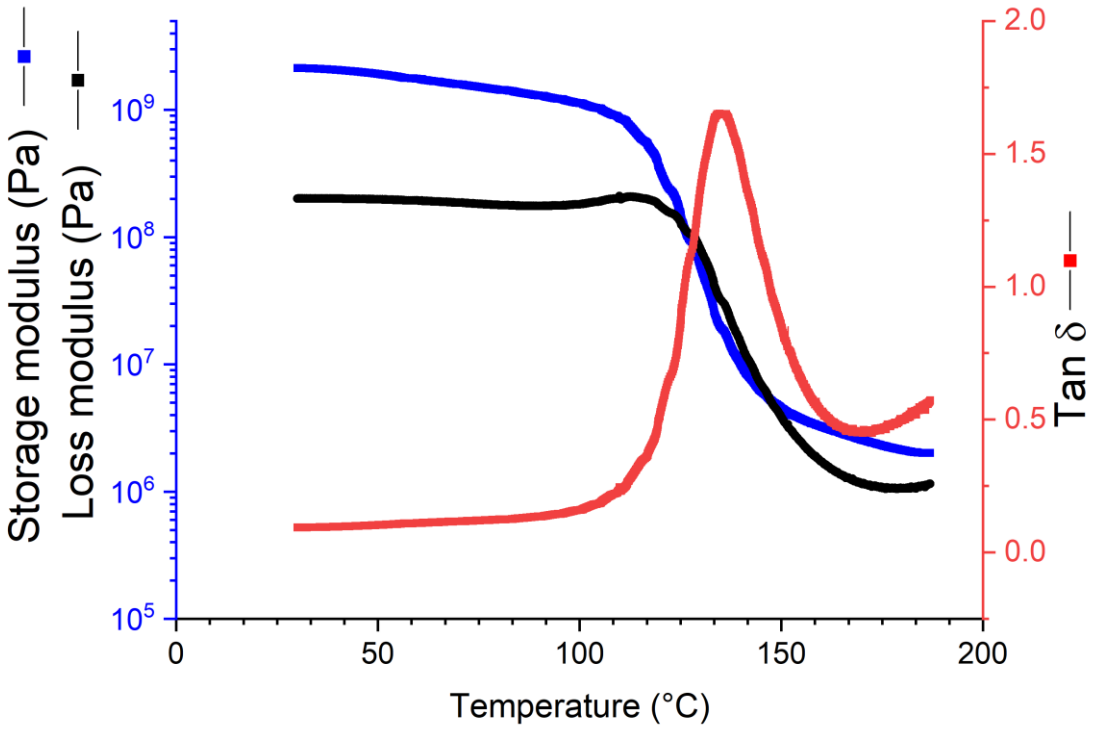

B1 Dynamic mechanical analysis of the PMMA (Sigma Aldrich, MW~120 000) used here.